The development of partially coherent X-ray beam ptychography and adaptable optics for the study of nanomaterials



Thomas E. J. Moxham

Trinity College

University of Oxford

A thesis submitted for the degree of

Doctor of Philosophy

Trinity 2022

Abstract

Advances in synchrotron and X-ray free electron laser (XFEL) sources have led to ptychography emerging as a powerful tool in X-ray microscopy. Ptychography uses overlapping diffraction patterns scanned across a sample and computational techniques to reconstruct the complex probe and sample transmission functions with spatial resolutions beyond the image forming optics. Ptychography's ability to reconstruct the complex probe has seen it widely adopted as a metrology technique, particularly as focal sizes approach ever smaller length regimes. However, most sources do not yet produce completely coherent beams, which had previously restricted ptychography to specialised, high-coherence beamlines. Including a multimodal probe in the reconstruction algorithm developed in the presented study has alleviated this requirement, making it more widely accessible. As sources have evolved, so has the need for high quality X-ray optics for focusing. Aberrations introduced during fabrication degrade the performance of X-ray optics and their ability to achieve diffraction limited focusing. Corrective optics are a new method that can counteract these errors by introducing controlled wavefront modifications before the optic, which cancels out the distortions.

This thesis consolidates a range of work centred on improving the understanding of partially coherent ptychography. This includes successfully implementing partially coherent ptychography as an imaging and X-ray optic metrology technique developed for the B16 Test beamline at Diamond Light Source. And then its subsequent development into an at-wavelength metrology technique for characterising fabrication aberrations of X-ray optics. A new class of dynamic corrective optics is demonstrated and characterised using the aforementioned ptychography technique. The results will apply to a wide variety of high numerical aperture X-ray optics aiming to achieve diffraction limited focusing. Finally, some typical applications of partially coherent and regular ptychography are presented as case studies of nano-

materials. Gold nanoparticles are used to validate the imaging capabilities of the partially coherent ptychography technique and discuss how other decoherence effects can be accounted for, such as fly-scan ptychography. The processing steps of a typical ptychotomography experiment studying silica diatoms are presented, and the associated coherent properties are examined.

Acknowledgements

I would like to express my sincerest gratitude to my three supervisors Prof. Alexander Korsunsky, Dr. David Laundy and Dr. Kawal Sawhney, without whom most of this work would not have been possible. Together they have provided great insights into the various fields covered within the thesis and taught me a considerable wealth of information. It has been a true pleasure to work with them. I would like to thank the B16 beamline staff at Diamond Light Source, namely Dr. Oliver Fox, Dr. Vishal Dhamgaye and Mr. Andrew Malandain. They have been incredibly supportive and accommodating through numerous experimental sessions. I would also be remiss if I didn't mention my gratitude towards Dr. Aaron Parson for introducing me to ptychography and Dr. Benedikt Daurer for his later support on the ptypy project. I would also like to thank my Oxford colleagues, in particular, Dr. Cyril Besnard, Dr. Enrico Salvati, Dr. Leon Romano-Brandt, Dr. Sisini Sasidharan and Dr. Ali Marie, for their support during experimental sessions, intriguing discussions and assistance in performing SEM imaging.

The author acknowledges the receipt of a fully funded scholarship from the Department of Engineering Science, University of Oxford and Diamond Light Source in support of this research. Additionally, several scholarships and funding opportunities were provided by Trinity College, University of Oxford, including two academic graduate scholarships, a writing grant, and Kandiah Thirunavukkarasu scholarship. I also thank Diamond Light Source for providing access to numerous experimental sessions on the B16 and I13-1 beamlines and the use of HPC computing facilities that contributed to the results presented in this work. Colleagues are acknowledged for their technical assistance during the X-ray lithography fabrication at the Indus-2 facility. I thank Dr. Arndt Last from IMT/KIT for providing the LIGA gold knife edge. Finally, I thank my fiance, family and friends who have supported me unreservedly throughout all my endeavours.

Publications

Listed below are the publications resulting from the work presented in this thesis and the author's contribution. Additional publications not directly relevant to the body of work but which have still benefited from it or where the author made a substantial contribution have also been given.

First author publications

- Thomas E. J. Moxham, Aaron Parsons, Tuhne Zhou, Lucia Alianelli, Hongchang Wang, David Laundy, Vishal Dhamgaye, V., Oliver J. L. Fox, Kawal Sawhney & Alexander M. Korsunsky, "Hard X-ray ptychography for optics characterization using a partially coherent synchrotron source," *J. Synchrotron Rad.* **27**, 1688-1695 (2020). https://doi.org/10.1107/S1600577520012151

  Contribution: Theoretical conception, carrying out experimental data collection, writing processing software code, processing experimental data and writing the draft of the paper.

- Thomas E. J. Moxham, David Laundy, Vishal Dhamgaye, Oliver J. L. Fox, Kawal Sawhney, and Alexander M. Korsunsky, "Aberration characterization of x-ray optics using multi-modal ptychography and a partially coherent source," *Appl. Phys. Lett.* **118**, 104104 (2021). https://doi.org/10.1063/5.0041341

  Contribution: Theoretical conception, developing the background and theory, carrying out experimental data collection, writing processing software code, processing experimental data and writing the draft of the paper.

- Thomas E. J. Moxham, Vishal Dhamgaye, David Laundy, Oliver J. L. Fox, Hossein Khosroabadi, Kawal Sawhney, and Alexander M. Korsunsky, "Two-dimensional wavefront characterization of adaptable corrective optics and Kirkpatrick–Baez mirror system using ptychography," *Opt. Express* **30**, 9 (2022). https://doi.org/10.1364/OE.453239

Contribution: Theoretical conception, carrying out experimental data collection, writing processing software code, running model simulations, processing experimental data and writing the draft of the paper.

Co-author publications (Related)

- Kawal Sawhney, David Laundy, Thomas E. J. Moxham, Oliver J. Fox, and Vishal Dhamgaye, "Development of pseudo-perfect x-ray optics using refractive compensators," *AIP Conference Proceedings* **2054**, 060003 (2019). https://doi.org/10.1063/1.5084634

  Contribution: Carrying out experimental data collection, writing part of the draft paper.

- David Laundy, Vishal Dhamgaye, Thomas E. J. Moxham, and Kawal Sawhney, "Adaptable refractive correctors for x-ray optics," *Optica* **6**, 1484-1490 (2019). https://doi.org/10.1364/OPTICA.6.001484

  Contribution: Theoretical conception, carrying out experimental data collection, processing experimental data.

- Vishal Dhamgaye, David Laundy, Sara Baldock, Thomas E. J. Moxham and Kawal Sawhney, "Correction of the X-ray wavefront from compound refractive lenses using 3D printed refractive structures," *J. Synchrotron Rad.* **27**, 1518–1527 (2020). https://doi.org/10.1107/S1600577520011765

  Contribution: Carrying out experimental data collection.

- León Romano Brandt, John-Joseph Marie, Thomas E. J. Moxham, Dominic P. Förstermann, Enrico Salvati, Cyril Besnard, Chrysanthi Papadaki, Zifan Wang, Peter G. Bruce and Alexander M. Korsunsky, "Synchrotron X-ray quantitative evaluation of transient deformation and damage phenomena in a single nickel-rich cathode particle," *Energy Environ. Sci.* **13**, 3556-3566 (2020). https://doi.org/10.1039/D0EE02290J

Contribution: Carrying out experimental data collection, processing experimental data, writing part of the draft paper.

Co-author publications (Other)

- Cyril Besnard, Robert A. Harper, Thomas E. J. Moxham, Jonathan D. James, Malte Storm, Enrico Salvati, Gabriel Landini, Richard M. Shelton and Alexander M. Korsunsky, "3D analysis of enamel demineralisation in human dental caries using high-resolution, large field of view synchrotron X-ray micro-computed tomography," *Mater. Today Commun.* **27** 2352-4928 (2021). https://doi.org/10.1016/j.mtcomm.2021.102418

- Cyril Besnard, Robert A. Harper, Enrico Salvati, Thomas E. J. Moxham, León Romano Brandt, Gabriel Landini, Richard M. Shelton and Alexander M. Korsunsky, "Analysis of in vitro demineralised human enamel using multi-scale correlative optical and scanning electron microscopy, and high-resolution synchrotron wide-angle X-ray scattering," *Materials & Design* **206** 0264-1275 (2021). https://doi.org/10.1016/j.matdes.2021.109739

- Enrico Salvati, Cyril Besnard, Robert A. Harper, Thomas E. J. Moxham, Richard M. Shelton, Gabriel Landini and Alexander M. Korsunsky, "Finite Element Modelling and Experimental Validation of the Enamel Demineralisation Process at the Rod Level," *J. Adv. Res.* **29** 2090-1232 (2021). https://doi.org/10.1016/j.jare.2020.08.018

- León Romano-Brandt, Enrico Salvati, Eric Le Bourhis, Thomas E. J. Moxham, Igor P. Dolbnya and Alexander M. Korsunsky, "Nano-scale residual stress depth profiling in Cu/W nano-multilayers as a function of magnetron sputtering pressure," *Surface and Coatings Technology* **381** 0257-8972 (2020). https://doi.org/10.1016/j.surfcoat.2019.125142

- Eugene S. Statnik, Alexey I. Salimon, Cyril Besnard, Jingwei Chen, Zifan Wang, Thomas E. J. Moxham, Igor P. Dolbnya and Alexander M. Korsunsky, "Ovine Bone Morphology and Deformation Analysis Using Synchrotron X-ray Imaging and Scattering," *Quantum Beam Sci.* **4** 2412-382X (2020). https://doi.org/10.3390/qubs4030029

- Fatih Uzun, Alexey I. Salimon, Eugene S. Statnik, Cyril Besnard, Jingwei Chen, Thomas E. J. Moxham, Enrico Salvati, Zifan Wang and Alexander M. Korsunsky, "Polar transformation of 2D X-ray diffraction patterns and the experimental validation of the hDIC technique," *Measurement* **151** 0263-2241 (2020). https://doi.org/10.1016/j.measurement.2019.107193

- Enrico Salvati, Cyril Besnard, Robert A. Harper, Thomas E. J. Moxham, Richard M. Shelton, Gabriel Landini, and Alexander M. Korsunsky. "Crack Tip Stress Field Analysis of Crack Surface Contact and Opening during In Situ Wedge Loading of Human Enamel." *Key Engineering Materials* **827** 85–91 (2019). https://doi.org/10.4028/www.scientific.net/kem.827.85

- Benjamin de Jager, Thomas E. J. Moxham, Cyril Besnard, Enrico Salvati, Jingwei Chen, Igor P. Dolbnya and Alexander M.Korsunsky, "Synchrotron X-ray Scattering Analysis of Nylon-12 Crystallisation Variation Depending on 3D Printing Conditions," *Polymers* **12** 2073-4360 (2020). https://doi.org/10.3390/polym12051169

Contents

1 Introduction **2**

2 Principles of X-ray optics & synchrotron radiation **7**

2.1 X-ray sources & properties 7

2.1.1 Bending magnets & insertion devices 8

2.1.2 Source emittance and brilliance 11

2.2 Interaction with matter 13

2.3 X-ray detectors 17

2.4 Optical elements 20

2.4.1 Numerical aperture 21

2.4.2 Compound refractive lenses 22

2.4.3 Fresnel zone plates 26

2.4.4 Kirkpatrick–Baez mirror 27

2.5 Scanning and full-field microscopy 30

2.6 Wavefront propagation 31

2.6.1 The Helmholtz equation 32

2.6.2 Rayleigh-Sommerfeld solution 33

2.6.3 Fresnel & paraxial approximation 34

2.6.4 Fraunhofer diffraction 36

2.6.5 Projection approximation 36

3 Ptychography & diffractive imaging **39**

3.1 Background and theory 39

3.1.1 Single-shot coherent diffraction imaging 39

3.1.2 Ptychography extension 43

3.2 Iterative phase retrieval 45

3.2.1 Difference map algorithm 46

3.2.2 Extended ptychographic iterative engine 47
3.3 Probe illumination 49
3.4 Partially coherent ptychography 51
3.4.1 Statistical correlation functions 51
3.4.2 Spectral decomposition 52
3.4.3 Quasi-monochromatic approximation 53
3.4.4 Coherent mode representation 54
3.5 Oversampling criteria 56
3.6 Resolution evaluation 59
3.7 Software packages 61

4 Optics characterisation using ptychography 64

4.1 The wavefront error 64
4.2 Focal size factors 65
4.2.1 Strehl ratio and rms error 67
4.2.2 Zernike polynomials 68
4.3 Coherent ptychography metrology 69
4.3.1 Experimental data collection 70
4.3.2 Ptychography reconstruction 72
4.3.3 Beam caustic & focal properties 74
4.3.4 Wavefront characterisation 76
4.4 Optimising source coherence 78
4.5 Partially coherent ptychography metrology 79
4.5.1 Focal properties 80
4.5.1.1 Experimental setup 81
4.5.1.2 Ptychography reconstruction 83
4.5.1.3 Beam caustic & focal properties 86
4.5.2 Source coherence properties 87
4.5.3 Aberration characterisation 91

4.5.3.1 Theory & background 92
4.5.3.2 Experimental setup 94
4.5.3.3 Reconstruction processing 97
4.5.3.4 Beam and focal properties 100
4.5.4 Comparison with previous results 102
4.6 Results & discussion 104

5 Aberration correction using refractive structures 107
5.1 Corrective optics methods 107
5.1.1 Custom planar structures 109
5.1.2 Fabrication methods 112
5.1.3 Radially symmetric structures 114
5.2 Knife edge scanning 115
5.3 Adaptable corrective structures 118
5.3.1 Theory & background 118
5.3.2 Experimental setup 121
5.3.3 Results & discussion 125
5.4 Kirkpatrick–Baez mirror correction 126
5.4.1 Experimental setup 128
5.4.2 Ptychography reconstructions 131
5.4.3 Wavefront characterisation 132
5.4.4 Focal profile results 136
5.4.5 Simulated scanning microscopy 138
5.5 Results & discussion 141

6 Applications to nanomaterials 143
6.1 Branched gold microflower ptychography 143
6.1.1 Sample preparation 144
6.1.2 High resolution partially coherent ptychography 146

6.1.2.1 Experimental data collection . . . 146
6.1.2.2 Ptychography reconstructions . . . 148
6.1.2.3 Spatial resolution analysis . . . 151
6.1.2.4 Further improvements . . . 153
6.1.3 Probe overlap & fly-scan ptychography . . . 154
6.1.3.1 Experimental data collection . . . 154
6.1.3.2 Single & multi-modal reconstructions . . . 157
6.1.3.3 Effect of probe overlap . . . 159
6.1.4 Results & discussion . . . 161
6.2 Ptychotomography of silica diatoms . . . 163
6.2.1 Sample preparation . . . 165
6.2.2 Experimental data collection . . . 165
6.2.3 Ptychography processing . . . 167
6.2.3.1 Algorithm optimisation . . . 168
6.2.3.2 Decoherence analysis . . . 171
6.2.3.3 Projection phase processing . . . 172
6.2.4 Tomographic processing . . . 174
6.2.4.1 Alignment of projections . . . 174
6.2.4.2 Tomography reconstructions . . . 177
6.2.4.3 Morphology & electron density . . . 177
6.2.5 Spatial resolution . . . 182
6.2.6 Results & discussion . . . 183

7 Conclusion **185**

Bibliography **188**

List of Symbols

λ wavelength

E energy

ω spectral frequency

k wavenumber

δ refractive index decrement

β real part of refractive index

n refractive index

r_e classical electron radius

n_e electron density

N_a Avogadro constant

$\boldsymbol{k}$ wavevector

μ absorption coefficient

$\boldsymbol{r}$ real space coordinate

$\boldsymbol{q}$ reciprocal space coordinate

γ Lorentz factor

$\hbar$ reduced Planck constant

$w(x, y)$ wavefront error

ΔX path length difference

$\Delta\varphi$ phase difference

σ_{rms} RMS wavefront error

$I(\boldsymbol{r})$ far-field intensity

$\mathcal{F}$ Fourier transform

$\mathcal{F}^{-1}$ inverse Fourier transform

$P(\boldsymbol{r})$ complex probe function

$O(\boldsymbol{r})$ complex sample function

Δw detector pixel pitch

$\psi(\boldsymbol{r})$ complex scalar wavefield

ζ normalized degree of coherence

$\psi(\boldsymbol{r})$ complex scalar wavefield

β_n modal weights/power

ζ normalized degree of coherence

$\gamma(\boldsymbol{r})$ degree of coherence

1 Introduction

Since their discovery [1], X-rays have been invaluable for studying matter's chemical, elemental and structure. Their short wavelength and profound penetration ability reveal interior features unattainable using other forms of electromagnetic radiation or electron beams [2]. Several diverse techniques, such as X-ray diffraction (XRD), fluorescence (XRF) and absorption spectroscopy (XAS), can be combined with optics to probe matter at the nanoscale. The demand for X-rays has been such that dedicated research facilities beyond conventional lab based sources [3] have been developed known as third generation synchrotrons [4] and X-ray free electron laser (XFEL) [5]. These sources produce X-ray radiation with high flux, low emittance and short pulse duration, allowing dynamical systems to be studied *in situ* with high spatial and temporal resolution. The electron beam source has been compressed into ever smaller volumes of phase space through successive generations of undulator technology [6]. It now produces diffraction limited hard X-rays in both horizontal & vertical directions. To exploit these sources for nanoprobe and microprobe experiments, a large proportion of the radiation must be collected while maintaining an undistorted X-ray wavefront [7].

The properties that make hard X-rays desirable to study materials also complicates their optical transportation and manipulation. Focusing any radiation is achieved by exploiting its refractive [8, 9], diffractive [10, 11] or reflective [12] interaction with matter to impart a converging phase disturbance on the incident wavefield. As the refractive index is slightly less than unity for most materials in the hard X-ray regime [13], these optical elements differ in many aspects compared to their visible light counterparts. Refractive focusing lenses are concave and consist of many lenslets stacked together, reflective optics must work at near grazing incidence [14, p. 25], and diffractive optics require small spatial features on the order of the radiation wavelength. With the drive towards higher numerical aperture optics,

it has become apparent that profile errors and surface roughness introduced during fabrication have become one of the primary limiting factors. These errors cause undesired perturbations of the X-ray wavefront [15, p. 526], which, when propagated to the focal plane, cause degradation to the focus by increasing the full width half maximum (FWHM) and decreasing the peak intensity.

The several orders of magnitude shorter wavelength of X-rays than visible light make them much more sensitive to fabrication errors on the atomic scale. This places enormous demands on the fabrication tolerances of all X-ray optical elements and means based on current technologies [16, 17] that either improved fabrication methods or some form of post correction is required. Good quality X-ray mirrors, for example, can cost hundreds of thousands of pounds to produce and require many months to years of waiting for production to complete [18]. Wavefront correction aims to introduce perturbations to the wavefront, which cancel out those originating from the aberrated optic. This is most often achieved either using bimorph mirrors [19, 20] or custom refractive elements [7, 21]. The latter is well known in visible and UV optics, most famously employed to correct the faulty mirror of the Hubble space telescope [22], but has only been demonstrated recently with X-rays thanks to advances in micro-fabrication techniques such as deep X-Ray lithography [23]. While the weak refraction of hard X-rays makes it difficult to achieve strong focusing, corrective refractive optics can produce small perturbations to the wavefront on the order of picometers with structures on the order of microns [7]. Furthermore, absorption is typically negligible since the refractive element is relatively thin.

Achieving such corrections requires precise knowledge of the perturbed wavefront, which is performed using online and offline metrology methods. Although optics can be evaluated using offline methods such as optical metrology [24] and Fizeau interferometry [25], additional factors such as misalignment errors [26, 27] and upstream optics further affect performance. In many cases, several metrology methods will be used to validate the measurement. This has led to the develop-

ment of many at-wavelength metrology methods [28] performed *in situ* and at the optics designed wavelength. The most common techniques such as speckle tracking [29], Hartmann sensing [30], grating interferometry [31] and pencil-beam scanning [32] are ray/deflection based techniques which measure the local trajectory of rays determining the measured intensity pattern. Many of these have additionally found applications beyond optical metrology, primarily in phase contrast imaging [33]. Ultimately, these techniques are limited by the fabrication accuracy of the deflecting structures, the scanning motor precision and detector pixel size. As the focal size of X-ray optics has approached ever smaller nanoscale capabilities, ptychography [34, 35] and coherent diffraction imaging (CDI) [36] techniques have become the only suitable candidates for accurately characterising performance.

Improvements in source coherence and computing equipment have seen ptychography [34, 35] and other CDI methods [37] widely adopted as standard imaging techniques by many synchrotron facilities. These are computational imaging techniques which use diffraction intensities to reconstruct the complex illumination and transmission functions and are capable of spatial resolutions beyond the diffraction limit of even the most precisely fabricated optics [38]. Ptychography is one such technique that can image samples with an extended field of view using diffraction patterns at different overlapping positions [34, 35]. Its ability to accurately recover the illuminating probe [39, 40] has also led to its use as an at-wavelength metrology technique [28]. It has been used extensively to characterise nano-focusing optics [41–45] and to measure wavefront errors [46], as the recovered complex scalar wavefield of the probe can be propagated to any plane along the optical axis. Although a highly coherent radiation source is usually required, there is enough overlap redundancy to account for a vast array of decoherence effects. The most popular method is using multi-modal probe and sample states [47], but it can also be achieved using deconvolution schemes either during [48] or after [49, p. 81] reconstruction. Its use as a metrology technique for X-ray optics with partially coherent light has recently

been demonstrated by the present [50, 51] and other [52, 53] authors.

Ptychography primarily suffers from two limitations, including the long scan times and resolution dependent scattered signal, both of which are remedied with greater flux. This has led to partially transverse [54] and longitudinal [55] coherent ptychography setups with superior resolving capabilities. As the amount of flux from sources has increased, fly-scan ptychography [56–58] has also shown promise at significantly reducing scan times. This continuously scans the sample as detector acquisitions are taken and introduces a decoherence effect similar to partially coherent light that is correctable when adequately sampled [56]. The reduction in scanning times has seen the most benefit in combined ptychography and tomography [59] (ptychotomography) that yields quantitative volumetric information on the nanoscale [60]. The two-dimensional ptychography scans are performed at different projection angles, thereby compounding the scan time. Ptychotomography, in particular, has brought exciting insights across many scientific fields, including the biological structure of algae cells [61], human bone ultrastructure [59, 62, 63], *in situ* catalytic studies [64, 65], magnetisation dynamics [66] and single particle battery cathodes [67, 68], to name a few. Compared to other imaging techniques such as scanning (SEM) and transmission (TEM) electron microscopy, the samples can be much larger, don't have to be placed under vacuum and feature no charging.

This thesis, presents advancements in hard, partially coherent X-ray ptychography to investigate corrective refractive elements for X-ray optics and study nanomaterials. The structure of the work is organised as follows. Chapter 2 reviews the core scientific principles of synchrotron physics, the main types of X-ray optics relevant to the work and scalar wavefront propagation methods are presented. Chapter 3 describes the fundamentals of partially coherent ptychography and CDI. The first two chapters are predominantly literature review, and the rest of the original work is broadly broken down into three parts. The development of partially coherent ptychography on the B16 Test beamline [69] and its subsequent use as an at-wavelength

metrology techniques is described in chapter 4. Aberration correction of different X-ray optics using refractive structures is presented in chapter 5 using knife edge scanning and the previously described partially coherent ptychography. Finally, in chapter 6, experimental results using ptychography with actual samples rather than test objects is shown. This presents both ptychography and ptychotomography studies on gold nanoparticles and silica diatoms which are expected to form part of a more comprehensive study incorporating other methodologies. This thesis contains material which has previously been or is about to be published, details of which are provided in the preceding section.

2 Principles of X-ray optics & synchrotron radiation

2.1 X-ray sources & properties

Most of the experiments throughout this thesis were performed at Diamond Light Source (DLS), a third generation synchrotron located on the Harwell Science Campus near Oxford [70]. X-rays, like visible or ultraviolet light, are part of the continuous electromagnetic spectrum and are roughly divided into the soft regime (between 100 eV and 4 keV) and the hard regime (between 4 keV and 100 keV). Early X-ray sources and lab based setups today produce radiation by accelerating electrons through a potential difference and directing them onto a dense target material, usually tungsten [1, 3]. The electrons release X-rays as they decelerate in the target and produce a smooth, broad-band spectrum[1] with an energy range from zero up to the incident electron energy. This type of source suffers from two significant drawbacks. A large radiation fan is produced as the emission happens over large solid angles. Secondly, the electron current determines the maximum flux and is limited by the anode cooling efficiency. [14, p. 30].

Synchrotron radiation was first observed as an undesirable effect by experimental particle physicists as it amounted to the largest source of energy loss by accelerated particles [71]. From classical electrodynamics, all accelerated charges radiate away energy in the form of electromagnetic waves. For non-relativistic velocities, the total power radiated is given by the Larmor formula in no particular direction [72]. However, for charged particles travelling at ultra-relativistic velocities, the total power radiated is described by the relativistic Larmor formula. It's maximised in the acceleration direction, resulting in a narrow angular divergence [73, p. 72]. The radiation

[1] This will include narrow peaks superimposed along the curve at the characteristic energy of the target material corresponding to X-ray fluorescence.

produced in this way has a characteristic polarisation, and the frequencies generated can range over the entire electromagnetic spectrum. The first experiments operated parasitically off existing particle accelerators, but the popularity and demand for X-rays soon saw dedicated (second and third generation) synchrotron radiation facilities built. Most are over a decade old and are undergoing storage beam [74] upgrades to reduce the emittance further and increase the brightness such that the source is diffraction limited in both the horizontal and vertical directions; these are known as fourth generation sources [6].

2.1.1 Bending magnets & insertion devices

A synchrotron comprises five main elements: the electron source, a booster ring, a storage ring, a radio-frequency cavity, and beamlines. The storage ring is the main component of the synchrotron. It takes the shape of a multi-edge polygon with a bending magnet at each vertex, gently deflecting the electron beam and insertion devices along each edge manipulating it. The electron beam is kept as small as possible with periodic multi-pole focusing magnets, and the energy loss due to radiation emission is compensated in a radio-frequency cavity. The electron beam consists of electron bunches, the maximum number is governed by the storage ring circumference and the radio-frequency wavelength. These bunches add a periodic time structure to the resulting synchrotron radiation; most facilities offer a special single bunch mode to observe long time interval dynamical processes at a reduced flux. A depiction of the three main types of magnets used at synchrotrons is shown in Fig. 2.1. The divergence for each is proportional to the Lorentz factor γ governed by the electron beam properties.

Bending Magnet: These were the first types of magnets used in particle accelerators to keep the charged particle beam in a closed loop; they're also called dipole magnets [69]. The radiation cone is emitted tangentially to the orbit of the electron beam, and as BMs define the geometry of the ring, the dipole field strength cannot be varied, which in turn fixes the photon beam spectrum. The characteristic energy

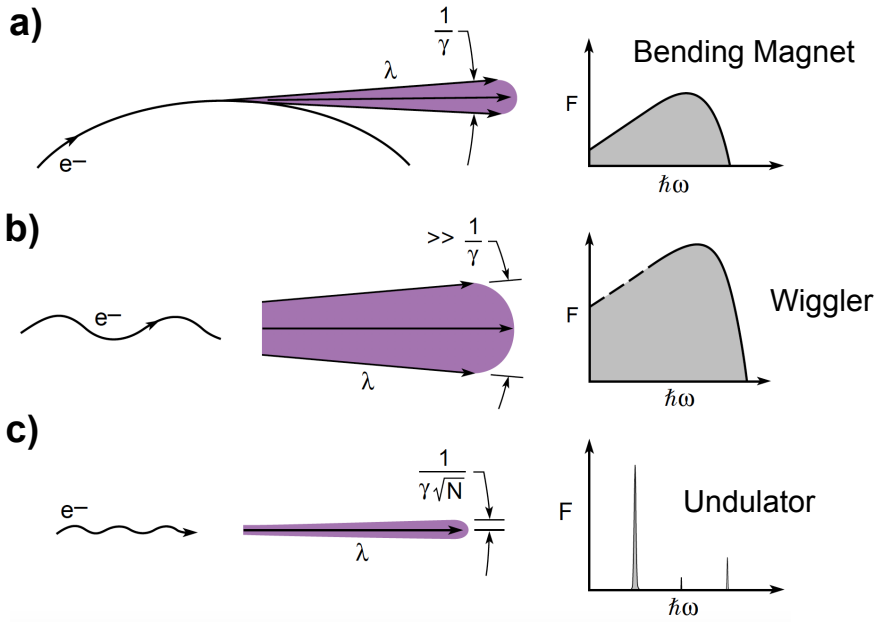


Figure 2.1: Three main types of sources used at third generation synchrotrons (a) bending magnet, (b) wiggler and (c) undulator. The left-hand side depicts the electron beam trajectory and radiation emission angle, where γ is the Lorentz factor and N is the number of magnetic periods. The right-hand side depicts the relative flux (F) for the different X-ray energies ($\hbar\omega$) produced [77, p. 124].

at which the flux peaks is given by [14, p. 38],

$$E_c[\text{keV}] = 0.665 E_e^2[\text{GeV}] B[\text{T}] \tag{2.1}$$

where B is the magnetic field and E_e is the electron beam energy, and the units are shown in brackets. While the flux peaks at E_c BMs still produce a smooth, broad-band spectrum making them useful for carrying out experimentation. The primary drawback is the significant horizontal emittance and upper hard X-ray energy limit; however, the vertical divergence is relatively small and proportional to $1/\gamma$.

Insertion Devices: These magnetic arrays are inserted between the straight sections of adjacent BMs to increase the number of available sources and produce photon beams with enhanced properties. They consist of a periodic magnetic array with an alternating polarity which forces the electron beam to oscillate in the transverse direction as it travels through the section. Analytically the devices are distinguished via the dimensionless deflection parameter $K = \alpha\gamma$, where α is the

maximum angle of deflection of the electron beam [75]. Depending on the oscillation amplitude, IDs can be further classified into two groups: wigglers have $K > 1$ where the amplitude of oscillation is larger than the beam opening angle, while undulators have $K < 1$ where the trajectory is contained within the photon beam cone. Therefore IDs are fully characterised by the deflection parameter K, the number of periods N and the spatial period λ_u.

- **Wigglers:** These use strong (often superconducting) magnets to apply a large amplitude oscillation to the electron beam. The electron bunches traverse successive circular arcs with opposite curvature emitting a continuous broadband spectrum which sums incoherently to produce an intensity proportional to $2N$, the number of poles. The deflection parameter K can be freely chosen to reach much higher energies than those on BM sources such that the peak critical energy is given by [75],

$$E = E_c \sqrt{1 - \left(\frac{\theta\gamma}{K}\right)^2} \tag{2.2}$$

  where E_c is the critical energy as in Eq. (2.1) and θ is the observation deflection angle. Additionally, the vertical divergence is similar to BMs of the same field strength; however, the horizontal divergence is much more significant and proportional to K/γ. The radiated power of wigglers is exceptionally high, typically on the order of kW, which is capable of ionising air and damaging many synchrotron optics without proper precautions.

- **Undulators:** These use weaker, permanent magnets to apply a small amplitude oscillation to the electron beam such that the radiation emission at one oscillation is in phase with the radiation emission from subsequent oscillations. The total emitted photon beam is formed of a coherent sum of the radiation amplitudes and the intensity of the beam scales with N^2. The undulator emission spectrum is characterised by strong harmonics with energies

given by,

$$E_n = \frac{\hbar\lambda_u}{2n\gamma^2}\left(1 + \frac{K^2}{2} + \gamma^2\theta^2\right) \tag{2.3}$$

where n is the harmonic number and θ is the emission angle with respect to the undulator axis.[2] The smaller electron beam oscillations mean undulators produce photon beams with small divergences that scale with $1/\sqrt{N}\gamma$ in both the horizontal and vertical directions. Undulators also offer unique control over the polarisation of the radiation for example producing circularly polarised light by imparting a spiraling component on the electron beam [76].

2.1.2 Source emittance and brilliance

Two crucial (related) quantities can be used to quantitatively characterise the properties of emitted radiation from different types of sources: brilliance and emittance. The brilliance gives a single figure of merit to radiation sources by taking into account the most desirable properties [78, p. 18], it's given by,

$$\mathcal{B} = \frac{\varphi}{4\pi^2\varepsilon_h\varepsilon_v} \tag{2.4}$$

where φ is the X-ray photon flux for a given bandwidth $\Delta E/E$ centred at an energy E. With the typical units of brilliance being ph/s/mm^2/mrad^2/0.1%. The quantities ε_h and ε_v refer to the photon beam emittance in the horizontal and vertical direction respectively and quantify how well confined the beam is,

$$\varepsilon_{h,v} = \Sigma_{\mathrm{ph}_{h,v}}\Sigma'_{\mathrm{ph}_{h,v}} \tag{2.5}$$

where $\Sigma_{\mathrm{ph}_{h,v}}$ is the photon beam size with typical units of µm and $\Sigma'_{\mathrm{ph}_{h,v}}$ is the photon beam divergence with typical units of mrad at the source. The electron beam also possesses an emittance with a similar form to Eq. (2.5) which remains

[2] The spectrum forms sharp peaks at discrete energies with energy bandwidths proportional to $\Delta E/E = 1/nN$, each harmonic will also vary in the amount of flux it contains.

constant around the orbit by Liouville's theorem [79] but depends on the electron bunch size and divergence.

The total photon beam emittance given by Eq. (2.5) therefore depends on the electron beam properties as well as the individual magnet source and is conveniently described by a convolution of both contributions such that the photon beam source size and divergence are given by,

$$\Sigma_{\mathrm{ph}_{h,v}} \simeq \sqrt{\sigma^2_{e_{h,v}} + \sigma^2_{r_{h,v}}} \qquad \Sigma'_{\mathrm{ph}_{h,v}} \simeq \sqrt{\sigma'^2_{e_{h,v}} + \sigma'^2_{r_{h,v}}} \tag{2.6}$$

where $\sigma_{e_{h,v}}$ and $\sigma'_{e_{h,v}}$ are the electron beam size and divergence respectively and $\sigma_{r_{h,v}}$ and $\sigma'_{r_{h,v}}$ are the single-electron size and divergence respectively. The single electron size and divergence are individual properties of the ID device and are approximated by a Gaussian [78, p. 47] with the corresponding emittance given by $\varepsilon_{r_{h,v}} = \lambda/4\pi$.

Hence the primary method of increasing synchrotron brilliance to date has been by reducing the electron beam source size and divergence. An electron beam is said to be diffraction limited if its emittance is much smaller than the single-electron emittance such that $\sigma_{r_{h,v}} \ll \sigma_{e_{h,v}}$ and $\sigma'_{r_{h,v}} \ll \sigma'_{e_{h,v}}$ and therefore negligible in Eq. (2.6). Since $\varepsilon_{r_{h,v}}$ represents the fundamental emittance limit of the ID source, there is little motivation to reducing the electron beam emittance $\varepsilon_{e_{h,v}}$ beyond this as it will not have any impact on the photon beam profile. As we shall no longer refer to the electron beam anymore, the photon beam is referred to as just the beam from henceforth. Fourth generation synchrotron sources feature diffraction limited sources in both the horizontal and vertical directions, unlike third generation sources, which are only diffraction limited in the vertical direction. As the diffraction limited X-ray beam emittance scales with wavelength, producing a diffraction limited storage ring is much more challenging for higher photon energies.

2.2 Interaction with matter

X-rays can interact with an atom either by absorption or scattering. However, we focus on the latter given its prevalence within the work. Scattering can be visualised classically as the radiated wave response of an electronic charge acceleration by an incident X-ray electric field [14, p. 5]. If the incident and scattered wavelength are the same, then the scattering is necessarily elastic (Thomson) and is the primary process exploited to investigate the structure of materials. However, if energy is transferred to the electron and lost in the process such that the wavelengths are different the scattering is deemed inelastic (Compton). For the rest of the work we assume magnetic scattering contributions are negligible[3] given the electrical interaction is a factor of $\hbar\omega/m_e c^2$ stronger and results in 10^4 intensity signal contribution [81]. The kinematical diffraction approximation is also used and assumes that scattering only occurs at one time within the sample volume.

Elastic scattering from an atom with Z electrons can be described classically as a superposition of scattering contributions from different volume elements of the electron density $\rho(\boldsymbol{r})$. If we consider an incident wave, the phase difference between the incident and scattered wave due to the volume elements is given by,

$$\Delta\phi(\boldsymbol{r}) = (\boldsymbol{k} - \boldsymbol{k}') \cdot \boldsymbol{r} = \boldsymbol{Q} \cdot \boldsymbol{r} \qquad |\boldsymbol{Q}| = \frac{4\pi \sin\theta}{\lambda} \tag{2.7}$$

where $\boldsymbol{k}$ and $\boldsymbol{k}'$ are the incident and scattered wavevector respectively and $\boldsymbol{Q}$ is the scattering vector. As the scattering is elastic, the modulus of the two wavevectors is the same $|\boldsymbol{k}| = |\boldsymbol{k}'|$ and allows the scattering vector to be solved in terms of the scattering angle θ and incident wavelength, λ as shown.

Therefore a volume element $\mathrm{d}\boldsymbol{r}$ at a position $\boldsymbol{r}$ will contribute an amount $r_0\rho(\boldsymbol{r})\mathrm{d}\boldsymbol{r}$ to the scattered wavefield such that the total scattering amplitude can be found by

[3]There has been particularly interesting work conducted by Donnelly on magnetic scattering using ptychography to study three-dimensional magnetic dynamics on the nanoscale [80].

integrating over all points within the volume,

$$r_0 f^0(\boldsymbol{Q}) = r_e \int \rho\,(\boldsymbol{r})\, e^{i\boldsymbol{Q}\cdot\boldsymbol{r}} \mathrm{d}\boldsymbol{r} \tag{2.8}$$

where $f^0(\boldsymbol{Q})$ is the atomic form factor and r_e is the Thomson scattering length or classical electron radius. The atomic form factor of Eq. (2.8) is simply the Fourier transform of the electronic charge distribution of the atom and in the limit that $\boldsymbol{Q} \to 0$ all volume elements scatter in phase such that $f^0(0) = Z$.

In reality, electron-photon interactions at the atom length scale are purely governed by quantum mechanics [82, p. 780]. The classical model of the electron response possesses a single resonance frequency, but quantum mechanically, a range of probabilistic frequencies will feature. These can be accounted for in the semi-classical atomic form factor by introducing dispersive corrections,

$$f(\vec{Q}, \hbar\omega) = f^0(\vec{Q}) + f'(\hbar\omega) + i f''(\hbar\omega) \tag{2.9}$$

where f' and f'' are the dispersive corrections, the $\hbar\omega$ describes the terms energy dependence. The dispersive corrections behaviour is highly dominated by tightly bound inner shell electrons, which contribute little to the scattering vector $\boldsymbol{Q}$ hence its dependence is dropped. The extremal values of the dispersive corrections are most noticeable when the incident X-ray energy is close to the atom absorption edges; the resonant behaviour is manifestly element specific.

The interaction of electric fields with materials will be governed by the Maxwell equations (discussed more in section 2.6), with the current density governed by Eq. (2.9) summed over all atomic contributions [77, p. 52]. Comparing the result with the standard form of the wave equation, an expression for the energy-dependent refractive index is given by,

$$n(\omega) = 1 - \frac{n_a}{2\pi} r_e \lambda^2 (f_0 + f'(\hbar\omega) - i f''(\hbar\omega)) \qquad n_a = \frac{\rho N_A}{M} \tag{2.10}$$

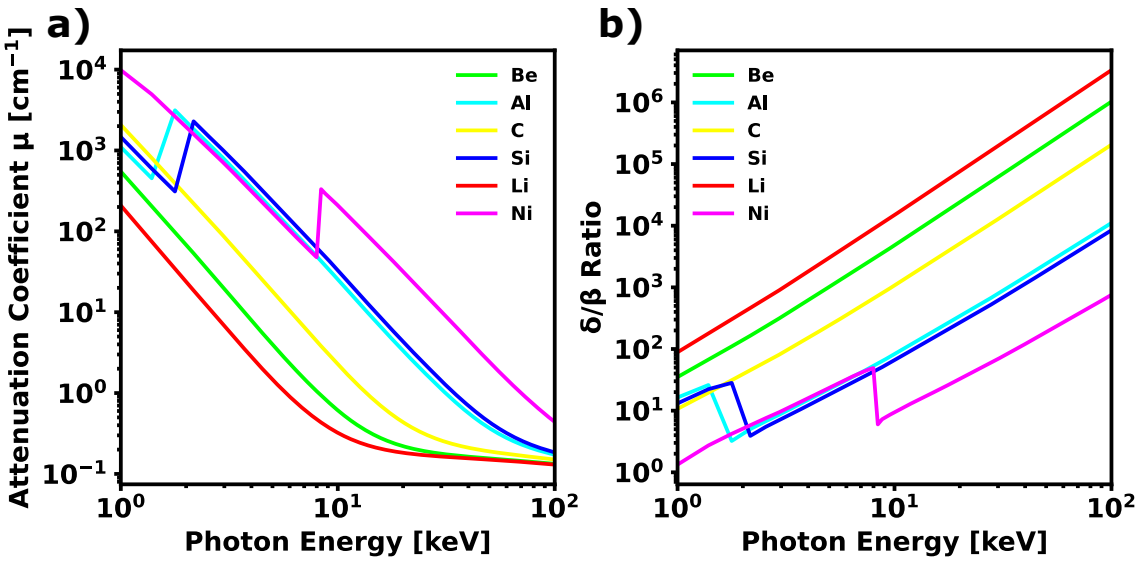


Figure 2.2: (a) Attenuation coefficient and (b) refractive index ratio δ/β for different materials at typical synchrotron energy ranges. Calculations were performed using the Henke dataset [13].

where n_a is the atomic number density with N_A being Avogadro's number, ρ the mass density, and M the molar mass. Of particular interest is the quadratic dependence of $n(\omega)$ on the wavelength λ. As the refractive index for X-rays deviates only a small amount from unity, it's commonly written in the form,

$$n(E) = 1 - \delta(E) + i\beta(E) \tag{2.11}$$

where $\delta(E)$ is the refractive index decrement governing the refractive properties and is typically of the order of 10^{-6} for hard X-rays. The imaginary part $\beta(E)$ of the refractive index governs absorption. In general, the real and imaginary parts are not decoupled from one another and are actually related by the Kramers-Kronig relations [83]; however, this is beyond the scope of the thesis.

- **Absorption:** The imaginary part of the refractive index translates to a decay of the incident wavefield amplitude. It's more commonly regarded as the Beer-Lambert law governing attenuation for which the transmitted intensity passing

through some thickness z of a homogenous material is given by,

$$I(z) = I_0 e^{-\mu z} \qquad \mu = \frac{4\pi\beta}{\lambda} \tag{2.12}$$

where I_0 is the incident intensity and μ is the linear absorption coefficient. This is formed of photoabsorption (τ), scattering (μ_s) and pair production (μ_p) such that the total attenuation is given by $\mu = \tau + \mu_s + \mu_p$. Pair production doesn't occur below 1 MeV, and photo-absorption scales as $\tau \sim Z^3/E^3$.

- **Refraction & Reflection:** The interaction of X-ray photons with matter at the interface between media of differing refractive index is governed by Snell's law [84]. This relates the incident grazing angle[4] to the refracted or reflected ray angle and is given by,

$$n_1 \cos\theta_1 = n_2 \cos\theta_2 \tag{2.13}$$

where n_1 and n_2 are the refractive indices of two materials with respective incident θ_1 and refracted/reflected θ_2 angles of incidence. X-rays undergo total external reflection at grazing angles below the critical angle $\theta_c = \sqrt{2\delta}$ in contrast to visible light, which undergoes total internal reflection. This is found by Taylor expanding θ in Eq. (2.13) and is on the order of mrad.

- **Diffraction:** Crystalline materials scatter incident wavefields coherently to form constructive interference peaks. It forms the basis of crystallography and is a special case of Laue diffraction relating the incident wavelength to the scattered angle and is governed by Bragg's law,

$$n\lambda = 2d \sin\theta \tag{2.14}$$

[4]Normally Snell's law is formulated in terms of normal angles of incidence however due to the refractive index being almost unity X-rays work in grazing incidence for reflection.

where n is the diffraction order, d is the lattice spacing and θ is the scattered angle. The wavelength λ must be of the order of the interatomic distances which is satisfied for hard X-rays. Monochromators work off the reverse principle to diffract desired wavelengths from a known crystal structure.

2.3 X-ray detectors

X-ray detection is notoriously difficult, especially at higher energies, as their deep penetration and sparse interaction also apply to the detecting medium. Photographic film was the medium of choice for over a century [1] due to its high spatial resolution, large acquisition area and relatively low cost. However, quantitative analysis of results and the move to digitisation has seen its demise [85, p. 349]. As with most technological advances within synchrotron physics, detectors were initially used for high-energy physics experiments and have developed rapidly in the past decades with the adoption of more synchrotron & XFEL sources [86, 87]. Broadly they can be classified into two groups: *counting* and *integrating* [88, p. 212]. Counting detectors can discriminate and detect individual photons, whereas integrating detectors accumulate a signal proportional to the photon beam intensity over a given period of time. This section reviews the predominant detector parameters and their relevance within different experimental scenarios.

- **Spatial resolution:** The minimal resolvable distance on a detector is determined by the detector pixel size and its associated point spread function (PSF). The pixel size is the fundamental resolution limit imposed on a detector system, and the relative positions of photons cannot be determined with better accuracy than it. For most detectors, arrays from hundreds to thousands of pixels with sizes ranging from microns to hundreds of microns are used. The pixel size also has a great effect on the other parameters discussed here. The PSF describes the detector response to a point source and degrades the intensity via convolution with the signal. In many cases, though, the sig-

nal from one pixel leaks into neighbouring pixels, increasing the extent of the PSF. For detectors, its best value is a single pixel; however, for most systems, it's greater than this.

- **Quantum efficiency:** Photons incident on a detector have a probability equal to the quantum efficiency of generating a measurable electron in the detecting media that can be recorded [89]. Therefore, quantum efficiency is an evaluation of a detector's ability to discriminate individual X-ray photons. The quantum efficiency for photons with an energy E is related to the material absorption[5] as discussed in section 2.2 and given by,

$$\eta = 1 - e^{-\mu(E)z} \tag{2.15}$$

where $\mu(E)$ is the absorption coefficient and z thickness of the detecting material. Many X-ray detectors have near-unit quantum efficiency $\eta \approx 1$ however, by Eq. (2.15) the material (or chip) thickness has considerable effect meaning there is always some trade-off between detector PSF and efficiency. Coherent diffraction imaging requires single photon-counting, high efficiency detectors to perform properly and reconstruct; therefore feature most within the thesis.

- **Signal to noise:** Discrete measurements of photons are inherently statistical which means the actual intensity values fluctuate randomly about the mean value [88, p. 207]. This is independent of detector design, and for X-ray photons, follow Poisson statistics such that for N_0 mean photons falling on a detector element, the variance is given by [90],

$$\sigma^2 = N_0\eta \tag{2.16}$$

where η is the quantum efficiency defined by Eq. (2.15). The detector design

[5]For hard X-rays photo-absorption is the dominant pathway.

will also be influenced by other sources of noise such as signal conversion, read-out noise and dark or background noise. Photon-counting detectors have no read-out noise,[6] since a predefined energy threshold must be set and only photons with charges proportional to this are recorded [91, 92]. This means no calibration image is required, and long time measurements can be performed. For the majority of ptychography experiments performed, Medipix [93] and Eiger [94] photon-counting detectors were used.

- **Dynamic range:** The ratio of the largest detectable signal to the smallest (non-zero) detectable signal is given by the dynamical range [95]. Saturation occurs after this limit is reached, and the signal between pixels cannot be distinguished. It's most often expressed in base-2 logarithmic units of bits which cannot exceed the electronics digitisation limit and is defined as,

$$\mathrm{DR} = \log_2\left(\frac{X_{\mathrm{signal}}}{X_{\mathrm{noise}}}\right) \tag{2.17}$$

  where X_{signal} and X_{noise} are the maximum and minimum noise level that can be detected. This ratio will be experimentally specific; most typical imaging experiments require around a modest 12-bit range, whereas coherent diffraction imaging techniques require at least 16-bit or higher [95, 96] to distinguish the intense direct beam and relatively weaker scattered signal [97].

- **Other points:** Finally, a few concluding points about detector considerations. An increasingly important factor is frame rates and readout times; with femtosecond X-ray pulses at XFELs, quick acquisitions [98] are required to harness these types of sources for fast dynamical processes, and detector technology is currently the main limitation. Energy sensitivity is another factor; most experimental techniques and analyses will require some *a priori*

[6] So long as the threshold energy is higher than the noise of the electronics and the dark signal of the detector is zero.

information about the monochromaticity of the beam, which can be set with most CCDs using energy thresholding [91]. The purchase of detectors can be the highest equipment cost of a beamline, especially for bespoke beamline techniques. Most facilities will have a dedicated detector research group to mitigate this cost and perform repairs in-house. Detectors are also subjected to near constant X-ray exposure [99] such that radiation damage and efficiency degradation over time must also be taken into account.

2.4 Optical elements

All optical experiments, regardless of wavelength, require the ability to manipulate and control beams of light to be of any benefit. Focusing is the most fundamental technique and serves two primary purposes: firstly, it increases the flux density compared with an aperture of the same size, and secondly extends the capability of many techniques to achieve local probing and spatially resolved measurements. This is achieved by imparting a convergent perturbation to the wavefront by exploiting the interaction of light with matter through reflection, refraction and diffraction [84]. The most critical differences between visible light and X-rays concern the wavelength of radiation and index of refraction (2.2) of the focusing materials, which are nearly equal to unity for X-rays [100]. This introduces additional challenges when focusing using the three fundamental interactions of light with matter: diffractive elements must be fabricated accurately at the nanoscale, reflective elements require glancing angles in the mrad regime and useful refractive elements absorb X-rays just as quickly as they refract them.

As all components of a synchrotron, from the electron source to the X-ray detectors are continuously improved, so is the need to develop X-ray optics that exploit these new and exciting properties. Tremendous advancements in even the past three decades have seen hard X-ray beam sizes reduced by around a factor of three in magnitude, from tens of microns [8, 101] to tens of nanometer [19, 102].

Although nanofocused beams can be achieved in a number of ways, the most noteworthy developments the synchrotron community has adopted include Fresnel Zone Plates [11, 103], Kirkpatrick–Baez mirrors [12, 104] and nano-focusing compound refractive lenses (NFLs) [8, 105]. These have seen the most research investment in wave-optical modelling and fabrication methodologies to achieve ultimate diffraction limits. Other notable focusing optics which will not be discussed in detail but deserve mentioning include multilayer Laue lenses [17], kinoform lenses [106], adiabatic lenses [107], multilayer mirrors [108], and waveguides [109]. In this section, we will discuss the design, functionality and properties of three of the main types of X-ray focusing elements used throughout the thesis; further in-depth reviews of focusing X-ray optics are available in [14, 110].

2.4.1 Numerical aperture

The most basic imaging systems consist of a lens, object and image. Ray diagrams can be used to determine the image location, size, orientation and type formed when placed at a given location along the optical axis. These properties are related by the lens equation and magnification factor and given by,

$$\frac{1}{f} = \frac{1}{p} + \frac{1}{q} \qquad M = -\frac{q}{p} \tag{2.18}$$

where f is the focal length, q is the object distance and p is the image distance. The magnification factor M determines the ratio between the object and image size, with positive and negative sign conventions for virtual and real images, respectively.

The numerical aperture is a single dimensionless number that quantifies the angular acceptance of an optical system, that is, the range of angles over which a system can accept or emit light [111] and is given by,

$$\mathrm{NA} = n \sin\theta = n \sin\left[\tan^{-1}\left(\frac{D}{2f}\right)\right] \approx n\frac{D}{2f} \tag{2.19}$$

where n is the refractive index of the surrounding medium between the object and image (usually air), θ is the maximum half angle that can enter or exit the lens, D is the lens aperture and f is the lens focal length. The far-right approximation in Eq. (2.19) holds when the aperture D is much smaller than the focal length f.

The predominant metric used to access the performance of different types of optics is its achievable focal spot size or optical system resolution. The smallest focal spot size is limited by the optics numerical aperture and is known as the Abbe diffraction limit [15, p. 467]. This is the fundamental resolution limit of any optical system due to the physical effects of diffraction[7] and given by,

$$d = \alpha \frac{\lambda}{2n \sin \theta} = \alpha \frac{\lambda}{2\mathrm{NA}} \tag{2.20}$$

where λ is the wavelength of radiation and α is a constant chosen depending on the profile of the focusing element aperture. When the aperture is circular, the focus is an Airy disc and $\alpha = 1.22$ is known as the Rayleigh criteria [113] with the size d the distance between the intensity peak and first-order minima.[8]

2.4.2 Compound refractive lenses

X-ray refraction is a very weak phenomenon due to the relatively low ratio between the refractive index decrement and absorption coefficient; indeed, Röntgen never witnessed the phenomenon himself and thought it impossible [1]. It wasn't until over one hundred years after their discovery that Yang developed the first theoretical design of Compound Refractive Lenses [114] (CRLs) and Snigirev demonstrated it experimentally at the ESRF [8]. Early CRLs were fabricated simply by drilling holes into aluminium blocks; however, this primitive design suffered greatly from

[7] This is based on the traditional view of optics, new nano-fabrication methods have revolutionised visible optics with so-called meta lenses which manipulate light on the sub-wavelength scale to overcome these traditional limitations [112].

[8] In fact, the Rayleigh criteria is generally accepted by microscopists as the minimum resolvable detail within an imaging system, another useful metric is the FWHM given when $\alpha = 0.88$ as it can easily be compared with optics which feature Gaussian type apertures.

spherical aberration.[9] Lengeler rectified this with parabolic CRLs, which have since become the standard used today at synchrotron and XFEL facilities [9]. Within this section, refraction as a means of X-ray focusing is reviewed, the shape of lenses and key optical performance formulas are presented, and fabrication aberrations relevant to later sections will also be briefly discussed.

As with visible light, X-ray refraction occurs at the interface between two different media with refractive indices n_1 and n_2, and is governed by the real part of the refractive index and Snell's law [15, p. 40]. A consequence of the refractive index decrement of most materials being less than one means X-rays refract away from the surface normal when passing from air into the material. This means individual X-ray lenses must be concave in shape to focus light rather than convex as in visible optics. The exact profile of the individual lenses will depend on several factors, including the desired focal quality, shape of incident light and experimental setup. The ideal profile for a single lens focusing point to point (as on synchrotron beamlines) is a Cartesian oval [115] and an elliptical profile when focusing collimated beams [116]. However, for large source distances and apertures much smaller than the focal length, both the aforementioned profiles are generally well approximated by the parabolic profile which reduces the geometric aberrations to negligible values.

The focal length and profile for a single plano biconcave lens can be derived using Fermat's principle and equating all optical path lengths through the system such that rays arriving at the focal plane are all in phase [14, p. 104]. Reducing the focal length can then be achieved by either decreasing the radius of curvature (which also limits the geometrical aperture [117]) or by stacking many lenses together, which gives a compound lens with a focal length,

$$f_{thin} = \frac{R}{2N\delta} \qquad f_{thick} = \frac{R}{2N\delta} + \frac{l}{6} \tag{2.21}$$

[9] This was well known from visible optics however the effect is compounded with X-rays optics when many lenses are stacked together.

where R is the radius of curvature, δ is the refractive index decrement, N is the number of lenses and l is the total length of the lens. The thin lens focal length f_{thin} assumes ideal thin lenses [84] whose focal lengths sum reciprocally. In general, though, CRLs are not arbitrarily thin, especially in the case of nano-focusing, and their length l can be of the order of the focal length. A more thorough consideration of the successive convergence within the stack gives the thick lens focal length f_{thick} as measured from the centre of the optic [118].

The major drawback of CRLs and limiting performance factor is photo-absorption, especially when many lenses are used. Since the CRLs are parabolic in profile and the absorption is governed by the Beer-Lambert law, the effective aperture intensity is Gaussian in distribution. The size is usually defined by the beam waist where the intensity drops to $1/e^2$, and neglecting the inter-lens thickness d is given by,

$$D_{\text{eff}} = \sqrt{\frac{8R}{\mu N}} = 4\sqrt{\frac{f\delta}{\mu}} \tag{2.22}$$

where μ is the attenuation coefficient and f is the focal length. This also demonstrates why a large δ/μ ratio is a good figure of merit concerning the choice of lens material as shown in Fig. 2.2. Improvements in fabrication technology have also made possible refractive lens variants including adiabatic lenses [107] and Fresnel/kinoform refractive lenses [106], which attempt to use less material to achieve the same focusing properties as CRLs.

With values for the effective aperture and focal length, it's possible to derive the diffraction limited focal size in terms of its optical properties. The FWHM of the focal peak best describes the diffraction limit scaling factor α since the distribution will be Gaussian in distribution[10] such that the diffraction limit and numerical

[10]Fraunhofer diffraction theory finds the focal spot will be the Fourier transform of the lens aperture which in this case is already a Gaussian.

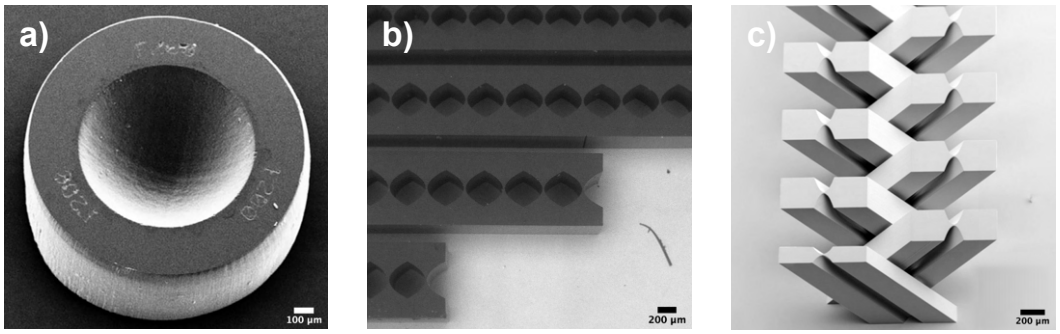


Figure 2.3: (a) A single radially symmetric parabolic Diamond lenslet fabricated using laser ablation [119]. (b) A series of planar parabolic CRLs fabricated using deep X-ray lithography in SU-8 polymer. (c) More complex lens designs known as Taille-lens fabricated using deep X-ray lithography, reproduced with permission Copyright 2022 The Optical Society [120].

aperture of the optic are given by,

$$d = \frac{2\sqrt{2\log 2}}{\pi}\lambda\sqrt{\frac{f\mu}{\delta}} \qquad \text{NA} = 2\sqrt{\frac{\delta}{f\mu}} \tag{2.23}$$

From Eq. (2.23) smaller diffraction limits require small focal lengths and large δ/μ ratios. Additionally in the low attenuation limit, the numerical aperture is upper bounded by the critical angle of total reflection $\sqrt{2\delta}$, which fundamentally constrains the lens diffraction limit [107].

X-ray lenses are generally restricted to being either radially symmetric or planar in shape, as shown in Fig. 2.3a and Fig. 2.3b, respectively. However, more exotic geometries have been developed lately with advanced Lithography fabrication methods [120], as shown in Fig. 2.3c. Planar lenses are fabricated accurately at the micron scale which means they can be designed with small radii of curvature and hence focal lengths, this has seen them primarily employed as nano-focusing lenses [107, 117]. These are restricted in the materials that can be used and require two arrays with different focal lengths in a crossed geometry if both transverse planes require focusing [121]. Radially symmetric lenses can be cheaply manufactured from low atomic number metals such as beryllium or aluminium using an embossing process; however, this usually adds unwanted spherical aberrations [119]. As they can be fabricated from radiation hard materials and cooled easily, they're useful as

pre-focusing/secondary source optics on high-flux beamlines and at XFELs [122].

2.4.3 Fresnel zone plates

Fresnel Zone Plates (FZP) have been known about for over a century and use the diffractive property of light to focus monochromatic X-rays. They consist of concentric rings of alternating regions of transparent and opaque material that decrease in thickness with increasing radius. It's fully specified by three parameters which define the focal length and aperture given by [77, p. 342],

$$f_n = \frac{D dr_N}{n\lambda} \qquad D = 4N dr_N \tag{2.24}$$

where D is the lens aperture, dr_N is the narrowest ring width, N is the total number of zones and n is the focal length order. The placement of zones is designed such that constructive interference at the focal plane occurs from the transparent regions while destructive interference is absorbed in the opaque regions. This limits their use with high-energy X-rays as the opaque zones begin to transmit more intensity, and thicker structures are typically challenging to fabricate [123].

In addition to the main lens, a central stop is usually placed at the centre of the optical axis to stop the direct beam that has not diffracted with the lens (zeroth order) and an order sorting aperture is placed close to the focus to select the desired diffraction order. With values for the aperture and focal length, it's trivial to derive the optics numerical aperture and diffraction limited focal size from Eq. (2.20) and is given by,

$$d_n = \alpha \frac{dr_N}{n} = 1.22 \frac{dr_N}{n} \tag{2.25}$$

where a factor of $\alpha = 1.22$ is chosen as the Rayleigh criteria due to the circular aperture. As can be seen from this relation, smaller focal sizes can only be achieved by reducing dr_N which is limited by fabrication methods or using higher order diffraction modes which are much less intense. Additionally, to avoid chromatic

aberrations, the number of zones N, must be less than the inverse relative spectral bandwidth $\lambda/\delta\lambda$, together, these define a natural set of constraining parameters for the lens design [124].

The most promising rival to FZPs are Multilayer Laue Lenses (MLLs) [125–127] which are planar one-dimensional FZPs consisting of variable thickness thin films stacked upon one another [128]. These types of optics are much more tailored to higher energy X-rays [129]; they can be fabricated using a wider variety of materials and are typically deposited using magnetron sputtering, which can control film thickness (and hence outer zone thickness) with atomic accuracy [130]. While flat MLLs share the same focusing principle as FZPs, this doesn't consider propagation effects within the optic. As such, more exotic geometries have been proposed which generally group the optic into four principal categories: flat, tilted, wedged and curved MLLs [125]. As with FZPs, the main drawback to MLLs is the low efficiency of around 10% however, this is still a relatively new and developing field of X-ray optics and focal spots less than 20 nm have been readily reported by a variety of research groups [38, 102, 131, 132].

2.4.4 Kirkpatrick–Baez mirror

Reflective optics possess many advantages over refractive and diffractive optics: they have much higher efficiencies, the potential for larger apertures, radiation hardness and most importantly, achromaticity. This has seen their adoption at many beamlines [122, 133–135]. Due to the low reflectivity of X-rays, mirrors must operate under grazing incidence, and as with refractive optics the interaction is governed by Snell's law. If we consider the case of an X-ray incident from air ($n_1 = 1$) onto some mirror surface ($n_2 < n_1$), the critical angle θ_C (with respect to the mirror surface) at which light is externally reflected can be derived as [136],

$$\theta_C = \cos^{-1}\left(\frac{n_2}{n_1}\right) = \cos^{-1}(1-\delta) \approx \sqrt{2\delta} \tag{2.26}$$

where δ is the refractive index decrement of the mirror surface and we have used the Taylor approximation valid for small θ_C. Hard X-rays exhibit total external reflection under glancing angles on the order of mrad. To increase the critical angle and limit the physical length of the mirror, heavy metallic elements[11] such as gold, platinum or rhodium can be coated on the mirror surface [137].

The Kirkpatrick–Baez mirror (KB) system was one of the first methods proposed to focus X-rays [12]; two curved mirrors are employed, which focus light in each of the transverse planes. Ellipsoidal mirrors are the ideal shape for point-to-point focusing (as on synchrotron beamlines), and their shape becomes approximately parabolic for large source distances, which can be easier to fabricate; the focal length for an elliptical mirror is given by [138],

$$f = \frac{2}{R \sin\theta} \qquad R = \frac{2pq}{(p+q)\sin\theta} \tag{2.27}$$

where R is the local radius of curvature, θ is the grazing angle of incidence, q is the source to mirror distance and p is the mirror to image distance. Since the mirrors are not optically thin, the two mirrors require complementary focal lengths to avoid an astigmatic focus; this also results in two different magnification factors, which may be beneficial in some case.[12]

While several factors impact the focal spot, the physical aperture is ultimately limited by the acceptance angle 2ε as viewed from the focus. This sets the upper and lower limit on the numerical aperture and diffraction limit of the system, respectively, and is related to the critical angle of incidence [139],

$$d \approx 1.76\frac{\lambda}{\sqrt{2\delta}} = 1.76\sqrt{\frac{\pi}{r_0 n_e}} \qquad \mathrm{NA} \approx \frac{\sin\theta_C}{4} = \frac{\sqrt{2\delta}}{4} \tag{2.28}$$

[11] There will be some absorption in the reflecting medium in the form of an evanescent wave which will reduce the reflectivity, as such a range of coatings can be applied in the form of lanes to maximise the reflectivity over a range of X-ray energies.

[12] Synchrotron sources are generally more prominent in the horizontal direction than the vertical so Kirkpatrick–Baez mirror systems can be designed to magnify the horizontal direction more strongly resulting in uniform focal size.

where r_0 is the classical electron radius and n_e is the electron density. Eq. (2.28) indicates the performance of KB mirrors is limited by its materials properties; for example, a platinum coating achieves the smallest focal size of 25nm. Focal performance is also affected by slope error [140] and surface roughness [141], both of which have significantly improved recently due to advances in ion beam figuring (IBF) fabrication techniques [142–144].

It's also worth briefly mentioning graded multilayer coatings [19, 145, 146] for KB mirrors, which work by depositing alternating materials with a lateral thickness gradient to fulfil the Bragg requirement along the length of the mirror. When incident light satisfies the modified Bragg equation (corrected for refraction effects) given by [139],

$$\Lambda = \frac{\lambda}{2\sqrt{n^2 - \cos^2\theta}} \tag{2.29}$$

where Λ is the multilayer period. The reflected light at each interface is superimposed coherently, yielding larger reflectivity constants. The multilayer spacing Λ can also be tuned to satisfy Eq. (2.29) with much larger incident angles than the typical critical angle θ_C. As such, the diffraction limit of the optics is purely limited by the multilayer periodicity and given by,

$$d = \frac{0.88}{1/\Lambda_2 - 1/\Lambda_1} \qquad \text{NA} = \frac{\lambda}{2}\left(\frac{1}{\Lambda_2} - \frac{1}{\Lambda_1}\right) \tag{2.30}$$

where $\Lambda_{1,2}$ is the multilayer period at the respective edges of the mirror. Diffraction limited spots less than 5nm have been theorised [136] and to date 7nm have been experimentally achieved [19]. The primary drawback of multilayers is the spectral bandwidth $\Delta E/E$ reduction, which can only range from around 1%-10%. Recent developments have seen the fabrication of a variety of bilayer coatings [146–149] intended for use at different X-ray energies, as well as their adoption at synchrotron and XFEL facilities [150, 151].

2.5 Scanning and full-field microscopy

Transmission X-ray microscopy techniques mainly fall into two types of experimental setup namely; scanning (STXM) and full-field (TXM) microscopy [77, p. 366]. Full-field microscopes capture the whole field of view with a single acquisition whereas scanning microscopy relies on a bright well focused spot that scans over the sample. A detector then measures the intensity, and an image can be formed by correlating these measurements with the sample's scanning position. The fundamentals of both are summarised below including their relative strengths and weaknesses.

- **Full-field microscopy:** This optical arrangement is the same as the classical visible light microscope. An objective lens is used to focus an incident X-ray beam on the sample and project a magnified image onto a condensing lens. This lens removes the diverging component of the wave such that only a magnified image of the sample is detected. In principle, any X-ray focusing optics can be used; however, FZPs are most commonly used as they focus on-axis and possess the highest numerical aperture, refer to section 2.4 for more information. In the soft X-ray regime, TXM can routinely achieve less than 10 nm resolution, most commonly investigating biological samples in a tomographic mode [152]. In the hard X-ray regime phase contrast techniques can additionally be used in tandem to improve the contrast [153]. If a divergent wave (formed by a lens or source) without an objective lens is used TXM is referred to as being in a cone-beam geometry and simply gives a magnified projection of the sample. This is more commonly used by lab-based sources but can also be used at synchrotrons to increase the flux by removing the need for lenses. However, the resolution is limited by the source spot size and the image will require some method of phase retrieval/post processing.

- **Scanning microscopy:** The setup for STXM is similar to the TXM, except a single focusing optic is used to concentrate the incident X-rays onto

the sample. This is then raster scanned through the focused beam using high-precision motion stages, and the intensity is then recorded sequentially at each position. Again any type of focusing optics can be used, but Kirkpatrick–Baez mirrors are most commonly used due to their high efficiency and achromaticity. The main benefit to STXM is it adds local probing capabilities to many techniques such as X-ray diffraction [154], fluorescence [155] and absorption spectroscopy [156], many of which can be performed simultaneously. Indeed the main theme of this thesis ptychography can be thought of (and is referred to) as a special case of STXM. The main drawback of the technique is the much longer acquisition times which range from minutes to hours compared to the seconds TXM takes. This places additional constraints on the stability of the setup and the types of samples (radiation hardness) that can be probed. The resolution is determined by the focal size extent, which is fully optimised for coherent, aberration free optics and long source to optic distances to reach the diffraction limit.

2.6 Wavefront propagation

All electromagnetic radiation obeys Maxwell's equations: the collection of coupled partial differential equations which form the foundation of classical electromagnetism, optics, and electric circuits [15, p. 75]. When the diffracting features are larger than the radiation wavelength, Maxwell's equations reduce to scalar diffraction theory and can be solved analytically for many applications [157]. We will focus on physical optics, which considers wave phenomenon in the context of optical elements and image formation. This is an essential consideration for modern synchrotron sources where a large fraction of the radiation is coherent and geometric (or ray-based) optical theory fails to model the phenomena properly [158]. In this section, we provide a brief introduction to scalar diffraction theory and the solutions and respective approximations that can simplify calculation complexity. This

field has been reviewed extensively previously and the reader is directed to those texts for a comprehensive treatment of the subject [15, 88, 159]. A schematic of the diffraction regimes is shown in Fig. 2.4 and also demonstrates how the wavefield from a simple aperture propagates.

2.6.1 The Helmholtz equation

In a linear, homogeneous, isotropic, non-dispersive and non-magnetic medium, all components of the electric and magnetic fields obey the d'Alembert wave equation and are uncoupled from one other [15, p. 430]. Therefore the disturbance is fully characterised by a single complex field $\Psi(\boldsymbol{r}, t)$ and governed by the scalar wave equation,

$$\nabla^2 \Psi\left(\boldsymbol{r}, t\right) - \frac{n^2}{c^2} \frac{\partial^2 \Psi\left(\boldsymbol{r}, t\right)}{\partial t^2} = 0 \tag{2.31}$$

where n is the refractive index of the medium and c is the speed of light in a vacuum. Given a volume of free space with a field described by Eq. (2.31), the complex field can also be spectrally decomposed as a superposition of monochromatic fields using the Fourier integral,

$$\Psi\left(\boldsymbol{r}, t\right) = \frac{1}{\sqrt{2\pi}} \int_0^\infty \psi\left(\boldsymbol{r}\right) \exp\left(-i\omega t\right) \mathrm{d}\omega \tag{2.32}$$

where $\psi\left(\mathbf{r}\right)$ is the spatial wavefield and ω is the angular frequency. Substitution of this into Eq. (2.31) yields the time-independent equation for the spatial wave function, also known as the Helmholtz wave equation and given by,

$$\left(\nabla^2 + k^2\right) \psi\left(\boldsymbol{r}\right) = 0 \qquad k = \frac{\omega}{c} = \frac{2\pi}{\lambda} \tag{2.33}$$

The Helmholtz equation forms the basis of scalar diffraction theory, which concerns itself with constructing solutions subject to specific boundary conditions. We also note that $\Psi\left(\mathbf{r}, t\right)$ is regarded as the complex field amplitude, its modulus squared corresponding to the optical intensity.

2.6.2 Rayleigh-Sommerfeld solution

Determining the complex field amplitude $\psi(\mathbf{r})$ at some point in space is accomplished by finding a general solution to the Helmholtz equation Eq. (2.33) using Green's integral theorem [160, p. 384]. The Helmholtz–Kirchhoff diffraction integral allows the value at any given point to be expressed in terms of the boundary values of the wavefield on any closed surface surrounding it [159, p. 42],

$$\psi(P_1) = \frac{1}{4\pi} \iint_S \left\{ \frac{\partial \psi(P_0)}{\partial n} \left[\frac{\exp(ik\boldsymbol{r})}{\boldsymbol{r}} \right] - \psi(P_0) \frac{\partial}{\partial n} \left[\frac{\exp(ik\boldsymbol{r})}{\boldsymbol{r}} \right] \right\} \mathrm{d}s \tag{2.34}$$

where P_0 and P_1 are points on the source and propagated wavefield respectively enclosed by the bound surface S and $\partial/\partial n$ denotes differentiation in the direction of the outward unit normal to the surface S. The most popular solutions to Eq. (2.34) are the Fresnel-Kirchhoff (FK) and Rayleigh-Sommerfeld (RS) solutions, both of which offer excellent agreement with experimental observation [161].

Physical inconsistencies of the FK theory were removed by Sommerfeld, who eliminated the necessity of imposing boundary conditions on both the disturbance and its normal derivative simultaneously, as such RS will be the subject of our discussion and is given by,[13]

$$\psi_Z(x_1, y_1) = \frac{Z}{i\lambda} \iint_\Sigma \psi_0(x_0, y_0) \frac{e^{ikR}}{R^2} \cos(\hat{R}, \hat{n}) \, \mathrm{d}x\mathrm{d}y \tag{2.35}$$

where x_1 and y_1 are coordinates in the propagated plane, Σ is over the source area, and $\cos(\hat{R}, \hat{n})$ is the cosine of the angle between the source and propagated vector planes $\hat{R}$ and the propagation direction $\hat{n}$; finally, R is the distance from a point on the source plane to a point on the propagated plane and given by,

$$R = \sqrt{Z^2 + (x_0 - x_1)^2 + (y_0 - y_1)^2} \tag{2.36}$$

[13] Interestingly, the RS theory is also limited to diffraction by planar surfaces whereas the FK theory can handle surfaces of any shape [162], though this doesn't affect the work within this thesis.

The planar RS solution, as in Eq. (2.35) is a statement of the Huygens–Fresnel principle; that is, the propagated wave is an infinitesimal sum of spherical wave point sources (or wavelets) originating on the source wavefield [163].

The general form of the RS integral Eq. (2.35) simplifies to a convolution when the source and observation planes are parallel to one another and can be rewritten in terms of Fourier transforms by the convolution theorem such that,

$$\begin{aligned} \psi_Z(x,y) &= \mathcal{F}^{-1}\left\{\mathcal{F}\left\{\psi_0(x,y)\right\} H(p_x,q_y)\right\} \\ H(p_x,q_y) &= \exp\left(ikz\sqrt{1-(\lambda p_x)^2-(\lambda y_x)^2}\right) \end{aligned} \tag{2.37}$$

where q_x and q_y are the respective reciprocal space coordinates and $H(p_x, q_y)$ is the RS transfer function; this is more generally known as an angular spectrum propagation. For negative square root values in Eq. (2.37), the solution is a non-propagating evanescent wave [15, p. 639], while positive values change the relative phases of the various frequency components. Eq. (2.37) is valid for all propagation regimes but mainly used for small distances as both source, and observation planes will have the same sampling frequency, which can exceed the field of view.

2.6.3 Fresnel & paraxial approximation

In general, such a rigorous solution, as shown previously, is not required. In the paraxial approximation, the object extent and diffraction size are considered small relative to the propagation distance Z such that R can be binomially expanded,

$$R = Z\sqrt{1+\frac{(x_0-x_1)^2}{Z^2}+\frac{(y_0-y_1)^2}{Z^2}} \approx Z+\frac{(x_0-x_1)^2}{2Z}+\frac{(y_0-y_1)^2}{2Z} \tag{2.38}$$

By assuming the paraxial approximation (the cosine term in Eq. (2.35) is one) and substituting in the binomial approximation above Eq. (2.35) simplifies to the

Fresnel diffraction integral given by [159, p. 67],

$$\psi_Z(x_1, y_1) = \frac{e^{ikZ}}{i\lambda Z} \iint \psi_0(x_0, y_0)\, e^{\frac{ik}{2Z}\left[(x_0-x_1)^2+(y_0-y_1)^2\right]}\, \mathrm{d}x_0\, \mathrm{d}y_0 \tag{2.39}$$

As the binomial expansion is applied to the exponential phase, this can be viewed as approximating the spherical wavelets in Eq. (2.35) by paraboloids instead. The Fresnel integral may also be expressed as a convolution [88, p. 12] and viewed as the propagated field convolved with the Fresnel propagator given by,

$$\psi_Z(x, y) = \psi_0(x, y) * P_Z(x, y) \qquad P_Z(x, y) = \frac{e^{ikZ}}{i\lambda Z} e^{\frac{ik}{2Z}\left(x^2+y^2\right)} \tag{2.40}$$

From a computational standpoint, the Fresnel diffraction integral can be conveniently expressed in terms of Fourier transforms and multiplicative factors; and as such Eq. (2.39) can be rewritten as,

$$\psi_Z(q_x, q_y) = \frac{e^{ikZ}}{i\lambda Z} e^{\frac{iZ}{2k}\left(q_x^2+q_y^2\right)} \mathcal{F}\left\{\psi_0(x, y)\, e^{\frac{i\pi}{\lambda z}(x^2+y^2)}\right\} \tag{2.41}$$

This is most suitable and easier to sample for larger Z distances due to the reciprocity relation. Applying the convolution theorem to Eq. (2.40) it can also be rewritten as [88, p. 12],

$$\psi_Z(x, y) = \mathcal{F}^{-1}\left\{\mathcal{F}\left\{\psi_0(x, y)\right\} \cdot \mathcal{F}\left\{P_Z(x, y)\right\}\right\} \tag{2.42}$$

This form is most suitable and easier to sample for small Z distances due to the reciprocity relation. The accuracy of the Fresnel integral is ultimately limited by the binomial order in Eq. (2.38) and is used without loss of accuracy when [164],

$$Z \gg \sqrt[3]{\left(\frac{\pi}{4\lambda}\left[(x_0 - x_1)^2 + (y_0 - y_1)^2\right]\right)^2_{\max}} \tag{2.43}$$

where the "max" notation indicates the maximum value of interest for a given source and observation plane. Eq. (2.43) can also be relaxed for wavefields with little spatial variation, such as simple apertures illuminated by plane waves. The dimensionless Fresnel number gives a looser criterion,

$$N_F = \frac{a^2}{\lambda Z} \tag{2.44}$$

where a is the most significant extent in the wavefield source plane. The so called Fresnel or near-field regime takes place when $N_F \lessapprox 1$ for a given scenario.

2.6.4 Fraunhofer diffraction

The Fresnel diffraction integral is further simplified for large propagation distances such that the quadratic phase factor in Eq. (2.39) can be assumed flat subject to,

$$Z \gg \frac{(x^2 + y^2)_{\max}}{2} \tag{2.45}$$

We, therefore, obtain the Fraunhofer diffraction integral, which is simply the Fourier transform of the source wavefield multiplied by a phase factor and given by,

$$\psi_Z(q_x, q_y) = \frac{e^{ikZ}}{i\lambda Z} e^{\frac{iZ}{2k}(q_x^2 + q_y^2)} \mathcal{F}\{\psi_0(x, y)\} \tag{2.46}$$

We can also define a corresponding Fraunhofer or far-field condition using the previously defined Fresnel number Eq. (2.44), which is valid when $N_F \ll 1$ for a given scenario.

2.6.5 Projection approximation

The interaction of light with matter is essential to studying optical elements and scattering from samples for imaging; once again, this can be conveniently modelled with scalar diffraction theory and the Helmholtz equation.[14] As in 2.6.3 for where

[14]We restrict our analysis to linear, isotropic, non-magnetic materials were the electric permeability is time independent or static.

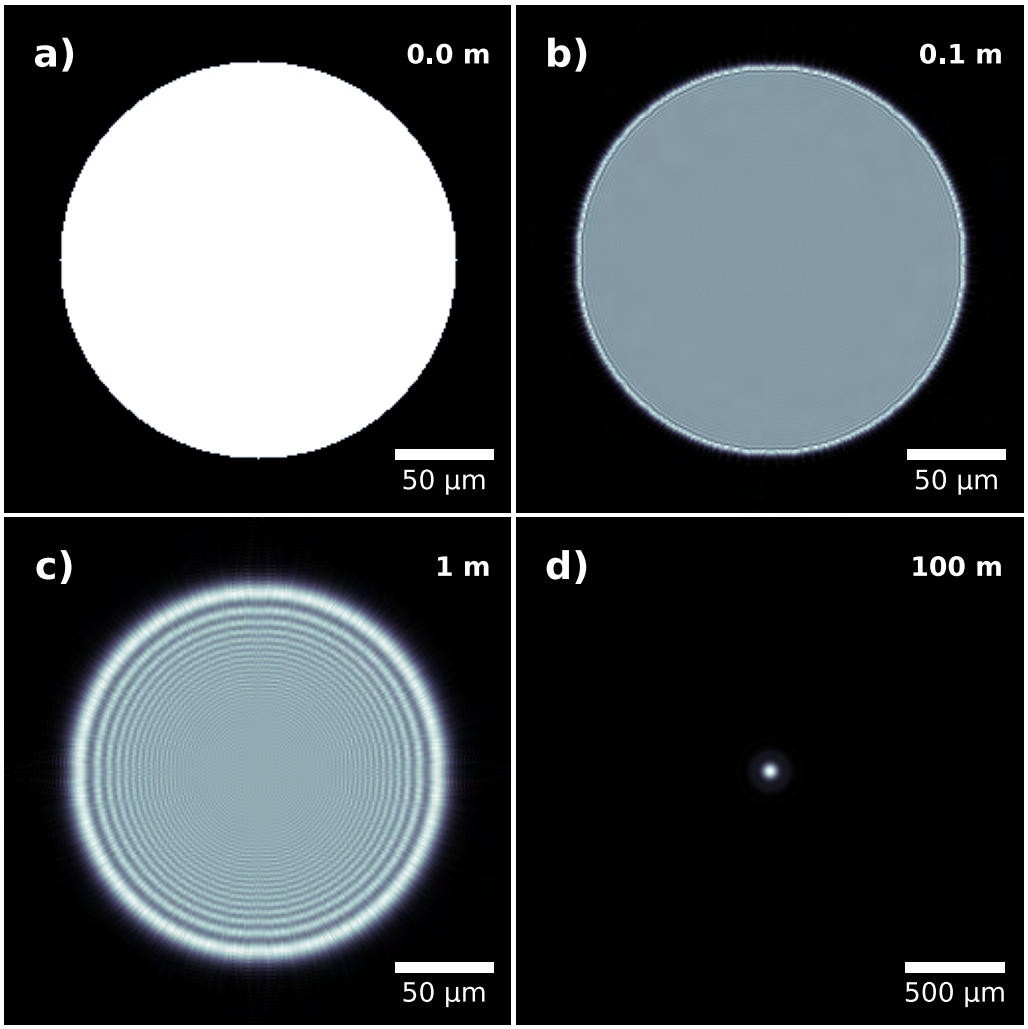


Figure 2.4: Schematic of the diffraction intensity from a simple (a) two-dimensional circular aperture using (b) Rayleigh-Sommerfeld, (c) Fresnel and (d) Fraunhofer diffraction regimes detailed in this section.

the wavefield divergence is small, the paraxial approximation can be applied and gives rise to the inhomogeneous paraxial equation [88, p. 70],

$$\left(2ik\frac{\partial}{\partial z} + \nabla_\perp^2 + k^2\left[n^2\left(\boldsymbol{r}\right) - 1\right]\right)\psi\left(\boldsymbol{r}\right) = 0 \qquad \tilde{\psi}\left(\boldsymbol{r}\right) = \psi\left(\boldsymbol{r}\right)e^{ikz} \tag{2.47}$$

where $\nabla_\perp$ is the transverse Laplacian operator and $n(\boldsymbol{r})$ is the position dependent refractive index. It's assumed that the incident wavefield is plane and modulated by a slowly varying complex envelope[15] and the paraxial approximation was used to neglect the second order derivative with respect to z in the Helmholtz equation.

[15]We will refer to this envelope function as the wavefield, even though in reality it differs from the true wavefield by some linear phase factor.

The projection approximation then assumes ray-paths through the sample are not significantly different compared to without the sample present and amounts to neglecting the transverse Laplacian operator coupling neighbouring ray trajectories. This reduces Eq. (2.47) to a first order partial differential equation (also known as the first order eikonal approximation) with solution,

$$\begin{aligned} \psi\left(\boldsymbol{r}_{\perp}\right) &= \psi_0\left(\boldsymbol{r}_{\perp}\right) \exp\left[-ik \int \delta\left(\boldsymbol{r}\right) - i\beta\left(\boldsymbol{r}\right) \mathrm{d}z\right] \\ &= \psi_0\left(\boldsymbol{r}_{\perp}\right) O(\boldsymbol{r}_{\perp}) \end{aligned} \tag{2.48}$$

where ψ_0 is the incident wavefield or complex probe function, $\delta(r)$ and $\beta(r)$ are the refractive index components and $O(\boldsymbol{r}_{\perp})$ is the complex transmission function, most commonly separated into amplitude and phase components. The complex transmission function also demonstrates matter absorption according to the Beer-Lambert law as well as the phase shift experienced by the wavefield.

3 Ptychography & diffractive imaging

3.1 Background and theory

Microscopy methods that use probing radiation such as STXM are fundamentally limited in spatial resolution by the system's point spread function originating from either the optics or coherent properties of the beam [159]. To overcome this restriction, researchers extended ideas from crystallography that has resolved atomic scale structures for over a century to non-crystalline samples [165]. Instead of directly imaging the sample, coherent diffraction imaging (CDI) techniques rely on the Fourier relationship between a coherent wave exiting a scattering object and its far-field diffraction pattern. The well known phase problem occurs since detectors only record the intensity of a wavefield, and the phase information is lost. Reconstruction of this lost phase is known as phase retrieval and is achieved in several ways computationally. The resolution is then limited by the NA of the detector, the wavelength of the radiation[1] and the detector signal to noise. Additionally, CDI techniques provide quantitative information of the sample phase and absorption. This differs from techniques such as differential phase contrast and holography, which use the sample phase shift to enhance contrast in the recorded intensity.

3.1.1 Single-shot coherent diffraction imaging

The development of coherent imaging techniques can find its origins with Gabor, who invented inline holography to overcome the resolution limitation of electron microscopes at the time [165]. This technique uses a highly coherent beam to illuminate a sample with a reference wavefield with compact support such that the

[1]The combination of high NA and longer wavelengths in the visible regime mean CDI and traditional lens based microscopy resolutions are comparable. In this regime, it's commonly used in the Fourier geometry for quantitative phase measurements.

sample phase is encoded in the reference wavefield as intensity variations. Sayre was the first to propose extending the solution to the phase problem in crystallography technique to non-crystalline structures, subject to sufficient sampling [166]. He recorded the first diffraction pattern of a diatom [167]; however, no reconstruction was attempted. It wasn't until over a decade later that Miao reconstructed an image of a gold dot array [168] from measured diffraction intensities using an iterative phase retrieval algorithm called the Hybrid Input-Output (HIO) algorithm first proposed by Fienup [169]. This reconstructed an image with a spatial resolution of 75 nm using soft X-rays, a considerable achievement at the time, and later also retrieved the 3D volume [170]. This ignited exponential growth in the field, and has since grown significantly in both size and scope; a review of the basic principles of CDI follows as a helpful precursor to ptychography.

The principal objective of CDI methods is to recover the unknown phase of a given diffraction pattern intensity. This is recorded at some distance as the propagated exit wavefield of some illumination probe and sample transmission function. Mathematically this means finding the complex values of the wavefield $\psi(\boldsymbol{r})$ that agree with the experimentally measured intensities and obey the following equation,

$$I(\boldsymbol{q}) = |\mathcal{F}\{\psi(\boldsymbol{r})\}|^2 \tag{3.1}$$

where $\psi(\boldsymbol{r})$ is the exit wavefield at the sample plane.[2] In his paper [166], Sayre used a recently published sampling theorem by Shannon [171] to argue that the phase problem could be solved if the recorded diffraction pattern was sufficiently oversampled at twice the Nyquist frequency.

$$\sigma_{x,y} = \frac{\lambda z}{\Delta w D} \tag{3.2}$$

[2]This assumes a far-field experimental setup as is the case within the thesis, but near-field is also possible with different sampling conditions not discussed.

where λ is the radiation wavelength, z is the detector distance, D is the aperture size and Δw is the detector pixel size. Reconstruction occurs when the intensity is oversampled with $\sigma_{x,y} > 2$; however, it's typically much larger. Limiting the aperture spatial extent corresponds to a restriction of the highest frequency that can be recorded in the diffraction pattern.

Most algorithmic implementations are built on the ideas first proposed by Gerchberg & Saxton (GS) [172] and the error reduction (ER) algorithm. With each iteration, the reconstructed wavefield is transformed back and forth between real and reciprocal space[3] using the Fourier transform with support and modulus constraints applied, respectively. The support constraint is applied in real space and sets all values outside the known aperture size to zero. The modulus constraint is applied in the reciprocal space and replaces the wavefield moduli generated from the Fourier transform step with those measured experimentally but keeps the phase component unchanged. Additional *a priori* information can also be included such as the positivity constraint in which the electron density of the specimen is real and positive as with hard X-rays. A typical iteration of the GS algorithm is given below.

1. **Modulus Projector:** The modulus projector maps the measured intensity modulus onto the calculated Fourier wavefield modulus according to,

$$\pi_F\{\psi(\boldsymbol{r})\} = \mathcal{F}^{-1}\left\{\frac{\mathcal{F}\{\psi(\boldsymbol{r})\}}{|\mathcal{F}\{\psi(\boldsymbol{r})\}|}\sqrt{I(\boldsymbol{q})}\right\} \tag{3.3}$$

   where $I(\boldsymbol{q})$ is the measured intensity and $\psi(\boldsymbol{r})$ is the reconstructed wavefield.

2. **Support Projector:** The support projector restricts the signal spectrum by

[3]The Fourier operator conveniently defines the sample and detector pane in the real and reciprocal space, respectively.

applying a support constraint that zeros everything outside the aperture,

$$\pi_S\{\psi(\boldsymbol{r})\} = \begin{cases} \psi(\boldsymbol{r}) & r \in S \\ 0 & r \notin S \end{cases} \tag{3.4}$$

where S is the support region. This is usually not known precisely but can be iteratively refined using a shrink-wrap method [173].

3. **Wavefield Update:** The reconstruction is iteratively updated by applying the previously described projection operators in turn to the current wavefield,

$$\psi_{n+1}(\boldsymbol{r}) = \pi_S \cdot \pi_F\{\psi_n(\boldsymbol{r})\} \tag{3.5}$$

where each of the projection operators act on the wavefield in turn and this is known as the error reduction algorithm.

Several algorithms have since arisen that use a similar projection-based approach and can be helpful in specific circumstances or paired with one another to reduce stagnation; these include the Hybrid Input-Output (HIO) [169], the Solvent Flipping (SF) [174], the Relaxed Averaged Alternating Reflections (RAAR) [175], the Difference Map (DM) [176]; a good review of the comparative performance is provided in [177]. The primary drawback of the CDI technique is its limited spatial extent; even for large propagation distances and small pixel sized detectors, the coherence length over the aperture then becomes the limiting factor. For certain samples, there can be additional complications with the twin image problem, whereby the wavefield conjugate simultaneously exists in the reconstruction. Finally, a lot of useable flux is wasted with finite support apertures compared to focusing optics.

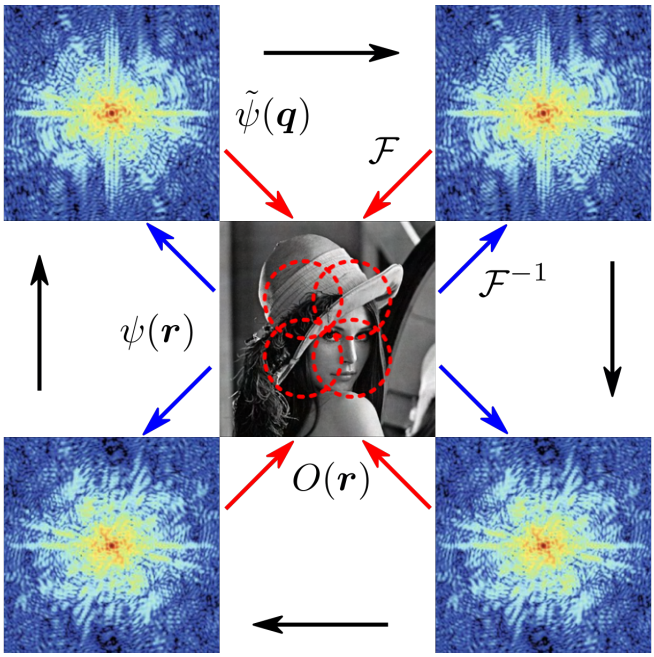


Figure 3.1: Schematic representation of a ptychography reconstruction which loops through all diffraction patterns at different positions on the sample and projects back and forth between the real and reciprocal space.

3.1.2 Ptychography extension

The majority of issues associated with CDI were rectified with the development of ptychography, which has seen wide adoption as a standard technique at many facilities. The naive approach to extending CDI's field of view capabilities is to take a number of acquisitions at different sample positions, reconstruct these independently, and then stitch them together. However, it was remarked by Hoppe & Hegerl [180] and demonstrated by Faulkner & Rodenburg [181] that overlapping diffraction patterns deliver a much better reconstruction. This additional "overlap" constraint introduces redundancy in the data which removes the dreaded twin image problem as well as increases the iterative algorithms' convergence success and robustness to noise. Whilst a direct inversion solution is possible by the Wigner Distribution Deconvolution (WDD) method [182], a more robust and experimentally relaxed method is to solve the problem iteratively. This was first demonstrated by Rodenburg using the Ptychographic Iterative Engine (PIE) [34].

Ptychography scans are performed by scanning a localised illumination (probe)

over an extended sample with the illuminated areas between adjacent scan positions overlapping. At each scan position, the diffraction pattern intensity is recorded at some distance in the far-field. By the projection approximation 2.6.5, the exit wave is simply given as the product of the probe and sample functions. The collection of far-field intensity patterns is then given by,

$$I_j(\boldsymbol{q}) = \left|\mathcal{F}\left\{\psi_j(\boldsymbol{r})\right\}\right|^2 = \left|\mathcal{F}\left\{P(\boldsymbol{r})\, O(\boldsymbol{r}+\boldsymbol{r}_j))\right\}\right|^2 \tag{3.6}$$

where $\psi_j(\boldsymbol{r})$ is the exit wavefield of the jth view scan position, $P(\boldsymbol{r})$ and $O(\boldsymbol{r})$ are the complex probe and sample functions respectively. Mathematically the aim of the phase retrieval is to find values for the probe $P(\boldsymbol{r})$ and sample $O(\boldsymbol{r})$ functions that satisfy Eq. (3.6) and agree with the experimentally measured intensities.

Experimentally, the relative positions of the diffraction intensities are realised by scanning the sample using high-precision stages with respect to a fixed illumination. Pinhole apertures can be used; however, produce diffraction intensities with a high dynamic range and must be positioned very close to the sample. Focusing optics are more commonly used[4] as they provide a higher flux density at the sample position and generate a variable probe size at defocused positions, the need for which is discussed in the proceeding section. Initially, the probe was presumed known; however, it was found that excessive data redundancy meant the probe function could also be reconstructed simultaneously [39]. This considerably improves the sample reconstruction quality and also saw ptychography spun out as an optical metrology technique [41, 42]. Convergence is greatly enhanced by adequately modelling the initial probe and relies on *a priori* knowledge of the optics used.

If the overlap redundancy is large enough, ptychography can correct for many common sources of experimental degradation in the post experimental reconstruction, including partial coherence [47], background noise [183], position uncertainty

[4]This has been partly rectified in CDI with Fresnel CDI [178, 179]; however, accurate *a priori* determination of the initial probe without any sample is also required [36].

[184, 185], detector distance [186], and probe instability [187], to name a few. Position uncertainty occurs when there is a difference in the actual and recorded scan positions. For significant errors, an annealing procedure [184] is usually used, which generates a subset of random positions around each point. The position with the smallest error is then taken as the updated position. An alternative method is calculating the gradient difference between the generated and measured intensities [185]. This procedure is much less computationally demanding and offers sub-pixel refinement, so it's usually included as part of the ML refinement. The effect of an error in the sample to detector distance results in scaling of all the real space coordinates [186]. This can be corrected by using a lateral position correction algorithm similar to how drifts are also corrected, for example, a random walk correction scheme [188].

3.2 Iterative phase retrieval

Iterative algorithms are the most common class of phase retrieval and, since being implemented computationally are usually referred to as engines [189]. These build on the same principles as the original methods developed by Gerchberg & Saxton [172] and Fienup [169] for work in CDI. All ptychographic engines will similarly apply the modulus constraint but differ in how they update the sample and probe functions through the overlap constraint [190]. The different methods all possess their strengths and weaknesses, which is why no one method has found dominance in the previous decades,[5] the main factors that vary between them are as follows [177]: the success of initial convergence, number of tuning parameters, robustness to noise, implementation computationally and its reconstruction speed. The first iterative algorithm was the Ptychographic Iterative Engine (PIE) [34] which updates each diffraction pattern sequentially, whereas later methods act in parallel through a projection formalism [35, 175, 191]. It's also common to link engines, where the output from one will form the input to the next [192]. Furthermore, in many cases,

[5]Different research groups will also typically only work on their method, which could also be the reason why no method has fallen out of favour.

the same algorithm performance will differ slightly between implementations due to differences in coding languages and how it's written.

3.2.1 Difference map algorithm

The first method to simultaneously reconstruct both the complex probe $P(\boldsymbol{r})$ and sample $O(\boldsymbol{r})$ functions was developed by Thibault [39], and the solution can be found as the intersection of two constraint sets. Projection operators enforce the constraints and act on the high dimensional state vector $\Psi = (\psi_1(\boldsymbol{r}), \psi_2(\boldsymbol{r}), \ldots \psi_N(\boldsymbol{r}))$, which is composed of the individual exit wavefields. The state vector is then projected onto the constraint sets such that the Euclidean distance between the current and projected states is minimised. The projection operators are given by,

$$\Pi_F(\Psi) : \psi_j \longrightarrow \psi_j^F = \pi_F(\psi_j) \tag{3.7}$$

$$\Pi_O(\Psi) : \psi_j \longrightarrow \psi_j^O = P(\boldsymbol{r})\, O(\boldsymbol{r} - \boldsymbol{r}_j) \tag{3.8}$$

where Π_F is the Fourier modulus and Π_O is the overlap projector, respectively. Since the overlap constraint cannot be applied analytically, it can be found by minimising the Euclidean distance between the current state Ψ and projected state $\Pi_O(\Psi)$ according to,

$$\mathcal{L} = \sum_j \int |\psi_j(\boldsymbol{r}) - P(\boldsymbol{r})O(\boldsymbol{r} - \boldsymbol{r}_j)|^2 \, \mathrm{d}\boldsymbol{r} \tag{3.9}$$

where $\mathcal{L}$ represents a typical cost minimisation problem, the minima of which is found where the gradients of the distance vanish and give rise to the set of coupled equations for the probe and sample update,

$$P(\boldsymbol{r}) = \frac{\sum_j O^*(\boldsymbol{r} - \boldsymbol{r}_j)\, \psi_j(\boldsymbol{r})}{\sum_j |O(\boldsymbol{r} - \boldsymbol{r}_j)|^2} \tag{3.10}$$

$$O(\boldsymbol{r}) = \frac{\sum_j P^*(\boldsymbol{r} + \boldsymbol{r}_j)\, \psi_j(\boldsymbol{r} + \boldsymbol{r}_j)}{\sum_j |P(\boldsymbol{r} + \boldsymbol{r}_j)|^2} \tag{3.11}$$

The probe and sample coupling means it's impossible to apply the probe and sample update simultaneously; however, it's sufficient to apply the updates alone for a few iterations. Using the projection operators and selecting the DM tuning parameters [176], the update is applied iteratively on the whole state vector,

$$\Psi_{n+1} = \Psi_n + \Pi_F \left[2\Pi_O \left(\Psi_n\right) - \Psi_n\right] - \Pi_O \left(\Psi_n\right) \tag{3.12}$$

In between this, the probe and sample update according to Eq. (3.10) and Eq. (3.11), we observe that $\Psi_{n+1}\left(\boldsymbol{r}\right) = \Psi_n\left(\boldsymbol{r}\right)$ only when the probe and sample product satisfy the Fourier constraint. Since the probe is only updated every full iteration, it's not as prone to stagnation in local minima; we also find that most of the computational steps can be parallelised and run simultaneously on different processors.

Convergence of the DM algorithm is monitored using the distance between the n and $n+1$ estimate of the high dimensional state vector, i.e., $\varepsilon_{n+1} = |\Psi_{n+1} - \Psi_{n+1}|^2$. In the presence of noise, as with all experimental setups, this value will rarely converge to zero but instead oscillate around a stable solution. Therefore the error ε_{n+1} is usually averaged over several iterations and when this value is constant, the reconstruction is said to have converged to a stable solution [39]. The validity of the solution is usually assessed using the reconstructed probe, as the optical parameters are usually known in advance, e.g. the aperture size at the optic plane. To ensure the reconstruction is not some local minimum solution, a few reconstructions can be run using initial probes with different defocused profiles. The smallest difference map error ε_{n+1} will be the true solution.

3.2.2 Extended ptychographic iterative engine

The extended ptychographic iterative engine (ePIE) was a further development by Maiden and Rodenburg [40] of the PIE following Thibault's inclusion of probe retrieval in the DM reconstruction. The Fourier modulus projection operator is very similar to the DM, except that it's applied at every exit wavefield position instead

of every iteration. The overlap constraint again cannot be applied analytically and at each position seeks to minimise the Euclidean distance between the sets,

$$\mathcal{L} = \sum_j \int \left|\psi_{n,j}\left(\boldsymbol{r}\right) - \psi'_{n,j}\left(\boldsymbol{r}\right)\right|^2 \mathrm{d}\boldsymbol{r} \qquad \psi_{n,j}\left(\boldsymbol{r}\right) = P\left(\boldsymbol{r}\right) O\left(\boldsymbol{r} - \boldsymbol{r}_j\right) \tag{3.13}$$

where the n index is the current iteration and $\psi'_n\left(\boldsymbol{r}\right)$ is the Fourier modulus constrained exit wavefield. The solution is found using the gradient descent scheme; only the derivative of Eq. (3.13) is required. The updated probe and sample function are then given as,

$$P_{n+1}\left(\boldsymbol{r}\right) = P_n\left(\boldsymbol{r}\right) + \alpha \frac{O^*\left(\boldsymbol{r} + \boldsymbol{r}_j\right)}{\left|O\left(\boldsymbol{r} + \boldsymbol{r}_j\right)\right|^2_{\max}} \left[\psi_{n,j}\left(\boldsymbol{r}\right) - \psi'_{n,j}\left(\boldsymbol{r}\right)\right] \tag{3.14}$$

$$O_{n+1}\left(\boldsymbol{r}\right) = O_n\left(\boldsymbol{r}\right) + \beta \frac{P^*\left(\boldsymbol{r} - \boldsymbol{r}_j\right)}{\left|P\left(\boldsymbol{r} - \boldsymbol{r}_j\right)\right|^2_{\max}} \left[\psi_{n,j}\left(\boldsymbol{r}\right) - \psi'_{n,j}\left(\boldsymbol{r}\right)\right] \tag{3.15}$$

A single iteration ends after looping through all the positions and their associated wavefields; the order is usually randomised to reduce the likelihood of probe stagnation in local minima, a common issue with ePIE. The tuning parameters α and β are used to control the rate of convergence and are normally set between 0 and 1, with higher and lower values increasing and stabilising the rate, respectively. Further improvements have been introduced to keep the PIE family competitive with other methods [193]. They are based on modified weights of the probe and sample update known as rPIE, as well as adding ideas from neural networks such as momentum acceleration known as mPIE. The PIE family cannot be natively[6] parallelised; however, modern GPUs offer computational times that reduce each position calculation to a point on par with parallelised methods.

Unlike the DM method, the ePIE method is based on a gradient descent scheme which is typically much slower to converge to the true solution [193]. Convergence of the ePIE algorithm is usually monitored using the Fourier space error [177], which

[6] Attempts have been made such as dividing the calculation up and processing these individually; however, the results are never quite as good as the original implementation [194].

quantifies how the Fourier transform of the current exit wavefield $\Psi_{n,j}(\boldsymbol{q})$ fits the measured intensity $I_j(\boldsymbol{q})$ as a whole. It is defined by,

$$E_n = \frac{\sum_j \sum_{\boldsymbol{q}} |\sqrt{I_j(\boldsymbol{q})} - \Psi_{n,j}|^2}{\sum_j \sum_{\boldsymbol{q}}} \tag{3.16}$$

Convergence is achieved once the error metric E_n attains a constant value. This may require adjustment of the tuning parameters or a better initial guess of the probe in order to converge in a realistic number of iterations. As with the DM, the solution is usually validated using the reconstructed probe and known optical parameters, and the smallest E_n solution is taken to be the true solution.

3.3 Probe illumination

Unlike traditional single-shot CDI which assumes a flat illumination, probe retrieval in ptychography means, any compact illumination can be used subject to it obeying the sampling criteria described in section 3.5. Fresnel or key-hole CDI [179] has alleviated this restriction in the single-shot CDI community somewhat but the results are still not as good as those achieved with ptychography. One caveat of ptychography is that a good initial approximation of the probe is usually required to achieve a convergent reconstruction [39]. This requires some *a priori* knowledge of the probe used, such as the focal length or aperture size in order to model it beforehand properly. The three primary methods of probe illumination in ptychography are described below.

- **Pinhole Aperture:** This is the simplest to experimentally implement and easiest to model in the reconstruction [39, 40]. However, the element has to be placed close to the sample due to edge diffraction from the aperture, which can reduce the flexibility of the setup. The far-field intensity also produces a beam with high counts in the central beam spot and low counts at the larger scattered angles [195]. This means the signal-to-noise corresponding to high

frequency components of the sample will be less. It can also be challenging to fabricate pinholes of small enough aperture, especially for hard X-rays, and there is no flexibility to change the size of the probe other than to use a different aperture. Furthermore, the coherence length at high coherence beamlines is usually much larger than the used pinhole size meaning a significant portion of the flux is simply wasted,

- **Focusing Optic:** This is the most common method implemented today on most beamlines employing various focusing devices; however, FZPs tend to feature the most commonly due to their ease of use and more stable nature. Focusing optics can capture far larger portions of the coherent beam and also spread the intensity over a greater area of the detector to alleviate the issues with dynamical range [195]. They also offer far greater flexibility in terms of the beam size, which can be achieved via translation of the sample along the optical axis to different defocused positions. Focusing also encodes more significant information about the sample in the diffraction intensity as the focused wavefront consists of a sum of plane waves at different angles [196]. As a result, when the sample is scanned, the same point will be scattered and encoded at different positions on the detector.

- **Structured Probe:** The noticeable benefits of using focusing optics with high phase diversity have led to the development of customised optics for ptychography [195]. The simplest known about and used previously in traditional single-shot CDI was a diffusing medium in front of the pinhole aperture [197]. These drastically increase the incident wavefield angular range but must also be positioned at the sample plane to ensure the probe remains compact. Within ptychography, the only method investigated so far has been the introduction of aberrations to FZP optics, manifesting as an increased phase diversity when propagated to the sample plane [196]. These have shown aus-

picious results in improving the quality of reconstructions and even increasing the resolution. However, as more significant aberrations are introduced, the focusing performance will begin to degrade to a point where the required probe size sampling can no longer be achieved.

3.4 Partially coherent ptychography

So far, it has been assumed that the beam is coherent such that all points on the wavefield have a fixed amplitude and phase relative to one another [15, p. 286]. In reality, most light sources, including synchrotrons, are statistically spontaneous and emit randomly over a broad energy range due to their extended nature. Furthermore, any source or sample instability occurring during the acquisition will further degrade the diffraction contrast and may be treated as an ensemble average that emulates a partially coherent effect. The theoretical and experimental characterisation of the coherence properties of beams is fundamental for proper planning, conducting and analysing coherent based techniques [198]. Synchrotron sources have previously been shown to obey the Gaussian statistics of a polarised thermal light source such that the wavefield can be considered stationary and homogenous and that statistical optics can be applied [199, p. 116]. This section is mainly dedicated to the description of transverse coherence given its prevalence within the thesis, longitudinal effects are generally negligible[7] given the quality of double crystal monochromators used in most experiments.

3.4.1 Statistical correlation functions

The central concept in optical coherence theory describes partially coherent sources with space-time correlations [200]. It's most commonly envisaged using a collection of two pinhole apertures to represent the points on the wavefield with the location and contrast of the interference fringes described by the first-order correlation

[7]Broad bandwidth ptychography [55] offers exciting potential with the much narrower harmonic bandwidths from fourth generation undulator sources; however, its treatment is different.

function or mutual coherence function (MCF). For two complex scalar values of the wavefield at different points in space and time, defined as [90, p. 163],

$$\Gamma(\boldsymbol{r}_1, \boldsymbol{r}_2, \tau) = \langle \psi(\boldsymbol{r}_1, t)\psi^*(\boldsymbol{r}_2, t+\tau)\rangle \tag{3.17}$$

where $\psi(\boldsymbol{r}_1, t+\tau)$ and $\psi(\boldsymbol{r}_2, t)$ are the field values at the points $\boldsymbol{r}_1$ and $\boldsymbol{r}_2$ respectively, τ is the time delay and the brackets denote a time averaging much longer than the X-ray field fluctuation. Although higher-order correlation functions are possible [201, p. 7], X-ray sources have been shown to be thermally Gaussian in nature such that Eq. (3.17) completely defines the wavefield [198]. The MCF is most commonly normalised to give the Complex Degree of Coherence (CDC) given by,

$$\gamma(\boldsymbol{r}_1, \boldsymbol{r}_2, \tau) = \frac{\Gamma(\boldsymbol{r}_1, \boldsymbol{r}_2, \tau)}{\Gamma(\boldsymbol{r}_1, \boldsymbol{r}_1, 0)\Gamma(\boldsymbol{r}_2, \boldsymbol{r}_2, 0)} = \frac{\Gamma(\boldsymbol{r}_1, \boldsymbol{r}_2, \tau)}{\sqrt{I(\boldsymbol{r}_1)}\sqrt{I(\boldsymbol{r}_2)}} \tag{3.18}$$

where we have also taken the self-correlation of the field to be the intensity distribution, given that this will ultimately be what is measured. The absolute value of the CDC is then bounded by $0 \leq |\gamma(\boldsymbol{r}_1, \boldsymbol{r}_2, \tau)| \leq 1$ with the extreme upper and lower bounds corresponding to no correlation between points (incoherent) and complete correlation between points (coherent), respectively. Intermediate values are partially correlated, with the wavefield similarly termed partially coherent.

3.4.2 Spectral decomposition

In most circumstances, it's more intuitive, particularly from an experimental perspective, to consider the temporal field correlations in terms of their optical frequencies, such that a time-independent correlation function can be defined. Following Mandel & Wolf [90, p. 170], the Cross-Spectral Density (CSD) function forms a Fourier transform pair with the MCF in the time-frequency domain and is given by,

$$W(\boldsymbol{r}_1, \boldsymbol{r}_2, \omega) = \int \Gamma(\boldsymbol{r}_1, \boldsymbol{r}_2, \tau)e^{i\omega\tau}\mathrm{d}\tau \tag{3.19}$$

which is performed over the entire variable range of integration and gives a measure of the correlation between spectral amplitudes of the same frequency ω at points $\boldsymbol{r}_1$ and $\boldsymbol{r}_2$ on the wavefield. The CSD function is also most commonly normalised to give the spectral degree of coherence (SDC) given by,

$$\mu(\boldsymbol{r}_1, \boldsymbol{r}_2, \omega) = \frac{W(\boldsymbol{r}_1, \boldsymbol{r}_2, \omega)}{W(\boldsymbol{r}_1, \boldsymbol{r}_2, \omega)W(\boldsymbol{r}_2, \boldsymbol{r}_2, \omega)} = \frac{W(\boldsymbol{r}_1, \boldsymbol{r}_2, \omega)}{\sqrt{S(\boldsymbol{r}_1, \omega)}\sqrt{S(\boldsymbol{r}_2, \omega)}} \tag{3.20}$$

where we have also taken the self-correlation of the CSD to represent the spectral density, $S(\boldsymbol{r}, \omega)$ or the power spectrum of the wavefield. As with the CDC, the modulus of the CSD is bounded by the following inequality $0 \leq |\mu(\boldsymbol{r}_1, \boldsymbol{r}_2, \omega)| \leq 1$. The transverse coherent properties of a quasi-monochromatic beam are characterised by a single number, the degree of the transverse coherence given by [202, p. 5],

$$\zeta(\omega) = \frac{\int |\mu(\boldsymbol{r}_1, \boldsymbol{r}_2, \omega)|^2 S(\boldsymbol{r}_1, \omega) S(\boldsymbol{r}_2, \omega) \mathrm{d}\boldsymbol{r}_1 \mathrm{d}\boldsymbol{r}_2}{\left| \int S(\boldsymbol{r}, \omega) \, \mathrm{d}\boldsymbol{r} \right|^2} \tag{3.21}$$

where according to its definition, the values of $\zeta(\omega)$ lie in the range $0 \leq \zeta(\omega) \leq 1$ and define the fraction of coherent flux for a monochromatic wavefield of frequency ω. This is the comparative value for coherence based analysis in the thesis and is most easily recovered through multi-modal, partially coherent ptychography.

3.4.3 Quasi-monochromatic approximation

A standard optical element on synchrotron beamlines is the double crystal monochromator which reduces the spectral components of the beam to a narrow angular frequency range $\Delta\omega$. Under the quasi-monochromatic approximation [201, p. 7], the MCF may be rewritten using the sifting property of the delta function such that,

$$\Gamma(\boldsymbol{r}_1, \boldsymbol{r}_2, \tau) \approx J(\boldsymbol{r}_1, \boldsymbol{r}_2) e^{i\omega_0 \tau} \tag{3.22}$$

where ω_0 is the central angular frequency of the distribution and $J(\boldsymbol{r}_1, \boldsymbol{r}_2) = \Gamma(\boldsymbol{r}_1, \boldsymbol{r}_2, 0)$ is referred to as the Mutual Optical Intensity (MOI). Substitution of the quasi-

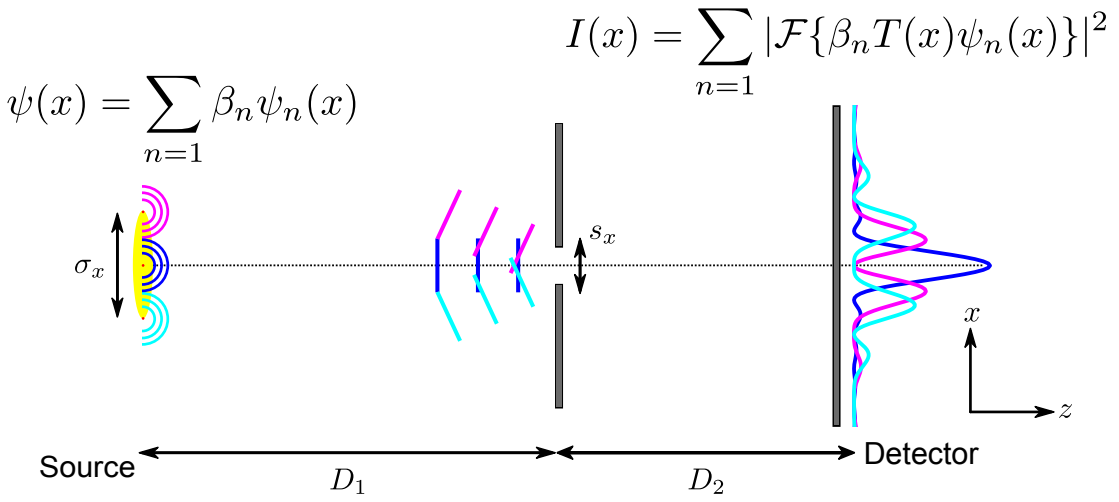


Figure 3.2: Schematic of the coherent mode representation of an extended synchrotron source demonstrating how coherent modes originate and propagate through a simple aperture to a far-field detector.

monochromatic approximation Eq. (3.22) into the CSD Eq. (3.19) defines the spectral density for a quasi-monochromatic field as,

$$W(\boldsymbol{r}_1, \boldsymbol{r}_2, \omega) \approx J(\boldsymbol{r}_1, \boldsymbol{r}_2)\delta(\omega - \omega_0) \tag{3.23}$$

where $\delta(\omega - \omega_0)$ is the Dirac delta function. That is to say, the wavefield can be considered fully temporally coherent and consisting of a single optical frequency ω_0. This approximation additionally leads to the equivalence of the CDC and SDC given by $|\gamma(\boldsymbol{r}_1, \boldsymbol{r}_2, \tau)| = |\mu(\boldsymbol{r}_1, \boldsymbol{r}_2, \omega_0)|$. The same conditions also lead to the spectral density being equivalent to the average intensity given by $S(\boldsymbol{r}, \omega) = \langle I(\boldsymbol{r})\rangle\delta(\omega - \omega_0)$.

3.4.4 Coherent mode representation

The exact properties of the full CSD function of Eq. (3.19) form a four-dimensional function; impractical for most computing applications, particularly CDI and ptychography. It has been shown previously [200] by Mercer's theorem[8] that under very general conditions, the CSD can be rewritten as a sum of independent coher-

[8] A fundamental theorem in functional analysis where a continuous, non-negative definite, hermitian Hilbert-Schmidt kernel may be expressed as a uniformly convergent series.

ent modes given by,

$$W(\boldsymbol{r}_1, \boldsymbol{r}_2, \omega) = \sum_{n=1} \alpha_n(\omega)\psi_n(\boldsymbol{r}_1, \omega)\psi_n^*(\boldsymbol{r}_2, \omega) \tag{3.24}$$

where $\alpha_n(\omega) \geq 0$ are the positive and real eigenvalues due to the hermiticity and non-negative definiteness of $W(\boldsymbol{r}_1, \boldsymbol{r}_2, \omega)$, which represent and are sometimes referred to as modal weights, equal to the relative power contribution of the mode. $\psi_n(\boldsymbol{r}, \omega)$ are the eigenfunctions, which form an orthogonal set and satisfy the Fredholm integral equation of the second kind given by,

$$\int W(\boldsymbol{r}_1, \boldsymbol{r}_2, \omega)\psi_n(\boldsymbol{r}_1, \omega)\mathrm{d}\boldsymbol{r}_1 = \alpha_n(\omega)\psi_n(\boldsymbol{r}_2, \omega) \tag{3.25}$$

In the coherent case, the CSD reduces to a single mode and the usual form of Eq. (3.19). Furthermore, the eigenfunctions may be orthonormal or, in case of an ambiguous eigenvalue degeneracy [203], orthogonalized by a Gram-Schmidt procedure. From Eq. (3.23) it's apparent that the MOI similarly decomposes as a set of coherent orthogonal modes.

$$J(\boldsymbol{r}_1, \boldsymbol{r}_2) = \sum_{n=1} \alpha_n\psi_n(\boldsymbol{r}_1)\psi_n^*(\boldsymbol{r}_2) \tag{3.26}$$

As the eigenfunctions can always be written in an orthonormal basis such that $\psi(\boldsymbol{r}) = \sum \beta_n\psi_n(\boldsymbol{r})$, this means that the eigenvalue β_n unit is simply transmitted power. A modes relative power is then defined by the fraction it contributes given by $\beta_n / \sum_n \beta_n$. This formulation is consistent with the work of Thibault and Menzel [47], which refer to the modes as states and incorporate the result into ptychography. A schematic representation of how eigenmodes arise from an extended synchrotron source is shown in Fig. 3.2.

The effective number of coherent modes $\mathcal{N}(\omega)$ places an upper bound on the optimal point for truncating the modal expansion of Eq. (3.26), which is necessary

since an infinite number of terms cannot be computed computationally. Previous studies have found the effective number of modes $\mathcal{N}(\omega)$ given by [204, p. 10],

$$\mathcal{N}(\omega) \leq \frac{\left(\int S(\boldsymbol{r},\omega)d\boldsymbol{r}\right)^2}{\iint |W(\boldsymbol{r}_1,\boldsymbol{r}_2,\omega)|^2 d\boldsymbol{r}_1 d\boldsymbol{r}_1} \tag{3.27}$$

One of the most common solutions to Eq. (3.27) is when the partially coherent source is of a Gaussian-Schell model, such that the spectral density and SDC are Gaussian functions and the CSD are given by [202, p. 7],

$$W(\boldsymbol{r}_1,\boldsymbol{r}_2,\omega) = \sqrt{S(\boldsymbol{r}_1)}\sqrt{S(\boldsymbol{r}_2)}\mu(\boldsymbol{r}_2-\boldsymbol{r}_1) \tag{3.28}$$

$$S(\boldsymbol{r}) = S(0,\omega)\exp\left[\frac{\boldsymbol{r}^2}{2\sigma_{x,y}^2}\right], \quad \mu(\boldsymbol{r}_2-\boldsymbol{r}_1) = \exp\left[\frac{(\boldsymbol{r}_2-\boldsymbol{r}_1)^2}{2\xi_{x,y}^2}\right] \tag{3.29}$$

where the parameters $\sigma_{x,y}$ define the RMS source size and $\xi_{x,y}$ the coherence length of the source in the x, y respective directions. Substitution of this model into the number of effective modes Eq. (3.27) results in the following relationship for the one-dimensional case [204, p. 12],

$$\mathcal{N}(\omega) \leq \max\left(\sqrt{1+\frac{4}{q_x^2}}, \sqrt{1+\frac{4}{q_y^2}}\right), \quad q_{x,y} = \frac{\xi_{x,y}}{\sigma_{x,y}} = \frac{\Xi_{x,y}}{\Sigma_{x,y}} \tag{3.30}$$

where $q_{x,y}$ defines the degree of coherence and according to the Gaussian-Schell model, remains constant along the length of the beam [202, p. 10]. This is a useful property as it allows us to use the Van-Cittert theorem to estimate $\Xi_{x,y}$ at the optic position with $\Sigma_{x,y}$ just the size of the optic aperture.

3.5 Oversampling criteria

Ptychography and CDI represent a class of computational imaging techniques that are based on the recording and reconstruction of discrete signals. Nyquist & Shannon showed to recover an original continuous signal[9] from its discrete sampled ver-

[9]Strictly the theorem is only valid for functions which have a Fourier transform that is zero outside some finite region of frequencies, which is the case in ptychography & CDI.

sion without loss of information the sampling interval must be smaller than half the reciprocal bandwidth [171]. The discrete Fourier transform of a two-dimensional discrete function is given by,

$$\mathcal{F}\{\psi(x,y)\} = \sum_{n=0}^{N-1}\sum_{m=0}^{M-1} \psi(x,y) \exp\left[-2\pi i \left(\frac{q_x x}{M} + \frac{q_y y}{N}\right)\right] \tag{3.31}$$

where x, y and q_x, q_y are the discrete coordinates in real space and reciprocal space, respectively, and M, N are the numbers of discrete points in real space along x, y directions. In far-field ptychography, as is considered in this thesis, the diffraction intensity at each position is given by the Fraunhofer propagation of the exit wavefield using the discrete Fourier transform of Eq. (3.31). This results in the following relationship between the sample and detector plane sampling periods,

$$\Delta x = \frac{\lambda z}{N \Delta w} \tag{3.32}$$

where Δx is the real (sample) space pixel size, Δw is the reciprocal (detector) space pixel size, N is the number of discrete pixels and z is the sample-to-detector distance. This means the ptychography reconstructed pixel size at the sample plane is solely determined by the experimental geometry. In ptychography, the diffraction intensities are sampled in both reciprocal space by the detector and real space by probe overlap. They are both discussed separately below.

- **Reciprocal Space:** Within traditional single-shot CDI, the intensity of a single diffraction pattern will be sampled at the detector plane by a factor $\sigma_{x,y}$ [37]. In the far-field regime, this is solely determined by the detector sampling pitch Δw, radiation wavelength λ, distance from the specimen plane z and maximum extent of the probe D such that the sampling ratio is,

$$\sigma_{x,y} = \frac{\lambda z}{\Delta w D} \tag{3.33}$$

According to the Nyquist-Shannon sampling theorem [171] to fully recover the real space signal at the sample plane, the detector sampling must be less than half the reciprocal bandwidth which means $\sigma_{x,y} > 2$. This imposes restrictions on the probe size based on the experimental geometry, $\sigma_{x,y}$ which is usually much larger than 2 and where the term oversampling comes from.

- **Probe Overlap:** Ptychography increases the oversampling of traditional CDI by measuring the same area on the sample more than once [205, p. 828]. Therefore in ptychography, sampling consists of both a real space and reciprocal space factor. The two sampling factors have been shown to be interchangeable without any loss of information [206, 207]. The overlap sampling factor is given as,

$$\omega_{x,y} = 1 - \frac{R}{D} \tag{3.34}$$

where R is the scanning step size, such that R/D represents just the reciprocal overlap ratio, which has been previously found to be optimal at around 60% [190]. This also assumes a linear overlap which may not be suitable given the more diverse set of scanning patterns that are typically used [208].

The combined ptychography oversampling factor is simply a product of both reciprocal space $\sigma_{x,y}$ and real space $\omega_{x,y}$ sampling factors. Furthermore, the total sampling will be the product of the two previously defined one-dimensional sampling ratios such that the total sampling ratio is given by [206],

$$S_{\Pi} = \left(\frac{\sigma_{x,y}}{1 - \omega_{x,y}} \right)^2 \tag{3.35}$$

Thus the fundamental ptychographic sampling occurs when $S_{\Pi} = 1$ with values greater and less than corresponding to over and under sampling, respectively. The result in Eq. (3.35) demonstrates that, unlike traditional CDI, ptychography does not depend at all on the probe size, and it's always possible to upsample the data in

post processing to some artificial detector with the correct sampling [209, p. 112].

The usual oversampling ratio given by Eq. (3.35) assumes a single, coherent probe. If multiple probe modes are required according to Eq. (3.26) to account for partial coherence, this relation will no longer hold. Previously it's been shown when the coherence length at the sample plane is less than the probe extent, this emulates a smaller probe size [210]. This is because parts of the sample separated by more than one coherence length do not contribute to the main coherent interference signal even if they are contained within the illuminating aperture.[10] To account for this, the authors proposed scanning with a step size less than half the coherence length i.e., $R < \xi_{x,y}/2$ and this was shown to be true with the use of simulations.

Therefore when the probe size is less than the coherence length $D < \xi_{x,y}$ the beam size D in the overlap sampling factor of Eq. (3.34) is replaced by $\xi_{x,y}$. However, the reciprocal space sampling factor of Eq. (3.33) will remain the same as the probe extent remains the same, meaning when the beam is partially coherent, the overall sampling factor S'_{Π} of Eq. 3.35 is not independent of beam size [206]. Furthermore, the overall sampling factor will be linearly dependent on the coherence length and hence coherence properties of the beam, which has been suggested previously [47] and demonstrated in the case of fly-scan ptychography [56–58]. Finally, a lower coherence bound will therefore only depend (as with regular coherent ptychography) on the scanning precision of R, and the pitch of the detector in order to distinguish different scan positions.

3.6 Resolution evaluation

There exists a broad range of definitions that constitutes the resolution or smallest resolvable feature within an imaging system [77, p. 357]. It's usually defined as the smallest distance between two points on a sample such that the points can still be distinguished as separate entities. The maximum drop in contrast between two

[10] This analysis assumes a coherent rather than multi-modal ptychography reconstruction, therefore can be regarded as the extreme condition on the coherent parameters.

points is usually defined by the Rayleigh criterion but others such as the Sparrow criterion also exist. Traditional X-ray microscopy methods can evaluate this quantity using test objects such as Siemens star with well known feature sizes or by scanning a knife edge at the focus [211]. The minimal resolved feature according to the prior criterion is then the system resolution and samples replaced will also image at the same resolution. With coherent imaging methods like ptychography, the resolution is highly dependent on the sample's scattering strength; therefore, the resolution of a test object will likely be different to a realistic sample. Line profiles can be taken across sharp boundaries on the sample and fitting an error function [212]; however, in many cases, it's more desirable to understand the response of the system over all resolution components, which is well characterised by a transfer function.

The Fourier ring correlation (FRC) has widely become the standard measure of resolution reliability of data in crystallography and 3D cryo-electron [213]. This measure involves finding the cross-correlation of two independently acquired datasets of the same object[11] as a function of recorded spatial frequency. First, the Fourier transform of the two object reconstructions is calculated, and then the normalised cross-correlation coefficients are determined for the corresponding rings in Fourier space according to [214],

$$\mathrm{FRC}(q_i) = \frac{\sum_{|\boldsymbol{q}|\in q_i} \tilde{O}_1(\boldsymbol{q})\tilde{O}_2{}^*(\boldsymbol{q})}{\sum_{|\boldsymbol{q}|\in q_i} |\tilde{O}_1(\boldsymbol{q})|^2 \sum_{|\boldsymbol{q}|\in q_i} |\tilde{O}_2(\boldsymbol{q})|^2} \tag{3.36}$$

where $\tilde{O}(\boldsymbol{q})$ is the Fourier transformed sample and $\tilde{O}^*(\boldsymbol{q})$ is its complex conjugate. This will produce a normalised curve with a magnitude of 1 for resolution features that are perfectly correlated and 0 for features that are completely uncorrelated. In practice, it's common to use only part of the reconstructed sample which doesn't contain edge artefacts where the probe overlap begins to break down [215]. Additional considerations must be made to remove any phase ramps and transverse

[11] Within ptychography it's possible to use the reconstructed probe in the FRC analysis, this can useful if two independent datasets weren't acquired as the scan data can be easily split in half.

shifts between the two objects, which would further degrade the resolution.

A single figure of merit for the resolution can be assigned by the intersection of the FRC with a threshold curve. It was observed that the threshold curve should change dynamically based on the number of voxels that are present at a particular Fourier frequency [216]. The usual threshold criteria is defined when the cross-correlation signal disappears into the noise, i.e. when the SNR = 1 and is defined as the 1-Bit threshold. However, the original cryo-electron tomography authors had enough redundancy in the dataset to split it into two halves to perform the comparison. It was reasoned that each half of the dataset only needed to satisfy an SNR = 0.5 defined at the 1/2-Bit threshold, so the complete dataset would have the desired an SNR = 1. This is not the typical case for ptychography as no splitting of the dataset usually occurs, and the complete set of diffraction patterns is used for the reconstruction. Instead, two independently acquired datasets will be used for the comparison, and the usual 1-Bit threshold criterion will be applied. With the later ptychotomography dataset, the 1/2-Bit threshold will be applied as the projection stack is redundant enough to be split similarly to how it was performed in the original paper for cryo-electron tomography.

3.7 Software packages

The widespread adoption of ptychography at many synchrotron and research facilities have resulted in several software packages being developed, many of which are open source and publicly available. Each typically implements many phase retrieval algorithms with various capabilities depending on the intended purpose. The performance/results of the same descript algorithm may vary slightly between software. With advances in computing hardware and the desire to display real-time results, most software also incorporates some form of CPU/GPU acceleration which can limit use and accessibility. Listed below are the software packages that have been used during the thesis as well as some of their main features.

- **PtyPy:** Originally developed by Thibault and Enders, this is an open source python based ptychography package [189]. During its use within the thesis, it primarily implemented the DM [35] and ML [192] algorithms, but now features a large library of additional algorithms including RAAR [175], sDR [191] and ePIE [40]. Many are accelerated with both CPU/GPU implementations. Algorithms are implemented in an engine structure which makes future additions very easy. It features additional capabilities including multi-modal probe and samples [47], orthogonal probe relaxation [187] and position correction [184]. Its primary use within the thesis was for the quick processing of ptychography scans while on the B16 beamline.

- **Ptyrex:** This is a python based package developed by Batey and used as the main reconstruction software for processing ptychography data on the I13-1 beamline at Diamond Light Source [209]. It implements the PIE family [205, p. 874] of algorithms and is GPU accelerated. It features additional capabilities, including multi-modal probe and samples [47], subpixel position refinement [184] and useful detector upsampling [217]. Its primary use within the thesis was processing ptychography scans while on the I13-1 beamline.

- **Ptycho:** As part of the initial project, research I developed my own python package to improve my understanding. This uses a similar data and engine structure as *ptypy*. It implements the DM [35] and rPIE [193] algorithms with GPU acceleration achieved using *CuPy* [218]. It's not the most efficiently implemented code; however, its main purpose is to be easily readable and act as a development sandbox. It features additional capabilities including multi-modal probe and samples [47] and subpixel position refinement [185]. Its primary use within the thesis was processing large B16 ptychography datasets that feature a lot of diffraction patterns and a number of probe/sample modes.

- **Shelves:** Developed by the cSAXS beamline at the Swiss Light source, this is an open source MATLAB based ptychography package that has only recently been made publicly available [219]. It implements the DM [35], PIE family [205, p. 874] and LSQ-ML [220] algorithms. Most algorithms are accelerated with both GPU implementations. It features several additional capabilities including multi-modal probe and samples [47], subpixel position refinement [185], experimental geometry refinement [220], variable wavefront and intensity refinement [187], and multi-slice methods for extended depth of field [221]. Its primary use within the thesis was post processing I13-1 ptychotomography data and B16 partially coherent ptychography data.

4 Optics characterisation using ptychography

4.1 The wavefront error

The wavefront is an imaginary surface representing points on a coherent, monochromatic wavefield with the same phase, i.e. where all points on the wave interfere constructively. According to Huygens principle [84], every point of an advancing wavefront may be regarded as a secondary point source of spherical wavefronts. From this, the propagation of wavefronts is taken to be in the direction normal to the surface. Optics achieve focusing by imparting a convergent surface on the incident wavefield such that each part arrives in phase and interferes constructively at the focus. Deviations about this surface are defined as the wavefront error [15, p. 526] and correspond to a change in the optical path length defined as,

$$\Delta X = \frac{\lambda \Delta \varphi}{2\pi} \tag{4.1}$$

where $\Delta\varphi$ is the phase difference between different parts on the wavefront surface. The optical path length (or path length) represents the difference in physical distance traversed between two rays of the same wavefield. For most optics, it's discussed in terms of fractions of the wavelength λ, which means for X-rays, it's usually quoted in pico meters. A schematic showing how wavefront error causes degradation to the performance of focusing optics is shown in Fig. 4.1. The path length difference on passing through a homogenous material is also conveniently just given by the product of the refractive index decrement $\delta(E)$ and thickness of the $t(x)$ material such that $\Delta X(x, E) = t(x)\delta(E)$. This is used for the design of refractive optics, including corrective elements, as discussed later in section 5.

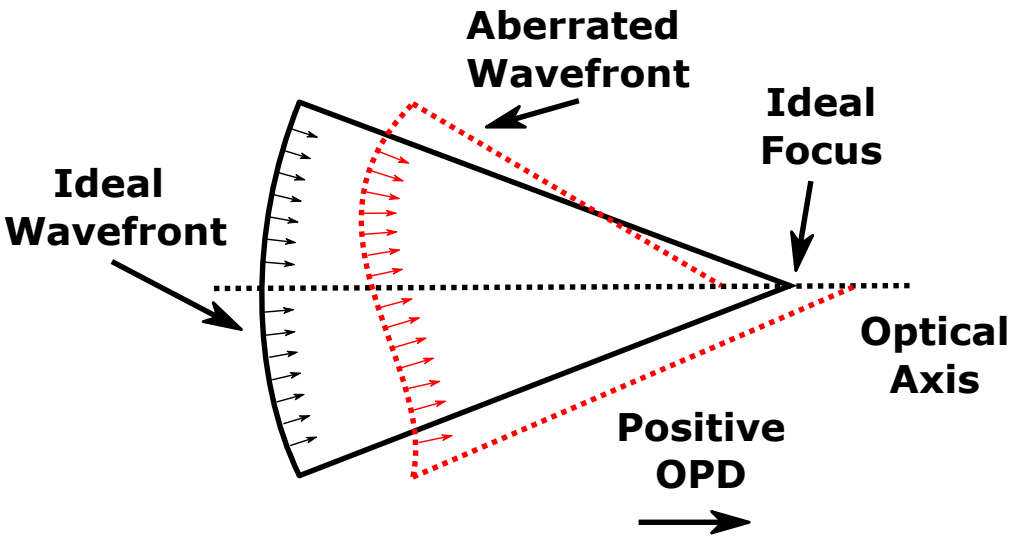


Figure 4.1: Effect of wavefront errors on the performance of focusing optics. Solid & dashed lines represent the ideal & aberrated wavefronts respectively. The Optical Path Difference (OPD) is the relative shift in path length across the wavefront surface and slope error is represented by arrows normal to this.

4.2 Focal size factors

Precise knowledge of the perturbed wavefront is crucial to understanding the source of errors if they are to be corrected and has led to the development of so called at-wavelength techniques [28]. These methods are performed *in situ* and at the designed wavelength of the optic to measure the wavefront error of optics as they would be used. The most common techniques such as speckle tracking [29], Hartmann sensing [30], grating interferometry [31] and pencil-beam scanning [32] are ray/deflection based techniques which measure the local trajectory of rays determining the measured intensity pattern. However, as source coherence has improved, the use of ptychography as an at-wavelength technique has risen to prominence [41–45]. Techniques will each have their advantages and drawbacks; thus, in reality, a few methods may be applied to characterise an optic completely and validate results. We have already covered in 2.4.1 that all focusing optics cannot produce focal spots smaller than the fundamental diffraction limit. In reality, there are several factors that can broaden and degrade the focal spot if not properly considered, which is the topic of discussion within this section.

- **Source demagnification:** Although not strictly an optical aberration the source demagnification factor is (currently) by far the greatest contributing factor to most synchrotron focusing setups.[1] The limited source to optic distance and inability to produce short focal length optics mean the demagnified image of the source is normally the most dominant focal size contribution and given by $d_{\mathrm{s}_{x,y}} = M\sigma_{\mathrm{s}_{x,y}}$ where $M = q/p$ is the magnification factor and $\sigma_{\mathrm{s}_{x,y}}$ is the source size, which for the B16 Test beamline is approximately 129.8 µm (h) × 34.4 µm (v) (FWHM) and the source to optic distance is typically around 42 m. This generally limits the shortest focal length optics (of around 100 mm) available on B16 to produce focal spots of 300 nm in size. The resulting focal width is a sum of the diffraction limited and demagnified source contributions $\theta_{\mathrm{tot}} = \sqrt{\theta^2_{\mathrm{diff}} + \theta^2_{\mathrm{sor}}}$. To overcome the demagnified source effect, several solutions have been proposed including the use of secondary sources with upstream pre-focusing optics [133] and apertures as well as purpose built building long beamlines [222].

- **Alignment errors:** The relative position of optical elements with respect to the beam greatly affects the focusing performance of X-ray optics and are generally categorised as either transverse or rotational misalignments. Transverse misalignments are caused by individual components (such as CRL lenslets) of the optic not being in line with one another [224] or by the optic aperture not being uniformly illuminated [225]. A common example of transverse misalignment is when independent focusing elements (like the individual mirrors of a Kirkpatrick–Baez system) are positioned incorrectly such that the longitudinal position of the two foci is different [226]. However, the more common and sensitive alignment errors for optics are rotational misalignments and in particular, the optic pitch or tilt angle is most significant. For each Kirk-

[1] With the exception of purpose built long beamlines [222, 223], which can have demagnification factors much greater than $M > 1000$.

patrick–Baez mirror, a misalignment of the pitch angle results in an additional cubic component added to the respective wavefront error [26, 27], which must be minimised before isolating any fabrication errors.

- **Fabrication aberrations:** The primary source of errors this thesis is concerned with are errors originating from the fabrication process of the optical element. For most optics, these can be categorised into surface roughness (or finish error) and shape error [227], the latter of which we will focus on. The surface roughness corresponds to smaller, high-frequency spatial errors and can be considered a local phenomenon which is usually small enough to be ignored. Errors over longer spatial periods on the order of the optic aperture are considered shape errors and are the deviation of the surface from the ideal shape. These manifest differently depending on the type of optic, for example, shape errors in refractive elements correspond to material thickness variations whereas in mirrors they originate from surface height deviations.

4.2.1 Strehl ratio and rms error

The wavefront deviation from an ideal spherical surface required for focusing is called the wavefront error $w(x, y)$ and is defined over an aperture $\Delta x \Delta y$. It's typically well characterised by its Root Mean Squared (RMS) value given by [15, p. 526],

$$\sigma_{\text{rms}} = \sqrt{\int_{-\Delta x/2}^{\Delta x/2} \int_{-\Delta y/2}^{\Delta y/2} \frac{w^2(x, y)}{\Delta x \Delta y} \, \mathrm{d}x\mathrm{d}y} \tag{4.2}$$

where we have also assumed without loss of generality that the wavefront error $w(x, y)$ can be defined to have zero mean defined over the entire length of its aperture such that it's subject to the following condition,

$$\int_{-\Delta x/2}^{\Delta x/2} \int_{-\Delta y/2}^{\Delta y/2} w(x, y) \, \mathrm{d}x\mathrm{d}y = 0 \tag{4.3}$$

For small RMS wavefront errors $\sigma_{\text{rms}} \ll \lambda$ the complex wavefield exponent can be expanded using a power series such that the aberrated intensity I to ideal (zero wavefront error) peak intensity I_0 ratio is given by the Strehl ratio,

$$\frac{I}{I_0} = 1 - \frac{4\pi^2\sigma_{\text{rms}}^2}{\lambda^2} \tag{4.4}$$

Thus for small wavefront errors, the focus profile is a sharp diffraction limited peak,[2] with the lost intensity forming satellite peaks and a much broader background outside this central peak. Diffraction limited focusing is typically defined for Strehl ratios greater than 0.8, realised for $\sigma_{\text{rms}} \lesssim \lambda/14$ or the Maréchal criterion [228].

4.2.2 Zernike polynomials

The most common method to characterise the source of wavefront errors is to decompose the error into an orthonormal base, namely the Zernike polynomials [15, p. 523]. They are defined for circular aperture optics and consist of a set of orthonormal functions of the normalised radial position r and azimuthal angle θ,

$$\begin{aligned} Z_n^m(r,\theta) &= R_n^m(r)\cos(m\theta) \\ Z_n^{-m}(r,\theta) &= R_n^m(r)\sin(m\theta) \end{aligned} \tag{4.5}$$

corresponding to the odd and even functions, respectively, where m and n are non-negative integers with $n \geq m \geq 0$ and R_n^m are the radial polynomials. Zernike polynomials are limited in range to -1 to +1 such that $|Z_n^m(r,\theta)| \leq 1$. The radial polynomials are similarly defined,

$$R_n^m(r) = \sum_{k=0}^{(n-m)/2} \frac{(-1)^k(n-k)!}{k!(\frac{n+m}{2}-k)!(\frac{n-m}{2}-k)!} r^{n-2k} \tag{4.6}$$

[2] In theory, the width of the focal profile should not change with small wavefront errors, however experimentally this is not the case as the satellite peaks will broaden the fitted profile.

The Zernike polynomials are an appealing choice as any number of terms can be chosen without affecting the value of the other terms. Additionally, the orthonormal coefficients are exactly the root mean square error for that particular type of aberration, which is useful for isolating the effects of specific types of errors. A schematic of the first few terms and their focal effects are shown in Fig. 4.2.

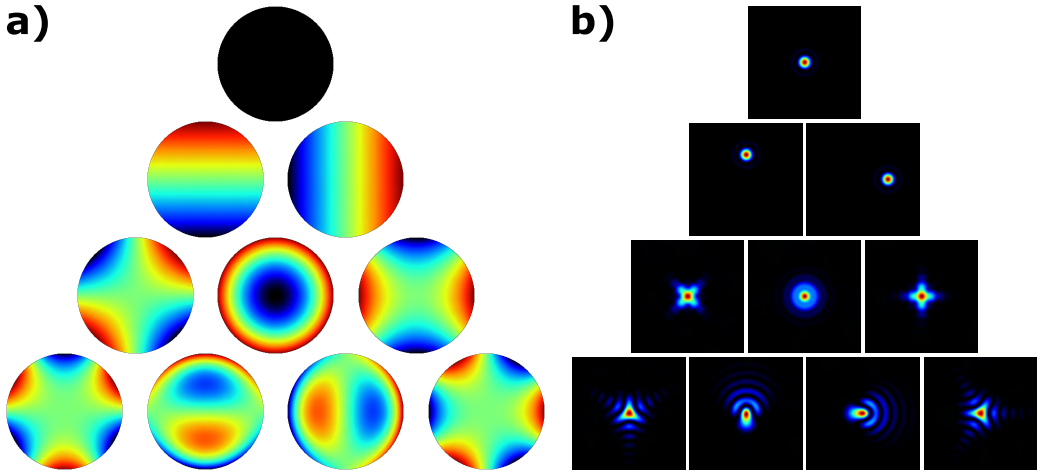


Figure 4.2: The first set of Zernike polynomials, (a) the wavefront error in the optic plane and (b) the resulting effect on the intensity at the focal plane. They are ordered vertically by radial degree and horizontally by azimuthal degree.

4.3 Coherent ptychography metrology

Ptychography reconstructs both the complex sample transmission and probe illumination functions [35, 40] making it well suited as a wavefront characterisation technique. The probe can be propagated to any optical axis plane using numerical methods to study the focal properties [41, 215], optimally align optics [226] and characterise optical aberrations [46]. It has been employed extensively to study nano-focusing optics [38, 53] as it provides two-dimensional, high spatial resolution information and overcomes the mechanical limitations of traditional methods.[3] Traditionally this requires a highly coherent source such as those found on long, insertion device beamlines at synchrotron [215, 229] and XFEL [230, 231] facilities. Here, the small source size and high photon flux mean that the beam can

[3]The most simple method to measure the focal intensity size is with a scanning knife edge; however, the X-ray beam size is now typically on the order of the scanning stage precision.

easily be made coherent by spatial filtering without detriment to the overall flux. Before discussing how the technique can be extended to partially coherent sources [50, 51], we present the conventional method for characterising the focal properties and fabrication aberrations of an optic using a highly coherent source.

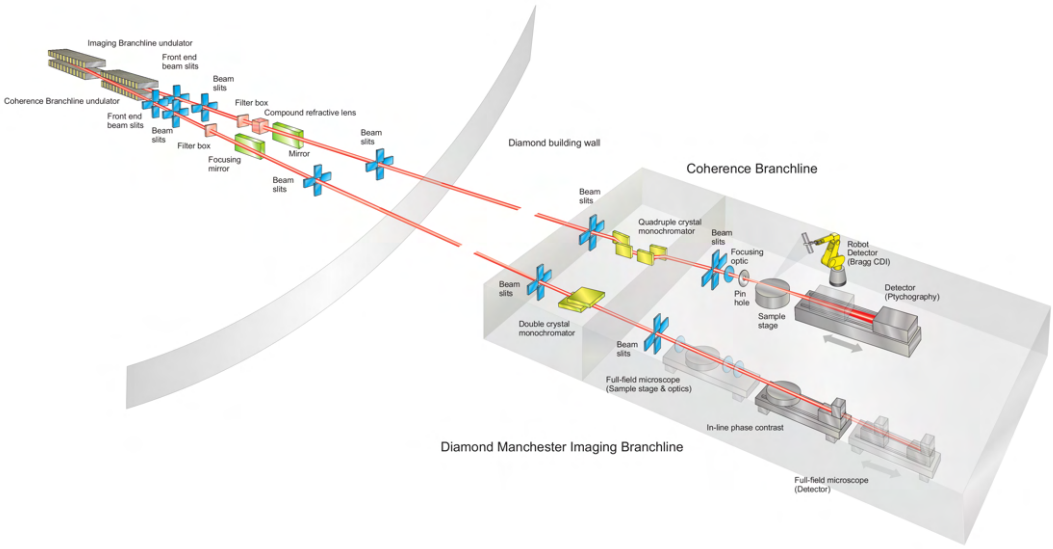


Figure 4.3: Schematic of the experimental setup (not to scale) of the I13 coherent beamline at the Diamond Light Source. The beamline is split into a coherent (I13-1) and imaging (I13-2) branch. Image provided courtesy of the I13 beamline, Copyright 2022 Diamond Light Source [232].

4.3.1 Experimental data collection

Experiments were performed at the I13 beamline [223] at Diamond Light Source, Didcot UK. This employs two undulators canted at 4 mrad to allow the independent operation of the coherent (I13-1) and imaging (I13-2) beamline branches. The vertical electron beam size is also significantly reduced by using a quadrupole magnet to refocus the electron beam in between and create a "mini-beta" section to allow both undulators to operate at low gap. For the I13-1 branch, this results in a 400 µm (h) × 13 µm (v) source size (FWHM) that produces harmonics in the 6 keV − 20 keV energy range. An ultra-high performance mirror located 28 m from the source is used to direct the beam in the right direction and filter out higher-order harmonics that would otherwise degrade the beam quality [233].

A set of interchangeable compound refractive lenses are additionally used to collimate the beam and prevent a large divergence at the external building. The horizontal transverse-coherence is improved with spatial filtering using S1 source slits positioned 13 m downstream of the undulator and are usually set to 100 µm width. The experimental setups are also located at a relatively long 250 m distance from the undulator source, which by the van Cittert–Zernike theorem also improves the transverse coherence. An X-ray energy of 9.7 keV corresponding to the undulators peak harmonic was selected by a horizontally mounted[4] quadruple crystal monochromator with an approximate energy bandpass $\Delta E/E \sim 10^{-4}$ to maximize longitudinal coherence.

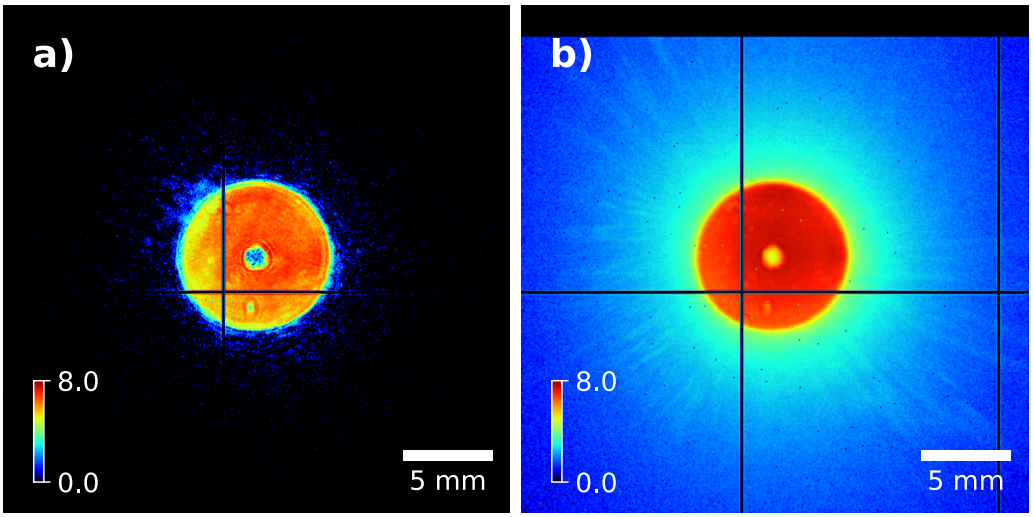


Figure 4.4: Diffraction intensity of a single nickel cathode particle used for coherent ptychography metrology. (a) Single frame acquired for 200 ms. (b) Integrated stack over 256 frames. Both images are cropped to the field of view used in ptychography 512 px (h) × 512 px (v) and are plotted on $\log_{10}$ scale.

The beam was focused using a FZP with a 400 µm geometric aperture, 150 nm outer zone width and an 80 µm fixed central stop. At 9.7 keV this gave a first-order focal length of 469 mm. This provided an estimated 5×10^7 photons/s with a beam size of 6 µm (h) × 6 µm (v) at the sample position. For the test object a single nickel-rich cathode particle was used, the full results of which have been

[4]The horizontal mounting minimises the effects of monochromator instabilities on the vertical coherence length and keeps the beam path directed along the same optical axis.

published previously [68]. This was mounted on high-precision smaract piezoelectric translational stages and positioned approximately 8 mm downstream of the focus. Scans were performed by translating the sample through the defocused beam and acquiring diffraction patterns at each position. This was performed over an area of 16 µm × 16 µm with a step size of 1 µm, which generated 256 diffraction patterns.

These were each acquired for 200 ms by a single-photon counting Excalibur[5] detector with a 55 µm (h) × 55 µm (v) pixel size and a 2069 px (h) × 1793 px (v) field of view positioned 9.47 m downstream of the sample. With this scanning geometry, the overlap sampling factor given by Eq. (3.34) was found to be 83% and the overall sampling ratio according to Eq. (3.35) was found to be $S_{\Pi} = 484$. A typical diffraction pattern, as well as the integrated intensity stack, is shown in Fig. 4.4. These highlight the large dead zones, which are problematic if not accounted for in the reconstruction with a detector mask and sparse scattering.

4.3.2 Ptychography reconstruction

The diffraction patterns were cropped to a region of interest around the optical axis measuring 512 px (h) × 512 px (v), which included only statistically relevant counts and resulted in a 43 nm effective pixel size. Dead and hot detector pixels were also disregarded from the reconstruction by generating a detector mask based on the integrated diffraction data stack. An initial flat sample transmission function and an ideal probe simulated from the optical parameters were used at the input. It was observed during the session there was significant jitter from the sample scanning stages was corrected by using position correction [184]. Ptychographic reconstructions were computed on a GPU processor in python using the *ptyrex* software [209]. 500 iterations of the Extended Ptychographic Iterative Engine (ePIE) [40] were run with the parameters set to $\alpha = 0.5$ & $\beta = 0.5$ until the Fourier error converged to stable minima. The reconstructed sample modulus and phase, complex probe and

[5]Excalibur belongs to the same family of detectors as that of Merlin and contains 48 medipix2 chips uniformly tiled in an 6 × 8 fashion separated by dead zones.

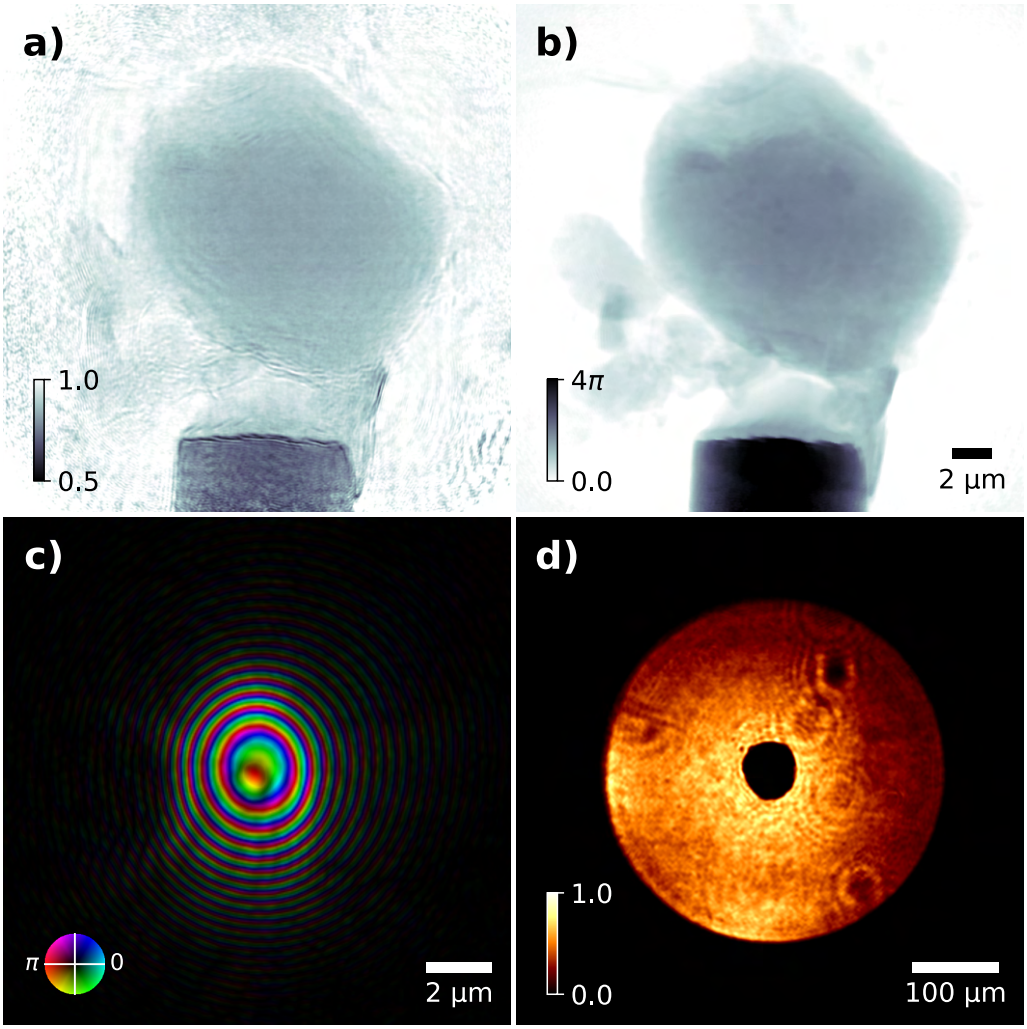


Figure 4.5: Ptychography reconstructions for coherent ptychography metrology. Sample (a) modulus and (b) phase of a single nickel-rich cathode particle. (c) Corresponding coherent probe. The colour wheel encodes brightness and hue as amplitude and phase respectively. (d) Optic aperture intensity.

aperture intensity are shown in Fig. 4.5.

The sample phase was unwrapped using an efficient unwrapping method based on sorting by reliability [234] as no issue arose due to residues or sharp edges. A phase ramp and offset were also fitted and subtracted using the air around the edges of the reconstruction for calibration. The sample modulus is generally most sensitive to artefacts due to the comparatively weaker interaction at hard X-ray energies. This is evident by its weak and noisy reconstruction in Fig. 4.5a. Grid artefacts due to the symmetric scanning nature of the grid pattern are also more apparent in the modulus. A spiral or Fermat scanning patterns are generally better alternatives

to avoid this [208] but are difficult to implement for fly-scan experiments. We can already observe from the reconstructed probe in Fig. 4.5c that it's a different size in the horizontal and vertical planes which should not be the case for a radially symmetric lens like the FZP. The intensity at the optic plane shown in Fig. 4.5d displays the correct aperture shape and size and was computed using the Fraunhofer far-field diffraction formula in section 2.6.4.

4.3.3 Beam caustic & focal properties

Since the ptychographic technique recovers a complex probe scalar field, we can numerically propagate along the optical axis using the angular spectrum formula from section 2.6.2 to analyse the focal properties and beam evolution. The probe was numerically propagated along the optical axis over a range of 25 mm and beam caustics were generated by integrating the intensity volume along the horizontal and vertical directions. The results for this are shown in Fig. 4.6 and also label the defocused position where ptychography scans were performed, as well as the focal planes defined as the plane which maximised peak intensity. It can be seen there is a significant astigmatism of around 1.83 mm between the two foci, and most likely results from a misalignment of the FZP pitch angle [235]. As spatial resolution in ptychography isn't determined by the focal size and is therefore insensitive to these misalignments, little attention is paid to performing and maintaining the alignment of optics and errors like this are common.

As the beam is astigmatic, focal planes were found for the horizontal and vertical planes separately. The reconstructed probe was propagated to each of the planes using the direct Rayleigh-Sommerfeld integral Eq. (2.35) with a finer sampling period in the propagated plane to decrease the pixel size. After fitting a Gaussian profile, this gave a horizontal and vertical FWHM focal size of 162 nm (h) $\times$ 140 nm (v) in their respective planes. This agrees well with the theoretical value predicted from the diffraction limited (section 2.4.3) and demagnified source (section 4.2) contributions, given the optic properties and experimental setup, which is around

165 nm (h) × 135 nm (v). The source slits are closed horizontally to around 50 µm to produce a completely coherent beam across the FZP aperture. For completeness, additional reconstructions were performed using a multi-modal approach [47] which found the majority of power concentrated in the first mode and no discernible difference between the coherent and multi-modal probes.

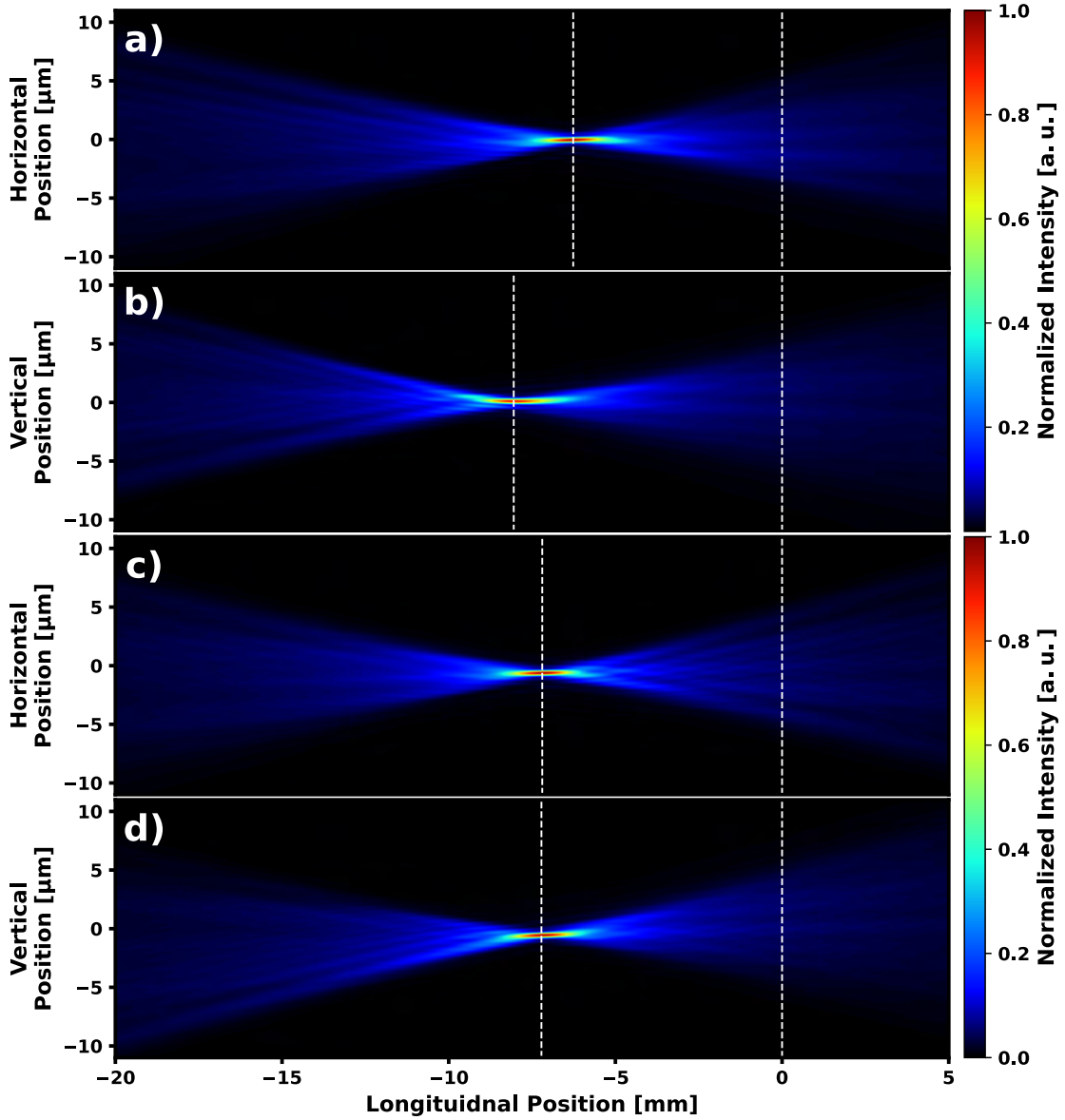


Figure 4.6: Beam caustics for coherent ptychography metrology. The (a) horizontal and (b) vertical caustics with astigmatism. The (c) horizontal and (d) vertical after the alignment correction using Zernike polynomials. The 0.0 mm dashed line is the ptychography sample plane and the other dashed lines correspond to the peak intensity focal position.

4.3.4 Wavefront characterisation

The beam caustic and focal intensity distribution only provide partial insight into the performance of an optic. To completely characterise the optical aberrations causing focal degradation, the wavefront error at the optic plane must be calculated. We first back propagated the reconstructed probe wavefield upstream a distance of 6.3 mm + 469 mm to the exit plane of the FZP using the angular spectrum method as in section 2.6.2. The intensity at this plane is the same as that shown in Fig. 4.5d and gives an aperture size of 404 µm. Although this method generates a large array, it preserves the sampling period and is required in order to ensure proper phase unwrapping. This was performed using a quality guided non-continuous path procedure [234], and residues (which would lead to phase vortices in the unwrapping) were masked out from the procedure using the optic intensity to generate a mask.

To uncover the wavefront error, a two-dimensional perfect spherical wave $\Delta\varphi(x, y)$ was fitted and subtracted to the unwrapped phase. The initial fitting parameter used the FZP designed focal length Δz and corresponds to the radius of curvature of a spherical wave defined by [46],

$$\Delta\varphi = -k\left(\sqrt{\Delta z^2 + x^2 + y^2} - \Delta z\right) \tag{4.7}$$

where k is the wavenumber and x, y are cartesian coordinates defined over the aperture of the FZP optic. After subtraction, we are left with a phase error which is easily converted into a wavefront error using Eq. (4.1). These results are shown in Fig. 4.7a, the RMS is 31.8 pm over the aperture which is very high for FZP.

Given the aperture of the FZP is circular, the wavefront error is most appropriately decomposed using Zernike polynomials as described in section 4.2.2. This was performed with the first 21 polynomials using the *zernike* python package [236] and the coefficients are displayed in Fig. 4.7c with the Z_2^2 vertical astigmatism and Z_3^{-1} coma aberrations dominating. Misalignment of the FZP pitch has previously been

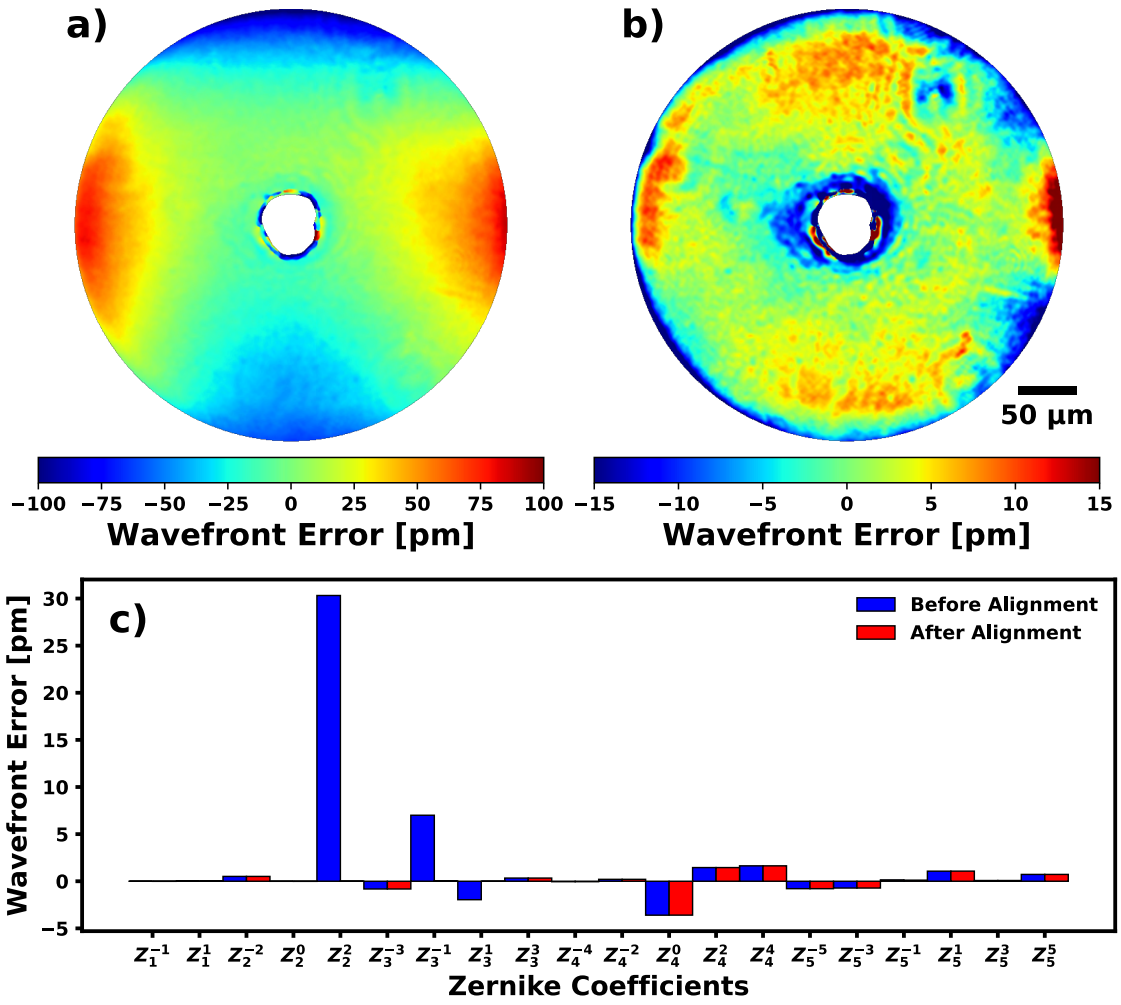


Figure 4.7: Two-dimensional wavefront error of a FZP for coherent ptychography metrology. (a) Before and (b) after subtraction of the misalignment Zernike contributions. (c) The Zernike coefficients before and after subtraction, the dominant coefficients Z_2^2 and Z_3^{-1} correspond to astigmatic and coma aberrations.

shown to produce both these types of error [235], with a path difference $l_{c,a}$ between the outer and central ray due to misalignment given by,

$$l_{c,a} = \frac{r_N^3}{2f^2}\theta - \frac{3r_N^2}{4f}\theta^2 \tag{4.8}$$

where r_N is FZP radius, f is the focal length and θ the pitch angle misalignment. Given a path length difference of $l_{c,a} = -91$ pm, the solution to Eq. (4.8) is just given by the quadratic equation and finds $\theta_1 = -2.15°$ or $\theta_2 = -2.17°$ which is similar to simulations shown previously [235]. To correct for the misalignment, these Zernike terms can be subtracted leaving the residual wavefront error as shown in Fig. 4.7b.

Furthermore, the beam caustics after subtraction are shown in Fig. 4.6c and Fig. 4.6d and there is no longer any focal astigmatism present.

The residual two-dimensional wavefront error shown in Fig. 4.7b has an RMS of 4.8 pm, which is much more reasonable than previously found but still quite large for a FZP. The dominant Zernike term after the misalignment contributions is a spherical term Z_4^0. It's possible this could arise from the upstream collimating CRL, where spherical aberrations are quite common. The prominent wavefront errors identified match with features observed in the intensity of Fig. 4.5. Fabrication aberrations in FZPs tend to be more random arising due to deformations of the concentric ring elements and therefore don't present as symmetric, Zernike type errors. This analysis was performed to demonstrate the procedure for ptychography wavefront characterisation, had we been interested in generating more precise profiles, the optic should have been realigned to minimise the Zernike misalignment terms. Ptychography is indifferent to the quality of the focusing probe so long as it's compact. Furthermore, other recent results suggest more aberrated (or structured) probes may actually benefit the reconstruction [195, 196].

4.4 Optimising source coherence

Most synchrotron sources do not (yet) produce completely coherent X-rays; therefore, coherent techniques typically spatially filter the beam to increase the coherent fraction. As the propagation distance between the source and optics is usually large, we can use the van Cittert–Zernike theorem [15, p. 574] to approximate the transverse coherence length at the optics position Ξ without any spatial filtering $\Xi_{x,y}^0$ and when using the S1 source slits to form a secondary source $\Xi_{x,y}^1$, which are given by,

$$\Xi_{x,y}^0 = \frac{\lambda(d_1 + d_2)}{\sigma_{x,y}} \qquad \Xi_{x,y}^1 = \frac{\lambda d_2}{s_{x,y}} \qquad \Xi_{x,y}^1 > \Xi_{x,y}^0 \tag{4.9}$$

where d_1 is the source to slits distance, d_2 is the slits to optic distance, $\sigma_{x,y}$ is the source size and $s_{x,y}$ is the slits size, x, y denote the horizontal and vertical planes,

respectively. This is shown schematically in Fig. 4.8 the experimental setup of the next section. The use of spatial filtering is only effective when $\Xi^1_{x,y} > \Xi^0_{x,y}$, which using Eq. (4.9) and the B16 experimental parameters occurs for S1 slits sizes smaller than $74\,\mu\text{m}\,(\text{h}) \times 20\,\mu\text{m}\,(\text{v})$.

The heavy power incident on source slits means most are typically not well calibrated or completely rectangular. Determination of their size is essential to quantitively compare the coherence properties recovered from ptychography with theoretical values based on the setup. For the optics considered, the focal contribution will be a combination of the demagnified source and diffraction limit such that the slit sizes can be determined more accurately by [237],

$$\mathrm{s}_{x,y} = \frac{d_2}{f}\sqrt{d^2_{x,y} - \sigma^2_{\text{diff}}} \tag{4.10}$$

where f is the optics focal length and $d_{x,y}$ is the measured focal size and σ_{diff} is the diffraction limited focal size. We assume the S1 source slits approximate a Gaussian source with the size given by the FWHM. The use of slits some distance from the source can be pictured as back projecting an image of the slits onto the source to selectively illuminate part of it; for certain geometries, a number of slit configurations are possible, which give the same coherence properties [238].

4.5 Partially coherent ptychography metrology

In the previous section 4.3, the performance and aberration characterisation of optics was performed using a highly coherent beam. In reality, though, most synchrotron sources are not entirely coherent but rather partially coherent. This is especially true for the B16 Test beamline [69], where most experiments within this thesis were performed. This features a large horizontal source size and divergence, and produces relatively low flux owing to its dipole magnet nature [78, p. 40]. The inclusion of decoherence effects in phase retrieval algorithms initially used a deconvolution scheme [239], which required *a priori* knowledge of the source spatial distribution. However,

the most recent and successful algorithmic improvements incorporate a multi-modal approach, which decomposes the probe as a sum of mutually incoherent modes [47]. Previous studies into partially coherent ptychography have generally been conducted using numerical simulations [203, 240] or with insertion device beamlines [54, 241] where a large portion of the beam is already highly coherent but limited success has so far been demonstrated with truly partially coherent sources [52]. In these studies, the optics focal size and position were characterised using the reconstructed multi-modal probe intensity; however, a detailed analysis of the wavefront error introduced by optical aberrations requires a single coherent probe mode and is discussed later in section 4.5.3.

4.5.1 Focal properties

Partially coherent light is most commonly accounted for in ptychography using a multi-modal approach as described in section 3.4. Each mode is treated as an independent probe that can be propagated separately through the optical scheme. An optics performance is then evaluated using the summed mutual optical intensity of the ensemble given by Eq. (3.26) in section 3.4.4. This can be used to evaluate the focal intensity and beam evolution. Multi-modal probes can be used to evaluate beams with a high coherent fraction; however, the dominant mode is usually only observed to change as the other modes contribute a very small fraction of the total power [53]. As each mode can be regarded as a separate point on the extended source, the geometric source demagnification effect is naturally accounted for.

Within this section, the successful implementation of ptychography using the B16 Test beamline at Diamond Light Source [69], a partially coherent source with a large source size and relatively low flux, is reported. Ptychography measurements are performed using a gold Siemens star test sample to recover the complex probe and sample functions from focused beams produced by both a FZP (section 2.4.3) and beryllium CRL (section 2.4.2). The recovered probe is back propagated to generate a beam caustic and measure the precise focal size and position. Additionally,

the spatial resolution of the Siemens star test sample is quantified and shown to be much greater than typically achieved on the beamline. The coherence properties recovered from the multi-modal ptychography are compared with values theoretically predicted by a Gaussian–Schell model based on the source characteristics and setup. The majority of results presented have been previously published [50].

4.5.1.1 Experimental setup

Experiments were performed at the B16 Test beamline [69] at Diamond Light Source, Didcot UK. This uses a dipole magnet source which features a relatively large 129.8 µm (h) × 34.4 µm (v) FWHM source size that produces a continuous energy spectrum in the 4 keV − 45 keV energy range. The beamline's primary function is to serve as a test bed for new and novel experimental techniques as well as support the optics and metrology group for testing X-ray optics, detectors and related equipment. As discussed in the previous section 4.4 the source slits located 18 m from the electron source were nominally set to 50 µm (h) × 50 µm (v) in order to improve the transverse coherence.[6] A double-crystal Si(111) monochromator was used to select an energy of 10 keV and 15 keV for the FZP and CRL setups, respectively, with an energy bandpass $\Delta E/E \sim 10^{-4}$ to maximize longitudinal coherence. The optics and other equipment are installed on a large granite block to reduce sources of instability in the experimental hutch, which is located 42 m from the source. A schematic of the experimental setup is shown in Fig. 4.8.

Two optics were characterised using ptychography during separate experimental sessions. The first was a tungsten FZP with a 245 µm geometric aperture, 123 nm outer zone width and 60 µm fixed central stop. At 10 keV this gave a first-order focal length of 243 mm and provided an estimated 2×10^5 photons/s with a beam size of 2.1 µm (h) × 2.9 µm (v) at the sample position. The second optic characterised was a beryllium CRL with 98 lenses, a geometric aperture of 1 mm and a radius of

[6] The vertical slits will produce more of the coherent fraction so could be much larger, these values were chosen as they still produced measurable signal at the detector.

curvature of 200 µm. At 15 keV this gave a focal length of 690 mm and provided an estimated 6×10^6 photons/s with a beam size of 3 µm (h) × 3 µm (v) at the sample position. A single-photon counting Merlin Medipix detector with a pixel size of 55 µm (h) × 55 µm (v) was used to collect the diffraction patterns [93]. For the FZP an older single chip, second-generation detector with a 256 px (h) × 256 px (v) field of view was mounted 2.72 m in the far-field, whereas the CRL setup used a newer quad chip, third-generation Medipix detector with a 512 px (h) × 512 px (v) field of view mounted slightly further downstream at 6 m from the sample.

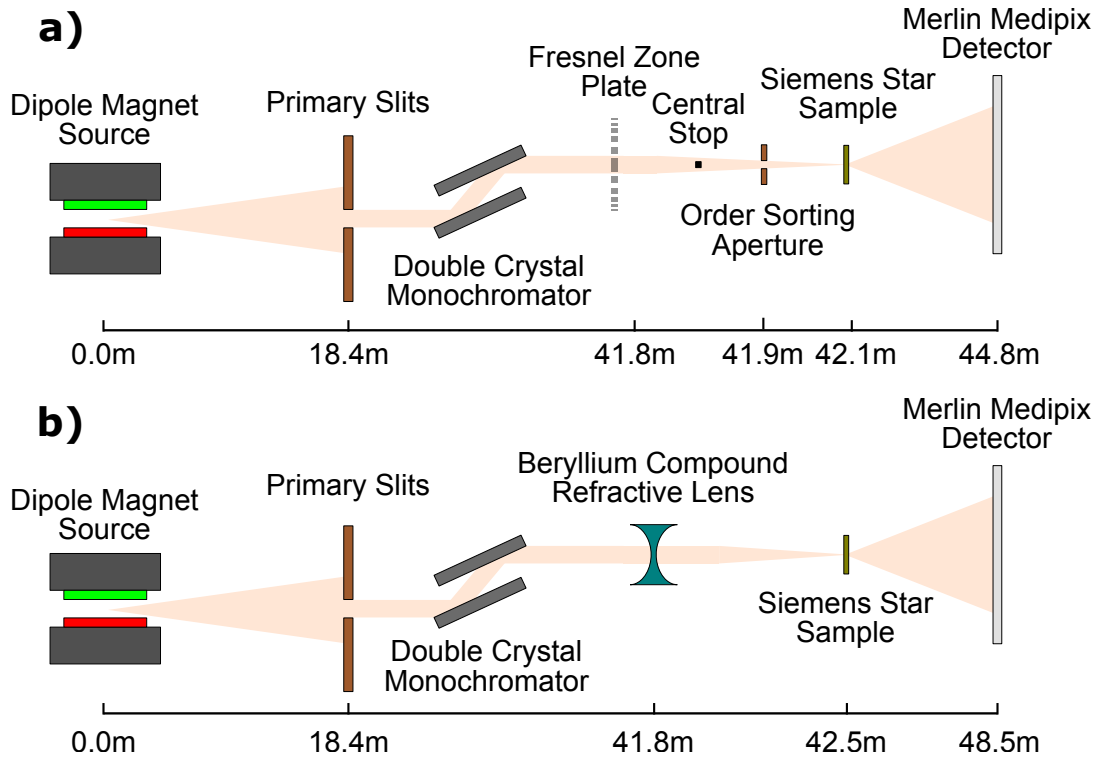


Figure 4.8: Schematic of the experimental setup with distances (not to scale) for (a) the FZP and (b) CRL focusing optics on the B16 Test beamline at the Diamond Light Source used for partially coherent ptychography metrology [50].

For the test sample, both setups used a 3 µm thick gold Siemens star on a silicon nitride substrate mounted on high-precision linear Attocube piezo stages slightly downstream of the focal plane. This has a diameter of 200 µm and an inner spoke separation of 1 µm as the smallest feature size. The optics were aligned, and the approximate focal position was found by scanning a gold knife edge in the beam. Small ptychography scans were then performed at a few positions along the optical

axis until a beam size satisfying the sampling condition [206, 207] was found. These were performed in a spiral fashion to avoid reconstruction artefacts [35] and with a much smaller step size than typically to compensate for the low spatial coherence.

At the optimised FZP probe position, a ptychography scan was performed over an area of 12 µm (h) × 12 µm (v) with a step size of 0.6 µm and individual exposure time of 1 s, which generated 1109 diffraction patterns. With this scanning geometry, the overlap sampling factor given by Eq. (3.34) was found to be 71% (h) & 79% (v) and the overall sampling ratio according to Eq. (3.35) was found to be $S_\Pi = 104$. Similarly, at the optimised CRL probe position, a ptychography scan was performed over an area of 12 µm (h) × 12 µm (v) with a step size of 0.3 µm and individual exposure time of 0.2 s, which generated 2581 diffraction patterns. With this scanning geometry, the overlap sampling factor given by Eq. (3.34) was found to be 90% and the overall sampling ratio according to Eq. (3.35) was found to be $S_\Pi = 903$.

4.5.1.2 Ptychography reconstruction

Ptychographic reconstructions were performed both during and after the experiment using the *ptypy* python package [189] with high-performance computing facilities to utilise CPU and GPU parallelisation for a wide variety of algorithms. The diffraction data was cropped to a region of interest around the optical axis, including only statistically relevant counts, which measured 180 px (h) × 180 px (v) for the FZP setup and 280 px (h) × 280 px (v) for the CRL setup to give a reconstructed pixel size of 35 nm and 32 nm for the two setups, respectively. Dead and hot detector pixels were also disregarded from the ptychographic reconstruction by generating a detector mask based on the integrated diffraction data stack. An initial reconstruction with 1000 iterations of the Difference Map (DM) algorithm [35] was used, followed by a refinement procedure using 1000 iterations of the Maximum Likelihood (ML) algorithm [192], both incorporating a multi-modal probe approach [47]. Reconstructions started with a flat sample function and a probe modelled using the optic design parameters. Probe modes were included as random perturbations of

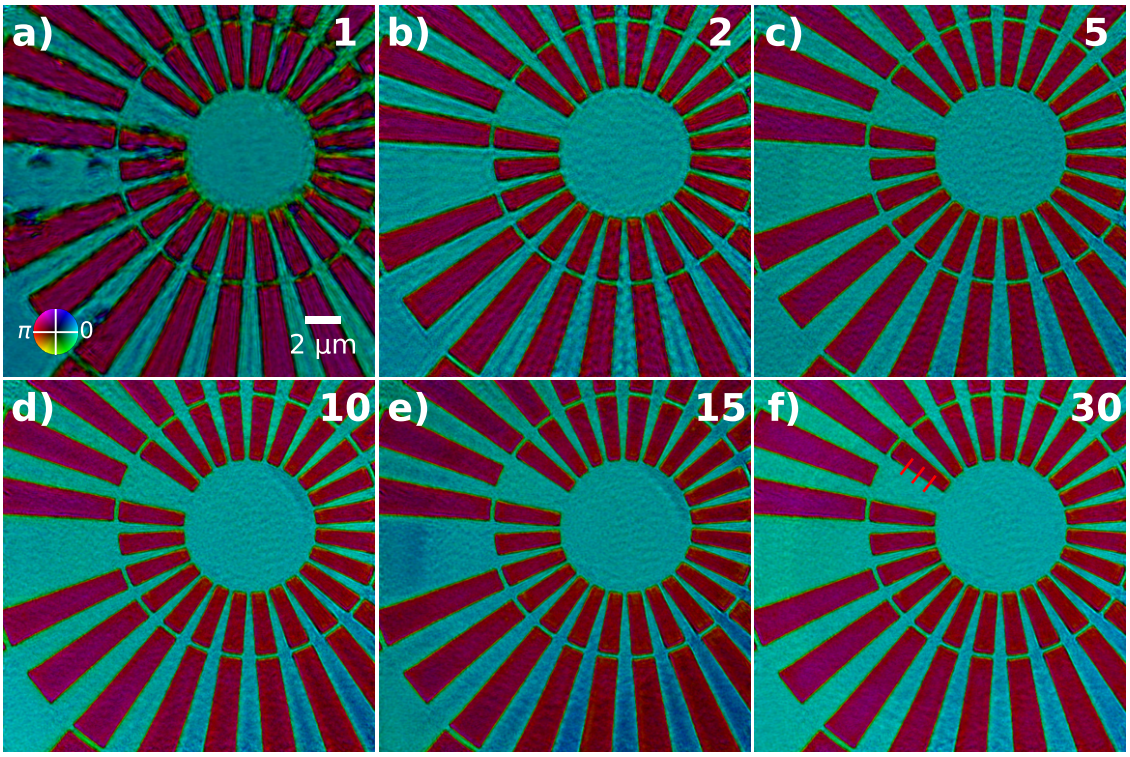


Figure 4.9: Sample reconstructions of the gold Siemens star used for partially coherent ptychography metrology. The number of probe modes varies from (a) 1 mode to (f) 30 modes and is displayed in the top corner. The colour wheel in (a) encodes brightness & hue as amplitude & phase respectively. The red lines in (f) indicate where line profiles were taken for spatial resolution quantification [50].

the initially modelled probe and scaled using the power theoretically predicted from a model of the source size.

The complex sample function of the Siemens star is shown in Fig. 4.9 reconstructed using different numbers of probe modes ranging from 1-30. As the sample is a binary object it's plotted as a complex function. The CRL setup produced a similar result and is shown in full in the publication [50]. The phase shift introduced by the gold Siemens star for both setups agrees well with the theoretical value calculated from the design; the measured shift with the FZP was 1.31π and should be 1.44π, the measured shift with the CRL was 0.89π and should be 0.96π. Even at these low levels of coherence ptychography is still able to converge upon a reasonable solution for the single (coherent) mode case in Fig. 4.9a, albeit of poor quality. Probe modes vastly improve the quality of the reconstruction and are included until

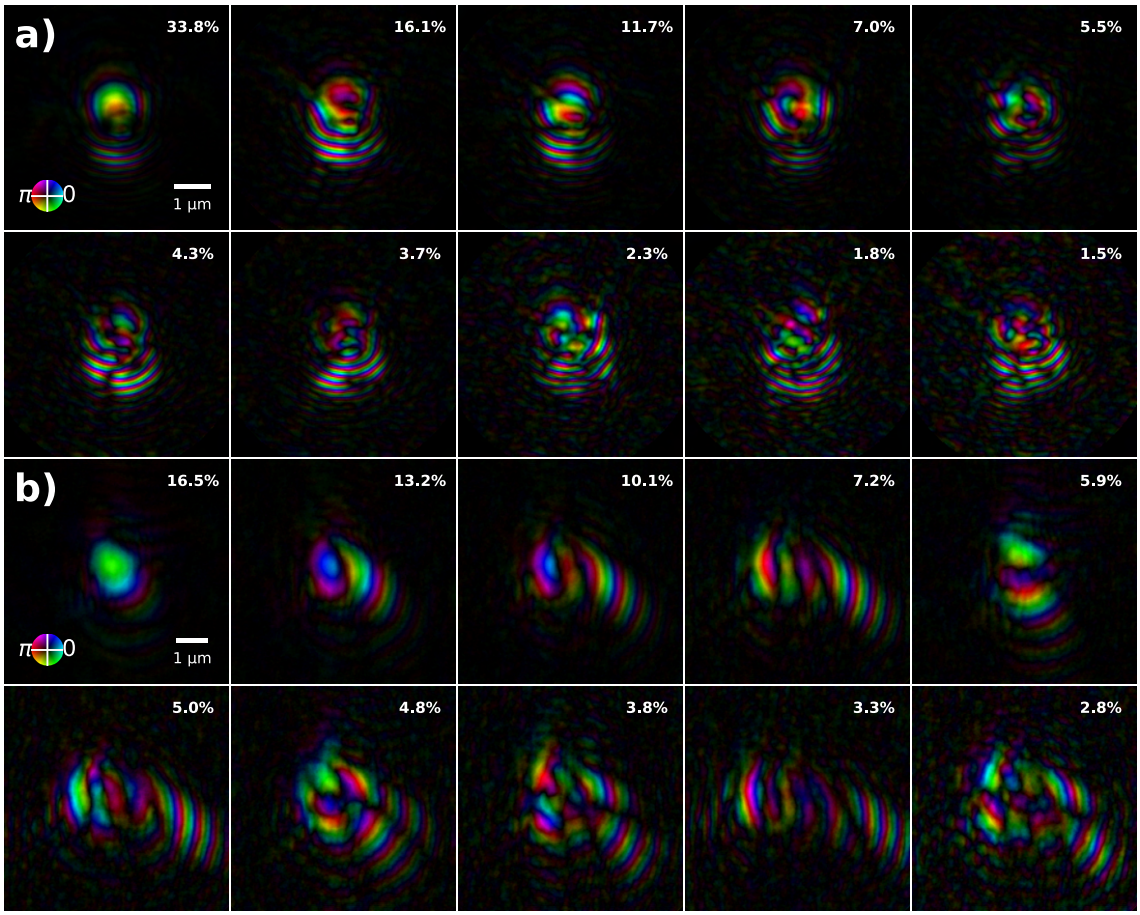


Figure 4.10: Probe ptychography reconstructions for partially coherent ptychography metrology. The first 10 dominant modes for (a) the FZP and (b) CRL. The relative power of each mode is displayed in the top corner. The colour wheel encodes brightness & hue as amplitude & phase respectively [50].

the relative power of the final mode is negligible, usually less than 1%. The probe modes form an orthonormal base, which can be found using the Gramm-Schmidt procedure [242, p. 544]; the first 10 dominant modes after orthogonalization and their respective power are shown in Fig. 4.10 for the FZP and CRL. Their relative power to one another is small, and there is no particular mode that concentrates most of the power, unlike highly coherent sources.

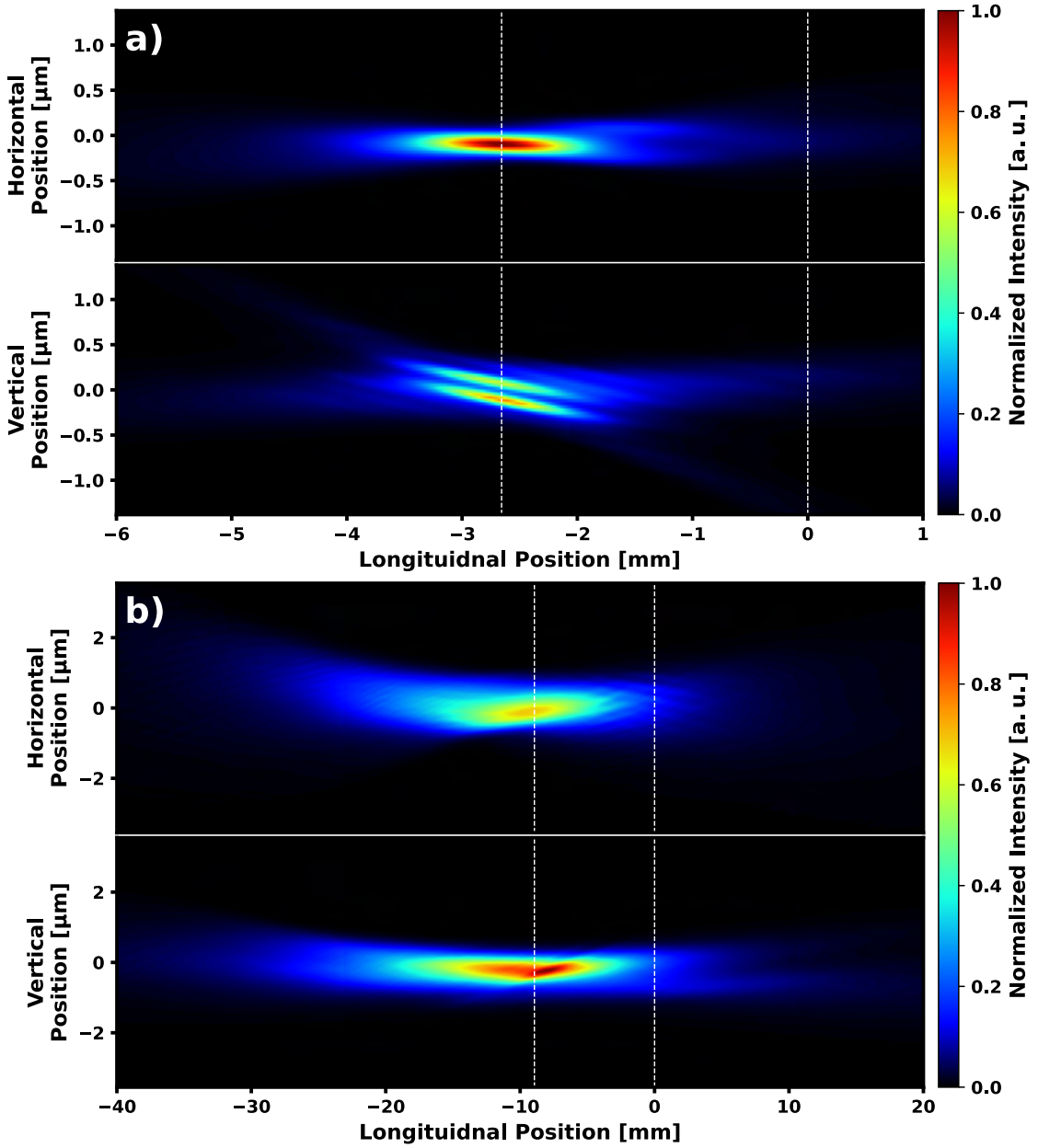


Figure 4.11: Beam caustics for partially coherent ptychography metrology. Horizontal & vertical caustics for the (a) FZP and (b) the CRL. Dashed lines mark the sample plane at 0.0 mm and peak intensity focal positions [50].

4.5.1.3 Beam caustic & focal properties

The multi-modal ptychography method reconstructs a set of complex, orthogonal modes at the sample position and we can use the angular spectrum diffraction formula in section 2.6.2 to numerically propagate each to any position along the optical axis. The intensity at any plane is related to the mutual optical intensity of the modal probe given by Eq. (3.26) and means each mode can be propagated

separately and its contribution to the intensity summed linearly. All probe modes for the FZP and CRL setups were propagated about the focal position to generate beam caustics for the horizontal and vertical directions, as shown in Fig. 4.11. The focal plane was defined as the plane which maximized peak intensity and was determined to be 2.7 mm and 9.1 mm upstream for the FZP and CRL setups respectively. Line profiles taken through the peak intensity point at the focal plane were fitted with a one-dimensional Gaussian profile and found the FWHM focal size for the FZP was 0.22 µm (h) × 0.41 µm (v) and the CRL was 0.92 µm (h) × 0.71 µm (v). These are limited by the secondary source demagnification effect according to Eq. (4.10) and are used to determine the actual size of the secondary source slits.

The FZP vertical focal profile and beam caustic are also clearly aberrated. From the optic aperture intensity which is discussed in the next section, the beam and FZP are not well aligned, and the aberration resembles a similar effect for a partially illuminated FZP studied previously [225]. Often the quality and reliability of the probe is evaluated using the sample and as can be seen in Fig. 4.9f, when a high number of probe modes are included there is good agreement of the sample with known feature sizes from the fabrication design and SEM images (not shown). The spatial resolution is sufficient to distinguish the 1 µm innermost radial spokes and is quantified further using the sample phase and taking line profiles across one of the sharp edges shown by the red lines in Fig. 4.9f. The profiles were extrapolated and differentiated such that a Gaussian profile could be fitted and gave a FWHM resolution of 81 nm for both setups, as shown in Fig. 4.13a. This is approximately double the reconstructed pixel size, which is the minimum spatial resolution achievable and suggests the diffraction data region of interest has been correctly selected and could even be increased until the values begin to diverge.

4.5.2 Source coherence properties

The coherent properties of the beam are incorporated into the multi-modal probe ensemble. As was covered in section 3.4.1, the degree of transverse coherence gives

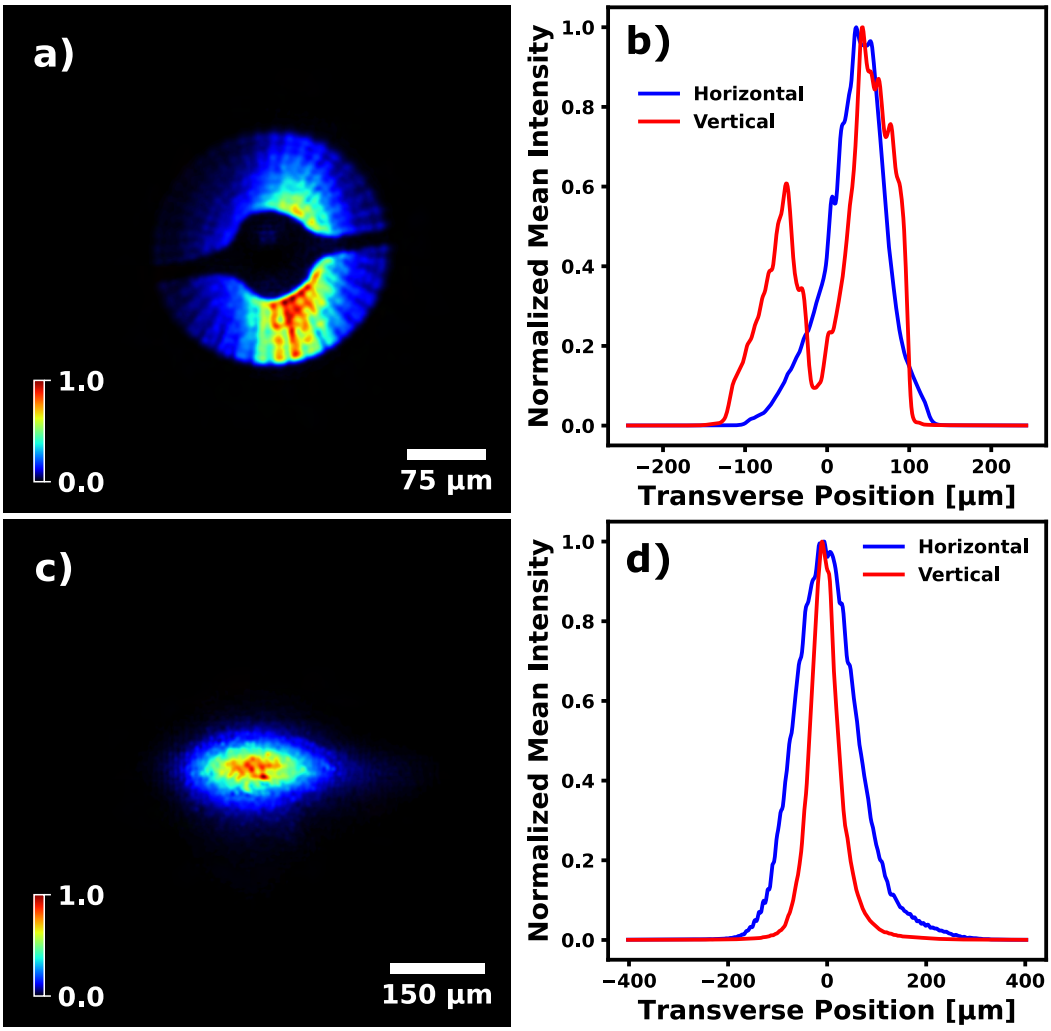


Figure 4.12: Optic aperture intensity for partially coherent ptychography metrology. (a) The FZP two-dimensional normalised intensity and (b) one-dimensional transverse mean line profiles. (c) The CRL two-dimensional normalised intensity and (d) one-dimensional transverse line profiles.

a single figure of merit and is equivalent to the fraction of coherent flux; it lies in the range $0 \leq \zeta \leq 1$ with complete spatial coherence when $\zeta = 1$ and complete spatial incoherence when $\zeta = 0$. For Gaussian-Schell sources, the relative power of the multi-modal probe is directly related to the degree of transverse coherence,

$$\frac{\beta_n}{\beta_0} = \left(\frac{1-\zeta}{1+\zeta}\right)^n \tag{4.11}$$

where β_n is the relative power of the n is the mode and β_0 is the dominant coherent mode. Validation of the result recovered from ptychography is achieved using some

	FZP at 10 keV		CRL at 15 keV	
	x	y	x	y
Secondary source size $s_{x,y}$ [µm]	21.2	39.1	31.8	24.4
Beam size at the optic positions $\Sigma_{x,y}$[µm]	72	120	140	71
Effective coherence length at optic $\Xi_{x,y}$[µm]	140	76	62	81
Degree of coherence $q_{x,y}$	1.96	0.63	0.44	1.14
Normalised degree of coherence $\zeta_{x,y}$	0.7	0.63	0.21	0.49
Total transverse degree of coherence ζ	0.211		0.108	
Ptychography degree of coherence ζ_{F}	0.231		0.118	

Table 4.1: Beam coherence properties for partially coherent ptychography metrology. Determined using the Gaussian-Schell model and ptychography for the FZP at 10 keV and the beryllium CRL at 15 keV, sizes are FWHM values.

basic properties of Gaussian-Schell sources and the experimental geometry parameters. The secondary source slit size $s_{x,y}$ is calculated according to Eq. (4.10) using the focal size and optic plane intensity, shown for both optics in Fig. 4.12.

All other related quantities are then derived from these values, with intermediate and final values for the calculations are displayed in Table 4.1. The secondary source is then modelled as a Gaussian-Schell source [202, p. 10] which assumes the source slits form a spatially uniform, plane two-dimensional source. The coherence length $\xi_{x,y}$ at the source position is then given by,

$$\xi_{x,y} = \frac{2s_{x,y}}{\sqrt{4k^2\varepsilon_{x,y}^2 - 1}} \tag{4.12}$$

where k is the wavenumber and $\varepsilon_{x,y} = s_{x,y}s'_{x,y}$ is the source emittance. Given values for the coherence length and source emittance, the degree of coherence $q_{x,y}$ and hence normalised degree of coherence are similarly given by,

$$q_{x,y} = \frac{\xi_{x,y}}{s_{x,y}} \qquad \zeta_{x,y} = \frac{q_{x,y}}{\sqrt{q_{x,y}^2 + 4}} \tag{4.13}$$

These values remain constant along the beam path; therefore, we also calculated both values at the optic position using the effective coherence length $\Xi_{x,y}$ from the van Cittern-Zernike theorem [88, p. 58] and beam size $\Sigma_{x,y}$ which also agree. Furthermore, for Gaussian-Schell beams the total transverse degree of coherence is

simply the product of the transverse components $\zeta = \zeta_x \zeta_y$.

The power spectrum of Eq. (4.11) was fitted to the multi-modal power distribution as is shown in Fig. 4.13 to determine the degree of transverse coherence. This found the FZP to be $\zeta_{\mathrm{F}} = 0.231$ and the CRL to be $\zeta_{\mathrm{F}} = 0.118$, with the lower CRL value expected, given the higher energy used. The beam size at the optics plane was calculated by propagating the multi-modal probe back using the Fraunhofer method and summing the intensity contributions according to Eq. (3.26), which is shown in Fig. 4.12a and Fig. 4.12c. For the CRL Gaussian profiles were fitted to one-dimensional line profiles through the aperture centre shown in Fig. 4.12d. For the FZP, the mean intensity along each transverse direction was calculated as shown in Fig. 4.12b and the size was determined where the intensity dropped below half its maximum value.

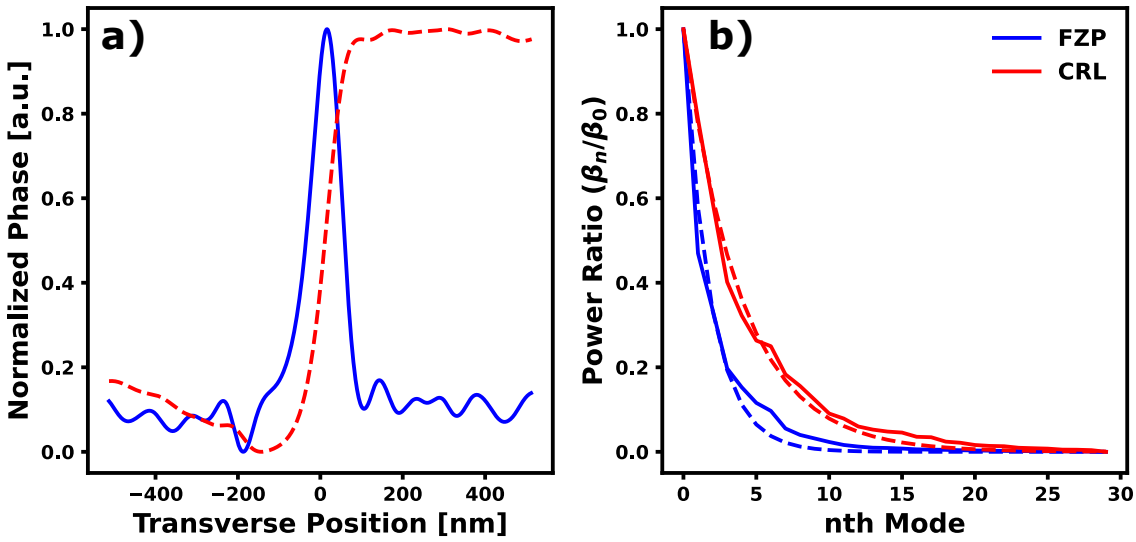


Figure 4.13: Resolution & multi-modal power analysis for partially coherent ptychography metrology. (a) Average line profile (blue) taken from Fig. 4.9f and its differential (dashed red). (b) The relative power spectrum of the multi-modal probe for the FZP and CRL and power law fitting (dashed) [50].

This found the FZP beam size to be 72 µm (h) × 154 µm (v) (FWHM) and the CRL size to be 140 µm (h) × 71 µm (v) (FWHM). These results were combined with the secondary source size calculated from the focal size. All other coherent properties were calculated from these and included in the Table. 4.1. The secondary source size

used for the FZP is completely coherent in the horizontal direction; this is confirmed by the multi-modal probes in Fig. 4.10a, which show a predominantly vertical p-lobe [49, p. 84] structure. The Gaussian-Schell and ptychography coherence properties for both optics agree well, with the CRL matching slightly better given its Gaussian distribution is easier to fit.

4.5.3 Aberration characterisation

The preceding section 4.5.1 evaluated the performance of focusing optics under realistic, partially coherent conditions. The mutual optical intensity of Eq. (3.26) used is an entangled representation of both the probe wavefield and coherent properties, which in many cases we wish to analyse separately. Furthermore, with the development of diffraction limited synchrotron sources, there is a desire to evaluate optics as they would perform under ideal, fully coherent conditions. For sources with a high coherent fraction, the analysis is usually performed on the (most powerful) or coherent mode [53], with the other modes typically contributing little power to the beam evolution. However, as the coherent mode power reduces, the validity of this approximation diminishes. This is the case for experiments performed on the B16 Test beamline [69]. The horizontal coherence length at the position of the optics is too small to illuminate the entire aperture of most X-ray optics which means a realistic assessment of performance using the coherent mode is impossible.

A secondary source would solve this issue, the simplest being to reduce the source slits enough that a point source is formed,[7] however, the flux is reduced beyond detection. Other groups have previously used upstream optics positioned to form a secondary source [46] however, the B16 beamline is not long nor accessible enough to gain any benefit from such a setup. Alternatively, a different deconvolution scheme could be used within the ptychography reconstruction [48, 49]; however, these methods are known to be stricken with difficulties arising from the imaging

[7] This differs from the spatial filtering that was described previously, the apertured slits would be small enough such that diffraction occurred and the new source was entirely coherent.

processing primarily due to the use of inverting Fourier transforms. A post processing deconvolution approach [49, p. 81] which used a minimisation procedure on the reconstructed multi-modal probe was implemented, but found to incorrectly decompose the probe as expected. This could result from the high levels of decoherence and fewer available degrees of freedom since only a point spread function and single probe mode is used rather than the full multi-modal ensemble.

This however led to the development of a ptychography method that shows decoherence effects arising from either the probe or sample can be accounted for by the other. When a multi-modal sample is assumed in the reconstruction, this results in a single, coherent probe, which is the version of the probe had the illumination over the entirety of the optic aperture been coherent i.e., it mimics the performance of the optic had the same experiment been performed on a high coherence beamline. This was already known and used within fly-scan ptychography to account for sample decoherence effects by implementing a multi-modal probe [56–58]. To assess the coherent performance of optics under partially coherent conditions, this principle is applied. A demonstration is performed by characterising an aberrated CRL and assessing its performance under coherent conditions; the results are compared with the design specifications as well as prior measurements. The findings of this study have previously been published in [51].

4.5.3.1 Theory & background

The theory is based on the ambiguous nature of the relationship between the reconstructed probe and sample states, which results from the definition of intensity. This ambiguity has previously been presented [203] with regard to how it can be broken within the reconstruction. From section 3.4.3, the Mutual Optical Intensity (MOI) can be written in terms of a product with the degree of coherence (DOC),

$$J(\boldsymbol{r}_1, \boldsymbol{r}_2) = P(\boldsymbol{r}_1)P^*(\boldsymbol{r}_2)\gamma(\boldsymbol{r}_1, \boldsymbol{r}_2) \tag{4.14}$$

where $P(\boldsymbol{r}) = \langle P(\boldsymbol{r}, t)\rangle$ is the probe, and $\gamma(\boldsymbol{r}_1, \boldsymbol{r}_2)$ is the degree of coherence which is assumed to only depend on the difference between the two points, i.e., $\gamma(\boldsymbol{r}_1, \boldsymbol{r}_2) = \gamma(0, \boldsymbol{r}_2 - \boldsymbol{r}_1)$. Sample dynamics, similarly occurring over the acquisition time of the detector $O(\boldsymbol{r}) = \langle O(\boldsymbol{r}, t)\rangle$ is described by its own density function and similarly decomposes as a product with some point spread function (PSF),

$$\rho(\boldsymbol{r}_1, \boldsymbol{r}_2) = O(\boldsymbol{r}_1)O^*(\boldsymbol{r}_2)\mu(\boldsymbol{r}_1, \boldsymbol{r}_2) \tag{4.15}$$

where $O(\boldsymbol{r}) = \langle O(\boldsymbol{r}, t)\rangle$ is the sample, and $\mu(\boldsymbol{r}_1, \boldsymbol{r}_2)$ is the object density function (ODF) which is again assumed to only depend on the difference between the two points, i.e., $\mu(\boldsymbol{r}_1, \boldsymbol{r}_2) = \mu(0, \boldsymbol{r}_2 - \boldsymbol{r}_1)$. This allows the propagated intensity to be written as a convolution of the probe DOC and sample ODF, for simplicity we consider only the far-field case such that quadratic terms in the propagator are small and can be ignored and the intensity is given by,

$$I(\boldsymbol{q}) = \int J(\boldsymbol{r}_1, \boldsymbol{r}_2)\rho(\boldsymbol{r}_1, \boldsymbol{r}_2)e^{-2\pi i(\boldsymbol{r}_2 - \boldsymbol{r}_1)\cdot\boldsymbol{q}}\mathrm{d}\boldsymbol{r}_1\mathrm{d}\boldsymbol{r}_2 \tag{4.16}$$

In order to demonstrate how the intensity can be written as a convolution, we first take the inverse Fourier transform of the far-field intensity and then substitute Eq. (4.14) and Eq. (4.15), which gives the far-field intensity as a convolution with the coherent wavefield intensity,

$$I(\boldsymbol{q}) = \tilde{\gamma}(\boldsymbol{q})\tilde{\mu}(\boldsymbol{q}) \circledast |\psi(\boldsymbol{q})|^2 \tag{4.17}$$

where the tilde over the DOC $\tilde{\gamma}(\boldsymbol{q})$ and ODF $\tilde{\mu}(\boldsymbol{q})$ denotes the Fourier transform of $\gamma(\boldsymbol{r}, 0)$ and $\mu(\boldsymbol{r}, 0)$ respectively and $|\psi(\boldsymbol{q})|^2$ denotes the diffraction pattern of the incident coherent wavefield. Inclusion of these effects in ptychography is most commonly achieved with a modal decomposition [47] of the MOI in Eq. (4.14) [200]

and density function in Eq. (4.15) [243] according to,

$$\begin{aligned} J(\boldsymbol{r}_1, \boldsymbol{r}_2) &= \sum_{n=1}^{N} \eta_n P_n(\boldsymbol{r}_1) P_n^*(\boldsymbol{r}_2) \\ \rho(\boldsymbol{r}_1, \boldsymbol{r}_2) &= \sum_{m=1}^{M} \mu_m O_m(\boldsymbol{r}_1) O_m^*(\boldsymbol{r}_2) \end{aligned} \tag{4.18}$$

where $P_n(\boldsymbol{r})$ are orthonormal probe modes with weight η_n and $O_m(\boldsymbol{r})$ are orthonormal sample modes with weight μ_m. For the case of full spatial coherence and a static sample, the equations simplify to the usual form $J(\boldsymbol{r}_1, \boldsymbol{r}_2) = P(\boldsymbol{r}_1)P^*(\boldsymbol{r}_2)$ and $\rho(\boldsymbol{r}_1, \boldsymbol{r}_2) = O(\boldsymbol{r}_1)O^*(\boldsymbol{r}_2)$. Substitution of this into the far-field intensity results in the following form,

$$I(\boldsymbol{q}) = \sum_{n=1}^{N} \sum_{m=1}^{M} \eta_n \mu_m \left| \mathcal{F} \left\{ P_n(\boldsymbol{r}) O_m(\boldsymbol{r} + \boldsymbol{r}_j) \right\} \right|^2 \tag{4.19}$$

We observe in the fully spatial coherent case where $\tilde{\gamma}(\boldsymbol{q}) = 1$, or for the completely static sample case where $\tilde{\mu}(\boldsymbol{q}) = 1$ that decoherence effects will be described by a single PSF in Eq. (4.17). As interchanging either of these functions does not change the form of the equation, it's assumed that decoherence effects can therefore be compensated by either the probe or sample described with the single PSF function corresponding to either decoherence effect. Furthermore, given that Eq. (4.17) and Eq. (4.19) are different representations of the same phenomenon, it's accounted for in ptychography using the multi-modal form of either the probe or sample.

4.5.3.2 Experimental setup

Experiments were performed at the B16 Test beamline [69] at Diamond Light Source, Didcot UK similarly to the previous ptychography experiments described in section 4.5.1.1. To maximize the available flux and illuminate the entirety of the CRL aperture at no point were slits used to filter the spatial coherence, which provided an approximate power of 1×10^8 photons/s with a beam size of $4.4\,\mu\text{m}\,(\text{h}) \times 4.4\,\mu\text{m}\,(\text{v})$ at the sample position. A double-crystal Si(111) monochro-

mator with a bandpass of $\Delta E/E \sim 10^{-4}$ was used to select an X-ray energy of 12 keV and maximise longitudinal coherence. The beam was focused using a beryllium CRL with a geometric aperture of 1 mm and 98 individual lenses each with a radius of curvature of 200 µm, giving a focal length of 432 mm and an effective aperture of 394 µm at 12 keV. For the test sample, a 3 µm thick gold Siemens star on a silicon nitride substrate was positioned at the focal plane. A single-photon counting Merlin Medipix detector with a pixel size of 55 µm (h) × 55 µm (v) and a pixel field of view of 512 px (h) × 512 px (v) was positioned 8.4 m downstream of this. The experimental setup is depicted in Fig. 4.14.

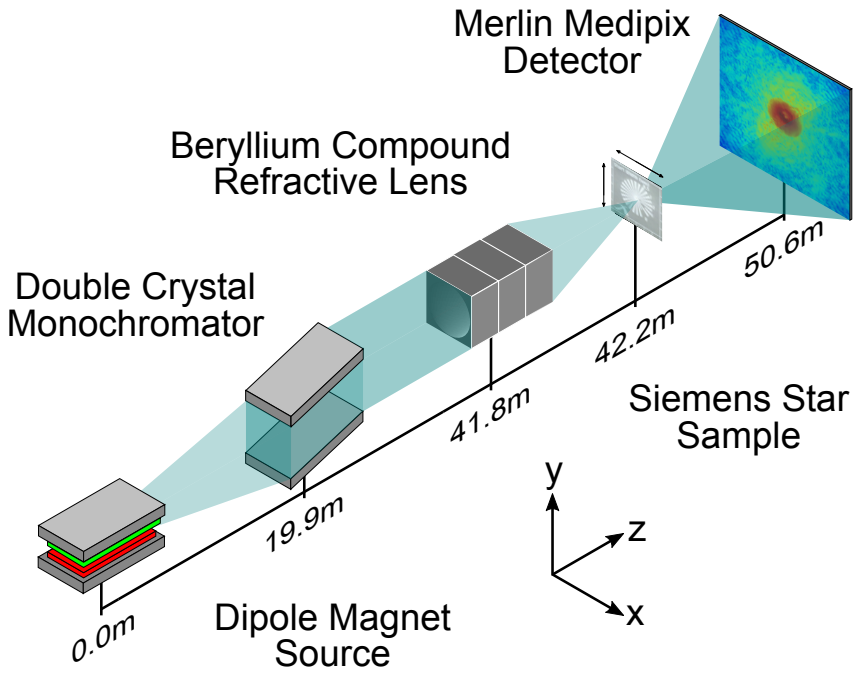


Figure 4.14: Experimental setup (distances not to scale) for aberration characterisation of a CRL optic using partially coherent ptychography on the B16 Test Beamline at Diamond Light Source [51].

The gold knife edge used to align the CRL was also used to find the focus such that the ptychography test sample could be aligned at this point. The focal position was chosen rather than some defocused distance as the CRL focal size is of the order of a few microns, which is already relatively large for ptychography scans. Additionally, given the low fraction of coherent flux we attempted to increase the oversampling of the setup as much as possible, which meant scanning with the

smallest focal size achievable as well as positioning the detector as far away as physically possible. Ptychography scans were then performed by translating the sample through the beam and acquiring diffraction patterns at each position, which was done in a spiral manner to reduce raster artefacts [35]. A scan was performed over an area of 32 µm (h) × 32 µm (v) with a step size of 0.5 µm and an individual exposure time of 0.5 s, which generated 4099 diffraction patterns. With this scanning geometry, the overlap sampling factor given by Eq. (3.34) was found to be 89% and the overall sampling ratio according to Eq. (3.35) was found to be $S_{\Pi} = 996$. Initial reconstructions were processed during the experimental session using the *ptypy* framework [189] and the difference map (DM) [35] algorithm with a multi-modal probe [47] featuring 10 probe modes.

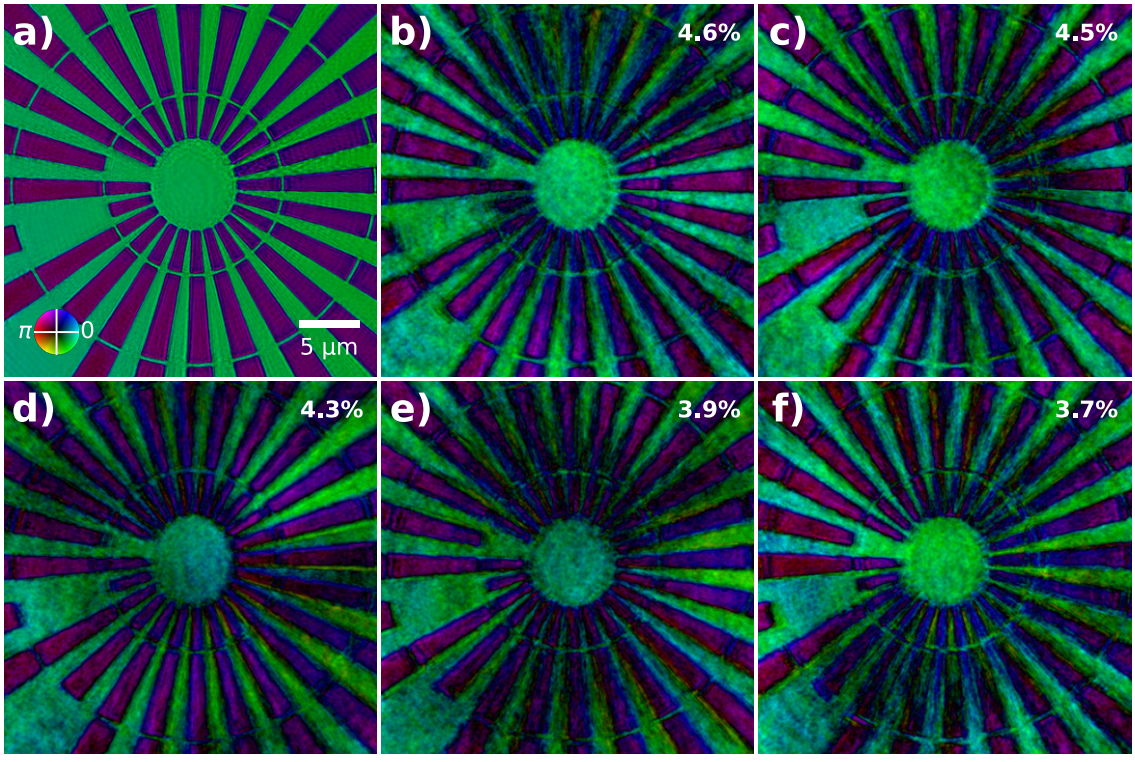


Figure 4.15: Sample reconstructions for aberration characterisation of a CRL optic using partially coherent ptychography. (a) Assuming a coherent sample & multi-modal probe [51]. (b-f) First 5 dominant modes assuming a multi-modal sample & coherent probe with relative modal power in the top corner. The colour wheel in (a) encodes brightness & hue as amplitude & phase respectively.

4.5.3.3 Reconstruction processing

Without the inclusion of a multi-modal probe, the ptychography reconstruction failed to converge; this differs from the previous case in section 4.5.1 where the decoherence effect simply degraded the reconstruction quality [47]. The optic aperture and the Van Cittert-Zernike coherence length [238] were used with Eq. (3.30) to estimate that at least 56 modes would be required. This is many more than typically used, and parallel ptychography implementations were not suitable for reconstruction due to the large memory requirements.[8] A more suitable method was found using the Regularised Ptychographic Iterative Engine (rPIE) [193], a slightly different version of the algorithm discussed in section 3.2.2. This involves a sequential update of the probe and sample functions by looping through all diffraction patterns individually, which avoids the large memory requirements. This was extended to use modal ptychography using the same minimisation procedure outlined in the supplementary material of [47]. A GPU implementation was employed to increase the reconstruction speed by using the CuPy python module [218] and running the program on an Nvidia Tesla P100 graphics card.

As explained by section 4.5.3.1, two separate reconstructions were run, one considering the probe and the other, the sample as the source of system decoherence. These are referred to as the coherent sample and probe reconstructions, respectively. The diffraction patterns were cropped to a region of interest around the optical axis measuring $256\,\mathrm{px}\,(\mathrm{h}) \times 256\,\mathrm{px}\,(\mathrm{v})$, which included only statistically relevant counts. Dead and hot detector pixels were also disregarded from the reconstruction by generating a detector mask based on the integrated diffraction data stack. For the first reconstruction, a single coherent sample was used, and probe modes were included up until the relative modal power in the final mode was negligible. This occurred at around 100 modes. In the second reconstruction, a single coherent probe was used

[8] Using the multi-modal DM algorithm a four-dimensional array is required, with 100 probe modes a memory of around 800 Gb is required, far beyond the capability of most systems.

and 100 object modes were included for consistency. Both reconstructions started from a flat sample and the simulated probe of an ideal CRL lens. Modes were included as random permutations for the respective multi-modal functions. The rPIE algorithm was run for 750 iterations until the Fourier error converged.

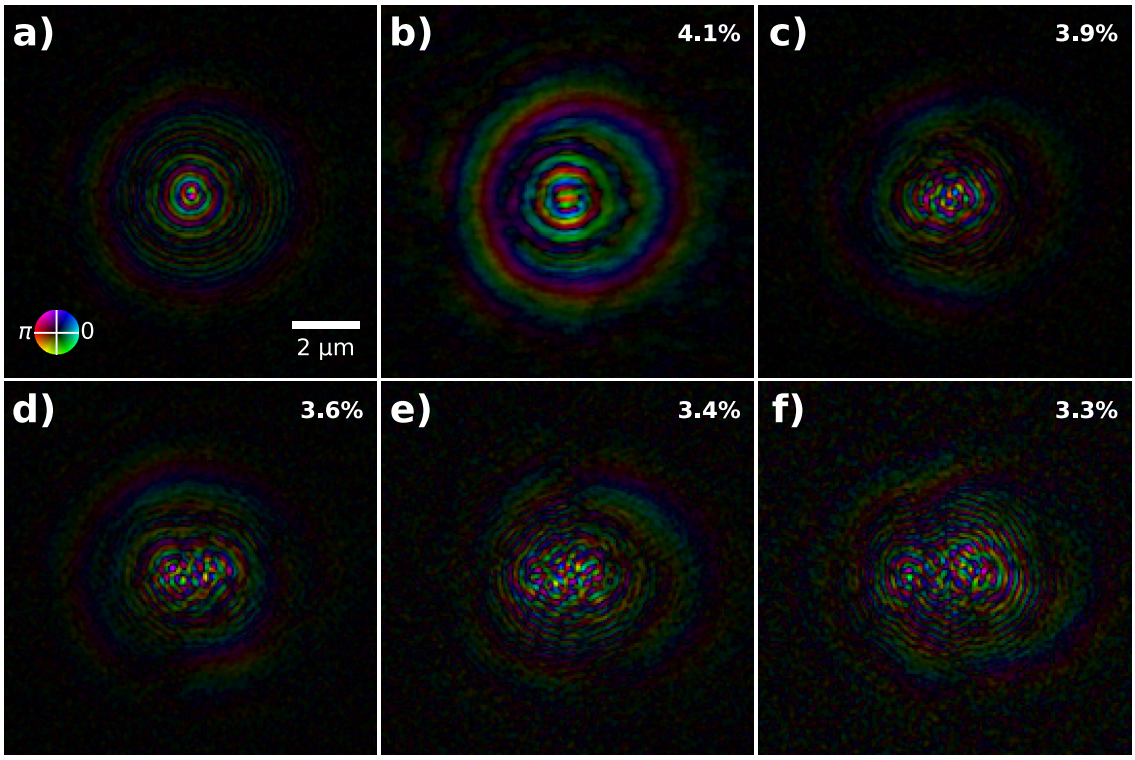


Figure 4.16: Probe reconstructions for aberration characterisation of a CRL optic using partially coherent ptychography. (a) Assuming a coherent probe and multi-modal sample [51]. (b-f) First 5 dominant modes assuming a multi-modal probe and coherent sample with relative power in the top corner. The colour wheel in (a) encodes brightness & hue as amplitude & phase respectively.

For the experimental geometry outlined, an effective pixel size of 62 nm was achieved. The coherent and multi-modal samples are shown in Fig. 4.15a and Fig. 4.15b-f and the corresponding coherent and multi-modal probes after orthogonalisation are shown in Fig. 4.16a and Fig. 4.16b-f. The relative power is displayed in the top right-hand corner of each image. The multi-modal sample alludes any real physical interpretation but features a power spectrum similar to the probes; the coherent sample is also slightly noisier than the previous partially coherent ptychography reconstructions, with periodic grid artefacts more noticeable and likely

owing to the low fraction of coherent flux. In the case of the probe, all modes are well contained within the central region, signifying they all only contribute to the probe's mutual intensity. The majority of structure forms in the horizontal plane as expected due to worse coherence in this direction. The multi-modal intensity contributions were summed according to Eq. (3.26) and the FWHM probe size at the sample plane was found to be around 1.65 µm (h) × 0.75 µm (v). This means the scan step size used was relatively large compared to the beam size and could also be responsible for introducing the grid artefact observed in the coherent object reconstruction.

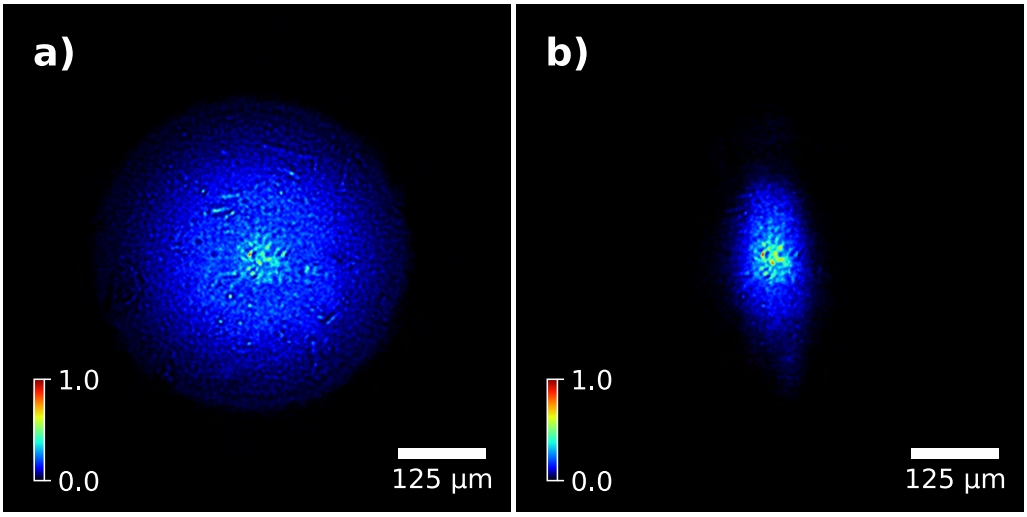


Figure 4.17: Optic aperture intensity for aberration characterisation of a CRL optic using partially coherent ptychography. (a) The coherent probe assuming a multi-modal sample. (b) Dominant modal probe assuming a multi-modal probe. Propagations used Fraunhofer diffraction and intensities are normalised.

It was found from the relative modal power spectrum shown in Fig. 4.20b and using Eq. (4.11), that the normalised degree of coherence was around 2.0%. This agrees well with the theoretically predicted value of 2.02%, calculated using the coherence length at the optic plane and the effective aperture of the lens. The intensity at the optic plane was calculated for the coherent and dominant multi-modal probe by back propagating each of the modes using the Fraunhofer diffraction and is shown in Fig. 4.17. Clearly, the coherent probe covers the entirety of the optics designed effective aperture while the dominant multi-modal probe is restricted by

the coherence length of the respective planes. This demonstrates why a different approach was required. The spatial resolution of the coherent sample reconstruction was sufficiently high to visually distinguish the 1 µm features separating the innermost radial spokes. To quantify the resolution further, the Fourier shell correlation [216], as discussed in section 3.6 was performed on the coherent sample phase of two independent ptychography scans over the same area and reconstructed with identical parameters. After alignment, the FRC between the two reconstructions was found to cross the 1-bit threshold with an estimated spatial resolution of 104 nm.

4.5.3.4 Beam and focal properties

As the method presented recovers both the coherent and multi-modal probe it gives us the ability to examine the optical performance under both actual and ideal conditions. This differs from many metrology methods which examine the coherent performance of X-ray optics by superimposing the measured wavefront error on a simulated ideal optic and propagating this to the focal plane. The angular spectrum diffraction formula of section 2.6.2 was used to numerically propagate the coherent and multi-modal probe along the optical axis about the focal plane. The multi-modal intensity was summed according to Eq. (3.26) and beam caustics were taken by integrating the intensity volume along the horizontal and vertical axes. The focal position was defined as the plane which maximised peak intensity and was determined to be 2.3 mm upstream of the sample position for both probes.

Slices through the propagated intensity volume for both probes demonstrate that the multi-modal probe is equivalent to the coherent probe convolved with some Gaussian point spread function as shown by Eq. (4.17) originating from the source contribution. The beam caustic for both probes and intensity slices at different positions are shown in Fig. 4.18. Optical aberrations, particularly spherical terms at the focus, are much more apparent in the coherent probe caustic. The focal size of the multi-modal probe was found to be 1.22 µm (h) × 0.62 µm (v) which agrees well with knife edge measurements taken during the experiment and the effect of

the demagnified source size on the focus. Similarly, the focal size of the coherent probe was found to be 160 nm (h) × 150 nm (v), which is on the order of the expected diffraction limit but broader due to the presence of fabrication errors.

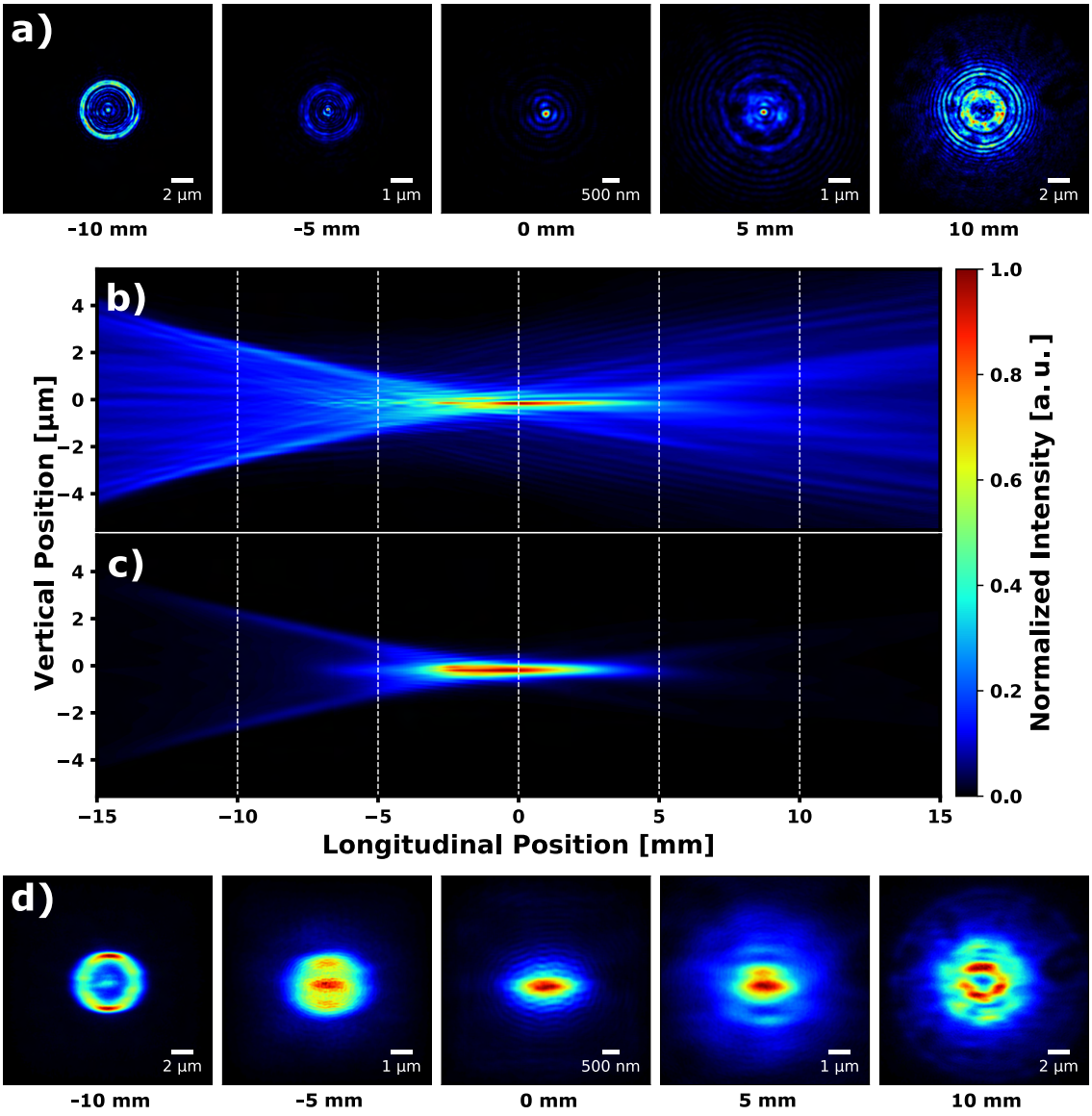


Figure 4.18: Beam caustics for aberration characterisation of a CRL optic using partially coherent ptychography. (a) Coherent probe intensity slices. (b) The coherent and (c) multi-modal probes vertical beam caustic about the focal position. (d) Multi-modal probe intensity slices [51]. Positions of the slices are also marked by the white dashed lines on the beam caustics in (b) and (c).

4.5.4 Comparison with previous results

The focal size and position obtained from the intensity at and around the focus provide only partial insight into the performance of an optic; as such, we will use the method presented in section 4.3.4 to extract the wavefront error from the coherent probe recovered from ptychography. The probe was first back propagated from the sample position by a distance of 2.3 mm + 432 mm to the exit plane of the CRL array using the angular spectrum method of section 2.6.2. The intensity distribution at this plane is similar to that shown in Fig. 4.17a and is Gaussian in profile owing to the attenuation at the edges of the lenslets with the measured effective aperture agreeing well with the optic design parameters and Eq. (2.22). The phase distribution was then unwrapped using the method presented in [244], which was found to be most effective at avoiding artefacts arising due to the presence of phase residues. From this, the phase of a perfect spherical wave according to Eq. (4.7) was fitted and subtracted.

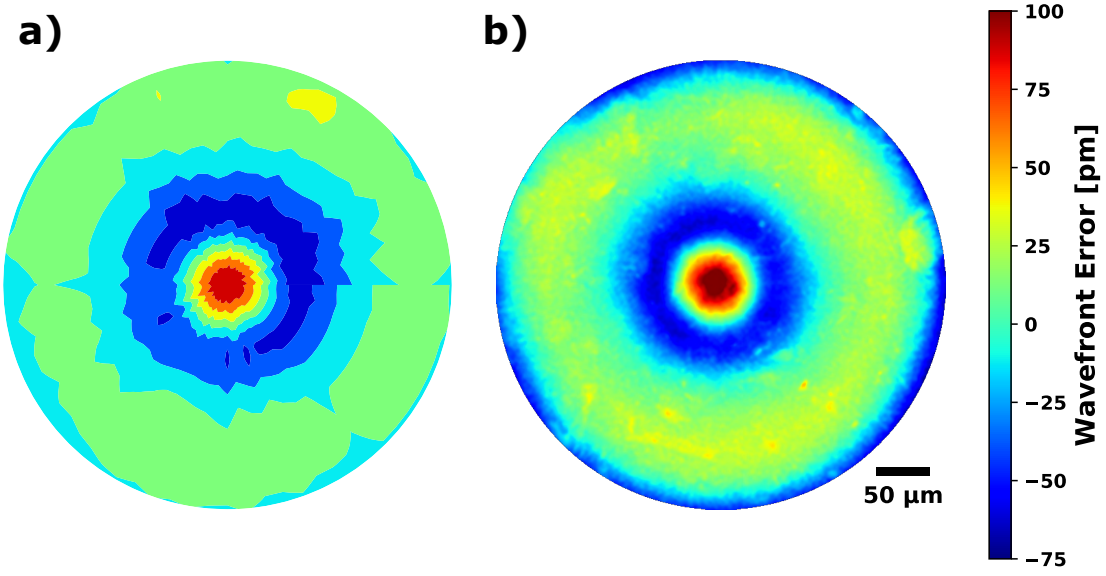


Figure 4.19: Two-dimensional wavefront error of a CRL optic using partially coherent ptychography. (a) A previous wavefront error measurement performed at 15 keV using knife edge scanning at different polar angles [245]. (b) The ptychography wavefront error performed at 12 keV and converted to the 15 keV form using Eq. (4.20) for comparison with previous results [51].

The phase error was then converted to a wavefront error using Eq. (4.1) to compare with the data previously measured. These measurements of the same beryllium CRL wavefront error have previously been performed using a knife edge technique (discussed more in section 5.1.3) and working at an energy of 15 keV, the results of which are published in [245]. To compare results with the ptychography experiment, we assume the wavefront error occurs due to thickness variations in the lens array, which will change depending on the beam energy according to,

$$\Delta X(E_1) = \Delta t\, \delta(E_1) = \frac{\delta(E_1)}{\delta(E_2)} \Delta X(E_2) \tag{4.20}$$

where $\Delta X(E)$ is the path length change, Δt is the aberration error thickness, $\delta(E)$ is the energy-dependent refractive index decrement for beryllium, and the subscripts 1 and 2 denote the measurements at 15 keV and 12 keV, respectively. Conversion of the wavefront error between energies simply corresponds to a scaling given by the ratio of the real refractive index decrement at the two different energies. The results of the knife edge and ptychography two-dimensional and radial wavefront error of the CRL are shown in Fig. 4.19 and Fig. 4.20a respectively.

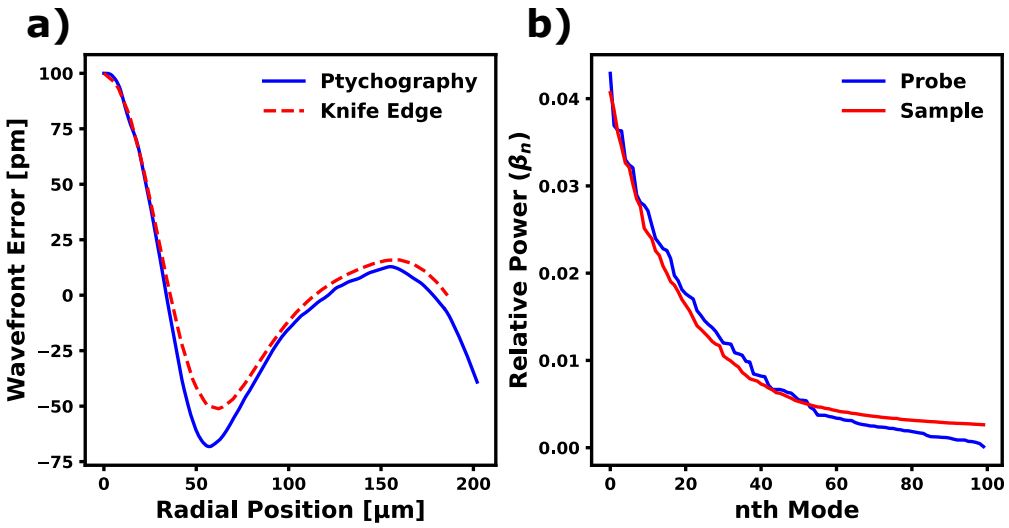


Figure 4.20: (a) One-dimensional radially averaged error of the two-dimensional wavefront errors in Fig. 4.19. (b) The full multi-modal power spectrum for the sample & probe shown in Fig. 4.15 and Fig. 4.16 respectively [51].

The ptychographic profile demonstrates visually good agreement with the knife edge results and even recovers the same asymmetry found around the 70 µm radial position. The root mean squared (RMS) wavefront error was found to be 27.3 pm, which is also in good agreement with the 24 pm found using the knife edge technique. While there is a slight difference in the RMS wavefront error and average radial profile, this is likely because the knife edge is a one-dimension technique that was repeated at various polar angles and thus, generated a fairly coarse two-dimensional grid of points for comparison. Furthermore, measurements were performed during two different sessions so the alignment of the individual lenslets may have shifted.

The ptychography method demonstrates a number of advantages firstly, the spatial resolution is very high, and the wavefront error covers the complete aperture of the lens.[9] Furthermore, both the actual and ideal performance of the optic can be assessed without the need to superimpose the wavefront error on an ideal optic. The Zernike polynomial decomposition has previously been performed [245] and finds the dominant contribution from spherical components, most likely arising from the pressing method used to fabricate individual lenslets.

4.6 Results & discussion

In summary, several developments in the field of partially coherent ptychography as an at-wavelength metrology technique have been presented. Initially formulated for purely imaging purposes, ptychography is now a critical metrology technique utilised by most synchrotron and XFEL facilities. The inclusion of a multi-modal probe to account for partially coherent light has widened the technique's accessibility such that it's no longer restricted to specialised, highly coherent beamlines. The main concluding points of this section are summarised below.

- A demonstration of how regular, highly coherent ptychography can be used to characterise X-ray optics was presented in section 4.3. Back propagation

[9] The knife edge method being insensitive to wavefront error where intensity is low, is unable to measure the wavefront error over the entirety of intensity dependent apertures such as CRLs.

of the probe allowed the wavefront error to be extracted and decomposed into Zernike coefficients such that errors arising from alignment and fabrication aberrations could be subsequently separated. The effect of the error on the focusing performance was found using the beam caustics, and suggestions of their origin, and future reduction was additionally discussed.

- The first successful demonstration of partially coherent ptychography using a synchrotron dipole bending magnet source was demonstrated in section 4.5.1. Initial tests focused on improving the coherence via spatial filtering of the beam; however, this reduced the effective size of the beam at the position of the optic making the technique unsuitable as an accurate metrology method.

- The coherent properties of the beam were computed from ptychography and found to agree with those predicted from a Gaussian-Shell model. Therefore, ptychography is an effective method for characterising the coherent properties of beams, providing greater spatial information than other methods.

- Line profiles across sharp features of the Siemens star test sample found the resolution to be around 81 nm, which is a factor of 3.6 times better than the 290 nm currently offered using the Kirkpatrick–Baez mirror setup.

- The limited coherence length at the optic plane led to a new modified version of using partially coherent ptychography as an at-wavelength metrology method which is presented in section 4.5.3. This considers the sample rather than the probe as the source of decoherence in the ptychography reconstruction and allows a completely coherent version of the probe to be reconstructed. As a single coherent probe is recovered, the wavefront error can be extracted, and the optics performance can be assessed under ideal, coherent conditions.

- Wavefront error results of the new method were compared with previously known results measured using a knife edge technique and found to agree very

well, with the ptychography method providing higher spatial resolution and a slightly larger measure of the effective aperture.

- The measurements performed in section 4.5.3 contained a degree of coherence of just 2%, which is the lowest coherent fraction which still resulted in a successful ptychography reconstruction on record. As insertion device beamlines tend to produce higher flux beams, scanning times and experimental configurations are likely to be more relaxed than what's been demonstrated. This paves the way forward for ptychography to be offered as a complementary, high-resolution imaging technique used by other non-specialized beamlines.

5 Aberration correction using refractive structures

5.1 Corrective optics methods

Correction of wavefront errors can either be achieved by developing better fabrication methods or by correcting for the errors introduced. The former method is preferable but comes with greater technical challenges as well as fabrication times and costs [16]. The newest generation of X-ray optics attempt to increase numerical aperture via various means, but all require fabrication tolerances on the nanometer scale to succeed. This includes the outer ring thickness for FZPs [103], the deposition thickness of MLL [17] and multi-layer mirrors [139] and the aspect ratio for nano-focusing CRLs [117]. As fabrication developments have plateaued in recent years, wavefront correction methods have seen rapid development and attempt to correct errors post manufacture [7, 19]. The aim of wavefront correction is to introduce perturbations to the incident wavefront which cancel out those originating from the aberrated optic. It has been readily applied in the visible light regime, most famously in optometry with the use of spectacles and contact lenses. Furthermore, it was used to correct the faulty mirror of the Hubble Space Telescope in both the visible and UV regimes [22]. Such methods are typically cheaper to implement, can account for errors introduced by existing beamline optics and can correct errors which may develop over time due to operation. The two primary methods[1] used for X-ray optics are listed below.

- **Deformable Mirrors:** These types of elements feature deformable mirrors with a high level of control of the mirror surface shape either using an electrode or mechanical methods [247]. The deformable mirror is positioned upstream

[1] Diffractive corrective optics have also been demonstrated previously [246]; however, they've not been as widely developed as the other two methods presented.

of the focusing optic and wavefront perturbations are introduced by changing the mirror surface [20, 248]. These corrective optics are achromatic so they are typically used in conjunction with the same type of optic such as a Kirkpatrick–Baez mirror system. They have also been used to produce one of the smallest 8 nm hard X-ray focal spots [19] . The primary drawback is the precision with which the wavefront errors can be controlled as nanometer deflections of the mirror surface only result in $\lambda/10$ wavefront error change, and the possible shapes are limited by the number of deflection points. Furthermore, these types of systems are typically expensive to implement and deflect the beam off axis prior focusing which complicates the geometry.

- **Refractive Structures:** The use of refractive optics for wavefront correction of X-ray optics was first proposed in [249] and successfully demonstrated in [7, 21]. The concept is analogous to how glasses correct poor vision. The structures add a known perturbation to the incident X-rays upstream of the focusing optic and can be easily installed inline on existing beamlines [250]. While the weak refraction of X-rays by most materials makes it difficult to achieve strong focusing, it's advantageous for wavefront correction as small, precise perturbations can be applied to the wavefront with minimal absorption. The thickness profiles can be fabricated using advances in microfabrication [23, 251] to produce structures tens of microns thick, which introduce wavefront perturbations on the order of $\lambda/100$ precisely. The primary drawback comes from the energy-dependent refractive index of the structure material, which means the perturbation introduced will also change with energy.[2] Absorption can also start to become an issue for larger wavefront errors which require thicker refractive structures or when used at lower energies.

[2]This may be beneficial for some optics, e.g. CRLs, such that the corrective optics work over the entirety of the optics energy range however, the two materials would need to be the same.

5.1.1 Custom planar structures

The main method of wavefront correction researched within this thesis used planar refractive structures. These consist of planar micron thick SU-8 structures deposited on silicon wafers using deep X-ray lithography, a microfabrication technique [23]. Optical elements can be simply modelled as complex transmission elements, the wavefield of which, after passing through an aberrated optical element is given by,

$$\psi'(x,y) = \psi_0(x,y) \exp\left[\frac{2\pi i}{\lambda} w(x,y)\right] \tag{5.1}$$

where $w(x,y)$ is the wavefront error as defined in section 4.1 and $\psi_0(x,y)$ is the ideal optic transmission function, i.e., for a focusing optic this would simply be a spherical wave. This assumes the optic is well approximated as a thin element; for example, with a CRL, each individual lens may contribute a small error to the wavefront [245], but it's the collective error that is corrected. Corrective structures are then introduced with a phase profile given by,

$$\Delta\varphi(x,y) = -\frac{2\pi i}{\lambda} w(x,y) \tag{5.2}$$

assuming the corrective and focusing optics are next to one another, such that the multiplicative nature of combining transmission elements cancels the wavefront errors. This is valid for corrective optics placed slightly upstream of the aberrated optic and with incident plane wavefields; however, corrective optics placed downstream of the focusing optic will require a free space propagation [252].

Many two-dimensional X-ray focusing optics consist of independent horizontal and vertical elements which, are simpler to produce. This generally results in more significant fabrication errors along the focus direction such that the wavefront error can be decomposed into separate one-dimensional contributions from each of the

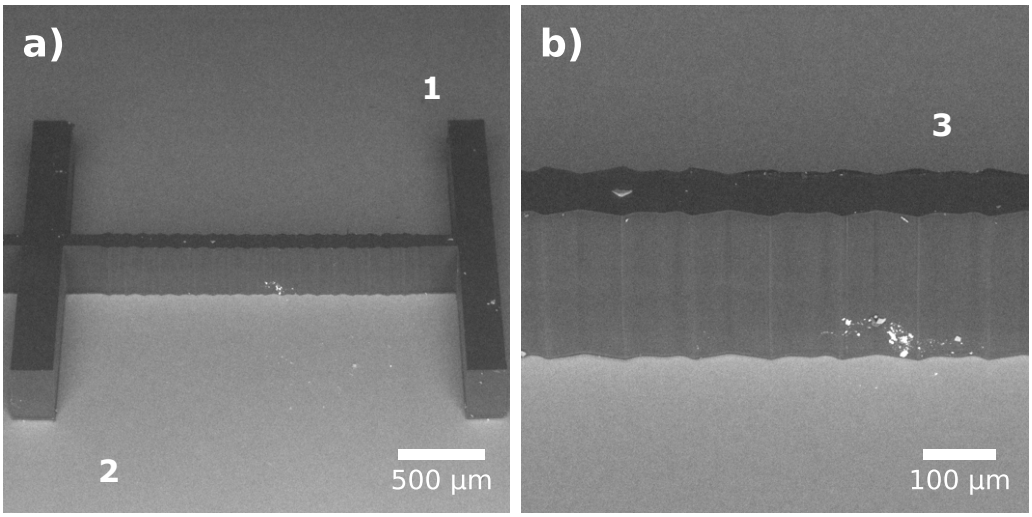


Figure 5.1: SEM images of custom SU-8 refractive structures for X-ray optics correction. (a) Large overview of a single structure, 1 labels the fiducial supports and 2 the silicon wafer substrate (b) Magnified view of the structure. Images were acquired at the Department of Engineering Science, University of Oxford.

transverse elements,

$$w(x, y) = w_h(x) + w_v(y) \tag{5.3}$$

With mirrors, for example, the grazing angle of incidence results in an illumination highly extended along the Kirkpatrick–Baez mirror's length. Whereas only a small portion is apertured across it resulting in a more significant figure error along the mirror length. This assumption means the horizontal and vertical optics can be corrected independently of one another.

The required thickness profile for refractive correctors can be calculated directly from the phase shift in Eq. (5.2), and the refractive index of the material; this is shown for the one-dimensional, planar corrective optic. Assuming an isotropic homogenous structure, the thickness profile is related to path length change and phase shift by,

$$t(x) = \frac{\Delta X}{\delta(E)} = \frac{\lambda \Delta \varphi}{2\pi\delta(E)} \tag{5.4}$$

where $\delta(E)$ is the energy-dependent refractive index decrement of the structure material and x is the one-dimensional positional coordinate. As the refractive index decrement for most polymers is on the order $\delta(E) \sim 10^{-6}$ at hard X-ray energies,

this means thicknesses $t(x)$ of a few microns can induce path length variations on the picometer scale. The structure thickness profile is, therefore simply a scaled, inverted copy of the wavefront error.

The most desirable properties of the refractive structure material are similar to those of nano focusing CRLs [117], with the primary requirement that micron-sized structures can be fabricated from the material. The technique chosen to fabricate the refractive structures is deep X-ray lithography [23] which can produce high aspect ratio structures up to 1 mm in depth with lateral transverse resolutions around 100 nm. SEM images of the first SU-8 custom structure iterations are displayed in Fig. 5.1. A discussion of the other fabrication methods that could/have been used and why they weren't chosen is presented in the proceeding section 5.1.2. The most efficient structures require a material with strong refraction-to-absorption ratio, which includes low atomic number, high density materials. This is difficult to match with the previous fabrication requirements but is well satisfied with an SU-8 polymer, the refractive and absorption properties of which is shown in Fig. 5.2. The radiation hardness of SU-8 has not been greatly studied; however, the structures show no signs of degradation after years of repeated use. The relatively inexpensive cost of fabrication means many can be produced and replaced as necessary.

Prior to my own involvement in the project, the optics group at Diamond Light Source used the following procedure for correcting aberrated optics using refractive structures. Firstly the wavefront error would be measured using either at-wavelength methods [28] such as knife edge scanning [250] and speckle wavefront metrology [253], or offline methods[3] within the nanometer optical metrology [24] such as Fizeau interferometry. From this, the thickness profile of the structure is generated according to Eq. (5.4) and then sent for fabrication, which is usually performed at the Indus synchrotron in India [254]. After this, the refractive structures would be received, installed and remeasured using at-wavelength metrology

[3]These techniques are limited to mirrors primarily and measure the surface slope error from which the effective wavefront error is then calculated.

methods [28] to observe the effect on the wavefront error and focal properties. Such a process typically involves many months, and numerous experimental sessions and is also highly prone to mistakes originating from optical misalignments [7, 255]. As such, the latest iteration of correctors known as adaptable refractive correctors were developed based on the same principles but with far greater flexibility and is the primary focus of this work, this is discussed and demonstrated in greater detail in section 5.3.

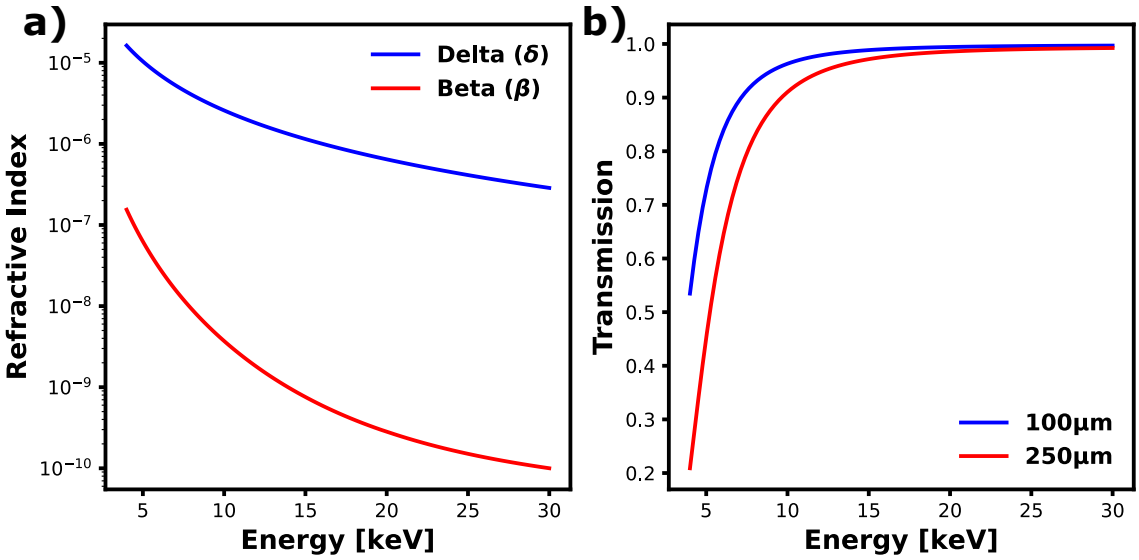


Figure 5.2: Optical properties of SU-8 polymer (a) Real and imaginary part of the refractive index. (b) Transmission through 100 µm and 250 µm thicknesses. Plots were generated using the Henke dataset [13] and confirmed experimentally.

5.1.2 Fabrication methods

From values of the wavefront error, the structure thickness can be calculated according to Eq. (5.4), and must then be fabricated from a material using micro-precision fabrication techniques. Advances in computing technology, particularly within the semiconductor industry, have led to many techniques being developed over the past decade. The ideal technique needs to produce structures which extend hundreds of microns to cover the aperture of most typical X-ray optics and can produce features with micron-scale transverse resolution. The material properties should also not be significantly altered by the process and should remain homogeneous and isotropic

such that Eq. (5.4) remains valid. Minimal manufacturing times and cost are also significant factors to mind. Below we list some of the most common methods that can be used to fabricate corrective structures and how they may or may not be suitable for use in this application,

- **Mechanical Machining:** Using miniaturised versions of conventional machining processes such as milling, drilling, and turning, such that material is removed conventionally by physical contact between the cutting tool and material. Although they can work with a wide variety of common X-ray elements, the thickness and transverse resolutions of the structures required are beyond the capabilities of most tools.

- **Focused Ion Beam:** A finely focused beam of ions (usually gallium) hits the target sample surface and sputters away a small amount of material. It provides high transverse and depth resolution, can accommodate most materials and also allows two-dimensional surfaces to be defined; however, is not suited for the removal of large volumes of material as would be required.

- **Laser Ablation:** A high-power short-pulse laser system creates a state of highly excited charged ions on the surface of the material which are then expelled. This can provide micron transverse resolution and removes large volumes of a wide variety of materials quickly [256]. The main drawback comes from the additional substrate thickness required but has previously been employed as a wavefront correction technique.

- **Deep X-ray Lithography:** Fabricates planar structures via exposure of a light-sensitive chemical photoresist through a masked geometric pattern to transfer the design into the material [23]. This provides thick structures up to 1 mm in depth with transverse resolutions on the 100 nm scale. One of the drawbacks is that only one-dimensional planar structures can be fabricated; however, more exotic designs can be achieved with angled exposures.

- **3D Printing:** Advances in 3D printing technology have led to a number of companies which offer commercial micro printers [257]. These primarily use either two-photon polymerisation resin or powder laser sintering as the fabrication and can produce millimeter-scale structures with up to 100 nm feature sizes. They are only limited by the material that is used and the speed at which structures are produced.

Given that the many two-dimensional X-ray focusing optics consist of independent horizontal and vertical elements that can be corrected independently, deep X-ray lithography was chosen as the main fabrication method for the structures. Using the refractor thickness function $t(x)$ the structures were first drawn using Computer Aided Design (CAD) and then sent to a specialist company for the production of an optical mask which is around 50 mm × 50 mm in size. On each optical mask, up to 190 separate objects (19 objects in 10 columns) can be drawn, each containing between 5 and 7 refractive structure elements, many tended to be repeated to allow for redundancy. Initial structure iterations were strengthened with a thin constant thickness profile through the middle of the structure; however, this increases the absorption unnecessarily, so later iterations use more periodic fiducials at the structure edges as indicated by label 2 in Fig. 5.1a. These also aid with the initial coarse alignment procedure. As part of the process, the optical mask is converted to a precision X-ray mask made from 8 µm thick gold; the structures were produced using X-rays in the energy range of 2.5 keV − 9 keV at the BL07 beamline at Indus-2 [254] using a well characterised SU-8 polymer. They are deposited on a silicon wafer and cleaved apart after fabrication into strips with a sequence of structures that can be mounted and translated into the X-ray beam.

5.1.3 Radially symmetric structures

The use of planar structures is (mostly) unsuitable for correcting radially symmetric focusing optics such as CRLs and FZP. Instead, structures which have thickness

variations in three dimensions are required [46]. The majority of wavefront error contribution for these optics comes from the dominant, rotationally invariant Zernike components. For demonstration, a rotationally invariant refractive corrector was manufactured using additive manufacturing based on the two-photon polymerisation technique and a nanoscribe printer. This was designed based on the wavefront error of the beryllium CRL that was characterised in section 4.5.3 and a reduction in the wavefront error and focal size was measured using a knife edge technique [245]. All orders of spherical aberrations were found to be corrected after the insertion of the rotationally invariant structures, but it was apparent that significant non-spherical aberrations still remained. Therefore, although planar lenses aren't suitable for the dominant spherical wavefront errors, within the Zernike spectrum there are predominantly two-dimensional errors such as astigmatism and coma aberrations in each transverse plane that could still be corrected. Similar to how the Alvarez-Loman lenses correct for lens astigmatism in the visible range [258]. Independent results from another research group exploring the use of additively manufactured refractive correctors also found similar results [256].

5.2 Knife edge scanning

The success of wavefront correction requires accurate metrology techniques to measure the wavefront error before, and after correction; these methods are best performed *in situ* and at the optics designed wavelength. In the previous chapter 4 ptychography was introduced as a powerful metrology technique that provided high-resolution, two-dimensional wavefront information [46]. The primary drawback of the ptychography technique is it requires two-dimensional mappings which compound the time each scan takes. An alternative method developed by the optics group at Diamond Light Source [250] extends the traditional knife edge scanning to a ray-based deflection technique. This works on similar principles to the pencil beam technique [32], but where the aperture is created computationally in the data

processing. As it is a ray-based technique, it can be used with both coherent and partially coherent light and isn't limited by diffraction effects like the aperture used in the pencil beam technique.

This is a "ray-based" deflection technique, which considers the propagation of light as rays directed normal to the wavefront surface [28]. The principle is to track the relative direction of rays to one another by measuring how they displace from on the detector. Unlike traditional knife edge scanning, an area detector is used such that each pixel can be mapped back to a corresponding point on the optic aperture. Referring to Fig. 5.3, if we consider a single pixel point P_2 on the detector, which maps back to a point P_1 on the optic and records the intensity as a function of the knife edge position Δy. The intensity plot as a function of knife edge position Δy will be a step function with an edge where the knife edge cuts the ray of interest [250]. The edge position is found by fitting an edge function based on the cumulative normal distribution and then locating the position where the intensity is reduced to 50% of the maximum. The Δy knife edge position is then converted to a slope error y_1' by dividing by the distance between the optic and knife edge position D_1.

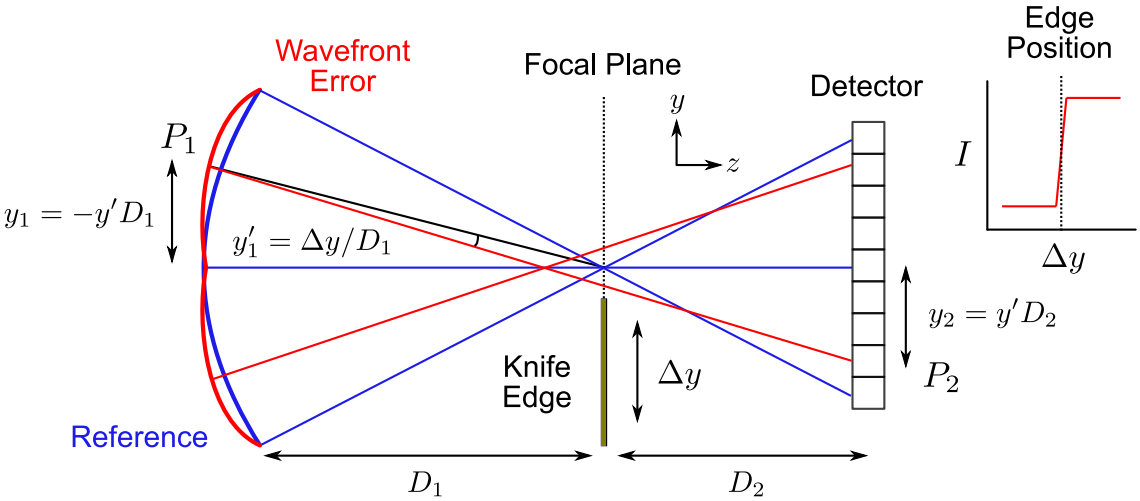


Figure 5.3: The knife edge scanning method is used to determine the wavefront error at a position y_1. Intensity is measured by detector pixel positioned D_2 from the focal plane as the knife edge is scanned in steps of Δy. Rays at the detector plane y_2 are mapped to a corresponding point on the optic aperture y_1. The relative intersection of the knife edge between different pixel positions defines the slope error. Schematic adapted from [250].

When repeated for all pixel positions on the detector, this will give the relative slope error y_1' between positions across the wavefront. The transverse position on the wavefront at the optic plane y_1 is mapped from the wavefront position at the detector according to $-y_1/D_1 = y_2/D_2$. To convert from slope error y_1' to wavefront error w_1 we simply integrate. For example, if we were scanning at the focus of an ideal optic, this step function edge should occur at the same knife edge position for all rays. This is because once the knife edge cuts the focus, the intensity should be zero for all pixels, resulting in zero edge position difference between all pixels and, when integrated, gives a constant wavefront error profile or zero error. Additionally, if the knife edge was located at some defocused distance away, rays at the edge of the beam would be cut first, resulting in a linear relative displacement of the step function edge position. When integrated, this results in a parabolic profile which can either be subtracted or minimised physically by moving closer to the focal position.

The transverse resolution y_1 is determined by the detector pixel size y_2 and the amount of magnification D_1/D_2. A small detector with a pixel size of 6.5 µm is usually positioned around ~ 1 m from the focus which for most X-ray optics results in y_1 having a sampling of less than 1 µm. Errors in the measurement of D_1 and D_2 only result in stretching or squeeze of the transverse position but can usually be measured quite reliably. The precision of the wavefront error is determined by the fitting of the step function to the detector intensity against the knife edge position Δy. This is, therefore determined by the knife edge scan step size, which is usually taken to be ~ 200 nm with at least 50 points on the curve. The knife edge object should be ideally flat with little to no surface roughness; this is not so much of an issue when scanned at the focus but begins to degrade the measurement when at some defocused position. It has been widely validated for a variety of X-ray optics and by other at-wavelength metrology techniques [28], including speckle tracking and interferometry. The main drawback is it can only be used with focusing type optics and only provides accurate information in one dimension.

5.3 Adaptable corrective structures

Wavefront correction methods can broadly be regarded as either static or dynamic. Static correctors use bespoke designs specific to each optical element being corrected and once installed cannot change over time [7, 21]. Dynamic correctors use some type of deformable optic which can be mechanically manipulated to alter the wavefront perturbation. These can correct for many different optics over a large energy range, and the correction can be adjusted over time if required. Until recently, the only form of dynamic corrective X-rays optics was the deformable mirror [20, 248]. As it was noted in section 4.2.1 from the Strehl ratio, it's not necessary for the wavefront error to be zero in order for an optic to achieve diffraction limited focusing and the RMS error needs only be less than $\lambda/14$ or the Maréchal criterion. It has been observed and studied that many wavefront errors are smooth and periodic in nature such that they may be decomposed using a Fourier series. For X-ray mirrors in particular, it's quite common that the surfaces are characterised by the power spectral distribution [227], the log of which typically exhibits a negative linear relation indicating the amplitude of the Fourier components reduces with the period. Through iterative developments of the previously described custom refractive structures, a system of structures has been developed which offers a dynamic wavefront correction that corrects the majority of wavefront error. This is achieved by combining two refractive structures with sinusoidal thickness profiles in series, with the relative displacement between the two structures allowing for a variable phase and amplitude perturbation of the wavefront [250].

5.3.1 Theory & background

The adaptable refractive corrector system (or adaptable correctors) consists of two planar refractive structures, each of which has an independent sinusoidal thickness profile that varies along the beam direction as a function of transverse position x,

such that the two respective structure thickness profiles are given by,

$$\begin{aligned} t_1(x) &= A\left(1+\sin\left[\frac{2\pi}{\Lambda}(x-x_0+\varepsilon)\right]\right)+t_0 \\ t_2(x) &= A\left(1-\sin\left[\frac{2\pi}{\Lambda}(x-x_0-\varepsilon)\right]\right)+t_0 \end{aligned} \tag{5.5}$$

where A is the structure amplitude, x_0 is the common translational offset of both structures, ε is the differential translational offset between the two structures and t_0 is a constant thickness used to strengthen and ensure the stability of the fabricated structure. A schematic of the structures is displayed in Fig. 5.4.

The X-ray path-length change according to Eq. (4.1) through each structure is a sinusoidal profile with a period Λ, and means their combination $t(x) = t_1(x) + t_2(x)$ is also sinusoidal with the same period but with a varying amplitude depending on the relative shift ε, using simple trigonometric identities,

$$t(x) = 2A\sin\left[\frac{2\pi\varepsilon}{\Lambda}\right]\cos\left[\frac{2\pi(x-x_0)}{\Lambda}\right]+2(A+t_0) \tag{5.6}$$

From this equation, it can be seen that the amplitude of the cosine term can be varied from $-2A$ to $2A$ by changing the differential offset between the two structures from $\varepsilon = -\Lambda/4$ to $\varepsilon = \Lambda/4$; similarly, the phase can be varied from $-\pi$ to π by moving both structures simultaneously over the range $x_0 = -\Lambda/2$ to $x_0 = \Lambda/2$.

This allows a range of sinusoidal wavefront profiles for dynamic correction, which feature variable phase and amplitude based on the relative translation between the two structures. The fixed period Λ parameter is also made variable by fabricating continuous structure sequences with the form given by Eq. (5.5) but with the period Λ slowly increasing from the start to the end of the series. This way, over a small aperture, the structure thickness is approximately the same, but it can also be changed significantly with a large translation. Originally the structures were designed to be mounted on separate stages with all translation and rotational degrees of freedom such that differential translation ε was achieved by translating

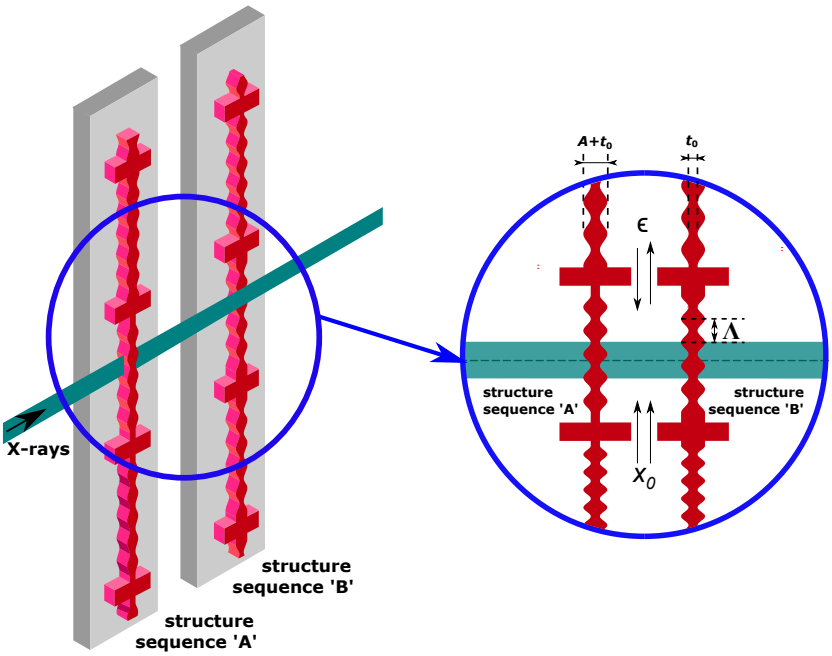


Figure 5.4: Schematic of the experimental layout showing a section of the two structure sequences which would be positioned upstream of an aberrated optic. Inset shows the vertical motion x_0 that changes the phase and ε that changes the amplitude of the sinusoidal wavefront correction [250].

just one structure. The most recent iteration of structures fabricates two series on the same silicon wafer substrate with some separation L typically around $\sim 1\,\mathrm{cm}$. As the separation L is much larger than the structure amplitude A, rotation around the axis normal to the silicon wafer surface results in differential motion between the two sequences i.e. ε in Eq. (5.6). This reduces the number of motion stages by half, as well as the setup space required upstream of the aberrated optic.

With the reduction in the number of stages, it's possible to combine correctors in series in order to perform higher-order corrections. For simple wavefront errors, the best period and amplitude range required is determined with a simple sinusoidal least squares fit. However, for high-order terms, a Fourier decomposition of the wavefront error is required according to,

$$\begin{gathered} w(x) = \frac{a_0}{2} + \sum_{n=1}^{N} a_n \cos\left(\frac{2\pi n}{\Lambda'} x\right) + \sum_{n=1}^{N} b_n \sin\left(\frac{2\pi n}{\Lambda'} x\right) \\ a_n = \frac{2}{\Lambda'} \int_{-\Lambda'/2}^{\Lambda'/2} w(x) \cos(nx)\,\mathrm{d}x \qquad b_n = \frac{2}{\Lambda'} \int_{-\Lambda'/2}^{\Lambda'/2} w(x) \sin(nx)\,\mathrm{d}x \end{gathered} \tag{5.7}$$

where a_n and b_n are all constant amplitudes and Λ' is the aperture size. The wavefront error can be decomposed into N Fourier components which are corrected for with N structures each with a different period Λ_N. Results are shown in Fig. 5.5 for the HKB wavefront error, which is discussed in the next section.

In Fig. 5.5a, the measured wavefront error (black) of the HKB is fitted with a single sinusoidal profile using least squares (blue), as well as a series approximation using the first three terms of the Fourier series (red) in Eq. (5.7). The corresponding Fourier components of the series are then also displayed in Fig. 5.5b. The wavefront error is already well approximated by a simple sinusoidal function with little gain with the inclusion of higher-order terms. In this case, only a single structure will be used for the correction. The series terms in Fig. 5.5b demonstrate the constructive and destructive nature of the Fourier series. It's likely the thickness and, therefore absorption of all structures required would be much higher than any gain from correcting the wavefront. Therefore, combining structures in series will only be beneficial for wavefront errors poorly estimated by single sinusoidal functions.

5.3.2 Experimental setup

Experiments were performed at the B16 Test beamline [69] at Diamond Light Source, Didcot UK a bending magnet beamline that provided an unfocused monochromatic X-ray beam for these experiments. The adaptable structures were used to correct a Kirkpatrick–Baez mirror system and a set of SU-8 planar CRLs with known fabrication aberrations. Each optic was mounted on a goniometer stage with all three translation and rotational degrees of freedom; the adaptable structures were likewise mounted a short distance upstream of the optics. Two sets of SU-8 planar CRLs were used at 15 keV. The first (lens 1) featured 44 individual lenslets, a geometric aperture of 400 µm and a radius of curvature of 100 µm, which gave a focal length of 1051 mm.

The second (lens 2) featured 19 individual lenslets, a geometric aperture of 250 µm and a radius of curvature of 25 µm, which gave a focal length of 655 mm. The

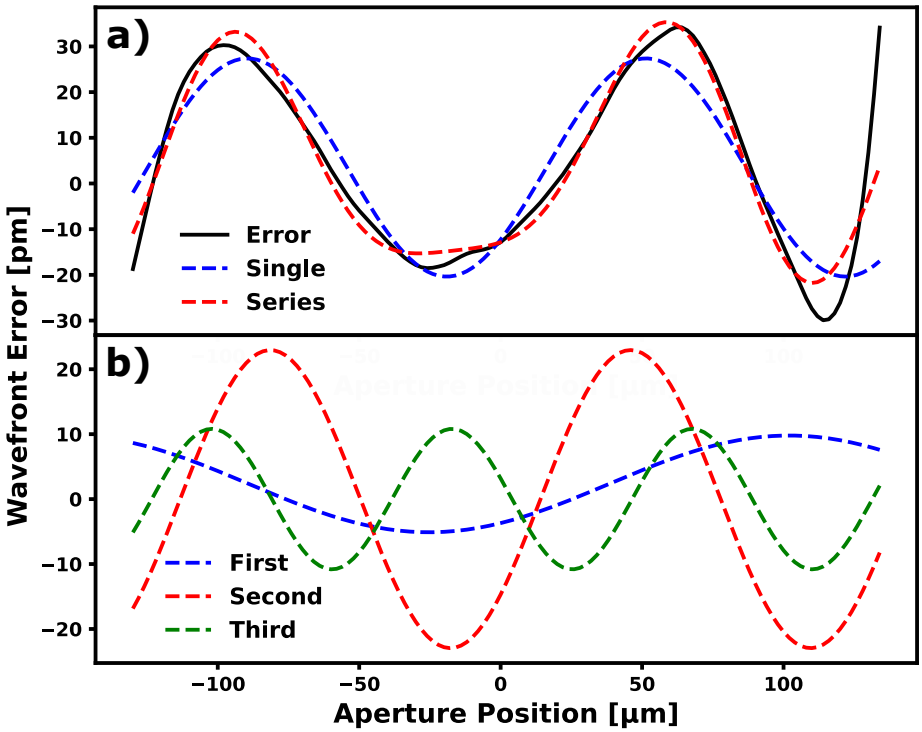


Figure 5.5: Decomposition of wavefront errors. (a) A simple sinusoidal and Fourier series with three terms fitting to the HKB wavefront error. (b) The corresponding Fourier terms use for estimating the HKB wavefront error in (a).

Kirkpatrick–Baez mirror system features a vertically focusing (VKB) and horizontal focusing (HKB) set of rhodium coated elliptical mirrors designed to work at 3 mrad grazing incident angle. Both mirrors have a 270 µm aperture and 125 mm horizontal and 235 mm vertical focal length, respectively. Measurements were performed at 18 keV for both mirrors and additionally at 15 keV for the HKB mirror.

Two adaptable structure series were mounted on separate goniometer stages[4] with all three translation and rotational degrees of freedom. Each series consisted of 46 sinusoidal profiles of 750 µm aperture, with periods ranging from 40 µm to 360 µm and an amplitude of 40 µm. This allows for a large range of wavefront error periods as well as a variable correction amplitude between 0 pm and 32 pm at 18 keV and between 0 pm and 45 pm at 15 keV. For the Kirkpatrick–Baez mirror system, the adaptable structures were first mounted vertically to correct the VKB mirror and then reorientated perpendicularly to correct the HKB mirror. A precision fabricated

[4]Later structure iterations as used in section 5.4 feature two series close to one another mounted on the same goniometer stage and used the structure pitch to vary the correction amplitude.

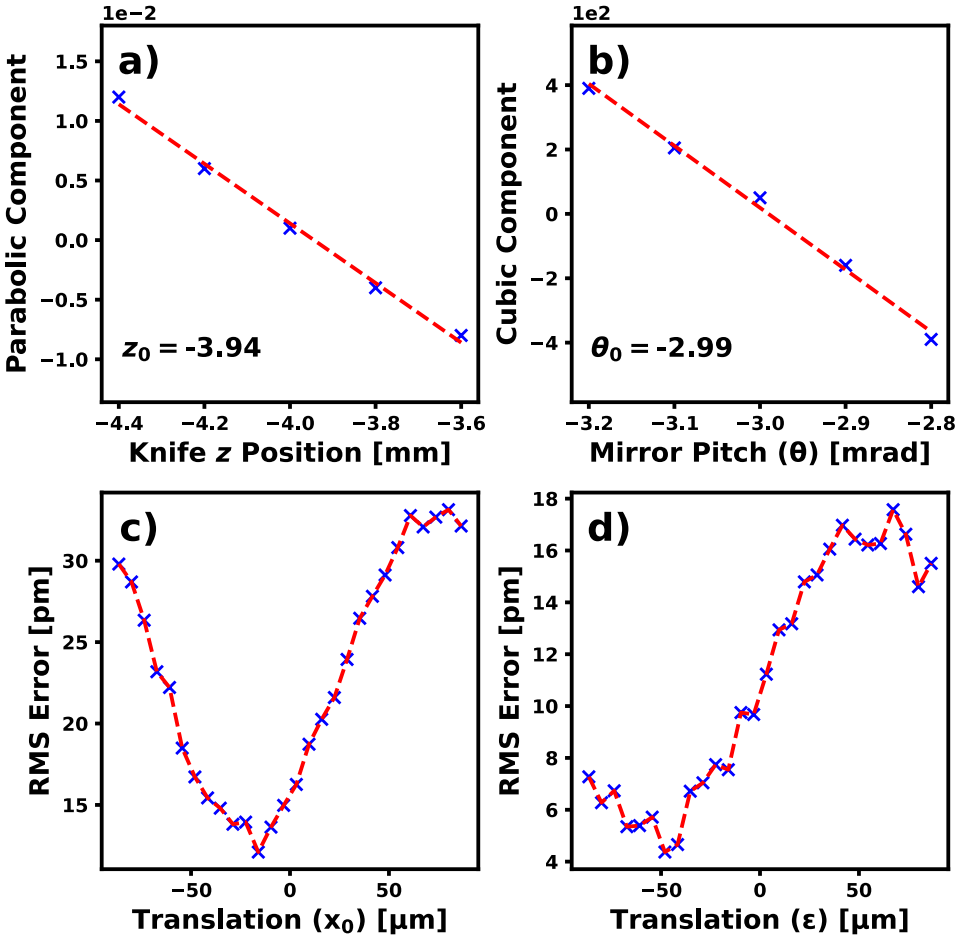


Figure 5.6: Alignment plots for the knife edge, HKB mirror and adaptable structures. (a) Parabolic component of the wavefront as a function of knife edge longitudinal position, the focus is located at z_0. (b) Cubic component of the wavefront error as a function of the mirror pitch angle, the aligned pitch is at θ_0. (c) Wavefront RMS error as a function of the adaptable structures common translational offset x_0. (d) Wavefront RMS error as a function of the adaptable structures differential translational offset ε

gold knife edge was mounted on a piezo translation stage close to the focal plane. To measure the wavefront error, the knife edge technique described in section 5.2 was used. Intensities were recorded by a Photonic Science CCD pixelated detector with a 6.5 µm pixel size 1360 px (h) × 1040 px (v) field of view, mounted 545 mm downstream of the focus. The wavefront RMS error was calculated according to Eq. (4.2) and used as the figure of merit for optimising the correction.

The SU-8 planar CRLs and Kirkpatrick–Baez mirror were first coarsely aligned by minimising the focal spot size and then further finely aligned using the knife edge scanning technique. The knife edge technique is most accurate when performed at

the focal plane; otherwise an additional parabolic term is included in the wavefront error, which must be subtracted [250]. The parabolic component is linearly correlated with the displacement from the focal plane thus a few scans at different positions in steps of 0.2 mm along the optical axis can be used to accurately find the focal plane, as shown in Fig. 5.6a. The most significant alignment axis of the optics is the pitch angle, which adds a cubic term to the wavefront error when misaligned [26]. This again correlates linearly so can be minimised by scanning each of the mirror's pitch angles in steps of 0.1 mrad, as shown in Fig. 5.6b. Adjusting the pitch angle also changes the longitudinal focal position [27], so a few iterations between longitudinal position alignment and optic pitch optimisation are performed.

It's worth noting the optimised pitch position may not necessarily produce the smallest focal spot but is instead used to isolate the wavefront error originating from fabrications aberrations and ensure the repeatability of the measurements. After alignment of the optic and knife edge, the measured wavefront error was then analyzed via a Fourier decomposition using Eq. (5.7) shown in Fig. 5.5. This was used to select the corrector period that would give the greatest RMS wavefront error reduction. The adaptable structures are inserted and coarsely aligned using direct beam and fiducial makers at the ends of the series, similar to how planar CRL lenses are aligned. Knife edge scans are performed as a function of the RMS wavefront error, with two types of knife edge scans used to finely align the adaptable structures according to Eq. (5.6). Mutual translation of both structures simultaneously changes the phase offset or x_0 in Eq. (5.6), and translation of a single series changes the differential offset between the two structures or ε in Eq. (5.6).

The structures are first referenced by finding the ε position where both series are completely out of phase such that there is no effect on the wavefront. At this position, a small offset is added which generates a small amplitude modulation of the wavefront and then x_0 is optimised by performing the simultaneous structure translation scan in steps of 5 µm as shown in Fig. 5.6c. At the minimal RMS value, a

Optic	X-ray Energy	Focal Length	Period (Λ)	Uncorrected RMS	Corrected RMS	Reduction Factor
Lens 1	15 keV	1051 mm	123 µm	4.0 pm	0.6 pm	7.0
Lens 2	15 keV	655 mm	96 µm	8.4 pm	1.3 pm	6.5
HKB	15 keV	125 mm	173 µm	14.2 pm	4.0 pm	3.6
HKB	18 keV	125 mm	173 µm	13.6 pm	4.5 pm	3.0
VKB	18 keV	235 mm	157 µm	2.9 pm	1.0 pm	2.9

Table 5.1: Measurement summary of wavefront correction using the adaptable refractive correctors for various aberrated optics and energies [250].

single series translation scan is performed in steps of 5 µm, and the optimum position is again found at the minimal RMS value as shown in Fig. 5.6d. The process is then repeated a few times iteratively with finer step sizes. This was performed for all optics, and the final results are presented in the next section. After correction, it's usually necessary to readjust both the knife edge longitudinal position and the optic pitch angle using the same method as outlined previously. The knife edge, HKB mirror and structure alignment plots used during an experimental session are shown in Fig. 5.6.

5.3.3 Results & discussion

The results with (blue line) and without (red line) the adaptable structures after the structure optimisation are displayed in Fig. 5.7, and summarised in the Table. 5.1. As can be seen, there is a significant reduction in the wavefront error in all cases. For the HKB and VKB mirrors, the wavefront error was reduced by a factor of about 3 and for the lenses by a factor of about 7 to leave residual RMS errors of between 0.6 pm and 4.5 pm. Furthermore, the two measurements on the HKB mirror at X-ray energies of 15 keV and 18 keV show very similar wavefront errors before correction. To achieve the optimum correction, the same period Λ structures were used, but different structure amplitudes A were required in order to account for the energy dependence of the refraction. This then produced similar wavefront errors at the two energies after correction. After correction, all optic RMS values are small enough to be considered diffraction limited according to the Strehl ratio given

by Eq. (4.4). Little difference was observed between the uncorrected and corrected focal size due to the dominant source size contribution; however, simulations based on the corrected wavefront errors recover diffraction limited focal size profiles with increased central peak intensity and are presented in the paper [250].

Although the lenses saw the largest reduction factor, the HKB mirror would see the most realistic gains as this optic has the largest wavefront error and also the highest numerical aperture of the optics tested. The other optics already have RMS wavefront errors considered to be diffraction limited for the energies used, so the difference seen when used during a practical microscopy experiment would be minimal. For these initial measurements, a single adaptable structure set was used; however, multiple correctors could be used in parallel to allow for higher-order spatial periods to be corrected for and further reduce the wavefront error. Similarly, two sets of orthogonally mounted adaptable correctors would also allow the simultaneous correction of wavefront errors originating from transversely paired focusing optics such as a Kirkpatrick–Baez mirror system. This is presented in the next section with wavefront measurements performed using ptychography. As the energy changes, so will the amplitude of the correction; however, with the latest structure design, the wavefront amplitude can simply be retuned by changing the relative rotation. Therefore, the adaptable structures can be considered pseudo achromatic optics, valid over a small energy bandpass $\Delta E/E$, however large energy changes would require adaptable structures with a larger/smaller amplitude range.

5.4 Kirkpatrick–Baez mirror correction

Of the aberrated optics corrected using the adaptable structures in the previous section, the Kirkpatrick–Baez mirror system is of most interest due to the high numerical aperture of the horizontal mirror and therefore warrants further examination. Although one-dimensional wavefront correction was shown to work assuming Eq. (5.3), its direct confirmation using the knife edge technique in section 5.2 is difficult

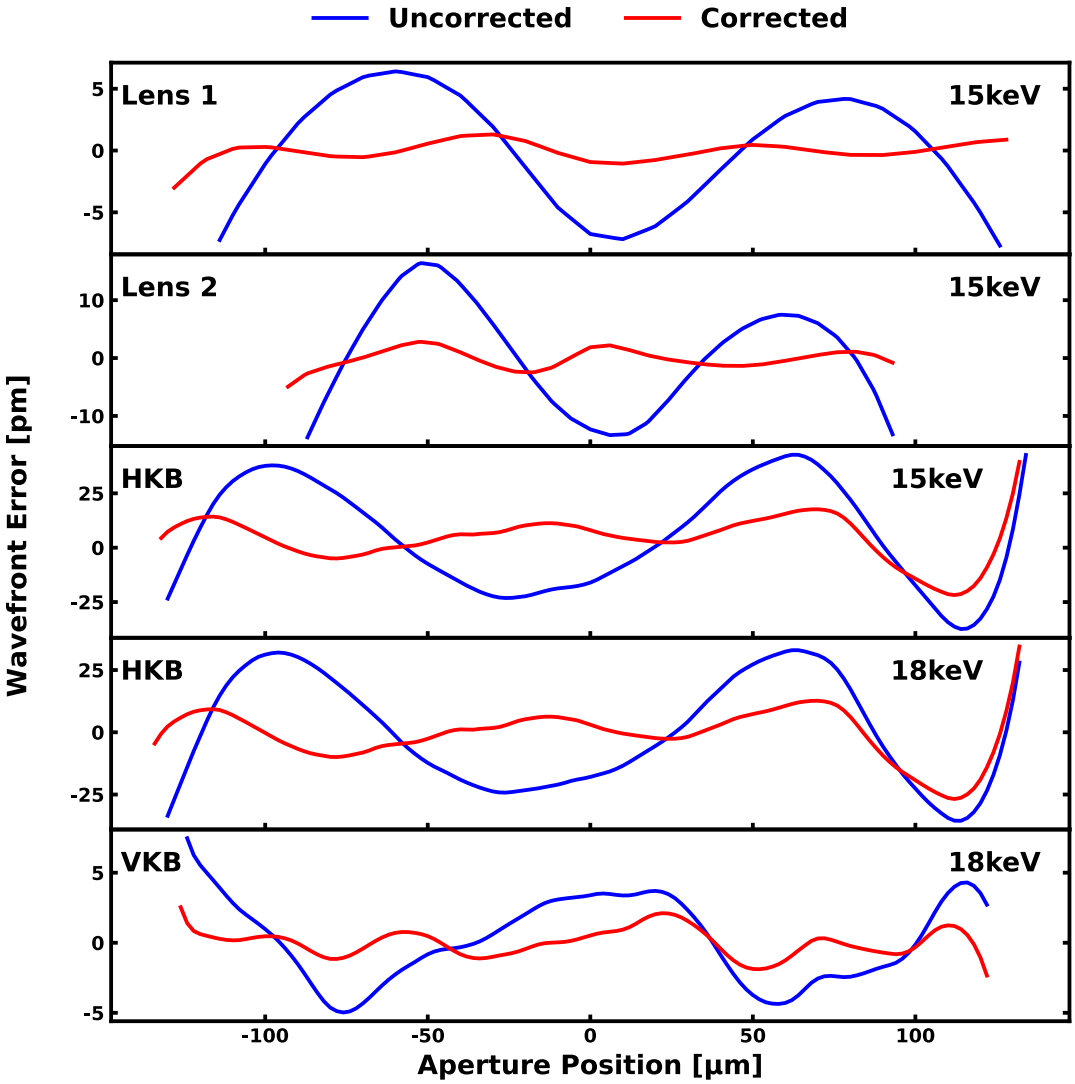


Figure 5.7: The wavefront error without (blue line) and with (red line) a single adaptable structure for different X-ray optics and energies. The wavefront error begins to diverge at the edges of the aperture due to low intensity [250].

to justify, given the technique is only sensitive to wavefront errors in the direction the edge scans. Scans could be repeated at a number of different polar angles as was shown in [245]; however, this drastically complicates the experimental setup and data post processing. An ideal solution comes from the use of ptychography metrology demonstrated earlier in chapter 4. In this section, we further investigate the effect of adaptable structures on the wavefront error and focusing performance of the Kirkpatrick–Baez mirror system. The two-dimensional error is first confirmed to decompose into horizontal and vertical components, which justify correction with planar corrective optics. The ptychographic technique allows the evaluation of the

focusing performance without the effect of the geometric source factor, i.e., for the fully coherent case. The recovered probe is additionally used to simulate the benefits of corrective optics on a typical scanning transmission X-ray microscopy experiment of gold nanoparticles. Furthermore, as the vertical focusing mirror employed is already of comparatively low figure error, a discussion follows of the situations which necessitate corrective optics.

5.4.1 Experimental setup

Experiments were performed at the B16 Test beamline at Diamond Light Source [69], a bending magnet beamline that provided an unfocused monochromatic X-ray beam. An X-ray energy of 12 keV was selected by a double crystal monochromator with an approximate $\Delta E/E \sim 10^{-4}$ energy bandpass to maximize longitudinal coherence. In order to maximise the available flux, no source slits were used to spatially filter the transverse coherence as in a normal ptychography experiment. This provided an approximate power of 10^8 photons/s with a beam size of 3.1 µm (h) × 2.3 µm (v) and 2.1 µm (h) × 1.6 µm (v) at the sample position for the uncorrected and corrected setups respectively. The beam was focused using an aberrated Kirkpatrick–Baez mirror system, which featured a vertically focusing (VKB) and horizontal focusing (HKB) set of rhodium coated elliptical mirrors designed to work at 3 mrad grazing incident angle. Both mirrors have a 270 µm aperture and 125 mm horizontal and 235 mm vertical focal lengths, respectively. These specifications were originally chosen to compensate for the source size asymmetry of the B16 beamline so that the focal size would be similar in both directions.

Two sets of adaptable correctors, one for each mirror, were positioned slightly upstream of the mirror system perpendicular to one another and slits were used to select an incident beam size matching the mirror aperture. An experimental schematic of the setup is shown in Fig. 5.8. The mirror and structure alignment was performed for each optic independently using the knife edge scanning method to measure the one-dimensional wavefront and as described in more detail in section

5.2. For the ptychography scan, a 3 µm thick gold Siemens star on a silicon nitride substrate was positioned slightly downstream of the focal plane on high-precision Attocube piezoelectric translational stages. Ptychography scans were performed by translating the sample through the beam and acquiring diffraction patterns at each position, which was done in a spiral manner to reduce raster artefacts [35]. Diffraction patterns were collected using a single-photon counting, third-generation Merlin Medipix detector with a pixel size of 55 µm (h) × 55 µm (v) and a pixel array of 512 px (h) × 512 px (v) positioned 238 mm downstream of the object.

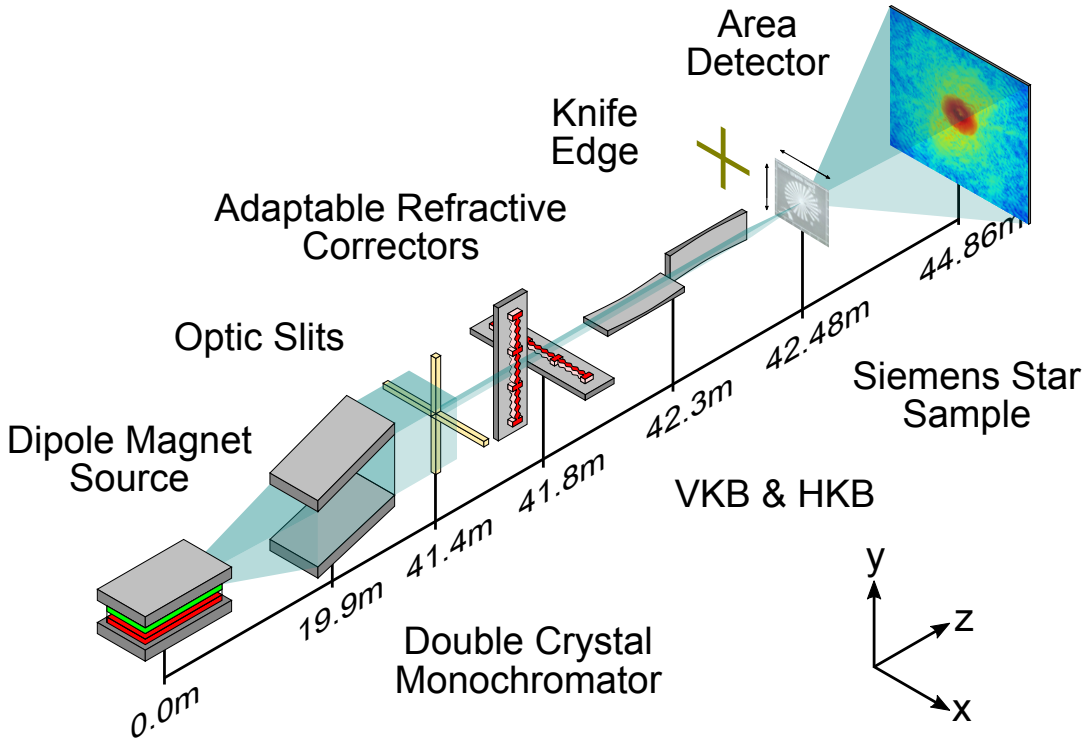


Figure 5.8: Schematic of the experimental setup and distances (not to scale) used for adaptable optics correction and ptychography wavefront measurements on the B16 Test beamline at the Diamond Light Source [259].

The scans were performed over an area of 24 µm × 24 µm with a 400 nm step between adjacent positions and 0.5 s exposure time which generated 7198 diffraction patterns. With this scanning geometry, the uncorrected overlap sampling factor given by Eq. (3.34) was found to be 87% (h) and 82% (v) and the corrected overlap sampling factor was 81% (h) and 75% (v). Both the uncorrected and corrected setups will have the same overall sampling ratio according to Eq. (3.35), which was

found to be $S_{\Pi} = 125$. A series of smaller area scans were performed at various defocused probe positions until high-quality reconstructions were obtained. Scans were then repeated with and without the adaptable structures inserted, which also included a slight adjustment of the individual HKB and VKB mirror pitch angles which is usually required after correction. Initial reconstructions were processed during the experimental session using the *ptypy* framework [189] and the difference map (DM) [35] reconstruction algorithm with a multi-modal probe [47]. This was performed on a reduced dataset and found to be most effective at finding an initial probe solution given only a simulated defocused ideal optic and an approximate power distribution.

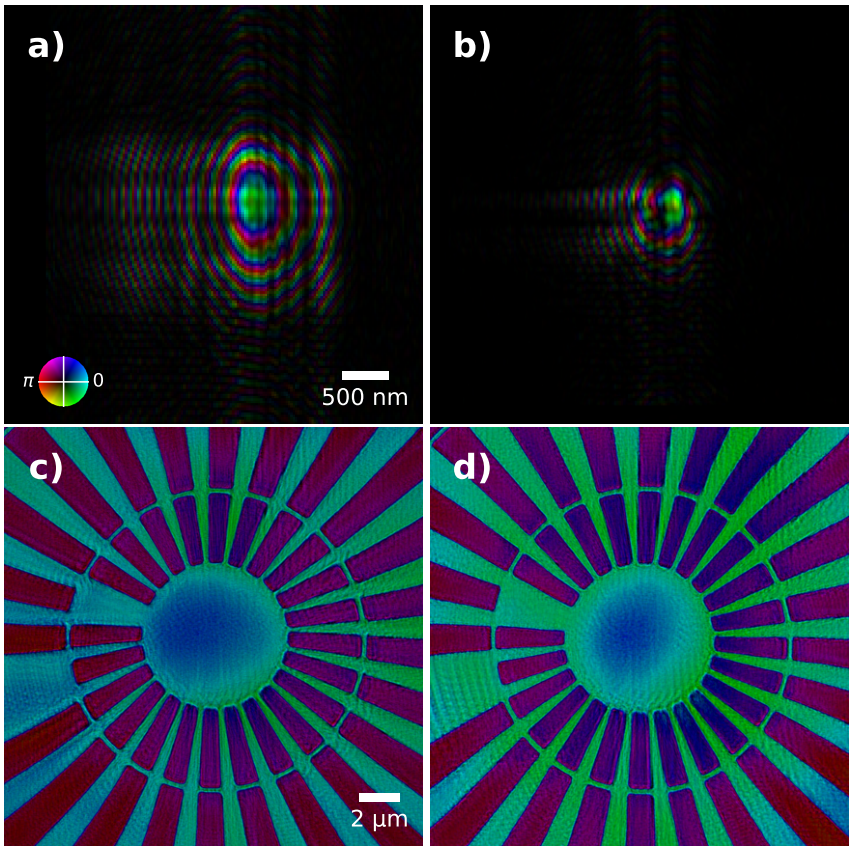


Figure 5.9: Ptychography reconstructions for the Kirkpatrick–Baez mirror correction. (a) Uncorrected & (b) corrected probes using a multi-modal sample [259]. (c) Uncorrected & (d) corrected sample using a multi-modal probe. The colour wheel in (a) encodes brightness & hue as the amplitude & phase respectively.

5.4.2 Ptychography reconstructions

Post experimental reconstructions were best achieved using a multi-modal implementation of the regularised ptychographic iterative engine (rPIE) [193] performed on the entire dataset. The diffraction patterns were cropped to a region of interest around the optical axis measuring $180\,\mathrm{px}\,(\mathrm{h}) \times 180\,\mathrm{px}\,(\mathrm{v})$, which included only statistically relevant counts and resulted in a 25 nm effective pixel size. Dead and hot detector pixels were also disregarded from the reconstruction by generating a detector mask based on the integrated diffraction data stack. Coherent probe and sample functions were recovered following the procedure outlined in section 4.5.3, where a multi-modal probe was used to reconstruct a single sample function, and a multi-modal sample was used to reconstruct a single probe function. The optic aperture and the Van Cittert-Zernike coherence length [238] were used with Eq. (3.30) to estimate that at least 38 modes would be required. Probe and sample modes were included until the relative modal power in the final mode was negligible, which in both cases occurred at 75 modes. As in Fig. 4.20b, the relative modal power spectrum of both the probe and sample agreed with one another and gave a slightly higher coherent fraction than previously due to the smaller mirror aperture.

The reconstructions started with a flat sample function and the previously reconstructed DM probe function; modes were then included as random permutations of the initial functions. The coherent results with and without the adaptable structures are shown in Fig. 5.9. Some artefacts towards the edge of the scan are noticeable; this could be because of the mirror stability, which is known to cause issues. Another possibility, which is observed in the coarse reconstruction is a variation in source intensity due to the long scan times. This could be corrected in the reconstruction processing using floating intensities; however, to date, it has not been implemented. The rPIE algorithm was then run for 500 iterations until the Fourier error converged to suitable minima. The power of the coherent probe and the dominant multi-modal probe mode was found to be approximately the same.

The coherent power was found to be 5.3×10^6 photons/s for the uncorrected mirror and 1.5×10^6 photons/s for the corrected mirror. The power reduction after correction occurs because of absorption within the support sections of the adaptable refractive structures, the thickness of which will be greatly reduced in future iterations due to better deep X-ray lithography fabrication methods.

5.4.3 Wavefront characterisation

Since the ptychographic technique recovers a complex scalar field, we can numerically propagate along the optical axis using the angular spectrum method from section 2.6.2 to analyse the focal properties and beam evolution. Before further processing, the power of the uncorrected and corrected probes was equalized to account for source intensity fluctuations and absorption of the structure supports. A small cubic component corresponding to a mirror pitch misalignment could not be optimised physically due to limitations using the knife edge technique was also fitted and subtracted.[5] Both probes were propagated along the optical axis, and beam caustics were generated by integrating the intensity volume along the horizontal and vertical directions. The results for this are shown in Fig. 5.10 and also label the defocused position where ptychography scans were performed, as well as the focal planes, defined as the plane which maximised peak intensity. It's evident the HKB mirror aberrations have a significant effect on the optics focusing performance; additionally there is significant astigmatism between both foci, which could be corrected for experimentally by translating the mirrors relative to one another.[6]

[5]The knife edge method requires a single focal point so the HKB focal point was chosen as the alignment reference, as it would see the greatest gain from corrective optics.

[6]This was not possible experimentally due to the mirror mounting in a custom enclosure limiting accessibility, an additional translation stage is planned to be included for future measurements.

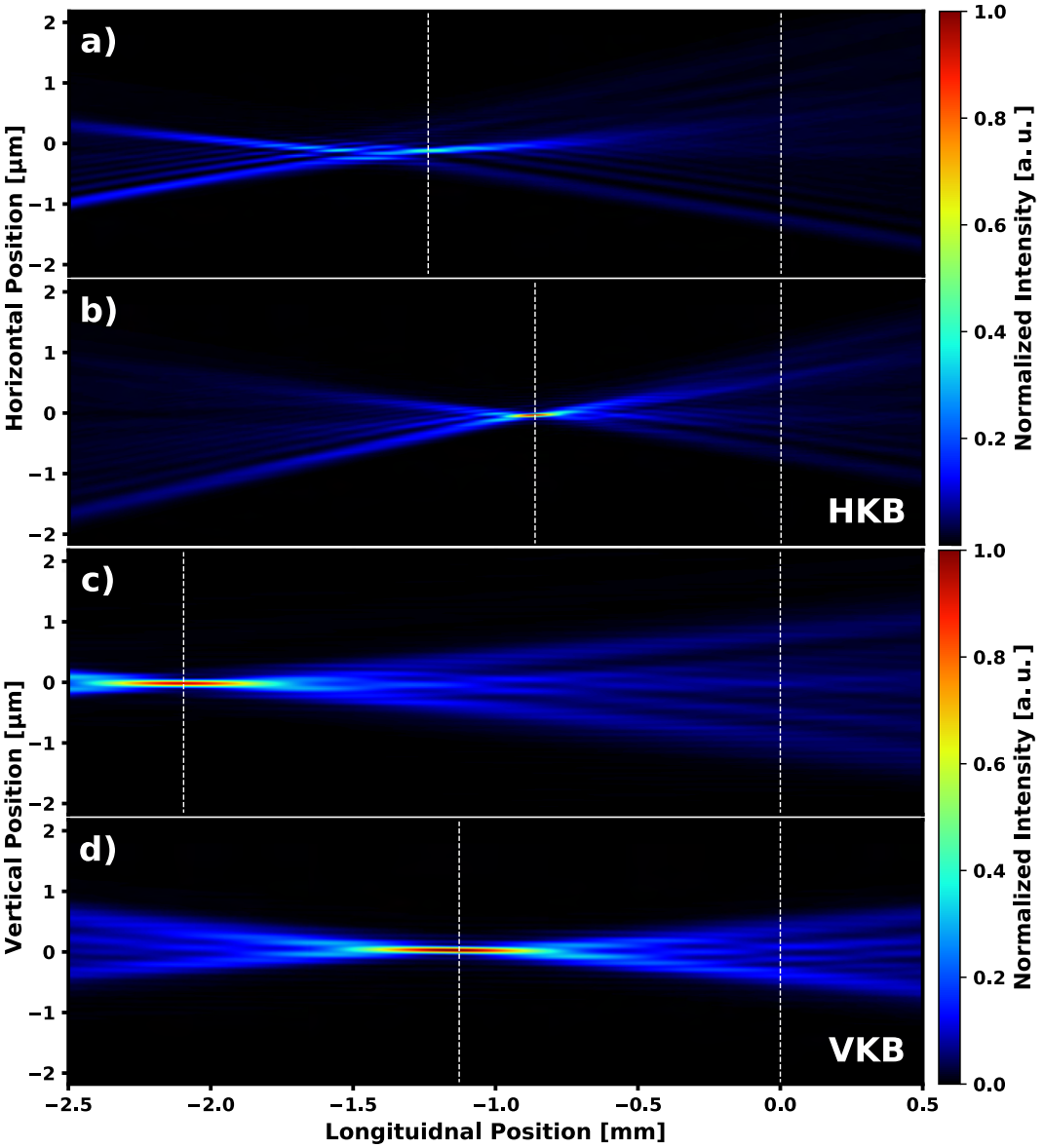


Figure 5.10: Beam caustics of the Kirkpatrick–Baez mirror correction. (a) Uncorrected and (b) corrected HKB caustic. (c) Uncorrected and (c) corrected VKB caustic [259]. The 0.0 mm dashed line indicates the sample plane and the other dashed lines correspond to the peak intensity focal position.

The beam caustic and focal intensity distribution only provide partial insight into the performance of an optic. To characterise completely the optical aberrations causing focal degradation and to measure the effect of corrective optics, the wavefront error at the optic plane must be calculated. We back propagated the probe wavefield upstream to each individual mirror position[7] for each of the uncor-

[7]The Kirkpatrick–Baez mirror is composed of two mirrors with different focal lengths and offset from one another, so propagation to the two different mirror planes is required.

rected and corrected probes and unwrapped the phase. At each mirror position, the parabolic phase profile of an ideal mirror was fitted and subtracted,

$$\Delta\varphi(x, y) = -k\left(\frac{x^2}{2f_x} + \frac{y^2}{2f_y}\right) \tag{5.8}$$

where k is the wave number and f_x and f_y are the effective horizontal and vertical focal lengths at that mirror position. The resulting phase error is easily converted to a path length (or wavefront) error using Eq. (4.1) and can be decomposed separately into horizontal and vertical contributions according to Eq. (5.3) by subtracting the mean error along the opposite axis. The full analysis generated four wavefront errors corresponding to the corrected and uncorrected HKB and the corrected and uncorrected VKB mirrors. These are displayed in Fig. 5.11.

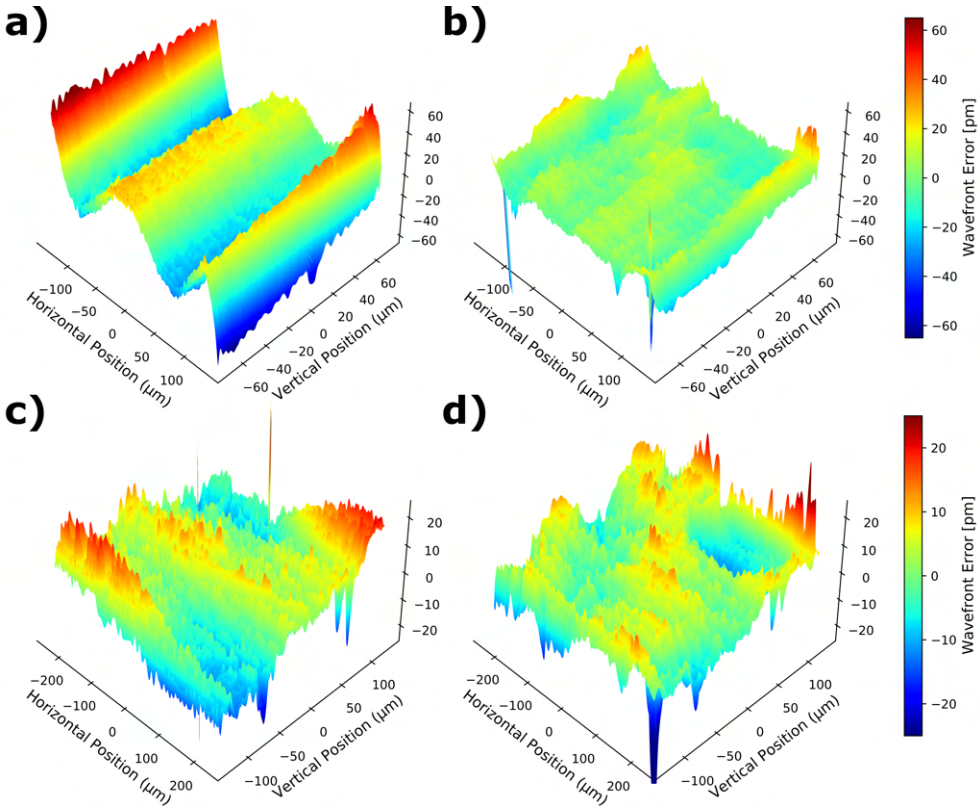


Figure 5.11: Two-dimensional wavefront error of the Kirkpatrick–Baez mirror correction. (a) Uncorrected and (b) corrected HKB mirror wavefront error. (c) Uncorrected and (d) corrected VKB mirror wavefront error [259].

From the two-dimensional wavefront errors, we can visually note a reduction in the error when refractive correctors are used. This is most apparent for the HKB mirror which features more prominent aberrations. To compare with results using the one-dimensional knife edge scanning technique, the two-dimensional wavefront errors were averaged along their respective planes. The profiles and RMS values agree well with one another and the previously reported results in section 5.3. These are shown in Fig. 5.12. The HKB RMS was reduced from 17.8 pm to 4.5 pm and the VKB RMS was reduced from 3.1 pm to 1.7 pm with the use of the corrective optics. The two-dimensional wavefront errors before correction clearly demonstrate the errors can be decomposed into their orthogonal components. This was confirmed by computing the standard deviation along the respective directions and found the HKB error standard deviation to be ±1.8 pm before and ±1.6 pm after correction; likewise, the VKB error standard deviation was found to be ±1.6 pm before and ±1.5 pm after correction.

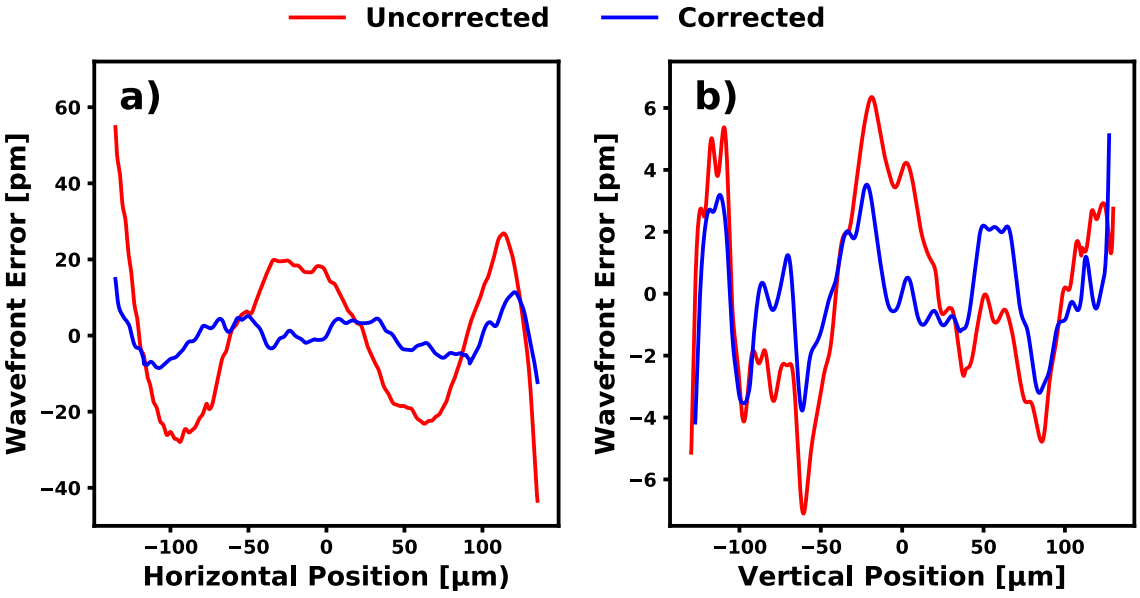


Figure 5.12: One-dimensional wavefront error of the Kirkpatrick–Baez mirror correction [259]. (a) Uncorrected & corrected HKB mirror wavefront error. (b) Uncorrected & corrected VKB mirror wavefront error.

Comparison of the standard deviation with the one-dimensional profiles in Fig. 5.12 we find the validity of decomposition diminishes as the wavefront error de-

creases. Therefore, the validity of the VKB RMS value after correction is questionable given the wavefront error decomposition no longer holds for this mirror however, the RMS error over the two-dimensional wavefront error is of similar value. This observation confirms that aberrations are most apparent along the length of the mirrors. The reconstructed pixel size of 25 nm was found to clearly resolve the focal intensity with at least 3 points on the central peak and gave values closely matching the diffraction limit; therefore, the probe resolution is maximized and around 50 nm. Given the same sampling period is maintained doing the propagation to the optic plane and wavefront processing, the resolution of the wavefronts is expected to be the same. The high spatial resolution of the ptychography technique is not only able to recover the larger slope error but also appears sensitive enough to measure higher frequency errors as well. This observation is important and would benefit from a dedicated study, ideally using a high-quality optic that featured little to no residual slope error, and comparison with another surface analysis technique, such as atomic force microscopy or Fizeau interferometry.

5.4.4 Focal profile results

The main aim of reducing the RMS wavefront error using corrective optics is to obtain a diffraction limited focal spot size and increase the central peak intensity. As was discussed in section 4.2.1 for small RMS wavefront errors $\sigma_{\mathrm{RMS}} \ll \lambda$ the complex wavefield exponent can be series expanded and results in a focal profile with a sharp diffraction limited peak and normalised intensity given by the Strehl equation Eq. (4.4). The lost intensity forms satellite peaks and a broader background outside this central peak which degrades signal-to-noise for scanning probe experiments. This is exacerbated by any source size contribution which will convolve with the focal PSF to broaden the central and satellite peaks further. In order to evaluate the focal properties, we first added a small parabolic term along the vertical direction to correct the astigmatism both with and without the correctors. This will negligibly change the numerical aperture of the optics and works on the same principle as how

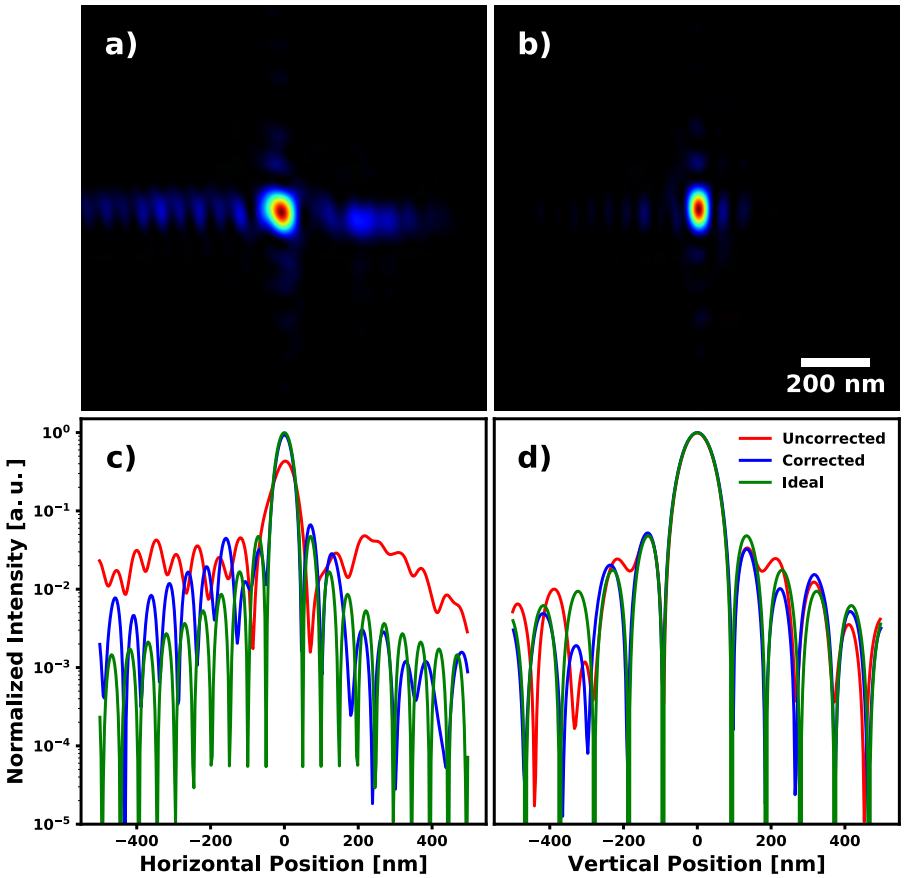


Figure 5.13: Focal plane intensity profiles of the Kirkpatrick–Baez mirror correction. (a) Uncorrected and (b) corrected two-dimensional focal intensity distribution. Uncorrected, corrected and ideal (c) HKB and (d) VKB one-dimensional focal intensity profiles on a logarithmic scale [259].

Alvarez-Loman lenses correct for astigmatism [258]. After this, the probes were back propagated to the focal plane, defined as the plane that maximised peak intensity, the intensity distribution of which is shown in Fig. 5.13a and Fig. 5.13b for the uncorrected and corrected mirror systems, respectively.

At the longitudinal focal position, horizontal and vertical line profiles were taken at the peak intensity. In order to evaluate the performance of each mirror separately, the power under each profile was then equalized. Gaussians were fitted and found the FWHM focal size to be 60.4 nm (h) × 77.9 nm (v) before correction and 41.1 nm (h) × 79.5 nm (v) after correction. To compare with the ideal case, we simulated the HKB and VKB mirrors using an ideal thin lens with the same aperture, focal length and incident beam flux. This gave a diffraction limited focal size of 41.7 nm (h) ×

78.5 nm (v) which also agrees well with the theoretically predicted value given by Eq. (2.28), as well as those recovered from the measured results after correction. The Strehl ratio improved from 0.43 to 0.94 for the HKB mirror and from 0.98 to 0.99 for the VKB mirror. These agree with the Strehl ratios predicted according to Eq. (4.4), and using the wavefront error RMS values found previously means both optics can be considered diffraction limited. The one-dimensional focal profile results are displayed in Fig. 5.13c and Fig. 5.13d. The HKB correction provides the majority of peak intensity gain and horizontal focal size reduction, while the VKB sees only a very slight increase in peak intensity as it can be considered diffraction limited prior to correction. The inclusion of any corrective optics for the VKB will reduce peak intensity gain due to absorption. Therefore adaptable refractive structures are most suited to correcting highly aberrated optics.

5.4.5 Simulated scanning microscopy

The satellite intensity peaks and higher background noise ultimately degrade the full field and scanning transmission microscopy (STXM) techniques that use focusing optics, such as X-ray fluorescence (XRF) imaging. Unfortunately, the large source size on the B16 Test beamline dominates the focal size contribution and makes a comparative sample study with and without the corrective optics very difficult. The same setup has been previously attempted on the I13-1 high coherence beamline at Diamond Light Source, where the flux is much greater and the source demagnification factor negligible. However, the optical bench and mirror mounting stability were unsuitable for nanometer focusing, with a clear vibrational instability of the focus occurring due to instability which became the primary source of focal degradation. Instead, a simulated XRF experiment of gold nanoparticles using the single and multi-modal probes from ptychography is presented. The simulated sample consists of randomly oriented gold nanocubes around 250 nm in size deposited on a silicon nitride substrate and positioned at the focus.

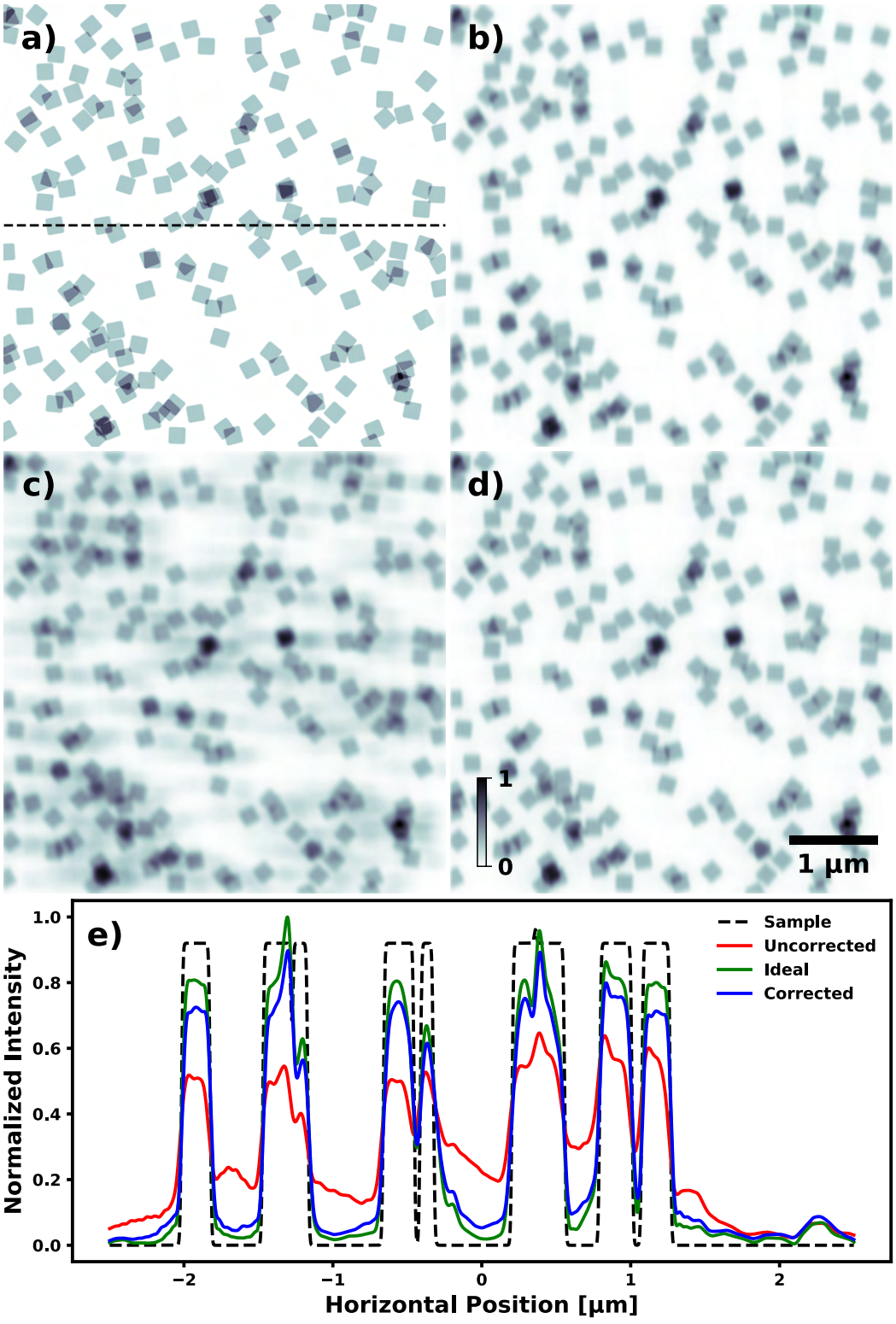


Figure 5.14: Coherent XRF simulation with gold nanocubes for the Kirkpatrick–Baez mirror correction [259]. Intensities corresponding to the (a) original sample, (b) ideal probe, (c) uncorrected mirror and (d) corrected mirror. (e) Line profiles indicated by the dashed white line in (a).

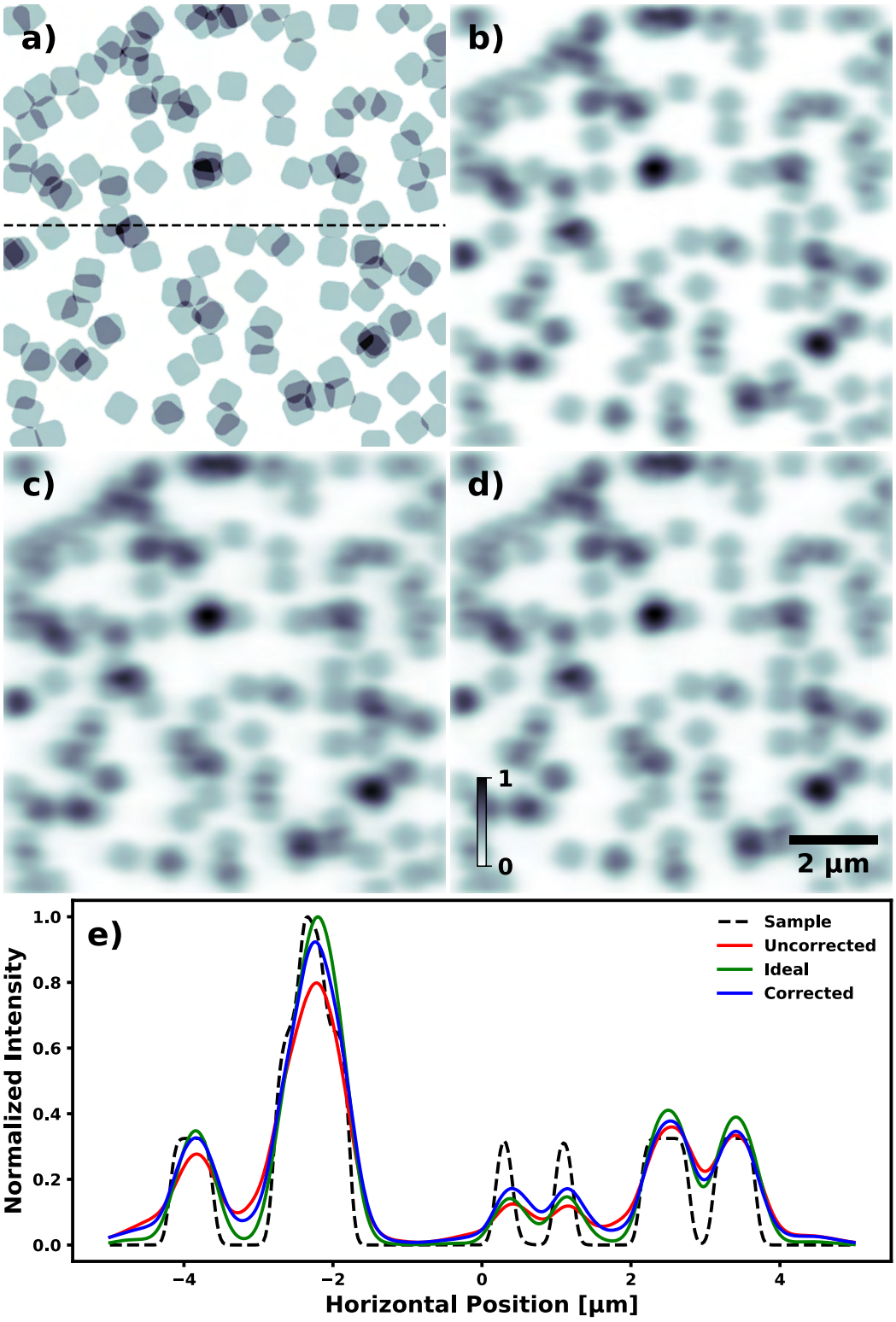


Figure 5.15: Partially coherent XRF simulation with gold nanocubes for the Kirkpatrick–Baez mirror correction [259]. Intensities corresponding to the (a) original sample, (b) ideal probe, (c) uncorrected mirror and (d) corrected mirror. (e) Line profiles indicated by the dashed white line in (a).

Subject to a sufficiently small scanning step, an imaging experiment is simply a convolution of the sample transmission with the point spread function or focal intensity of the optical setup. The results for the single, coherent probe simulation are shown in Fig. 5.14 for the original sample, ideal, uncorrected and corrected probes and demonstrate clearly the benefit of using corrective optics with little difference between the ideal and corrected images. The line profiles in Fig. 5.14e demonstrate the corrected optics don't increase the spatial resolution dramatically but instead vastly improve the contrast of the resolvable sample features. The most benefit is observed from samples with spatial features close to the size of the diffraction limit. The multi-modal probe was also used with slightly larger 1 µm gold particles to simulate how the system would perform under partially coherent conditions as shown in Fig. 5.15. As can be seen, there is only minimal change when adaptable refractive structures are used owing to the large source size contribution.

5.5 Results & discussion

In summary, the use of corrective elements for X-ray optics has been discussed with a new class of dynamic X-ray wavefront correction using adaptable refractive structures being presented. This design evolved from custom correctors, which used bespoke refractive elements to correct X-ray optics; however, required a lot of experimental and fabrication time to achieve. The adaptable correctors are a set of generic elements that aim to correct the majority of wavefront error approximately. As the field of X-ray optics develops, it's envisioned that some method of correction will be required in order for optics to achieve their full diffraction limited potential. The main concluding points of this section are summarised below.

- In section 5.3, adaptable structures were used to correct one-dimensional planar CRLs and a Kirkpatrick–Baez mirror X-ray optics at various hard X-ray energies, achieving diffraction limited RMS values in all cases. The adaptable corrector system demonstrates a quick, dynamic and low cost method of X-

ray optic correction. Future endeavours will see the installation of elements on new and existing beamlines at Diamond Light Source as part of facility upgrades.

- Adaptable correctors can be combined in series to closely match the desired wavefront error. Although not necessary for any of the optics studied, the method using a Fourier series decomposition was established.

- Correction of the Kirkpatrick–Baez mirror was further studied in section 5.4 by employing a two-dimensional wavefront correction and measuring the complete wavefront error using the ptychography technique of section 4.5.3. This confirmed that prominent aberrations along the length of the mirror are separable and can be corrected independently using planar, one-dimensional elements. The results match the prior results found in section 5.3 using the knife edge technique and provide additional information in the form of the two-dimensional wavefront error at each mirror position.

- The validity of wavefront error decomposition into orthogonal components was shown to diminish as the RMS error decreased. High-frequency surface roughness/finish errors would require a different method of correction than the planar adaptable corrector system shown.

- A simulated scanning microscopy experiment of the corrective optics on nanoparticles in section 5.4.5 suggests the benefits of wavefront correction will be most effective for scanning regimes working close to the diffraction limit. The effectiveness of wavefront correction was similarly demonstrated for the multimodal probe representing the partially coherent case and shown to only influence the results minimally. With the development of smaller, coherent sources at fourth generation facilities, either optics with low RMS error or aberrated optics with some method or correction will be required in order to achieve diffraction limited focal sizes.

6 Applications to nanomaterials

6.1 Branched gold microflower ptychography

The field of nanomaterials and specifically nanoparticles has become an active area of research in the past decade due to the novel properties they exhibit in comparison to their bulk counterparts. Functionalised particles have found applications in a wide variety of fields including drug delivery & medicine [260], catalysis [261], and the electronics industry [262] to name a few. The size, shape and elemental composition of particles are crucial features that affect the electronic, optical, magnetic and chemical properties of the material, and can be used to fine-tune desired properties [263, 264]. Nanoparticles are broadly categorised based on their chemical composition, but we will restrict our discussion to metallic nanoparticles. These are well-known to possess enhanced localised surface plasmon resonance[1] (SPR) characteristics and produce unique optoelectrical properties [265]. Gold nanoparticles are one of the most historically studied [266, 267] owing to their ease of synthesis and stable, non-toxic nature. Their wide biocompatibility and large surface plasmon resonance range have seen them widely employed for drug delivery [268], biological imaging [269], and effective cancer treatment [270].

Structural information about the crystallinity and phase is commonly characterised using X-ray diffraction (XRD) [271], which at small angles can also provide information about the average size distribution. The elemental composition is typically measured with energy dispersive X-ray spectroscopy (EDX) [272] using field emission scanning electron microscopes (SEM). Finally, the size, shape and morphology are measured using either scanning (SEM) or transmission (TEM) electron microscopes or atomic force microscopy (AFM) [272]. However, these methods suffer from many drawbacks, including sample thickness limitations, sensitivity to

[1] The collective oscillation of conductive electrons within the metal nanoparticle that are excited by incident photons. These produce a non-radiative electromagnetic surface wave that propagates in a direction parallel to the material surface.

electrons, difficult preparation methods, vacuum compatibility, only providing surface information and difficulty in performing *in situ* measurements to name a few. Although of lower spatial resolution, X-ray ptychography and other CDI techniques significantly ease the previously noted drawbacks. They've broadened the possibilities of dynamically studying the localised interactions of nanoparticles within materials, such as the biological effects of nanoparticles within cells [273, 274]. Their small feature range and strong interaction with X-rays mean metallic nanoparticles are useful, representative test samples that have been previously reported to assess ptychography technique developments [38, 275, 276].

6.1.1 Sample preparation

In addition to the conventional spherical morphology, gold micro/nano materials of rod, polyhedral, branched or dendritic structures have previously been reported [277]. Gold structures with three-dimensional (3D) architectures, such as flowers, urchins and stars with a large number of crystal surfaces, high surface-to-volume ratio, multiple corners and sharp tips exhibit exceptional surface plasmon resonance (SPR), surface enhanced Raman spectroscopic (SERS) and photothermal capabilities. Most colloidal synthetic methods for obtaining gold nanoparticles follow a strategy whereby solvated gold salt is reduced in the presence of surface capping ligands which prevent aggregation of particles by electrostatic and/or physical repulsion [267]. The size and morphology of the structure are greatly affected by reaction conditions as well as reagents such as the gold salts, reaction medium, reducing agents, surfactants etc. A number of methodologies such as electrodeposition [278], seedless approach, seed mediated growth and microbial synthesis [279] have been previously reported for the synthesis of gold microflowers. Similarly, the use of toxic reagents such as 1-hexadecyl trimethylammonium chloride (CTAC)4, cetyltrimethylammonium bromide (CTAB)5, silver nitrate (AgNO3)5, hydrogen peroxide (H2O2)6, poly(vinyl pyrrolodione) (PVP)1, hydroxylamine hydrochloride (NH2OH)7 have been widely used for the synthesis of gold microflowers.

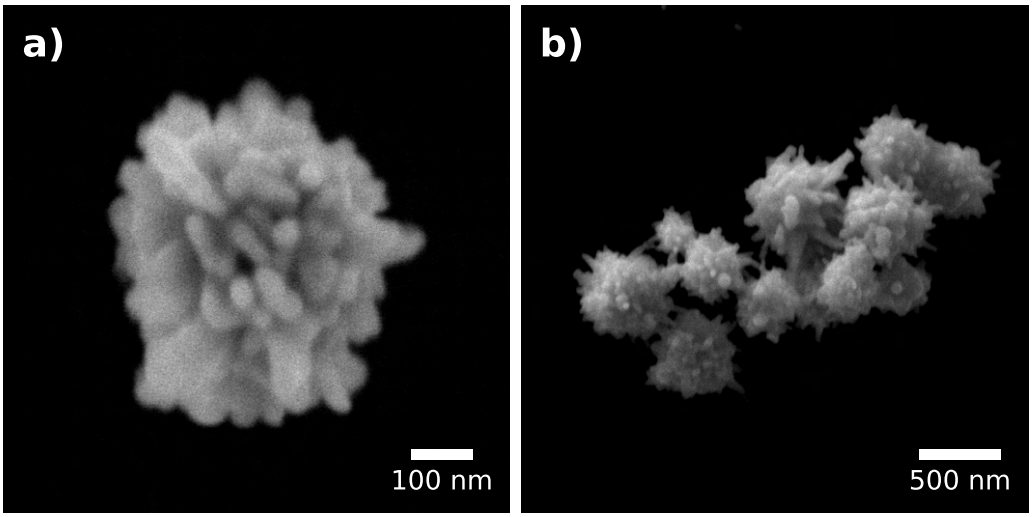


Figure 6.1: SEM images of gold microflowers (a) a single particle and (b) cluster of many particles which form as a droplet of the sample drys.

In order to advocate biocompatibility and ease of synthesis, a novel method of producing gold microflowers using an aqueous reduction methodology with ascorbic acid has been developed by my colleague Dr. Sisini Sasidharan at the Department of Engineering Science, University of Oxford [280]. For characterisation, colloidal droplets containing samples dispersed in water were deposited on aluminium foil and allowed to dry before imaging. The shape and morphology were characterised using SEM imaging with the size of single particles found to be around $500\,\text{nm} - 700\,\text{nm}$ with sharp tips ranging from $50\,\text{nm} - 80\,\text{nm}$. The results from this are displayed in Fig. 6.1 for a single particle as well as a cluster which naturally forms as the droplet drys. The elemental composition was confirmed to be that of gold using EDX analysis in the same microscope (not shown). Within the scope of the current section, two samples were prepared, the first was simply the deposited gold microflowers as previously described. Secondly, with the advent of micro/nano materials for various biological applications, it becomes increasingly important to study their presence and biodistribution within tissues. As the use of real biological tissues is difficult due to issues pertaining to accessibility and ethics, agarose hydrogels have been widely used as phantoms for mimicking tissues such as the liver, heart, brain etc. In the current study, gold microflowers were mixed with a 2% agarose solution to

form impregnated hydrogels such that their biodistribution could be studied.

6.1.2 High resolution partially coherent ptychography

As was previously shown in section 4.5.1 and section 4.5.3 the spatial imaging resolution attained using X-ray ptychography on B16, even with low levels of coherence, is much better than offered with the current availability of optics [69]. However, these values should be taken with caution in mind as is explained. The experiments were performed using a gold Siemens star test object which is commonly used for accessing the resolving capabilities of an optical setup. Firstly, the smallest measurable feature size is only 1 µm which means we cannot visually distinguish the resolution. Secondly, the gold thickness is around 3 µm and the resolving capability in ptychography is fundamentally limited by the largest scattering angle with detectable signal [205, p. 845].

This inertly means thicker objects will produce more signal at higher angles and as the sample size decreases so too will this scattering signal which is what usually becomes the limiting factor of hard X-ray ptychography. The gold Siemens star was most appropriate for the previous sections where the properties of the probe were the feature of interest but cannot be automatically assumed to be true for any sample imaged under the same conditions. To more accurately assess the realistic resolving capabilities of the B16 beamline, we will image the previously discussed gold microflowers under similar conditions to the aforementioned experiments. The results will be compared with similar measurements performed with higher coherence X-ray ptychography shown in section 6.1.3.

6.1.2.1 Experimental data collection

Experiments were performed at the B16 Test beamline at Diamond Light Source [69], a bending magnet beamline that provided an unfocused monochromatic X-ray beam. An X-ray energy of 8 keV was selected by a double crystal monochromator with an approximate $\Delta E/E \sim 10^{-4}$ energy bandpass to maximise longitudinal

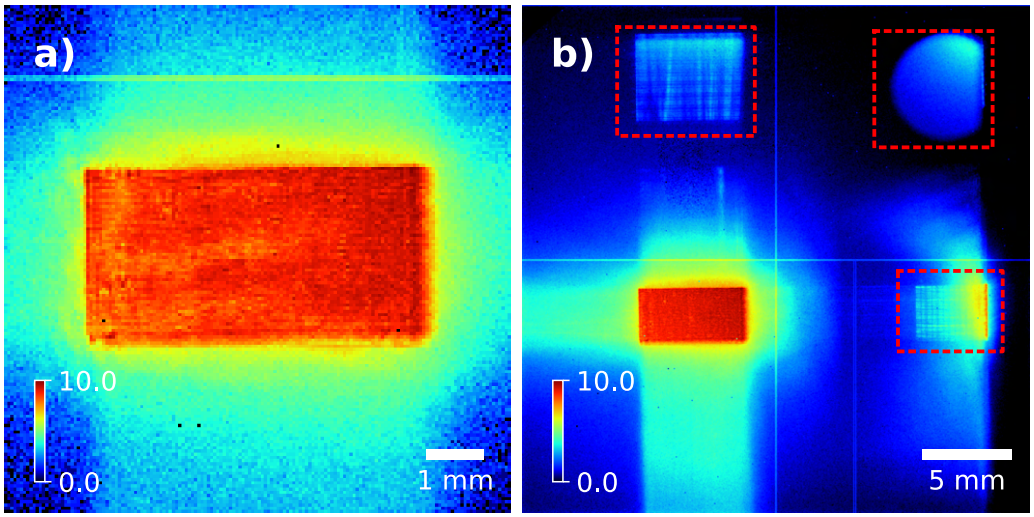


Figure 6.2: Diffraction intensity of gold microflowers for high-resolution imaging with partially coherent ptychography. (a) Single frame acquired for 5 s cropped to the field of view used in ptychography 160 px (h) × 160 px (v). (b) Full field of view integrated over 4446 frames. Red dashed boxes label direct beam and both images are plotted on $\log_{10}$ scale.

coherence. In order to maximise the available flux, at no point were source slits used to spatially filter the transverse coherence as in normal ptychography experiments. The beam was focused by using a Kirkpatrick–Baez mirror system which featured a 270 µm aperture and 125 mm horizontal and 235 mm vertical focal lengths. This provided a beam size of approximately 2.8 µm (h) × 2.7 µm (v) at the sample position. The experimental setup is very similar to that shown in Fig. 5.8 with the omission of the adaptable refractive structures. After the optics were aligned using the knife edge technique described in section 5.2, the previously used gold Siemens star was mounted first and aligned close to the focus using a visible microscope mounted above the setup. Initial ptychography scans were performed to find the optimum longitudinal sample position and produce a high-quality probe reconstruction that could be used for the later measurements with the gold microflowers.

The sample was prepared using the gold microflowers described in section 6.1.1, a single drop of the colloidal gold in water was deposited onto a holey carbon copper TEM grid and allowed to dry. It was imaged using SEM to find areas of interest and platinum markers were deposited[2] using focused ion beam (FIB). The TEM

[2]Due to the holey carbon substrate, large platinum markers were not possible as a very low

grid was mounted the same way as the Siemens star on aluminium washers such that the samples could be placed at approximately the same longitudinal position. Direct beam and a Photonics Science Mini FDI area detector were used to attempt to find features of interest; however, the 6.5 µm detector pixel size was too large to resolve any of the platinum markers.

Instead, a quadrant of interest was identified by scanning transmission X-ray microscopy (STXM), where a number of clusters and single particles were found. These were chosen as strongly scattering objects which are present in the scan field of view to help with reconstruction convergence [59]. Ptychography scans were performed in a spiral manner to avoid artefacts [35] over an area of 10 µm (h) × 10 µm (v) with a 150 nm step size between adjacent positions, which generated 4446 diffraction patterns. These were acquired for 5 s each by a single-photon counting Merlin Medipix detector with a 55 µm × 55 µm pixel size and a 512 px × 512 px field of view positioned 2.5202 m downstream of the sample. With this scanning geometry, the overlap sampling factor given by Eq. (3.34) was found to be 94% and the overall sampling ratio according to Eq. (3.35) was found to be $S_{\Pi} = 2241$.

6.1.2.2 Ptychography reconstructions

The diffraction patterns were cropped to a region of interest around the optical axis measuring 160 px × 160 px, which included only statistically relevant counts and resulted in a 44 nm effective pixel size. Dead and hot detector pixels were also disregarded from the reconstruction by generating a detector mask based on the integrated diffraction data stack. Initial reconstructions were performed using the rPIE algorithm previously described in section 4.5.3 with 75 probe modes; however, the reconstructions were of particularly poor quality even with parameter tuning. Higher quality reconstructions were achieved using a weak object reconstruction strategy [281], including 250 iterations of the difference map (DM) followed by 250 iterations of maximum likelihood (ML) refinement, both implemented in the

FIB current had to be used, which increased the deposition times considerably.

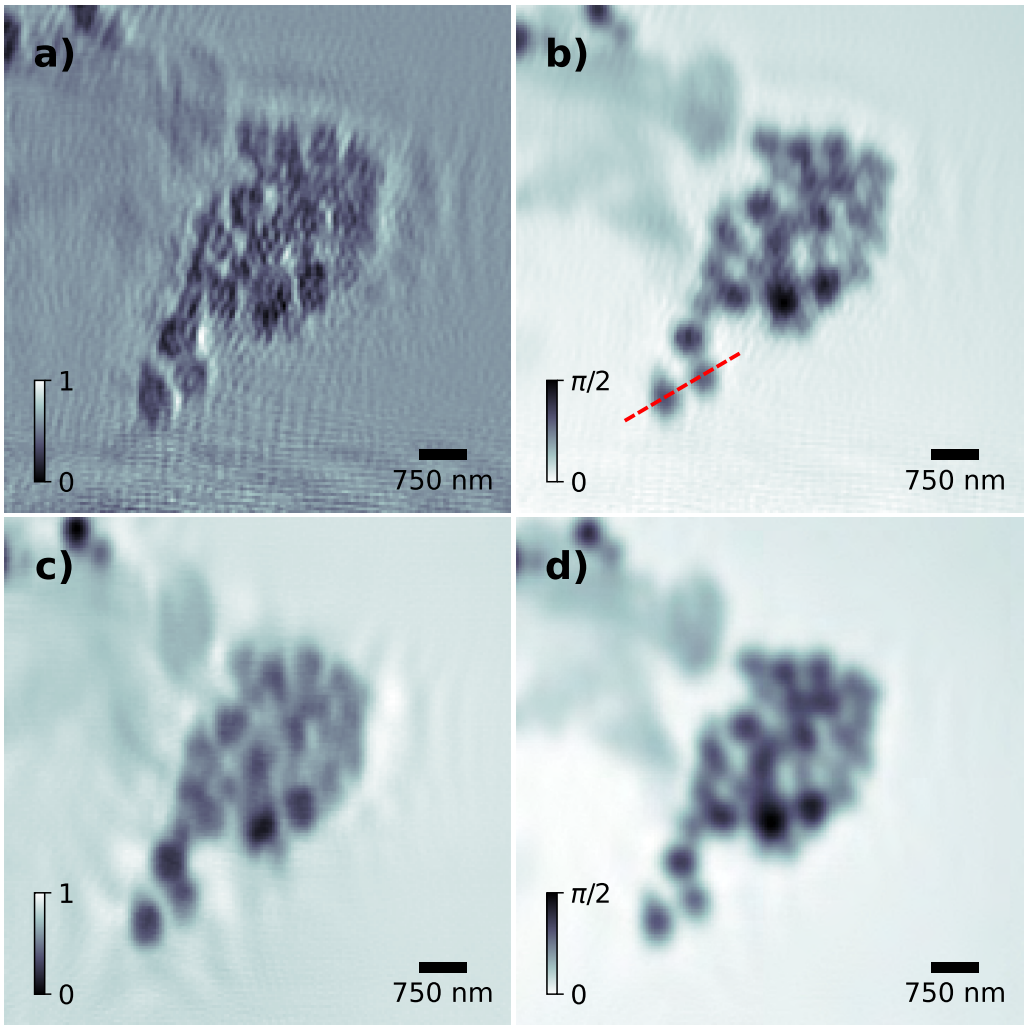


Figure 6.3: Partially coherent ptychography sample reconstructions of gold microflowers. (a) Modulus and (b) phase of the multi-modal reconstruction. (c) Modulus and (d) phase of the coherent reconstruction. The dashed red line denotes where line profiles were taken for resolution analysis in Fig. 6.5a.

ptycho shelves software [219]. From the coarse transmission plots, there is a lot of variable intensity between points, which the ML algorithm can account for in the reconstruction, unlike the simple rPIE implementation. Memory limitations using the *ptycho shelves* software restricts the crop size of the diffraction patterns and the number of modes that can be used.[3]

The effect of decoherence on the sample and probe was found by running two independent reconstructions, one using a multi-modal probe consisting of 35 modes and the other assuming a coherent probe consisting of a single mode. The recon-

[3]A reduced dataset with double the step size was also tested but found to degrade the reconstruction so the required memory could not be reduced that way either.

structed probe of the Siemens star was used to generate the initial probe for the gold microflower reconstructions and was found to almost match exactly, i.e. there was little difference between the Siemens star and gold microflower longitudinal positions. The sample modulus and phase for both reconstructions are shown in Fig. 6.3. There are more artefacts in the multi-modal reconstruction which is most likely due to mirror instability. This effect was similarly observed for reconstructions in section 5.4 and mirror instability has been measured on the beamline and found to occur on the tens of nanometer scale.[4] It would also explain why the more stable FZP and CRL optical setups see little to no noise in previous reconstructions (section 4.5.1) despite the fact they feature similar levels of decoherence but scan with much larger step sizes. This effect can be corrected in ptychography using orthogonal probe relation [187], which essentially reconstructs a unique probe for each scan position and is similar to how shot-to-shot variations are corrected for on XFELs performing ptychography [231]. In this instance however, the combination of the partial coherence originating from the source and the instability of the mirror would be too computationally demanding to correct for, although the sampling is likely high enough to account for it.

The corresponding single and multi-modal probe reconstructions are shown in Fig. 6.4 along with the multi-modal power spectrum shown in Fig. 6.5b. The normalized degree of coherence was found to be 17% using Eq. (4.11), which is largely in line with what's expected and comparable to the other previously performed experiments. As was found in section 5.4 the Kirkpatrick–Baez mirror possesses a relatively large astigmatism, combined with both mirrors having different defocusing strengths makes finding appropriate probe positions very difficult. The probe size at the sample was found to be around $2.8\,\mu\text{m}\,(\text{h}) \times 2.7\,\mu\text{m}\,(\text{v})$ and is the minimal size which maintained roughly the same horizontal and vertical sized beam. We can

[4]Focal size measurements performed on the I13 using the same mirror setup to assess the diffraction limited performance were rendered unusable due to this instability, its effect on the B16 beamline is much less due to the source demagnification factor.

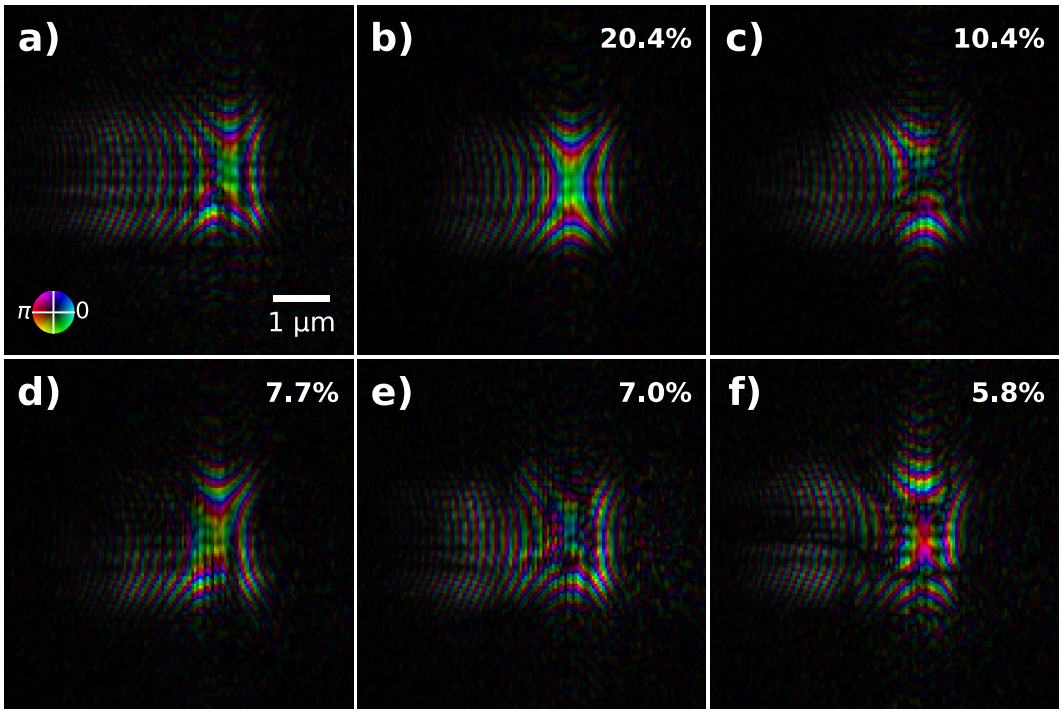


Figure 6.4: Partially coherent ptychography probe reconstructions of gold microflowers. (a) Assuming full coherence and a single mode. (b-f) Probe modes using a multi-modal approach, power is displayed in the top corner. The colour wheel in (a) encodes brightness & hue as the amplitude & phase respectively.

see from the phase distribution (and confirmed with beam caustic propagations) in Fig. 6.4 that the probe has opposite curvature in the horizontal & vertical directions meaning the sample is in-between the astigmatic foci i.e., downstream of one focus and upstream of the other. This is not ideal when trying to simulate the initial probe and also makes finding a probe with similar horizontal & vertical extent difficult. The total probe power was calculated for the multi-modal probe and found to be 1.2×10^5 photon/s, which is much lower than previously observed primarily, caused by air absorption at the lower energy. Due to experimental constraints, it was only possible to use a helium fly tube for half the distance between the sample and detector; this coupled with the lower energy, means we attenuate approximately 80% of the flux [282] from air absorption alone.

6.1.2.3 Spatial resolution analysis

The effect of partially coherent light on the reconstruction is visually observed in Fig. 6.3 to be similar to that of traditional X-ray microscopy and causes a blurring of the

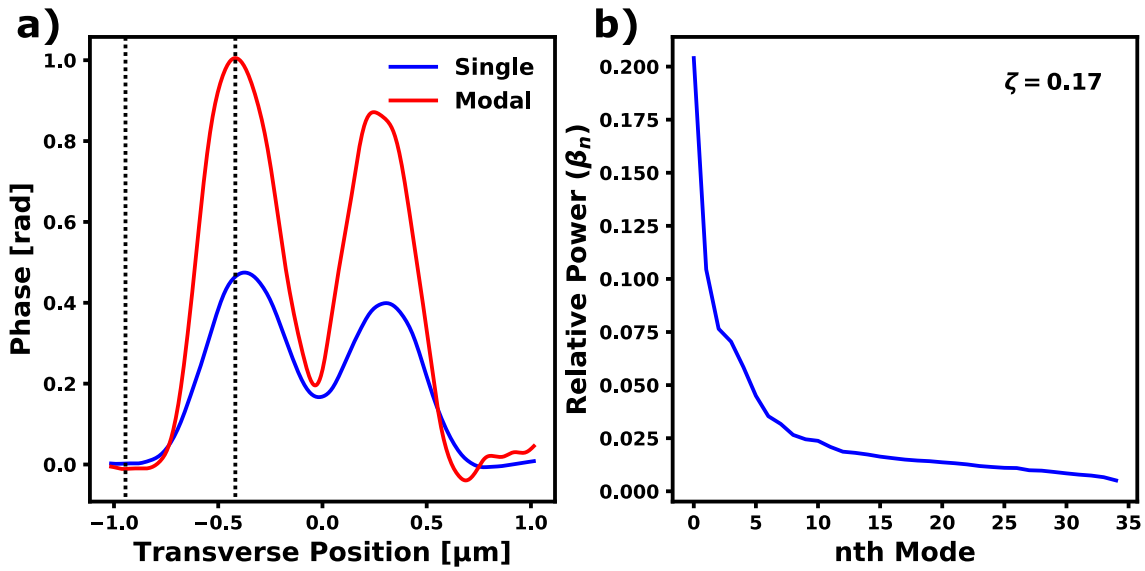


Figure 6.5: (a) Line profiles through the single and multi-modal phases shown in Fig. 6.3b by a red dashed line. Black dashed lines in (a) are where line profiles were taken for resolution evaluation. (b) Power spectrum of the multi-modal probe reconstruction, with ζ the normalized degree of coherence.

reconstructed modulus and phase by some point spread function (PSF). This is only expected to be valid for the case described here where the scan is highly oversampled by increasing the probe overlap ratio to compensate for the decoherence [210]. In many cases, it is expected the undersampling caused by the decoherence will simply result in a noisy, poor quality reconstruction or may not even reconstruct at all [47]. Line profiles taken through the phase of two particles indicated in Fig. 6.3b by the red dashed line are shown in Fig. 6.5a and clearly display different resolutions and phase shift values. A simple calculation of the phase shift induced by a gold nanoparticle of 500 nm thickness at 8 keV is around 0.967 rad, which is clearly much closer to the multi-modal probe values shown in Fig. 6.5a rather than the single probe. The resolution was estimated by differentiating the step profile displayed in Fig. 6.5a and fitting a Gaussian. This found the FWHM to be 180 nm for the multi-modal reconstruction and 300 nm for the single mode reconstruction, which means we gain a factor of 1.7 resolution using the multi-modal approach. Based on prior results, the experimental setup is almost certainly limiting the potential of the technique and this is discussed in the next section. A more universally accepted

resolution metric is the Fourier ring correlation which should ideally be applied here but was not due to the ptychography scan times.

6.1.2.4 Further improvements

The results of this study demonstrate like fly-scan ptychography [56, 58], if there is enough redundancy in the ptychography dataset, decoherence effects such as partially coherent light can be corrected. This adds the potential application of a new imaging technique available to the B16 beamline, which provides quantitative phase information and potentially higher resolving capabilities. It is also likely the current setup could be vastly improved, as although the oversampling ratio was $S_{\Pi} = 2241$ there are many artefacts in the sample reconstruction shown in Fig. 6.3. The current study was conducted in tandem with another beamline commissioning experiment which limited the use of optics, equipment and scan times. A future experiment solely dedicated to assessing the ptychography imaging performance on the B16 beamline is planned, and a number of adjustments will be made, the details of which and the reasoning behind are given below.

- **Optics:** The instability with the Kirkpatrick–Baez mirror is a major limitation and is typically why they are not used in ptychography setups. Additionally, the long exposure time means any instability during the acquisition would present as a further decoherence effect. In our case, the focal astigmatism also meant it was difficult to vary the beam size on the sample and model an initial probe. FZPs are much more stable and have shown high-quality reconstructions in previous sections 4.5.1. They also have the benefit of focusing inline, which makes alignment of the sample close to the focus straightforward unlike the mirror which focuses off-axis.

- **Detector:** Firstly, the use of a helium fly tube along the complete length of the sample to detector length will increase the recorded flux at the detector, reducing the need for long acquisitions and also reducing background scatter,

which is bound to affect the reconstruction. A pinhole or order sorting aperture close to the focus, which blocks direct beam and diffuse scattering, should also help improve the reconstruction. The current setup sees direct beam leak through the mirror aperture, as shown in Fig. 6.2b, which contributes to the background noise and saturates the detector more quickly.

6.1.3 Probe overlap & fly-scan ptychography

One of the major drawbacks of ptychography scanning is the long scan times which compounds when combined with other techniques such as ptychotomography [59]. Current motors still require settling times that are similar to the exposure time at each position [97] which results in considerable overhead given the typically thousands of diffraction patterns that are required in ptychography. This has led to developments in faster acquisition methods such as fly-scan ptychography [56–58, 283], whereby the sample is scanned continuously as the detector takes acquisitions. Continuous exposure, while the sample is still moving, introduces a decoherence effect that is equivalent to degradation in spatial coherence. Previous studies have related the effective coherence length to the scanning speed and detector acquisition time [283]. The probe overlap ratio is usually set very high as you gain in both overlap sampling and a reduction of the decoherence effect with little overhead added to the scan time. Multiple previous works have investigated how the coherent properties and modal decomposition of the probe change as various scan parameters are altered [56–58, 283]. In our work, we will use a single dataset which will have fixed decoherence properties and investigate how the reconstruction quality changes as a function of the probe overlap.

6.1.3.1 Experimental data collection

Experiments were performed at the I13-1 high coherence beamline [223] at Diamond Light Source; an undulator provided an unfocused monochromatic X-ray beam. An X-ray energy of 9.7 keV was selected by a horizontally mounted quadruple crystal

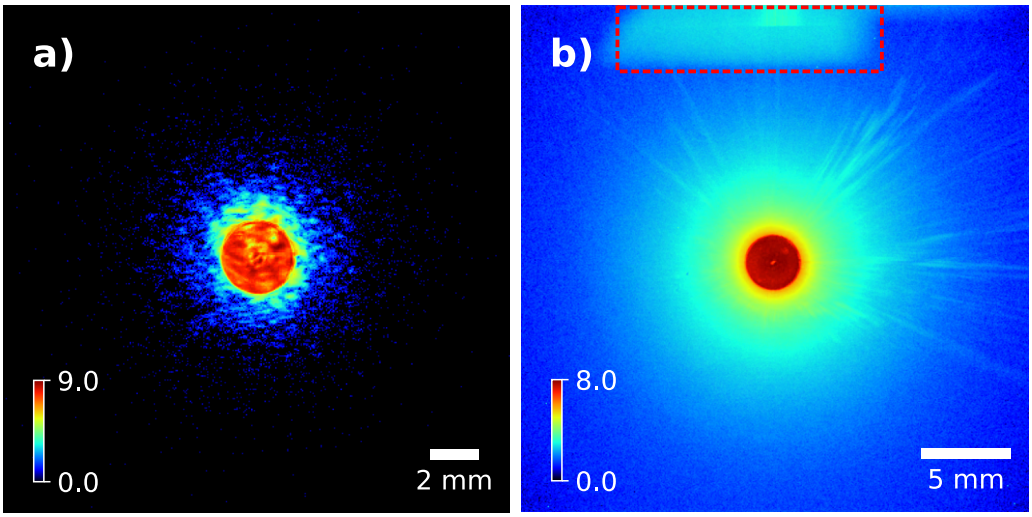


Figure 6.6: Diffraction intensity of the gold microflowers with fly-scan ptychography. (a) Single frame acquired for 40 ms cropped to the field of view used in ptychography 380 px (h) × 380 px (v). (b) Larger field of view integrated over 1250 frames. The red dashed box labels direct beam and both images are plotted on $\log_{10}$ scale.

monochromator with an approximate $\Delta E/E \sim 10^{-4}$ energy bandpass to maximize longitudinal coherence. Source slits were used to cut the horizontal beam size down to 50 µm and improve the horizontal coherence length. The beam was focused by using a FZP which features a 400 µm aperture, 150 nm outer zone width and 80 µm fixed central stop. At 9.7 keV this gave a first-order focal length of 469 mm.

This provided a beam size of approximately 4.2 µm (h) × 6.6 µm (v) at the sample position. The experimental setup is the same as that shown in Fig. 4.3. The sample consisted of gold microflowers embedded in 2% agarose and deposited as a droplet on a 25 µm Kapton sheet and allowed to dry; more details are provided in section 6.1.1. This was positioned approximately 5 mm downstream of the focus. These scans form part of a larger study which used ptychotomography to investigate the biological interaction of gold microflowers within simulated tissues, the full results from which have not been entirely processed so have been omitted.

We utilise the initial scans used to set up and calibrate the experimental parameters before the complete ptychotomography measurements were performed. Clusters of the gold microflowers of interest were identified using direct beam and a PCO edge area detector with a 500 nm effective pixel size. These were chosen as strongly

scattering objects which are present in the scan field of view to help with reconstruction convergence [59]. At these locations, ptychography scans were performed in a raster grid utilising a continuous fly scanning mode. The number of points, step size and exposure were all optimised until the ptychography reconstructions visually displayed no sign of probe raster artefacts.

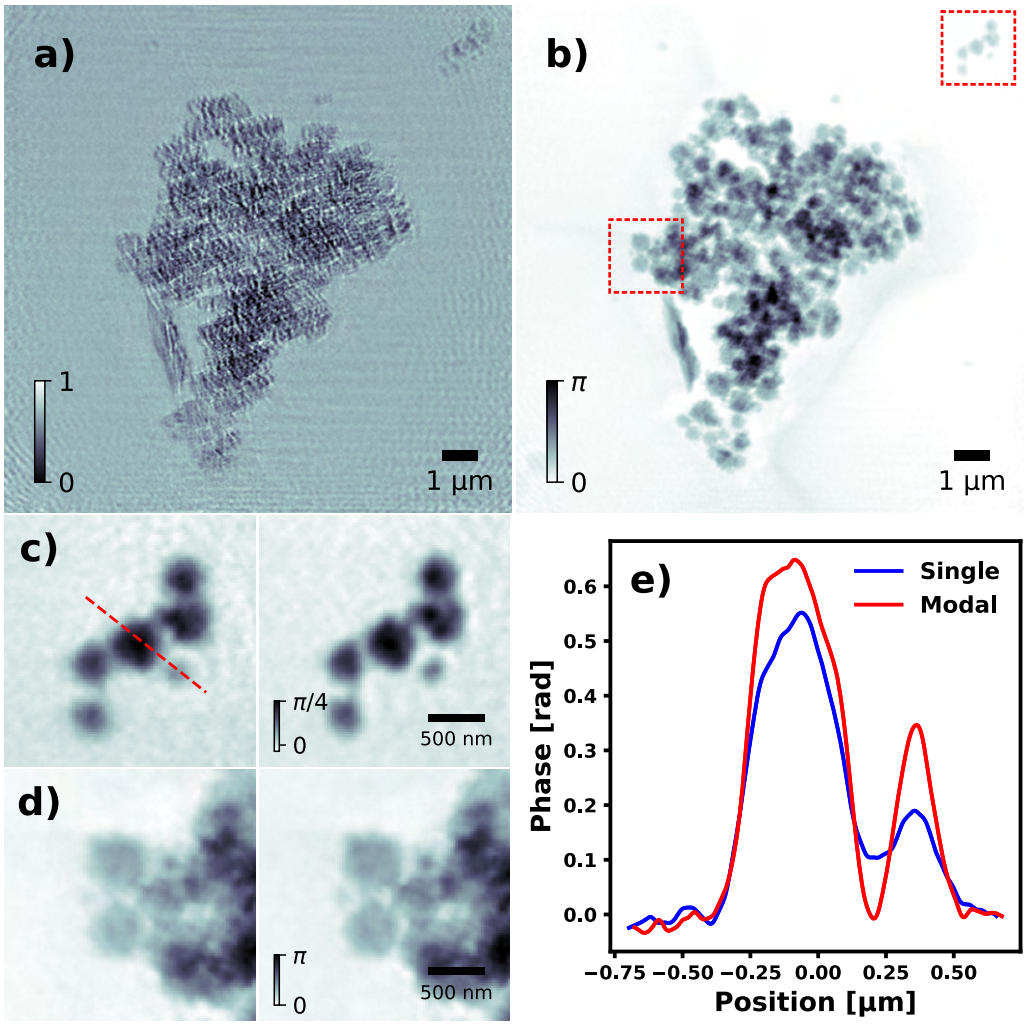


Figure 6.7: Sample reconstructions of gold microflowers with fly scan ptychography. (a) The modulus & (b) phase of the multi-modal reconstruction. Agarose is slightly visible around the main cluster. Magnified regions of the phase labelled by red dashed lines are shown in (c) and (d) with the left & right hand side showing the single and multi-modal probe reconstructions respectively. (e) Line profiles through two particles labelled by the red dashed line in (c).

Ptychography scans were then performed over an area of 12.5 µm (h) × 12.5 µm (v) with a 250 nm horizontal and 500 nm vertical step size between adjacent positions,

which generated 1250 diffraction patterns. These were acquired for 40 ms each by a single-photon counting Dectris Eiger2 detector with a 75 µm (h) × 75 µm (v) pixel size and a 1030 px (h) × 514 px (v) field of view positioned 4.9018 m downstream of the sample. With this scanning geometry, the overlap sampling factor given by Eq. (3.34) was found to be 94% (h) and 92% (v) and the overall sampling ratio according to Eq. (3.35) was found to be $S_\Pi = 648$.

6.1.3.2 Single & multi-modal reconstructions

The diffraction patterns were cropped to a region of interest around the optical axis measuring 380 px (h) × 380 px (v), which included only statistically relevant counts and resulted in a 22 nm effective pixel size. The cropped region was limited primarily by contamination of the diffraction intensities originating from direct beam leaking over the top of the Helium fly tube, as shown in Fig. 6.6b; larger regions of interest were attempted but saw a significant drop in reconstruction quality. Dead and hot detector pixels were also disregarded from the reconstruction by generating a detector mask based on the integrated diffraction data stack. To confirm the presence of decoherence effects, two reconstructions were run, the first assuming complete coherence and using a single probe mode, the second using a multi-modal approach and a probe with 15 modes.

Reconstructions were performed using 250 iterations of the difference map (DM) followed by 250 iterations of maximum likelihood (ML) refinement, both implemented in the *ptycho shelves* software [219]. The initial probe was modelled on the optical design parameters, and corresponding Hermitian modes were generated and included for the multi-modal reconstruction. The multi-modal reconstructed sample modulus and phase are shown in Fig. 6.7 with magnified views of the single and multi-modal reconstructions displayed in Fig. 6.7c and Fig. 6.7d. A line profile indicated by a dashed red line in Fig. 6.7c through one of the particles plotted is plotted in Fig. 6.7e demonstrates the resolution improvement of the multi-modal reconstruction. Without the inclusion of a multi-modal probe, the sample recon-

struction is blurred by some PSF originating from the fly-scan decoherence effect.

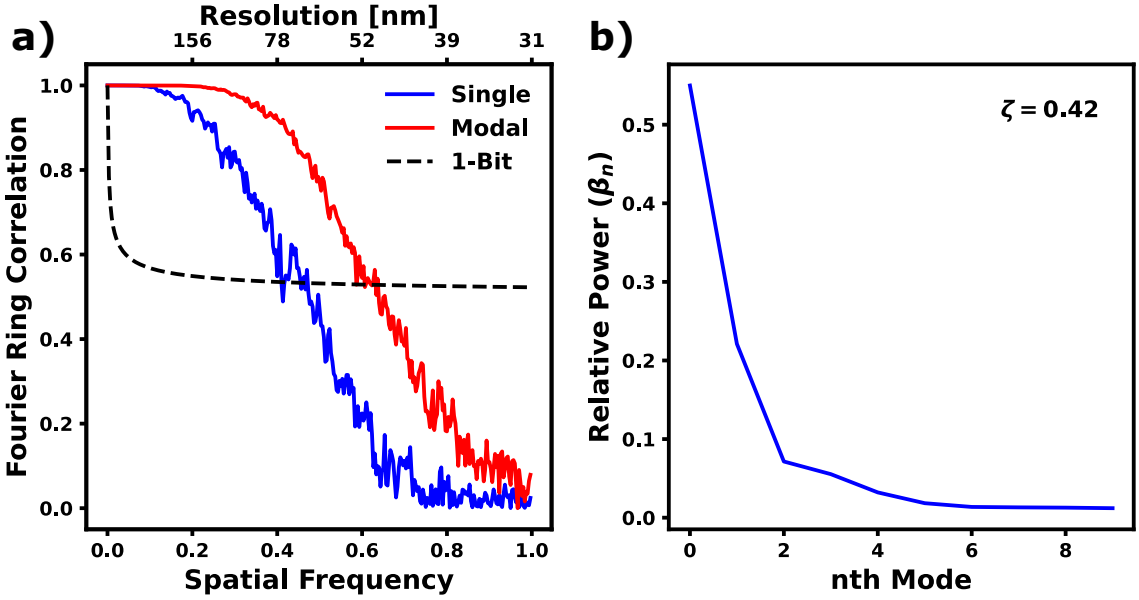


Figure 6.8: Resolution & power analysis of gold microflowers with fly-scan ptychography. (a) The FRC curve for the single & multi-modal probe reconstructions. (b) The relative power spectrum of the multi-modal probe shown in Fig. 6.9.

The resolution was determined using Fourier ring correlation, which is reviewed in section 3.6; this involved reconstructing two independently acquired datasets with the same parameters, aligning the sample phases and plotting the correlation curve. Where the curve crosses the 1-Bit threshold is the spatial resolution which in this case was determined to be 79 nm for the single and 47 nm for the multi-modal reconstruction, respectively. The line profiles taken across one of the collections of particles also shows a clear contrast improvement with the inclusion of the multi-modal probe. The larger particle size in Fig. 6.7e can be approximately estimated by taking the FWHM of the curve and is 390 nm; assuming the particles are spherical, this would induce a phase shift of 0.612 rad at 9.7 keV, which agrees well with observations.

The corresponding single and multi-modal probe modes are shown in Fig. 6.9, and the corresponding multi-modal power spectrum is shown in Fig. 6.8. The main mode (Fig. 6.9b) only contains around half the power suggesting the rest of the

distributed power is caused by the decoherence effect and a coherent mode should not be used. The second most powerful mode (Fig. 6.9c) exhibits a zero-crossing in the vertical direction or p-type mode which is a result of reduced coherence in the horizontal direction [49, p. 84]. This is the effect of the fly-scan primarily reducing the coherence length along its fast scan direction. The intensities at the optic plane of the next dominant modes (Fig. 6.9d and Fig. 6.9e) are still contained within the sharp aperture of the optic suggesting they don't arise due to detector imperfections or background scattering [49].

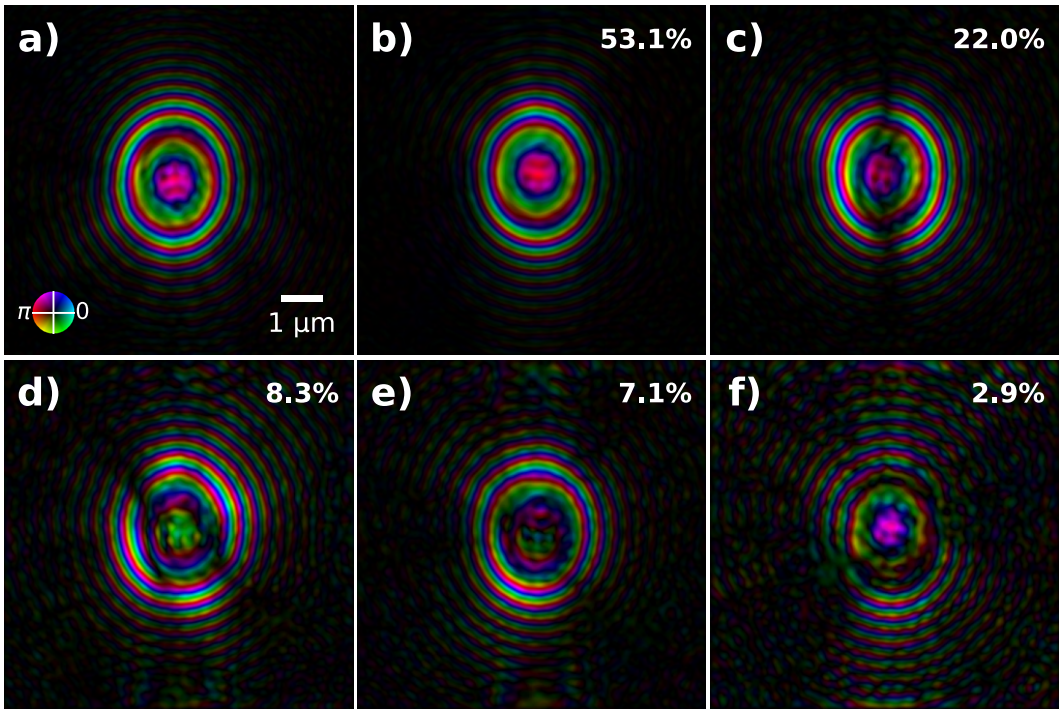


Figure 6.9: Probe reconstructions of gold microflowers with fly-scan ptychography. (a) Single & (b) multi-modal probes, with power in the top corner. The colour wheel in (a) encodes brightness & hue as amplitude & phase respectively.

6.1.3.3 Effect of probe overlap

As has been discussed in section 3.5 the overlap and overall sampling of the setup will have an effect on the ptychography algorithm's ability to reconstruct. This effect has been explored previously without regard for a multi-modal reconstruction method [240] here that case is considered. Given the small overlap ratio that occurs

with fly-scan ptychography and the decoherence effects that arise, it's possible to vary the overlap while still attaining a convergent reconstruction. For the following tests, the horizontal, fly-scan axis step size was varied from its original 250 nm step size up to 5 µm. The vertical overlap step size remained the same, and the horizontal beginning and end scan points for each row were also included to ensure the sample field of view remained constant through all tests.

To assess the effect of the overlap on the sample reconstructions, we consider the signal-to-noise ratio (SNR) rather than the Fourier ring resolution. This is because the overlap is a sampling quantity which will affect the overall reconstruction quality rather than necessarily what resolution is being obtained. An image with a low SNR may still have high-resolution with poorer contrast. The SNR is defined for the reconstructed phase images as [284],

$$\mathrm{SNR} = \sqrt{\frac{r_{cc}}{1 - r_{cc}}} \qquad r_{cc} = \frac{\langle (\varphi_1 - \langle \varphi_1 \rangle)(\varphi_2 - \langle \varphi_2 \rangle) \rangle}{\sqrt{\langle (\varphi_1 - \langle \varphi_1 \rangle)^2 \rangle \langle (\varphi_2 - \langle \varphi_2 \rangle)^2 \rangle}} \tag{6.1}$$

where the angled brackets denote the averaged value, r_{cc} is the correlation coefficient and φ is the reconstructed sample phase. Two reconstructions each starting with random sample functions, were performed for both the single and multi-modal probes across all scanning steps, and the SNR was calculated. The results of which are shown in Fig. 6.10a and demonstrate a clearly negative trend.

Although an exact trend cannot be determined from the results of Fig. 6.10a it's clear as the overlap ratio is decreased, so too does the reconstruction SNR. The modal reconstruction approach still offers a higher quality sample up to a point where the single and multi-modal SNRs will be similar, and there would be little gain in using a multi-modal reconstruction approach. The SNR reduction as the overlap ratio was decreased was confirmed visually by magnified views of the phase reconstruction, as shown in Fig. 6.10b for the single and Fig. 6.10c for the multi-modal reconstructions. The sample reconstruction is still of fairly good

quality apart from along the horizontal direction owing to the vertical overlap ratio remaining constant and relatively high. In terms of the sampling ratio, the effect of partially coherent light can be envisioned as introducing a number of further unknowns equal to the number of modes; the solution in ptychography is to either increase the reciprocal or overlap sampling ratios as explained in section 3.5. This explains why the multi-modal SNR decreases at a more rapid rate than just the single probe reconstruction in Fig. 6.10a.

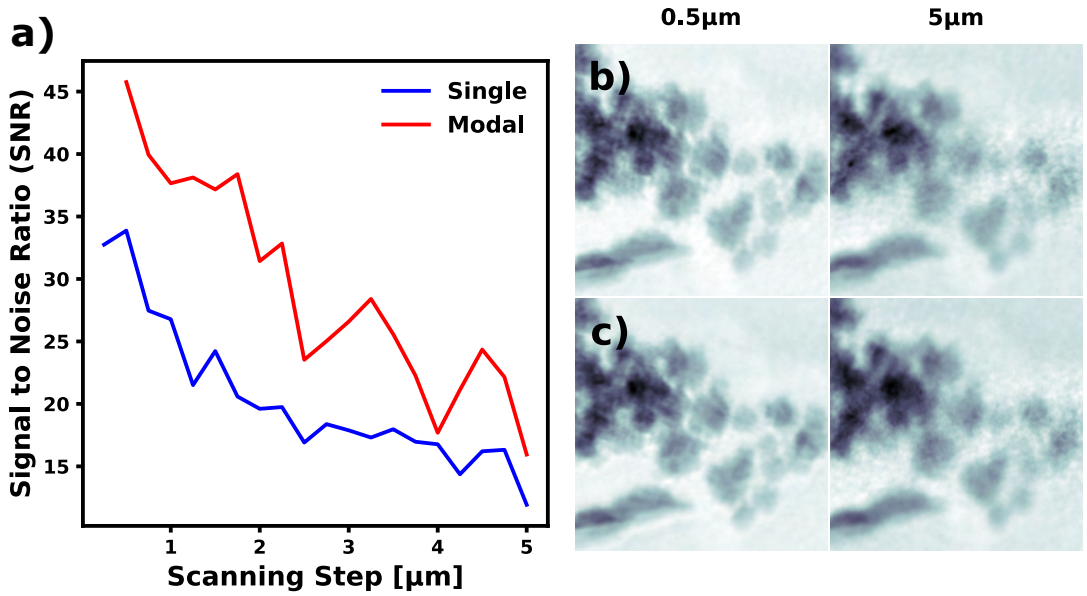


Figure 6.10: SNR of gold microflowers with fly-scan ptychography. (a) SNR ratio at different scanning step sizes for both single & multi-modal reconstructions. Effect of overlap step size for (b) the single & (c) multi-modal reconstructions.

6.1.4 Results & discussion

Within this section, the effect of partially coherent light and fly-scan decoherence on ptychography reconstructions of gold microflower nanoparticles has been studied. The main results from the sections are summarised below,

- An additional technique can now be utilised by the B16 beamline, which may find use combined with other X-ray techniques offered. Compared to other imaging techniques, ptychography offers greater quantitative data about samples, especially phase information with hard X-rays. An interesting potential

application is the imaging of biological samples and soft tissues which should see the potential for huge contrast improvements.

- Optimisation of the B16 ptychography setup will improve the resolving capabilities further. A more dedicated setup is required, which features stable optics, direct beam filtering and a detector fly tube. At this point, the source flux and sample will become the only limiting factor.

- Potential adoption of ptychography by other beamlines. As insertion device beamlines typically produce higher flux, the coherent properties can more easily be improved or relative scan times reduced. Therefore, partially coherent ptychography could be combined with their own specialised techniques to offer parallel high resolution capabilities. Following these results, discussions and some initial experimental sessions have already taken place in collaboration with other beamlines at Diamond Light Source.

- The effect of fly-scan ptychography was shown to cause the same decoherence degradation effect as partially coherent light in section 6.1.3. Accounting for this using a multi-modal probe reconstruction improves both the sample resolution and the phase information.

- Decoherence effects in ptychography appear to degrade images the same way as in normal X-ray microscopy experiments as long as the sampling rate is high enough it can be corrected. As the overlap sampling ratio is reduced, the multi-modal ptychography model becomes less able to properly reconstruct probe modes and the sample quality diminishes.

6.2 Ptychotomography of silica diatoms

Diatoms are unicellular photosynthesizing algae that possess the unique characteristic of being surrounded by an exoskeletal cell wall made of silica called a frustule. There are estimates there could be millions of species [285] with a diverse range of sizes and shapes, found in almost every aquatic environment, including fresh and marine waters. Living diatoms form a significant portion of the Earth's biomass and generate up to 25% of all oxygen produced [286], as well as play an important role in the circulation of silica in the hydrosphere. They are broadly classified by the two distinct shapes that exist: centric which is radially symmetric, and pennate which is bilaterally symmetric [287]. Most species fall into the latter category and are between 2 µm-100 µm in size. All diatom cells share a common overall topology and consist of two valves connected by a system of circumferential girdle bands. They reproduce predominantly asexually by binary fission and, during normal mitosis, can divide every couple of hours. The individual diatom grows by an extension of the girdle band that seals the gap between the two halves [288], once the growth is sufficient for division, the growth of new silica valves begins within the diatom. Each new organism then receives one of the two frustules.

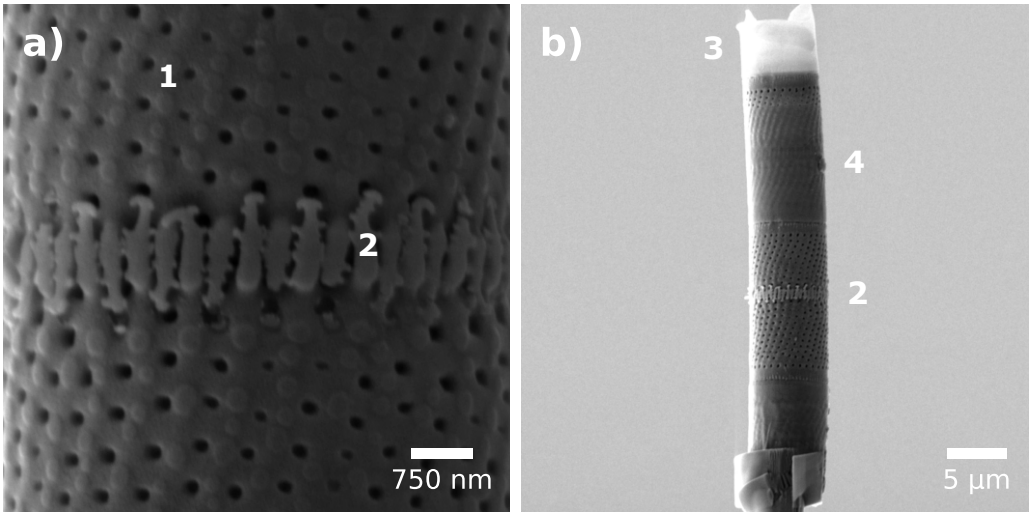


Figure 6.11: SEM images of *Aulacoseira* sp. silica diatom frustules. (a) Magnified views of the fastening" devices that connect cells into chain-shaped colonies [289]. (b) Sample mounting on tungsten needle for ptychotomography.

Recently there has been renewed scientific interest in diatoms, particularly in materials and engineering, as they offer a renewable source of raw materials and the potential of mass produced nanostructured materials [287, 290, 291]. Human fabrication methods are far from nature's in terms of precision, low energy, consumption and production rate, but hopefully if these technologies are more deeply understood, copied or mimicked and even modified, breakthroughs in nanofabrication may occur. The cell wall of diatoms consists of a hard but porous exoskeleton composed primarily of silica and is most likely to have evolved as a protection mechanism [292], with the abundance of silica serving as a structural scaffolding element. This siliceous wall is the most characteristic feature and can be highly patterned with a variety of nano and micropores, ribs, spines, ridges and elevations, all of which affect the electromagnetic, plasmonic, vibrational, and mechanical properties [290] and is usually used to delineate genera and species. The elaborate nanostructure of the silica frustules is realised by bioassisted "additive manufacturing" in which the precipitation of silica 10 nm-30 nm globules inside intracellular silica deposition vesicle (SDV) deposits along the protein nanofiber mesh [287].

Many previous works [289, 293, 294] have studied a plethora of different diatom species frustule structures using SEM and FIB sectioning. This provides the high resolution required but must be performed under vacuum and are only surface sensitive or destructive. An improved understanding of the detailed formation process of these nanostructures within the diatoms SDV requires observations beyond the surface with techniques which are non-destructive, of high spatial resolution and low dose. Previous non-destructive works studying the structure of diatoms include holotomography [295] and soft X-ray ptychography [296] both of which demonstrate excellent spatial resolution. Hard X-ray ptychotomography [59] is a similar technique that provides less noisy reconstructions than single-shot methods and high phase contrast between the soft biological matter and hard silica frustules. As single ptychotomography scan times on the I13 beamline have been reduced to only one

or two hours using fly-scan [297] this allows for dynamic studies of single diatom cells reproducing, which generally occurs on the order of a day. In this section, we will demonstrate a proof of principle experiment using hard X-ray ptychotomography to attain the morphological structure of a silica diatom frustule.

6.2.1 Sample preparation

For the following experiments, diatoms from the *Aulacoseira* sp. were used [298]; these are one of the most common freshwater diatoms and exhibit central frustules linked to one another by spines in order to form chain-shaped colonies. The shape of the linking and separation between spines and striae are important characteristics that distinguish species within *Aulacoseira*. There is usually a ringleiste which is an internal silica ledge that projects into the cell interior from the column. Diatoms were provided by Skolkovo Institute of Science and Technology, and preparation was assisted by by Dr. Joris Everaerts in the Department of Engineering Science, University of Oxford and have previously been described [289]. In order to mount single diatoms for tomographic imaging, the samples had to be imaged with SEM and manipulated with FIB. As diatoms are composed of hydrated organic (polysaccharide case, proteins, fat species, chloroplasts etc.) and mineral silica components charging effects would be present. Therefore the frustules of *Aulacoseira* sp. were purified in order to remove the organic matter by dispersing the diatoms in a mixture of dilute acid followed by multiple washes with distilled water. Following this, intact frustules were mounted on a tungsten needle tip and secured with platinum deposition for tomographic imaging. SEM images taken after mounting are shown in Fig. 6.11 and clearly also display the "fastening" devices by label 2 that connect cells into chain-shaped colonies as well as the nanosize valves on the surface.

6.2.2 Experimental data collection

Ptychotomography is a blend of ptychography and tomography, whereby the usual tomography projections are replaced by ptychography reconstructions instead [59,

299]. As such, the data collection, processing and clean-up are generally taken to be two independent processes.[5] It has been successfully used to image biomaterials [61], energy storage devices [68], catalysts [302] and earth sciences [303]. Experiments were performed at the I13-1 high coherence beamline [223] at Diamond Light Source; an undulator provided an unfocused monochromatic X-ray beam. An X-ray energy of 9.7 keV was selected by a horizontally mounted quadruple crystal monochromator with an approximate $\Delta E/E \sim 10^{-4}$ energy bandpass to maximise longitudinal coherence. The beam was focused by using a FZP which features a 400 µm aperture, 150 nm outer zone width and 80 µm fixed central stop. At 9.7 keV this gave a first-order focal length of 469 mm. This provided an approximate power of 8.9×10^6 photons/s and a beam size of 18.6 µm (h) × 18.6 µm (v) at the sample position. The sample consisted of a silica diatom frustule mounted on a tungsten needle, as described in section 6.2.1. This was positioned approximately 18 mm downstream of the focus and at the centre of rotation of a tomography stage.

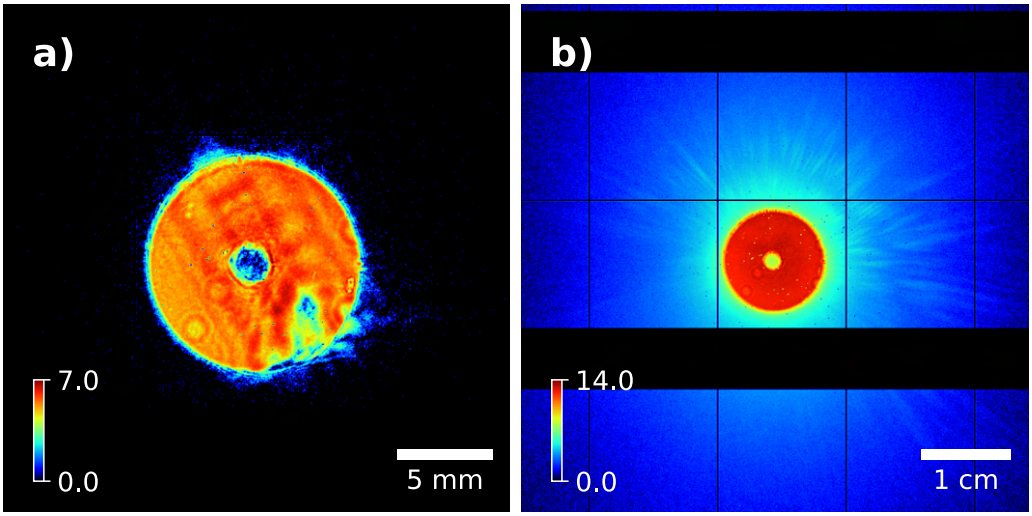


Figure 6.12: Diffraction intensity for ptychotomography of a silica diatom. (a) Single frame acquired for 100 ms cropped to the field of view used in ptychography 480 px (h) × 480 px (v). (b) Larger field of view integrated over 1024 frames. Both images are plotted on $\log_{10}$ scale.

Individual ptychography scans were performed in an angular range from −90° to

[5]Recent methods use both ptychography and projection data in the algorithm, which leads to higher quality reconstructions [300] or a reduction in the number of projections required [301].

90° about the vertical axis centre of rotation with an angular increment of 0.3° which generated 560 projections. At each angular position, a ptychography scan was performed over an area of 32 µm (h)×32 µm (v) in a raster fashion with a 1 µm horizontal and vertical step size between adjacent positions, which generated 1024 diffraction patterns. These were each acquired for 100 ms by a single-photon counting Excalibur[6] detector with a 55 µm (h) × 55 µm (v) pixel size and a 2069 px (h) × 1793 px (v) field of view positioned 14.773 m downstream of the sample. With this scanning geometry, the overlap sampling factor given by Eq. (3.34) was found to be 95% and the overall sampling ratio according to Eq. (3.35) was found to be $S_\Pi = 1368$. A typical diffraction pattern from one of the ptychography scans as well as the integrated intensity stack is shown in Fig. 6.12, this highlights the large dead zones, which can be problematic if not accounted for in the reconstruction with a detector mask. The large beam size was chosen as the primary experiment was imaging an enamel stick sample over a much larger field of view of around 100 µm (h) × 100 µm (v); thus this beam size offered the best compromise between scan time and resolution for that sample.

6.2.3 Ptychography processing

Decoupling the ptychography and tomography processing steps reduces the computational requirement and also allows each reconstruction to be optimised individually. Artefacts arising in each method are easily recognisable, while their combined interaction is unknown. The first phase of ptychotomography is independently processing each ptychographic projection and then combining them into a sinogram stack for later use with tomography. The processing steps are given as follows,

- Optimisation of the ptychography reconstruction parameters for an individual scan and then performing this on the entire projection stack.
- Analysis of the reconstructed phase for residues and vortices which may impact

[6]Excalibur belongs to the same family of detectors as that of Merlin and contains 48 medipix2 chips uniformly tiled in a 6 × 8 fashion separated by dead zones.

the next step and removal of phase ramps and global offsets.

- Unwrapping the sample phase, the complex transmission function bounds the phase between $-\pi$ and $+\pi$ even when this shift is exceeded physically.

We give greater detail to the post processing procedure of the sample transmission function in this section than earlier, as it has a much greater bearing on the final tomographic reconstruction. This processing pipeline is not unique, and most synchrotron beamlines will process datasets similarly to that detailed above. Ptychography projections were reconstructed using the *ptycho shelves* software [219], and sample post processing was achieved using custom python codes.

6.2.3.1 Algorithm optimisation

The diffraction patterns were cropped to a region of interest around the optical axis measuring $480\,\mathrm{px\,(h)} \times 480\,\mathrm{px\,(v)}$, which included only statistically relevant counts and resulted in a 72 nm effective pixel size. Dead and hot detector pixels were also disregarded from the reconstruction by generating a detector mask based on the integrated diffraction data stack. The initial probe was modelled on the optical design parameters. It was observed during the session there was significant jitter from the sample scanning stages, which is also corrected for in the reconstruction. Algorithms such as Difference Map (DM) [39] typically converge very quickly and are more robust to initial probe estimates but will fail to reach the actual solution in the presence of experimental noise [192]. The most important tuning parameter is the Fourier relaxation factor μ_{pfft}, which takes values between 0 and 1 and controls the level of noise accommodated in the reconstruction [296]. A larger factor can aid weaker scattering samples but also limits the attainable resolution; as we will be using an ML refinement procedure, we set it to a modest $\mu_{\mathrm{pfft}} = 0.1$. Significant position errors were observed and best corrected by using an annealing procedure [184]. The DM reconstructions were run for 250 iterations, after which the sample modulus and phase are shown in Fig. 6.13a and Fig. 6.13b; the modulus in par-

ticular highlights the artefacts due to the position errors, which results due to a reduction in overlap in that region.

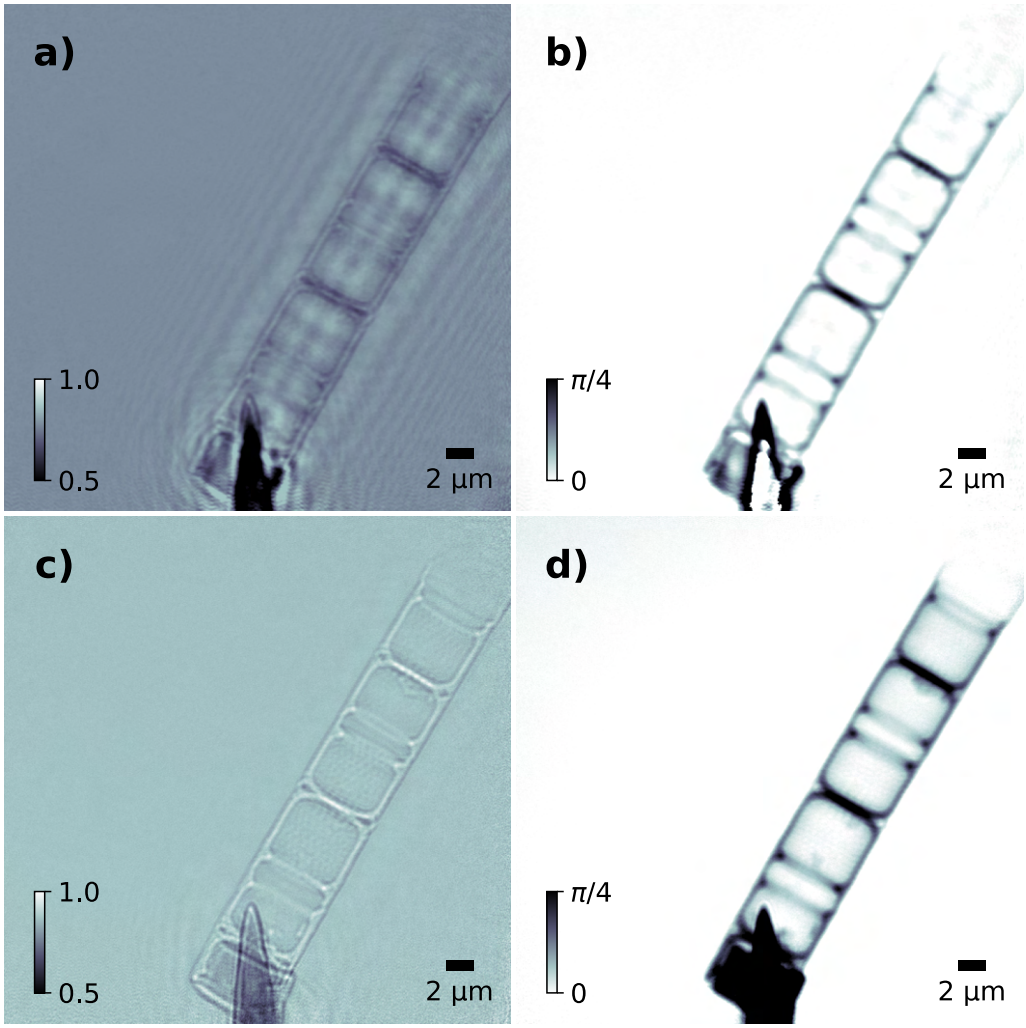


Figure 6.13: Sample ptychography reconstructions of a silica diatom for ptychotomography. (a) The modulus and (b) phase using the DM method. (c) The modulus and (d) phase after the ML refinement procedure.

The probe, sample and positions from the DM reconstruction are then used as the initial inputs for the maximum likelihood (ML) algorithm [192]. This accommodates a number of statistical models depending on the noise distribution of the experiment. Poisson is recommended for weaker scattering samples as the main source of noise arises due to detector counting, while a Gaussian model is recommended for strong scatterers [192]. The main tuning parameter is a quadratic regularization parameter μ, which determines the relative power given to the regularization pro-

cess. A value of $\mu = 0.05$, which is recommended in the literature and found to give the best results. Floating intensities were also implemented for the ML procedure, which allows the intensity of each diffraction pattern to change dynamically. This accounts for variable fluctuations in the probe intensity either due to source top-ups or monochromator instabilities. Subpixel position refinement is also implemented according to the process outlined using intensity gradients [185], which is advised to be included whenever the ML method is used, even if the stages are very accurate [219]. A least squares implementation of the ML method (LSQML) also allows for the experimental geometry to be refined and dynamic modelling of the incident wavefront to be accommodated [220]. This was included in the reconstruction but found to have little effect on the reconstruction. The final ML sample modulus and phase reconstructions are shown in Fig. 6.13c and Fig. 6.13d and demonstrate a remarkable improvement compared to the DM reconstructions. In particular, the diatom frustule valves are visible even in the modulus reconstruction, and silica deposits within the SVC are more clearly resolved in the phase.

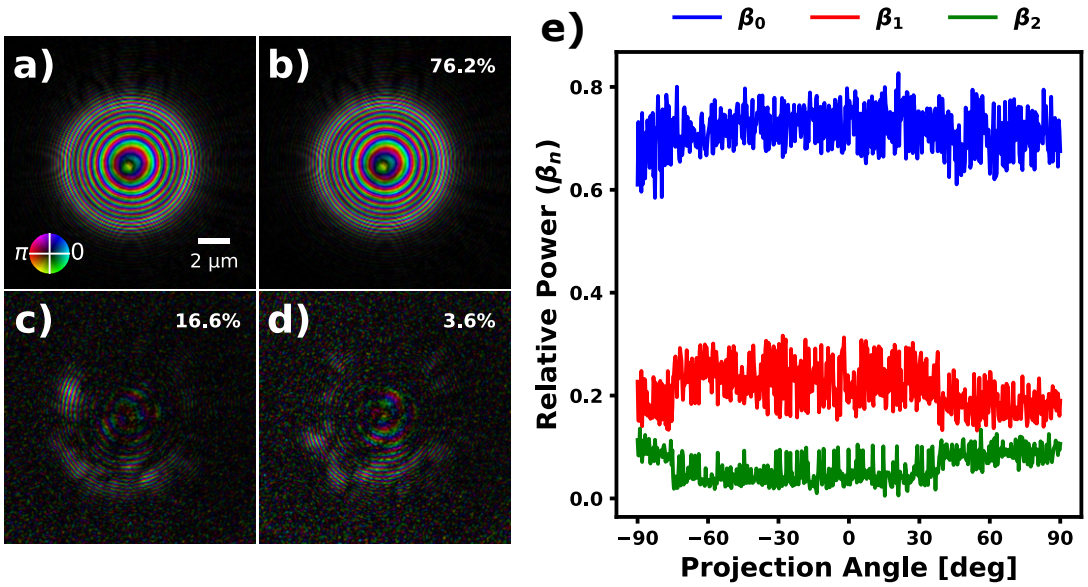


Figure 6.14: Probe ptychography reconstructions of a silica diatom for ptychotomography. (a) Single and (b-d) multi-modal probes with power in the top corner. The colour wheel in (a) encodes brightness & hue as amplitude & phase respectively. (e) Relative modal powers for all projections.

6.2.3.2 Decoherence analysis

In accordance with the theme of this thesis, the coherent properties were analyzed across all the ptychotomography scans. The initial probe used the previously reconstructed single probe and generated corresponding hermitian modes for the multi-modal reconstruction. Modes were included until the power of the final mode was less than 1% which occurred at 5 modes; however, up to 10 modes were tested to confirm the power distribution didn't change. The single and multi-modal reconstructed probes are displayed in Fig. 6.14. This found the probe is highly coherent, with around 76% of the power concentrated in the dominant mode and the other modes featuring little structure. This is expected given the horizontal source slits we severely reduced to 50 µm in order to produce a fully coherent beam across the FZP aperture; it also suggests at this time, the experimental setup was particularly stable. A comparison of the single and multi-modal sample reconstructions did not display any visual improvement. Usually, ptychotomography scans can use the projections at $-90°$ to $90°$ to perform a FRC; however, in this instance, these two projections were found to be slightly different, most likely due to angular misalignment of the rotation stage. Instead, both the single and multi-modal reconstructions were generated for all datasets, and the FRC was calculated using the tomography volume as shown in Fig. 6.20b; this again found no discernible difference between the single and modal reconstructions. The coherent properties were confirmed to remain consistent across projections by plotting their relative modal powers, as shown in Fig. 6.14b. As each individual scan took minutes to complete, an accurate measure of the source stability was not possible to conclude; scans using the fly-scan method and with a wider horizontal source aperture would be more sensitive to source stability.

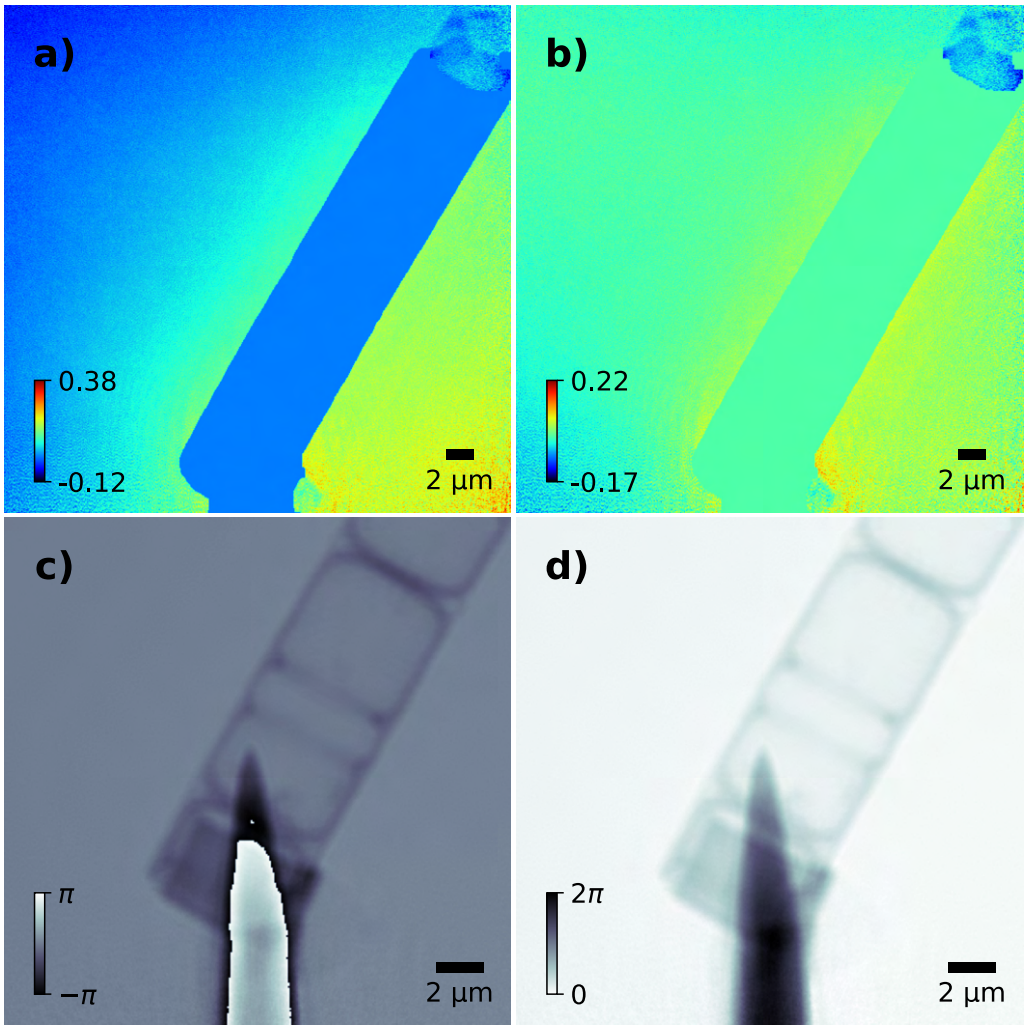


Figure 6.15: Projection phase processing of a silica diatom for ptychotomography. (a) Sample phase before & (b) after phase ramping is removed. (c) Sample phase before & (d) after phase unwrapping.

6.2.3.3 Projection phase processing

As is common with materials in the hard X-ray regime, the phase interaction is more dominant compared to absorption and provides greater contrast information; therefore, this will be the quantity used for the tomographic reconstruction. The reconstructed phase is sensitive to two ambiguities that arise due to the use of the Fourier transform for calculating the far-field intensity. Firstly according to the Fourier shift theorem, a shift in Fourier space at the detector plane corresponds to multiplication with a linear phase in the real sample space. This means that if the exact optical axis on which the diffraction patterns are cropped cannot be

determined, a linear phase ramp will be added to the reconstructed sample function. Secondly, constant phase terms in the sample plane will result in exactly the same diffraction intensity; therefore, a calibration region is necessary if absolute phase values are required. Both of these issues are well resolved with the inclusion of an air gap or flat region within the sample field of view, which can be used to calculate the corresponding ramp and offset. As tomography requires the sample to remain within the field of view for all projections, and the vertical alignment takes advantage of this fact, this requirement is usually satisfied for ptychotomography. To perform the correction, a mask was generated using the phase gradient and thresholding in order to find the air region of the projection. To this region, a linear gradient was fitted with which the gradient for the entire field of view could be subtracted.

Constant phase offsets were then corrected by determining the mean phase value left within the masked region and then subtracting this value from the entire field of view. The before and after results of the phase offset and ramp correction are shown in Fig. 6.15a and Fig. 6.15b; the slope is very minimal, which means the optical axis used was very close to the actual. As the reconstructed sample is the complex-valued transmission function, the computed phase will only be in the range $-\pi$ to π, which results in wrapping for larger shifts. Phase unwrapping works by applying a 2π offset at these phase discontinuities in order to obtain a continuous phase function. It's unproblematic if no phase residues are present but can cause issues at the boundary of sharp features. When phase residues are present, Goldstein's branch cut algorithm [304] can be used, which pairs positive and negative residues by so-called branch cuts such that the "charges" of the connected residues neutralise each other in the end. Problems can arise if there are isolated residues which don't form pairs, in which case an approach based on multiplying the phase with a corresponding anti-vortex plus further processing with ptychography may be more appropriate [305]. For these projections, no issues with unwrapping occurred, and a simple and efficient unwrapping method based on sorting by reliability was used [234]. The only area

where phase wrapping occurs in our projections is around the mounting needle, the results of which are shown in Fig. 6.15c and Fig. 6.15d.

6.2.4 Tomographic processing

After ptychographic reconstruction and processing of all projections, the procedure follows the usual tomographic reconstruction, with more attention paid to projection alignment. This is because the longer scan times and nanoscale resolution make projections more sensitive to misalignments. The processing steps are given as follows,

- Projection alignment with respect to one another in order to correct for transverse and rotational misalignment that arises during the scan acquisition.
- Tomographic reconstruction of the sample volume using the FBP and SART algorithms and its conversion to a quantitative electron density.

This processing procedure is not novel, and we approximately follow the standardised process of many previous ptychotomography experiments [59, 299]. As such a number of processing tools have been developed primarily in MATLAB [306] that we will make use of in addition to our own python codes.

6.2.4.1 Alignment of projections

The reconstructed projections will almost always feature some transverse misalignment between the projections; in our case, the positional errors found during the ptychography reconstruction amplify this effect. The alignment must be performed in both transverse planes and is achieved using progressively more accurate methods, which become more computationally demanding. The initial coarse alignments rely on computationally tracking projection features, and their level of success is dependent on the level of feature contrast. The accuracy of these can be improved within sample preparation with the use of fiducial markers [307]; these are often used in transmission electron tomography. The first rough alignment for both directions

uses a two-dimensional cross-correlation of neighbouring projections [308]; however, this does not necessarily lead to the most accurate solution and can also result in the accumulation of errors throughout the stack [299]. As the field of view remains unchanged, the vertical alignment can be achieved using the horizontally integrated phase, which remains unchanged for each projection. The projection phases were integrated along the horizontal as shown in Fig. 6.16a; for the unaligned case, and a high-band pass filter was also applied. The central 0° projection profile was chosen, and the others aligned with this. The calculated shifts were then applied to the actual projections and the integrated stack, after which is shown in Fig. 6.16b.

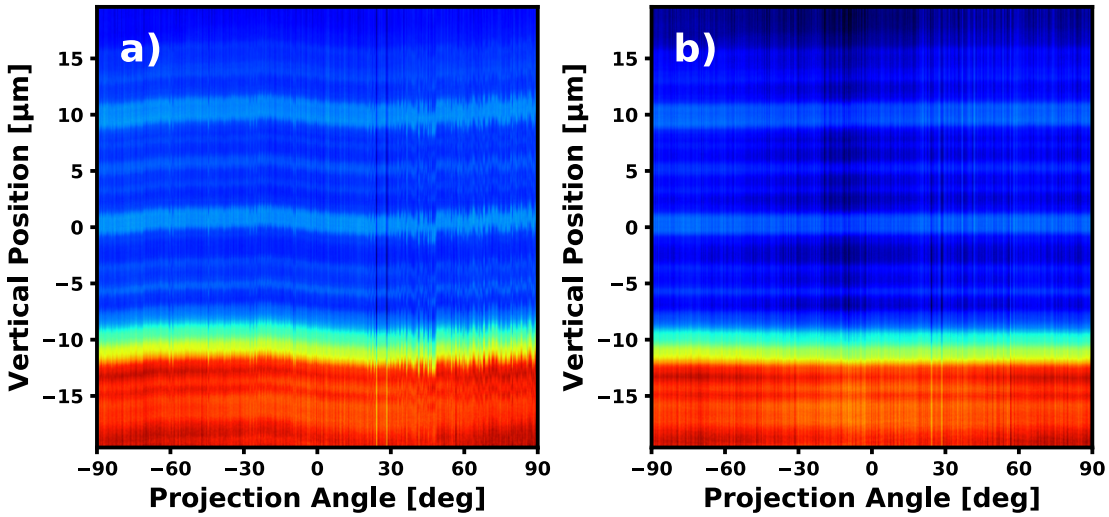


Figure 6.16: Vertical projection alignment of a silica diatom for ptychotomography. The horizontally integrated phase for all projections (a) before and (b) after the vertical alignment procedure.

Unfortunately, the horizontal alignment cannot be achieved in the same way as the integration of the projections along the vertical will not remain the same for different angles. One common approach typically used is the centre of mass alignment [59]. The centre of mass of the phase image can be calculated for each projection and then fitted to a sinusoidal profile such that the corresponding required shifts be calculated. This method is very sensitive to the accuracy of the previous vertical alignment. It was found that the centre of mass method did not provide much in the way of improvement in the alignment, possibly because there are very small

differences in the overall phase as demonstrated by the non-uniformity across the projection angle shown in Fig. 6.16b. Instead, an iterative reprojection method was used [309, 310], which aligns projections by reconstructing the misaligned tomographic volume and then using this to generate a new stack of projections. The misaligned projections are then aligned to the newly generated set of reprojections using subpixel cross-correlation, normally repeated for a few hundred iterations. They are based on the fact that the measurement and object reconstruction should be consistent only for a correct alignment geometry. This type of alignment is very computationally expensive; therefore, it's usually performed at progressively finer resolutions which is achieved by binning the data [196, 311]. The sinograms before and after alignment are shown in Fig. 6.17.

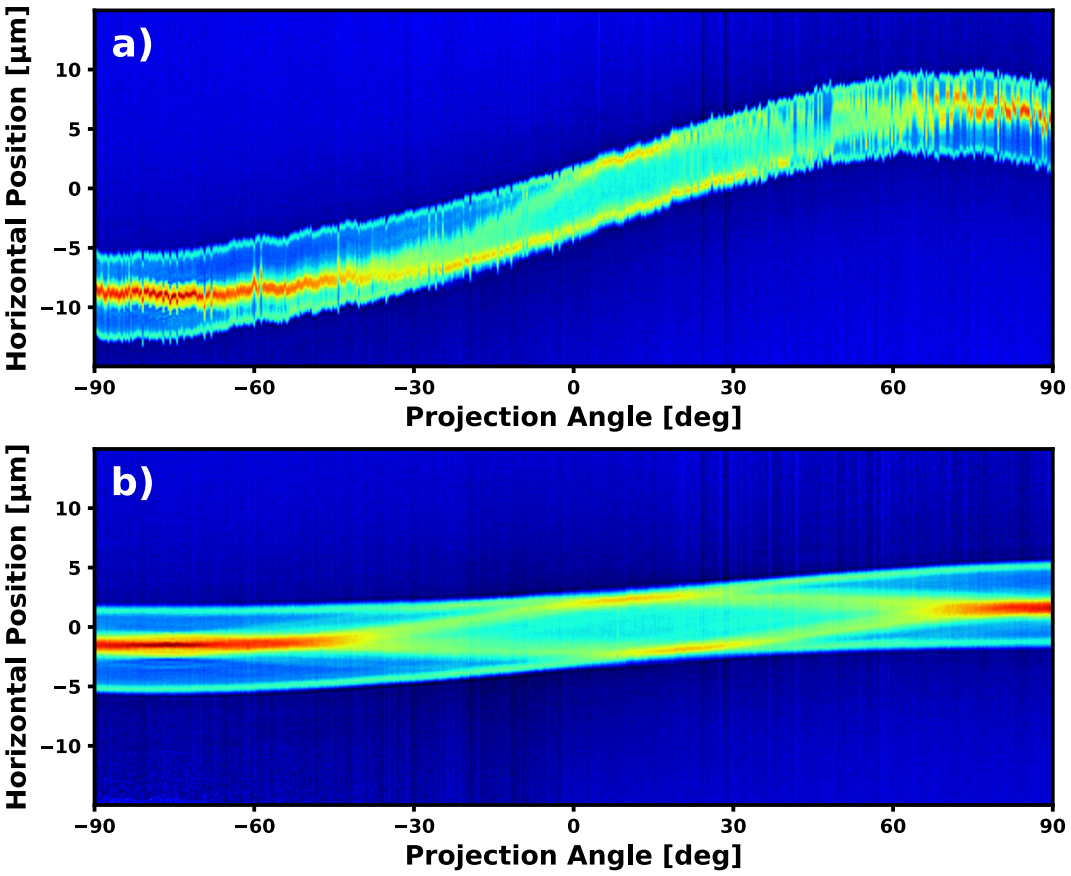


Figure 6.17: Sinogram projection alignment of a silica diatom for ptychotomography. Vertical slice through the phase projection stack (a) before and (b) after the iterative reprojection alignment procedure.

6.2.4.2 Tomography reconstructions

After all preprocessing steps, the projections are fed into the final tomographic reconstruction algorithm. As our phase projections don't suffer from any phase unwrapping issues, the data can be fed in as is. If issues were present, a gradient approach which uses the gradient of the back propagation filters, such as in the case of differential phase-contrast tomography, may be more appropriate [312]. For tomographic reconstruction both the Filtered Back Projection algorithm (FBP) [313] and Simultaneous Algebraic Reconstruction Technique (SART) [314] were computed, details of which are beyond the scope of this thesis. After reconstruction of the 560 input projections of $544\,\mathrm{px}\,(\mathrm{x}) \times 576\,\mathrm{px}\,(\mathrm{y})$ this produced a phase shift volume of $576\,\mathrm{px}\,(x) \times 544\,\mathrm{px}\,(y) \times 576\,\mathrm{px}\,(z)$ with 72 nm voxel size.

After reconstruction, slices were taken through the orthogonal planes of the volume and are shown in Fig. 6.18. The fact the sample was positioned at an angle to the centre of rotation doesn't seem to have affected the volume quality in anyway but does make taking informable slices more difficult. From Fig. 6.18a and Fig. 6.18b it's clear the SART algorithm is much better at suppressing noise outside the main volume compared with FBP. There also appear to be some very slight streaking artefacts, which is typically characteristic of a FBP reconstruction. The SART reconstructed volume is what is used for the rest of the study.

6.2.4.3 Morphology & electron density

A standardised procedure for quantitative comparison with other measurements and techniques is to convert the phase shift into an average electron density n_e for each voxel. This is directly proportional to the refractive index decrement δ section 2.2, which is in turn directly proportional to the reconstructed phase shift $\Delta\varphi$. The average electron density, therefore, is given by [315, p. 256],

$$n_e = \frac{2\pi}{r_e \lambda^2}\delta = \frac{\Delta\varphi}{r_e \lambda \Delta x} \tag{6.2}$$

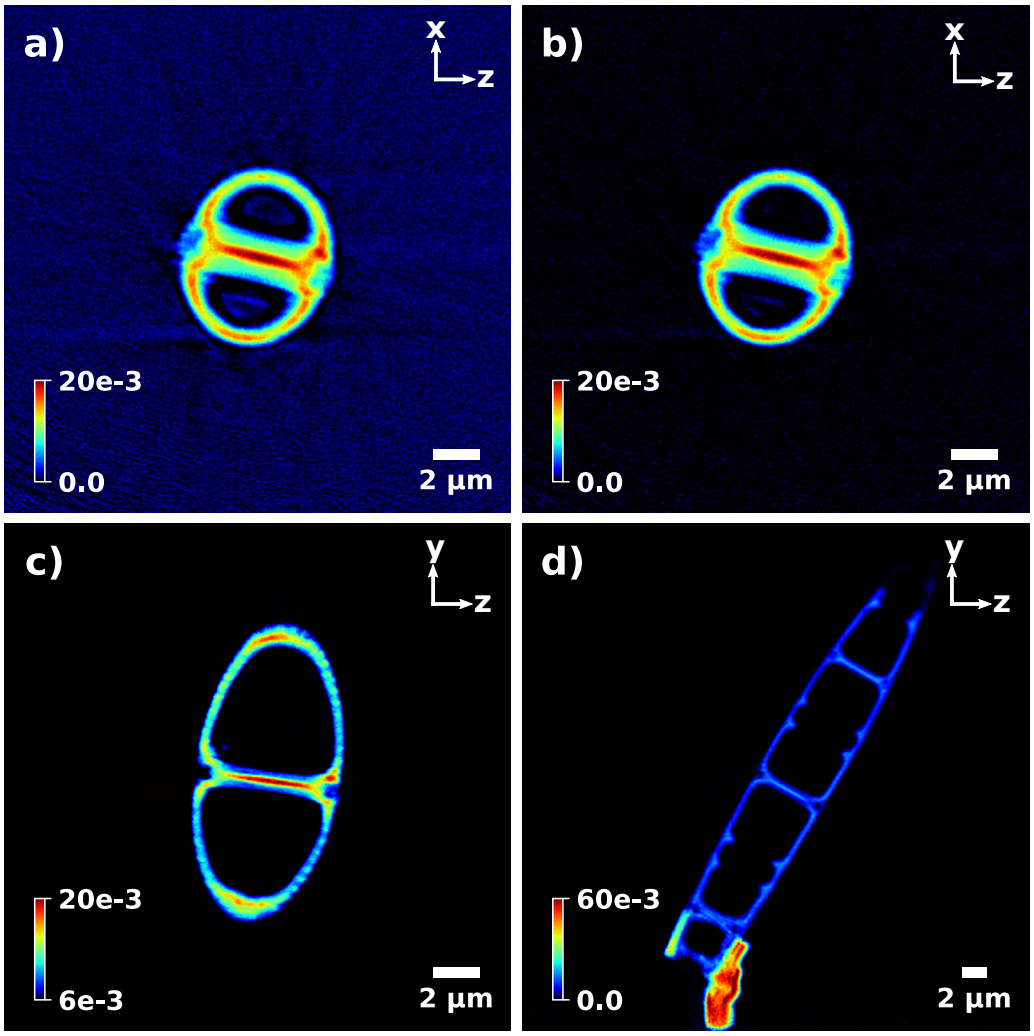


Figure 6.18: Orthogonal slices of the tomographic volume of a silica diatom. Vertical slices using (a) FBP and (b) SART. (c-d) Other two orthogonal slices using SART. The colourbars label the relative phase shift.

where r_e is the classical electron radius and λ is the X-ray wavelength. If the background has not been normalised before conversion, this should be done, i.e. air should possess zero phase shift. To gauge the distribution of different materials, a histogram of the average electron density and their relative frequency within the tomographic volume is shown in Fig. 6.20a, with the identifiable peaks labelled.

The different materials can be identified by visual confirmation of where within the volume the average electron densities correspond and using other information such as the SEM images and how the sample is mounted. Furthermore, we can compute the corresponding average voxel mass density of elements and compound

Material	Electron Density n_e	Density ρ [g/cm^3]		Refractive Index δ	
		Calculated	Tabled	Calculated	Tabled
Pt	0.45	18.6	21.45	3.3e-5	3.51e-05
W	0.45	18.6	19.25	3.3e-5	3.05e-05
Ga	0.21	7.64	5.1	1.54e-5	1.1e-05
Silica (i)	0.042	1.39	2.65	3.1e-6	4.89e-06
Silica (ii)	0.061	2.03	2.65	4.4e-6	4.89e-06

Table 6.1: Tomography material properties calculated from the electron density and compared with well known values from the Henke dataset [13].

materials using the average electron density by [315, p. 256],

$$\langle \rho \rangle = \frac{1}{N} \sum_{i=1}^{N} \xi_i \left(\frac{A}{Z} \right)_i u \, n_e \approx 2u \, n_e \tag{6.3}$$

where N is the number of elements, ξ_i is the relative mass fraction, Z is the atomic number A is the atomic weight and u is the atomic mass unit. The approximation made assumes $A/Z \approx 2$, which is suitably accurate for the majority of elements. A number of electron densities were chosen as indicated by the dashed black lines in Fig. 6.20a, and the corresponding mass densities and refractive index decrement were calculated, the results of which are shown in Table 6.1.

The histogram in Fig. 6.20a displays a number of features; firstly, the tungsten needle (iv) and platinum deposition (v) share the same peak distribution due to their similar densities. The presence of gallium from the FIB processing is labelled by the peak (iii). The diatom frustule silica distribution shows a peak at around (i) but also has a slight shoulder to it at point (ii), suggesting there are two different silica phases, with the latter denser. Comparing the calculated densities with the tabulated values in Table 6.1 we see all densities are slightly less than the expected values. The histogram was properly calibrated using the air density as a reference; thus it suggests there is some other systematic error causing the discrepancy. To visualise the tomographic reconstructions, the electron densities were imported into the Avizo software, which is used to manipulate three-dimensional data. Here the diatom was reorientated such that it was parallel to the vertical axis, and a colourmap

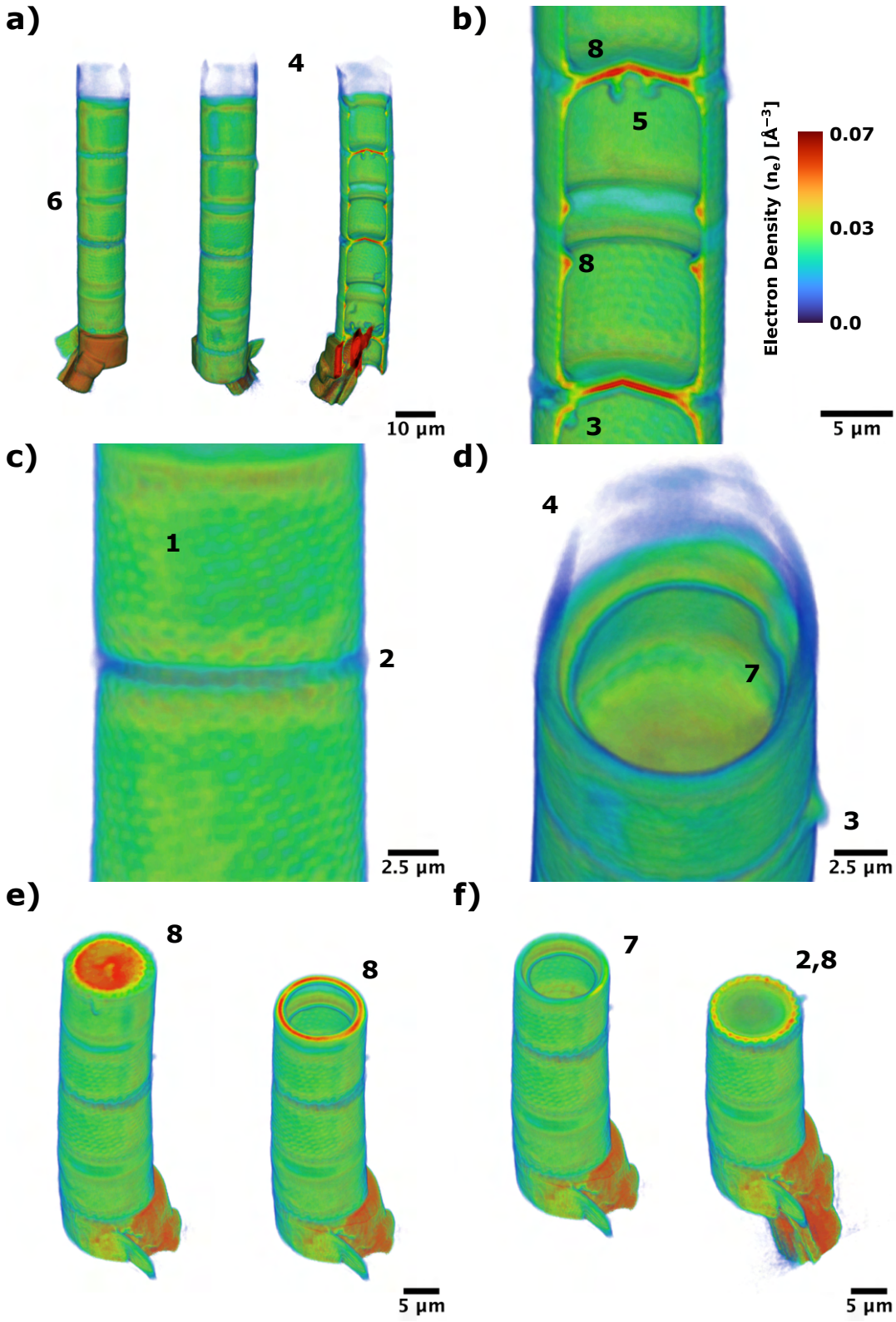


Figure 6.19: Morphological rendering of the silica diatom ptychotomography reconstruction. (a) Overview of the whole sample at different angles including a cross section. (b) Magnified cross section highlighting silica deposits within and different silica densities. (c) Magnified view of the outside surface. (d) Above view of the ringleiste structure at the ends of columns. (e) Cross sections highlighting different silica densities. (e) Cross sections showing a ringleiste inside and the spines which connect individual cells. The colourmap shown in (b) encodes electron densities by colour and relative transparence.

was applied to distinguish areas with different densities. The results from this have been plotted in Fig. 6.19 and display a number of interesting features which match up to the SEM images and histogram data.

1. **Valves/Striae:** Siliceous funnels such that two opposite valves and a linking girdle band form a frustule; their primary function is to allow the exchange of nutrients in and waste out of the cell.

2. **Spine:** A spine is a pointed, silica extension of the valve, which may be solid or hollow, long or short, single or many, and may arise at different points on the valve here they connect individual cells in a chain.

3. **Rimoportula:** A tubular process that extends out from the valve, which is simple and hollow, their primary purpose is to extrude polysaccharides and other carbon compounds.

4. **Broken Frustule:** The remnants of a previous diatom that was part of the same colony, it's of much lower electron density than everything else and only just distinguishable from the background noise.

5. **Silica Deposits:** The biomineral building blocks of diatoms are produced from within the cell in specialised vesicles; these silica deposits will subsequently be incorporated into the main cell wall.

6. **Long Spine:** An additional spine that appears to extend the complete length of the diatom colony; its primary purpose is likely to provide additional support to the linked structure.

7. **Ringleiste:** An internal, silica ledge that projects into the cell interior from the column. The ringleiste is only found in the genus *Aulacoseira* and is variously developed in different species of the genus.

8. **Silica Densities:** There is a measurable difference in the electron densities of the silica that forms the column caps, concentric middle braces, tall spline and interconnecting splines compared with the rest of the frustule.

Many of these feature definitions are taken from the online diatom glossary [316]. One of the most interesting findings from this study is the difference in silica densities at the column caps, concentric middle braces and splines. It can be observed from the original SEM images in Fig. 6.11a that the slight difference in contrast between the spines connecting frustules could be the result of different silica densities; however, the internal distribution was until now, unknown. Naturally, occurring silica has been commonly observed in different polymorphs including quartz, cristobalite, tridymite, coesite, stishovite, lechatelierite, and opal. However, usually, only a single polymorphic form will be present whereas here there are clearly two distinct phases. The regions of higher density silica are located at the conventional points of failure for this type of shape; thus the most logical conclusion is they provide additional structural support. The location and density differences in silica within the frustule structure provide further insight into the properties of diatoms and could further explain why they exhibit ultra-high stiffness and strength [287].

6.2.5 Spatial resolution

Spatial resolution was quantified for the ptychotomography results using Fourier shell correlation, which is reviewed in section 3.6, this involved splitting the projection data set into two and then performing two independent tomographic reconstructions with the same parameters. This was performed for both the single and multi-modal ptychography projections, which found little difference between the profiles suggesting there are very minimal decoherence effects. The correlation curves are shown in Fig. 6.20b. Where the curve crosses the 1/2-Bit threshold is the spatial resolution which in this case was determined to be 88 nm for both curves. The 1/2-Bit threshold is chosen in this case as the projection data is split

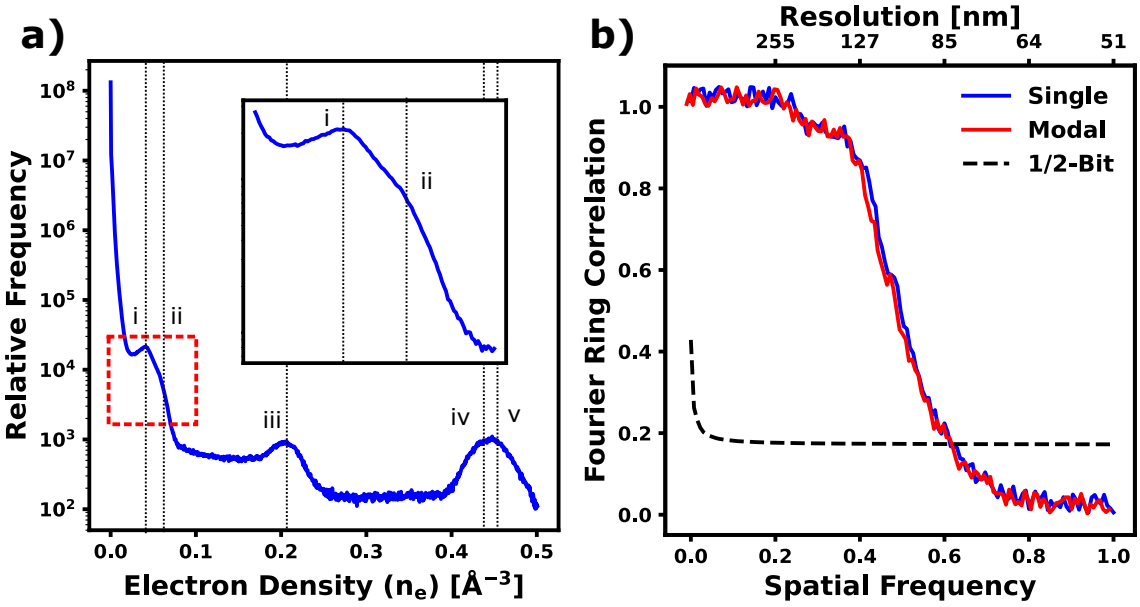


Figure 6.20: Electron density & resolution analysis of a silica diatom. (a) Electron density histogram with identifiable elements & compounds labelled. (b) FRC using for the single & multi-modal ptychography reconstructions.

into two datasets in order to perform the comparison; when the complete dataset is computed, this would give a sampling at the original 1-Bit threshold rate. Seeing as the number of horizontal pixels is approximately equal to the number of projections before the split, we are only just at the right sampling level for tomographic reconstruction. This is usually not a problem if only a small portion of the central volume close to the centre of rotation is used, as this will usually be properly sampled. In this case, the main silica diatom sample volume is very far away from the centre of rotation and also at an angle to it, which may result in a reduction of resolution.

6.2.6 Results & discussion

Within this section, the main processing steps of a typical ptychotomography experiment have been presented in order to study the morphological structure of a silica diatom. The main results from the sections are summarised below,

- The FRC spatial resolution of the reconstruction was not observed to change even with the inclusion of a multi-modal probe to correct or decoherence effects. This suggests the probe was highly coherent, and the experimental setup remained relatively stable throughout the scan acquisition.

- Within the present experimental setup, the probe used was significantly larger than it could have been in order to scan larger areas of the sample more quickly. In future experiments, an order of magnitude smaller probe would result in a much higher flux density and possibly result in higher spatial resolution capabilities.

- A high-resolution tomographic volume rendering of an intact silica diatom frustule has been produced; previously only part of frustules have been measured with X-ray tomography. This allows a novel visualisation of a number of internal structural features.

- Two different silica densities have been identified within the diatom frustule at structurally critical positions; this is possibly an evolutionary adaptation and could shed light on previous results that have found diatoms to exhibit ultra-high stiffness and strain characteristics.

- Potential to perform future *in situ* studies of diatoms. The beam size in ptychography can be easily changed such that the sample dose is effectively controlled; this combined with its potential for high phase contrast reconstructions makes it an ideal technique for imaging biological and soft tissues.

7 Conclusion

The successful implementation of hard X-ray ptychography on the B16 Test beamline was demonstrated in chapter 4.5.1 using a multi-modal form of the probe to account for partially coherent light [47]. This differs significantly from the majority of previous demonstrations of the technique that either simulated the effect [240] or used insertion device sources where a large proportion of the flux is already coherent [54, 241]. Ptychography scans were performed to evaluate the focal properties of a FZP and CRL X-ray focusing optic using a Siemens star test sample. The spatial resolution was quantified using line profiles [275] on the sample and found to be 82 nm which is a factor of 3.6 times smaller than what's currently offered using focusing optics. Initially, the fraction of coherent flux was increased with spatial filtering; however, this also reduced the beam size at the optic aperture meaning the true performance was not being accurately evaluated. This was rectified using the method presented in section 4.5.3. Furthermore, the analysis compared the coherent properties from the reconstructed multi-modal probe with those predicted using a Gaussian-Schell model and found good agreement. This means ptychography is a suitable technique for quantifying the coherent properties of X-ray sources [134].

In section 4.3 it was demonstrated how highly coherent ptychography could be used as a metrology technique to characterise a FZP. The resulting wavefront error was decomposed using Zernike polynomials [15, p. 523] in order to distinguish the alignment [235] and residual fabrication errors. Using partially coherent ptychography for wavefront characterisation required the development of a new technique due to the limited aperture envelope by the dominant coherent mode as shown in Fig. 4.17b. In section 4.5.3 the multi-modal ptychography method [51] was shown to be capable of compensating for partially coherent light by using either sample or probe mode decompositions. This technique was used to evaluate the performance of a CRL under both fully and partially coherent conditions, and the two-dimensional

wavefront error was shown to agree with previous results using the knife edge technique [245]. These results demonstrate that ptychography possesses enough redundancy to assess the coherent performance of optics even when partially coherent light is used. Furthermore, this method doesn't require specialist reconstruction methods [48, 49] and can be computed using most existing implementations of the multi-modal ptychography algorithm [47]. The coherent fraction of this setup was found to be only around 2% which is the lowest reported used for ptychography or CDI experiments and begins to blur the lines of what is deemed a CDI technique.

X-ray focusing optics are particularly sensitive to fabrication aberrations, which after the source demagnification factor is the largest contributing factor limiting diffraction limited focusing. Numerous corrective solutions have been demonstrated using bimorph mirrors [19, 20] and custom refractive optics [7, 21] to introduce wavefront perturbations that cancel with errors originating from the fabrication aberrations. In chapter 5 wavefront correction was demonstrated using dynamic refractive optics [250] to correct both planar CRLs and a Kirkpatrick–Baez mirror in one-dimension. This design evolved from bespoke [7] to sinusoidal thickness profiles which attempt to correct the majority of wavefront error. In all cases, the optics were found to be diffraction limited when correctors were used [250] with a maximum reduction factor of 7 achieved. This method of correction possesses numerous benefits over previous designs, as it can be varied as necessitated, such as when changing energies, can be used for many different optics and doesn't require lengthy fabrication times in between measurements. Achieving such corrections requires precise knowledge of the wavefront before and after correction, which was achieved quickly during the experimental session using a knife edge technique described in section 5.2. The adaptable refractive correctors are a quick, effective method of optics corrections that can be easily installed on existing beamlines.

A more in-depth study of the adaptable correctors [250] was presented in section 5.4 to study the simultaneous two-dimensional correction of an aberrated Kirk-

patrick–Baez mirror pair [12]. The horizontal mirror possessed the highest numerical aperture, and largest wavefront error, so will see the greatest benefit from corrective optics, whereas the vertical mirror was already considered diffraction limited prior to correction. Ptychography scans were performed with and without the corrective structures inserted, and the reconstructed probes were propagated to the two different mirror planes. The analysis confirmed the earlier one-dimensional knife edge results [250] and that more significant aberrations along the length of the mirror could be successfully decomposed and corrected independently. The decomposition is only valid for large wavefront errors and begins to break down for smaller errors which would require a different method of compensation. By employing the method presented in section 4.5.3 the performance of the corrective optics could be assessed under ideal, coherent conditions and concluded that for small wavefront errors, the corrective optics primarily reduce the background noise rather than increase the resolving capacity. Simulated imaging experiments of nanoparticles under fully and partially coherent conditions suggest the full benefit of corrective optics will be realized for optics working close to the diffraction limit.

A demonstration of partially coherent ptychography using a realistic test sample was confirmed possible on the B16 Test beamline in 4.5.1. Ptychography scans were performed using a Kirkpatrick–Baez mirror and found the resolution to be around 180 nm using Fourier ring correlation. It is expected there will be fewer reconstruction artefacts with a more optimized setup, or when performed on a different insertion beamline. The same gold microflower sample was also imaged under high coherence conditions using fly-scan ptychography [56–58], as shown in section 6.1.3. The degradation effect of the fly-scan was found to cause a similar decoherence effect as partially coherent light in the probe, and when its accounted for leads to a high-resolution reconstruction. Finally, in section 6.2 the processing steps for a ptychotomography [59] experiment are shown in the study of a silica diatom sample. The setup used a highly coherent beam that remained that way throughout

the data collection. There was no difference observed in the resolution between a single and multi-modal probe reconstruction. The processing steps necessary for ptychotomography reconstruction were discussed, including the optimisation of the ptychography reconstructions, preprocessing of the projection phases and the tomographic alignment procedure. The final three-dimensional volume of the diatom morphology revealed commonly expected features of the diatom as well as distinct differences in the silica density at structurally significant locations.

Ptychography has been adopted as a standard technique by many synchrotron and research facilities worldwide due to its high imaging resolution and redundant capability to correct experimental data degradation [47, 55, 184, 187]. As source brilliance continues to improve, this adoption is only likely to grow with further developments and variations tailored to the needs of other X-ray microscopy techniques. Unlike traditional CDI, the use of pinhole optics is almost completely absent from the ptychography setup as greater flux and phase diversity can be achieved with focusing optics [195, 196]. As focal sizes approach ever smaller nanoscale capabilities, ptychography and CDI have become the only suitable techniques for characterising performance [41–45]. This has led to ptychography and X-ray optics possessing a unique symbiotic relationship that has seen both fields develop at a rapid pace in the last decade and is reflected as a major theme within this thesis. Ptychography has been shown to no longer be a specialist technique restricted to highly coherent synchrotron sources but can now be routinely employed in order to extend the imaging capabilities of existing beamlines without the need for expensive optics and major equipment upgrades. In combination with the latest generation of X-ray and corrective optics, both fields will begin probing ever smaller length regimes resulting in new understandings at these length scales. This thesis contributes to both aspects and thus pushes ptychography and X-ray optics further in their development and wide adoption as established microscopy techniques.

Bibliography

[1] W. C. Röntgen, "Ueber eine neue art von strahlen," *Annalen der Physik*, vol. 300, no. 1, pp. 12–17, 1895.

[2] D. B. Williams and C. B. Carter, *Transmission Electron Microscopy*, vol. 4. Springer, Boston, MA, 2 ed., 2009.

[3] O. Hemberg, M. Otendal, and H. M. Hertz, "Liquid-metal-jet anode electron-impact x-ray source," *Applied Physics Letters*, vol. 83, no. 7, pp. 1483–1485, 2003.

[4] E. J. Jaeschke, S. Khan, J. R. Schneider, and J. B. Hastings, *Synchrotron Light Sources and Free-Electron Lasers*. Springer, Cham, 1 ed., 2016.

[5] P. Emma, R. Akre, J. Arthur, R. Bionta, C. Bostedt, J. Bozek, A. Brachmann, P. Bucksbaum, R. Coffee, F. J. Decker, Y. Ding, D. Dowell, S. Edstrom, A. Fisher, J. Frisch, S. Gilevich, J. Hastings, G. Hays, P. Hering, Z. Huang, R. Iverson, H. Loos, M. Messerschmidt, A. Miahnahri, S. Moeller, H. D. Nuhn, G. Pile, D. Ratner, J. Rzepiela, D. Schultz, T. Smith, P. Stefan, H. Tompkins, J. Turner, J. Welch, W. White, J. Wu, G. Yocky, and J. Galayda, "First lasing and operation of an ångstrom-wavelength free-electron laser," *Nature Photonics*, vol. 4, no. 9, pp. 641–647, 2010.

[6] S. Shin, "New era of synchrotron radiation: fourth-generation storage ring," *AAPPS Bulletin*, vol. 31, no. 1, p. 21, 2021.

[7] K. Sawhney, D. Laundy, V. Dhamgaye, and I. Pape, "Compensation of x-ray mirror shape-errors using refractive optics," *Applied Physics Letters*, vol. 109, no. 5, p. 051904, 2016.

[8] A. Snigirev, V. Kohn, I. Snigireva, and B. Lengeler, "A compound refractive

lens for focusing high-energy x-rays," *Nature*, vol. 384, no. 6604, pp. 49–51, 1996.

[9] B. Lengeler, C. Schroer, J. Tümmler, B. Benner, M. Richwin, A. Snigirev, I. Snigireva, and M. Drakopoulos, "Imaging by parabolic refractive lenses in the hard X-ray range," *Journal of Synchrotron Radiation*, vol. 6, pp. 1153–1167, Nov 1999.

[10] C. Jacobsen, "Soft x-ray microscopy," *Trends in Cell Biology*, vol. 9, no. 2, pp. 44–47, 1999.

[11] W. Chao, B. D. Harteneck, J. A. Liddle, E. H. Anderson, and D. T. Attwood, "Soft x-ray microscopy at a spatial resolution better than 15 nm," *Nature*, vol. 435, no. 7046, pp. 1210–1213, 2005.

[12] P. Kirkpatrick and A. Baez, "Formation of optical images by x-rays.," *Journal of the Optical Society of America*, vol. 38 9, pp. 766–74, 1948.

[13] B. Henke, E. Gullikson, and J. Davis, "X-ray interactions: Photoabsorption, scattering, transmission, and reflection at e = 50-30,000 ev, z = 1-92," *Atomic Data and Nuclear Data Tables*, vol. 54, no. 2, pp. 181–342, 1993.

[14] J. Als-Nielsen and D. McMorrow, *Elements of modern X-ray physics*. Oxford: Wiley-Blackwell, 2nd ed. ed., 2011.

[15] M. Born, E. Wolf, and E. Hecht, "Principles of optics: Electromagnetic theory of propagation, interference and diffraction of light," *Physics today*, vol. 53, no. 10, pp. 77–78, 2000.

[16] A. Schindler, T. Haensel, A. Nickel, H.-J. Thomas, H. Lammert, and F. Siewert, "Finishing procedure for high-performance synchrotron optics," in *Optical Manufacturing and Testing V* (H. P. Stahl, ed.), vol. 5180, pp. 64 – 72, International Society for Optics and Photonics, SPIE, 2003.

[17] J. Maser, G. B. Stephenson, S. Vogt, W. Yun, A. Macrander, H. C. Kang, C. Liu, and R. Conley, "Multilayer Laue lenses as high-resolution x-ray optics," in *Design and Microfabrication of Novel X-Ray Optics II* (A. A. Snigirev and D. C. Mancini, eds.), vol. 5539, pp. 185 – 194, International Society for Optics and Photonics, SPIE, 2004.

[18] J-TEC Corporation, "Jtec corporation high-precision x-ray mirror." `https://www.j-tec.co.jp/english/optical/high-precision-x-ray-mirror/`, Jul 2022.

[19] H. Mimura, S. Handa, T. Kimura, H. Yumoto, D. Yamakawa, H. Yokoyama, S. Matsuyama, K. Inagaki, K. Yamamura, Y. Sano, K. Tamasaku, Y. Nishino, M. Yabashi, T. Ishikawa, and K. Yamauchi, "Breaking the 10 nm barrier in hard-x-ray focusing," *Nature Physics*, vol. 6, no. 2, pp. 122–125, 2010.

[20] J. Sutter, S. Alcock, and K. Sawhney, "*In situ* beamline analysis and correction of active optics," *Journal of Synchrotron Radiation*, vol. 19, pp. 960–968, Nov 2012.

[21] F. Seiboth, A. Schropp, M. Scholz, F. Wittwer, C. Rödel, M. Wünsche, T. Ullsperger, S. Nolte, J. Rahomäki, K. Parfeniukas, S. Giakoumidis, U. Vogt, U. Wagner, C. Rau, U. Boesenberg, J. Garrevoet, G. Falkenberg, E. C. Galtier, H. Ja Lee, B. Nagler, and C. G. Schroer, "Perfect x-ray focusing via fitting corrective glasses to aberrated optics," *Nature Communications*, vol. 8, no. 1, p. 14623, 2017.

[22] J. H. Crocker, "Engineering the costar," *Opt. Photon. News*, vol. 4, p. 22, Nov 1993.

[23] E. Becker, W. Ehrfeld, P. Hagmann, A. Maner, and D. Münchmeyer, "Fabrication of microstructures with high aspect ratios and great structural heights

by synchrotron radiation lithography, galvanoforming, and plastic moulding (liga process)," *Microelectronic Engineering*, vol. 4, no. 1, pp. 35–56, 1986.

[24] S. Alcock, K. Sawhney, S. Scott, U. Pedersen, R. Walton, F. Siewert, T. Zeschke, F. Senf, T. Noll, and H. Lammert, "The diamond-nom: A non-contact profiler capable of characterizing optical figure error with sub-nanometre repeatability," *Nuclear Instruments and Methods in Physics Research Section A: Accelerators, Spectrometers, Detectors and Associated Equipment*, vol. 616, no. 2, pp. 224–228, 2010. X-Ray Mirror.

[25] M. Vannoni and I. Freijo Martín, "Large aperture fizeau interferometer commissioning and preliminary measurements of a long x-ray mirror at european x-ray free electron laser," *Review of Scientific Instruments*, vol. 87, no. 5, p. 051901, 2016.

[26] M. Idir, M. Rakitin, B. Gao, J. Xue, L. Huang, and O. Chubar, "Alignment of KB mirrors with at-wavelength metrology tool simulated using SRW," in *Advances in Computational Methods for X-Ray Optics IV* (O. Chubar and K. Sawhney, eds.), vol. 10388, pp. 209 – 215, International Society for Optics and Photonics, SPIE, 2017.

[27] T. Zhou, H. Wang, O. Fox, and K. Sawhney, "Auto-alignment of x-ray focusing mirrors with speckle-based at-wavelength metrology," *Opt. Express*, vol. 26, pp. 26961–26970, Oct 2018.

[28] K. Sawhney, H. Wang, J. Sutter, S. Alcock, and S. Berujon, "At-wavelength metrology of x-ray optics at diamond light source," *Synchrotron Radiation News*, vol. 26, no. 5, pp. 17–22, 2013.

[29] S. Bérujon, E. Ziegler, R. Cerbino, and L. Peverini, "Two-dimensional x-ray beam phase sensing," *Phys. Rev. Lett.*, vol. 108, p. 158102, Apr 2012.

[30] J. Hartmann, "Bemerkungen über den bau und die justierung von spektrographen," *Zeitschrift für Instrumentenkunde*, vol. 20, no. 17-27, pp. 47–58, 1900.

[31] T. Weitkamp, B. Nöhammer, A. Diaz, C. David, and E. Ziegler, "X-ray wavefront analysis and optics characterization with a grating interferometer," *Applied Physics Letters*, vol. 86, no. 5, p. 054101, 2005.

[32] O. Hignette, A. K. Freund, and E. Chinchio, "Incoherent x-ray mirror surface metrology," in *Materials, Manufacturing, and Measurement for Synchrotron Radiation Mirrors* (P. Z. Takacs and T. W. Tonnessen, eds.), vol. 3152, pp. 188 – 199, International Society for Optics and Photonics, SPIE, 1997.

[33] H. Wang, Y. Kashyap, and K. Sawhney, "From synchrotron radiation to lab source: advanced speckle-based x-ray imaging using abrasive paper," *Scientific Reports*, vol. 6, no. 1, p. 20476, 2016.

[34] J. M. Rodenburg and H. M. L. Faulkner, "A phase retrieval algorithm for shifting illumination," *Applied Physics Letters*, vol. 85, no. 20, pp. 4795–4797, 2004.

[35] P. Thibault, M. Dierolf, A. Menzel, O. Bunk, C. David, and F. Pfeiffer, "High-resolution scanning x-ray diffraction microscopy," *Science*, vol. 321, no. 5887, pp. 379–382, 2008.

[36] H. M. Quiney, A. G. Peele, Z. Cai, D. Paterson, and K. A. Nugent, "Diffractive imaging of highly focused x-ray fields," *Nature Physics*, vol. 2, no. 2, pp. 101–104, 2006.

[37] J. Miao, D. Sayre, and H. N. Chapman, "Phase retrieval from the magnitude of the fourier transforms of nonperiodic objects," *J. Opt. Soc. Am. A*, vol. 15, pp. 1662–1669, Jun 1998.

[38] H. Öztürk, H. Yan, Y. He, M. Ge, Z. Dong, M. Lin, E. Nazaretski, I. K. Robinson, Y. S. Chu, and X. Huang, "Multi-slice ptychography with large numerical aperture multilayer laue lenses," *Optica*, vol. 5, pp. 601–607, May 2018.

[39] P. Thibault, M. Dierolf, O. Bunk, A. Menzel, and F. Pfeiffer, "Probe retrieval in ptychographic coherent diffractive imaging," *Ultramicroscopy*, vol. 109, no. 4, pp. 338–343, 2009.

[40] A. M. Maiden and J. M. Rodenburg, "An improved ptychographical phase retrieval algorithm for diffractive imaging," *Ultramicroscopy*, vol. 109, no. 10, pp. 1256–1262, 2009.

[41] C. M. Kewish, P. Thibault, M. Dierolf, O. Bunk, A. Menzel, J. Vila-Comamala, K. Jefimovs, and F. Pfeiffer, "Ptychographic characterization of the wavefield in the focus of reflective hard x-ray optics," *Ultramicroscopy*, vol. 110, no. 4, pp. 325–329, 2010.

[42] A. Schropp, P. Boye, J. M. Feldkamp, R. Hoppe, J. Patommel, D. Samberg, S. Stephan, K. Giewekemeyer, R. N. Wilke, T. Salditt, J. Gulden, A. P. Mancuso, I. A. Vartanyants, E. Weckert, S. Schöder, M. Burghammer, and C. G. Schroer, "Hard x-ray nanobeam characterization by coherent diffraction microscopy," *Applied Physics Letters*, vol. 96, no. 9, p. 091102, 2010.

[43] S. Hönig, R. Hoppe, J. Patommel, A. Schropp, S. Stephan, S. Schöder, M. Burghammer, and C. G. Schroer, "Full optical characterization of coherent x-ray nanobeams by ptychographic imaging," *Opt. Express*, vol. 19, pp. 16324–16329, Aug 2011.

[44] M. Osterhoff, A.-L. Robisch, J. Soltau, M. Eckermann, S. Kalbfleisch, D. Carbone, U. Johansson, and T. Salditt, "Focus characterization of the NanoMAX

Kirkpatrick–Baez mirror system," *Journal of Synchrotron Radiation*, vol. 26, pp. 1173–1180, Jul 2019.

[45] A. Björling, S. Kalbfleisch, M. Kahnt, S. Sala, K. Parfeniukas, U. Vogt, D. Carbone, and U. Johansson, "Ptychographic characterization of a coherent nanofocused x-ray beam," *Opt. Express*, vol. 28, pp. 5069–5076, Feb 2020.

[46] F. Seiboth, M. Kahnt, M. Scholz, M. Seyrich, F. Wittwer, J. Garrevoet, G. Falkenberg, A. Schropp, and C. G. Schroer, "Quantitative characterization of aberrations in x-ray optics," in *Advances in X-Ray/EUV Optics and Components XI* (A. M. Khounsary, S. Goto, and C. Morawe, eds.), vol. 9963, pp. 88 – 95, International Society for Optics and Photonics, SPIE, 2016.

[47] P. Thibault and A. Menzel, "Reconstructing state mixtures from diffraction measurements," *Nature*, vol. 494, no. 7435, pp. 68–71, 2013.

[48] H. Chang, P. Enfedaque, Y. Lou, and S. Marchesini, "Partially coherent ptychography by gradient decomposition of the probe," *Acta Crystallographica Section A*, vol. 74, pp. 157–169, May 2018.

[49] B. Enders, *Development and application of decoherence models in ptychographic diffraction imaging*. PhD thesis, Technical University Munich, 2016.

[50] T. E. J. Moxham, A. Parsons, T. Zhou, L. Alianelli, H. Wang, D. Laundy, V. Dhamgaye, O. J. L. Fox, K. Sawhney, and A. M. Korsunsky, "Hard X-ray ptychography for optics characterization using a partially coherent synchrotron source," *Journal of Synchrotron Radiation*, vol. 27, pp. 1688–1695, Nov 2020.

[51] T. E. J. Moxham, D. Laundy, V. Dhamgaye, O. J. L. Fox, K. Sawhney, and A. M. Korsunsky, "Aberration characterization of x-ray optics using multimodal ptychography and a partially coherent source," *Applied Physics Letters*, vol. 118, no. 10, p. 104104, 2021.

[52] A. Macrander, M. Wojcik, J. Maser, N. Bouet, and R. Conley, "Focus of a multilayer Laue lens with an aperture of 102 microns determined by ptychography at beamline 1-BM at the Advanced Photon Source," in *X-Ray Nanoimaging: Instruments and Methods III* (B. Lai and A. Somogyi, eds.), vol. 10389, pp. 1 – 6, International Society for Optics and Photonics, SPIE, 2017.

[53] J. C. da Silva, A. Pacureanu, Y. Yang, S. Bohic, C. Morawe, R. Barrett, and P. Cloetens, "Efficient concentration of high-energy x-rays for diffraction-limited imaging resolution," *Optica*, vol. 4, pp. 492–495, May 2017.

[54] N. Burdet, K. Shimomura, M. Hirose, A. Suzuki, and Y. Takahashi, "Efficient use of coherent x-rays in ptychography: Towards high-resolution and high-throughput observation of weak-phase objects," *Applied Physics Letters*, vol. 108, no. 7, p. 071103, 2016.

[55] B. Enders, M. Dierolf, P. Cloetens, M. Stockmar, F. Pfeiffer, and P. Thibault, "Ptychography with broad-bandwidth radiation," *Applied Physics Letters*, vol. 104, no. 17, p. 171104, 2014.

[56] P. M. Pelz, M. Guizar-Sicairos, P. Thibault, I. Johnson, M. Holler, and A. Menzel, "On-the-fly scans for x-ray ptychography," *Applied Physics Letters*, vol. 105, no. 25, p. 251101, 2014.

[57] X. Huang, K. Lauer, J. N. Clark, W. Xu, E. Nazaretski, R. Harder, I. K. Robinson, and Y. S. Chu, "Fly-scan ptychography," *Scientific Reports*, vol. 5, no. 1, p. 9074, 2015.

[58] J. Deng, Y. S. G. Nashed, S. Chen, N. W. Phillips, T. Peterka, R. Ross, S. Vogt, C. Jacobsen, and D. J. Vine, "Continuous motion scan ptychography: characterization for increased speed in coherent x-ray imaging," *Opt. Express*, vol. 23, pp. 5438–5451, Mar 2015.

[59] M. Dierolf, A. Menzel, P. Thibault, P. Schneider, C. M. Kewish, R. Wepf, O. Bunk, and F. Pfeiffer, "Ptychographic x-ray computed tomography at the nanoscale," *Nature*, vol. 467, no. 7314, pp. 436–439, 2010.

[60] M. Holler, A. Diaz, M. Guizar-Sicairos, P. Karvinen, E. Färm, E. Härkönen, M. Ritala, A. Menzel, J. Raabe, and O. Bunk, "X-ray ptychographic computed tomography at 16 nm isotropic 3d resolution," *Scientific Reports*, vol. 4, no. 1, p. 3857, 2014.

[61] J. Deng, Y. H. Lo, M. Gallagher-Jones, S. Chen, A. Pryor, Q. Jin, Y. P. Hong, Y. S. G. Nashed, S. Vogt, J. Miao, and C. Jacobsen, "Correlative 3d x-ray fluorescence and ptychographic tomography of frozen-hydrated green algae," *Science Advances*, vol. 4, no. 11, p. eaau4548, 2018.

[62] P. Dong, S. Haupert, B. Hesse, M. Langer, P.-J. Gouttenoire, V. Bousson, and F. Peyrin, "3d osteocyte lacunar morphometric properties and distributions in human femoral cortical bone using synchrotron radiation micro-ct images," *Bone*, vol. 60, pp. 172–185, 2014.

[63] A. Ciani, H. Toumi, S. Pallu, E. H. Tsai, A. Diaz, M. Guizar-Sicairos, M. Holler, E. Lespessailles, and C. M. Kewish, "Ptychographic x-ray ct characterization of the osteocyte lacuno-canalicular network in a male rat's glucocorticoid induced osteoporosis model," *Bone Reports*, vol. 9, pp. 122–131, 2018.

[64] J. Ihli, L. Bloch, F. Krumeich, K. Wakonig, M. Holler, M. Guizar-Sicairos, T. Weber, J. C. da Silva, and J. A. van Bokhoven, "Hierarchical structure of nimo hydrodesulfurization catalysts determined by ptychographic x-ray computed tomography," *Angewandte Chemie International Edition*, vol. 59, no. 39, pp. 17266–17271, 2020.

[65] K. W. Bossers, R. Valadian, S. Zanoni, R. Smeets, N. Friederichs, J. Garrevoet, F. Meirer, and B. M. Weckhuysen, "Correlated x-ray ptychography and fluorescence nano-tomography on the fragmentation behavior of an individual catalyst particle during the early stages of olefin polymerization," *Journal of the American Chemical Society*, vol. 142, pp. 3691–3695, 02 2020.

[66] C. Donnelly, M. Guizar-Sicairos, V. Scagnoli, S. Gliga, M. Holler, J. Raabe, and L. J. Heyderman, "Three-dimensional magnetization structures revealed with x-ray vector nanotomography," *Nature*, vol. 547, no. 7663, pp. 328–331, 2017.

[67] Y.-S. Yu, M. Farmand, C. Kim, Y. Liu, C. P. Grey, F. C. Strobridge, T. Tyliszczak, R. Celestre, P. Denes, J. Joseph, H. Krishnan, F. R. N. C. Maia, A. L. D. Kilcoyne, S. Marchesini, T. P. C. Leite, T. Warwick, H. Padmore, J. Cabana, and D. A. Shapiro, "Three-dimensional localization of nanoscale battery reactions using soft x-ray tomography," *Nature Communications*, vol. 9, no. 1, p. 921, 2018.

[68] L. Romano Brandt, J.-J. Marie, T. Moxham, D. P. Förstermann, E. Salvati, C. Besnard, C. Papadaki, Z. Wang, P. G. Bruce, and A. M. Korsunsky, "Synchrotron x-ray quantitative evaluation of transient deformation and damage phenomena in a single nickel-rich cathode particle," *Energy Environ. Sci.*, vol. 13, pp. 3556–3566, 2020.

[69] K. J. S. Sawhney, I. P. Dolbnya, M. K. Tiwari, L. Alianelli, S. M. Scott, G. M. Preece, U. K. Pedersen, and R. D. Walton, "A test beamline on diamond light source," *AIP Conference Proceedings*, vol. 1234, no. 1, pp. 387–390, 2010.

[70] G. Materlik, T. Rayment, and D. I. Stuart, "Diamond light source: status and perspectives," *Philosophical Transactions of the Royal Society A: Math-*

ematical, Physical and Engineering Sciences, vol. 373, no. 2036, p. 20130161, 2015.

[71] F. R. Elder, A. M. Gurewitsch, R. V. Langmuir, and H. C. Pollock, "Radiation from electrons in a synchrotron," *Phys. Rev.*, vol. 71, pp. 829–830, Jun 1947.

[72] J. Larmor, "Xii. a dynamical theory of the electric and luminiferous medium," *Philosophical Transactions of the Royal Society of London. (A.)*, vol. 185, pp. 719–822, 1894.

[73] J. D. Jackson, *Classical electrodynamics*. New York ; Chichester: Wiley, 3rd ed. ed., 1999.

[74] M. Eriksson, "The multi-bend achromat storage rings," *AIP Conference Proceedings*, vol. 1741, no. 1, p. 020001, 2016.

[75] D. Attwood, *Soft X-Rays and Extreme Ultraviolet Radiation: Principles and Applications*. Cambridge University Press, 1999.

[76] J. A. Clarke, *The Science and Technology of Undulators and Wigglers*. Oxford Series on Synchrotron Radiation, Oxford: Oxford University Press, 2004.

[77] J. Bahrdt, W. Frentrup, A. Gaupp, M. Scheer, W. Gudat, G. Ingold, and S. Sasaki, "Elliptically polarizing insertion devices at bessy ii," *Nuclear Instruments and Methods in Physics Research Section A: Accelerators, Spectrometers, Detectors and Associated Equipment*, vol. 467-468, pp. 21–29, 2001. 7th Int.Conf. on Synchrotron Radiation Instrumentation.

[78] K.-J. Kim, Z. Huang, and R. Lindberg, *Synchrotron radiation and free-electron lasers : principles of coherent X-ray generation [electronic resource]*. Cambridge core, 2017.

[79] J. Liouville, "Sur le développement des fonctions ou parties de fonctions en séries," *J. Math. Pures Appl.*, vol. 2, pp. 16–35, 1837.

[80] C. Donnelly, V. Scagnoli, M. Guizar-Sicairos, M. Holler, F. Wilhelm, F. Guillou, A. Rogalev, C. Detlefs, A. Menzel, J. Raabe, and L. J. Heyderman, "High-resolution hard x-ray magnetic imaging with dichroic ptychography," *Phys. Rev. B*, vol. 94, p. 064421, Aug 2016.

[81] M. Blume, "Magnetic scattering of x rays (invited)," *Journal of Applied Physics*, vol. 57, no. 8, pp. 3615–3618, 1985.

[82] N. W. Ashcroft and N. D. Mermin, *Solid state physics*. 1976.

[83] R. de L. Kronig, "On the theory of dispersion of x-rays," *J. Opt. Soc. Am.*, vol. 12, pp. 547–557, Jun 1926.

[84] E. Hecht, *Optics*. Ebook central, fifth edition. global edition. ed., 2017.

[85] G. F. Knoll, *Radiation detection and measurement*. 4th edition ed., 2010.

[86] T. Hatsui and H. Graafsma, "X-ray imaging detectors for synchrotron and XFEL sources," *IUCrJ*, vol. 2, pp. 371–383, May 2015.

[87] A. Förster, S. Brandstetter, and C. Schulze-Briese, "Transforming x-ray detection with hybrid photon counting detectors," *Philosophical Transactions of the Royal Society A: Mathematical, Physical and Engineering Sciences*, vol. 377, no. 2147, p. 20180241, 2019.

[88] D. Paganin, *Coherent X-Ray Optics*. Oxford Series on Synchrotron Radiation, Oxford: Oxford University Press, 2006.

[89] M. J. Yaffe and J. A. Rowlands, "X-ray detectors for digital radiography," *Physics in Medicine and Biology*, vol. 42, pp. 1–39, jan 1997.

[90] L. Mandel and E. Wolf, *Optical coherence and quantum optics*. Cambridge: Cambridge University Press, 1995.

[91] J. Marchal, "Discriminator threshold dependence of the noise power spectrum in single-x-ray-photon counting silicon strip detectors," *Journal of Instrumentation*, vol. 5, pp. P11002–P11002, nov 2010.

[92] D. Walter, U. Zscherpel, and U. Ewert, "Photon counting and energy discriminating x-ray detectors benefits and applications," in *19"t"h World conference on non-destructive testing Proceedings*, (Germany), p. 4897, 2016.

[93] M. Campbell, "10 years of the medipix2 collaboration," *Nuclear Instruments and Methods in Physics Research Section A: Accelerators, Spectrometers, Detectors and Associated Equipment*, vol. 633, pp. S1–S10, 2011. 11th International Workshop on Radiation Imaging Detectors (IWORID).

[94] I. Johnson, A. Bergamaschi, J. Buitenhuis, R. Dinapoli, D. Greiffenberg, B. Henrich, T. Ikonen, G. Meier, A. Menzel, A. Mozzanica, V. Radicci, D. K. Satapathy, B. Schmitt, and X. Shi, "Capturing dynamics with Eiger, a fast-framing X-ray detector," *Journal of Synchrotron Radiation*, vol. 19, pp. 1001–1005, Nov 2012.

[95] C. Ponchut, "Characterization of X-ray area detectors for synchrotron beamlines," *Journal of Synchrotron Radiation*, vol. 13, pp. 195–203, Mar 2006.

[96] C. J. Hall and R. A. Lewis, "Detectors for x-ray coherent diffractive imaging," *Nuclear Instruments and Methods in Physics Research Section A: Accelerators, Spectrometers, Detectors and Associated Equipment*, vol. 604, no. 1, pp. 130–132, 2009. PSD8.

[97] M. Guizar-Sicairos, I. Johnson, A. Diaz, M. Holler, P. Karvinen, H.-C. Stadler, R. Dinapoli, O. Bunk, and A. Menzel, "High-throughput ptychography using eiger: scanning x-ray nano-imaging of extended regions," *Opt. Express*, vol. 22, pp. 14859–14870, Jun 2014.

[98] P. Vagovič, T. Sato, L. Mikeš, G. Mills, R. Graceffa, F. Mattsson, P. Villanueva-Perez, A. Ershov, T. Faragó, J. Uličný, H. Kirkwood, R. Letrun, R. Mokso, M.-C. Zdora, M. P. Olbinado, A. Rack, T. Baumbach, J. Schulz, A. Meents, H. N. Chapman, and A. P. Mancuso, "Megahertz x-ray microscopy at x-ray free-electron laser and synchrotron sources," *Optica*, vol. 6, pp. 1106–1109, Sep 2019.

[99] J. Zhang, E. Fretwurst, R. Klanner, H. Perrey, I. Pintilie, T. Poehlsen, and J. Schwandt, "Study of x-ray radiation damage in silicon sensors," *Journal of Instrumentation*, vol. 6, pp. C11013–C11013, nov 2011.

[100] C. G. B. F.R.S., "Xxxii. note on experiments to detect refraction of x-rays," *The London, Edinburgh, and Dublin Philosophical Magazine and Journal of Science*, vol. 31, no. 184, pp. 257–260, 1916.

[101] M. Kumakhov, "Channeling of photons and new x-ray optics," *Nuclear Instruments and Methods in Physics Research Section B: Beam Interactions with Materials and Atoms*, vol. 48, no. 1, pp. 283–286, 1990.

[102] F. Döring, A. Robisch, C. Eberl, M. Osterhoff, A. Ruhlandt, T. Liese, F. Schlenkrich, S. Hoffmann, M. Bartels, T. Salditt, and H. Krebs, "Sub-5 nm hard x-ray point focusing by a combined kirkpatrick-baez mirror and multilayer zone plate," *Opt. Express*, vol. 21, pp. 19311–19323, Aug 2013.

[103] J. Kirz, "Phase zone plates for x rays and the extreme uv," *J. Opt. Soc. Am.*, vol. 64, pp. 301–309, Mar 1974.

[104] J. Susini, "X-ray mirrors for high-brilliance synchrotron beamlines: R & d at the esrf," in *Proc.SPIE*, vol. 1740, 1 1993.

[105] B. Lengeler, C. G. Schroer, M. Kuhlmann, B. Benner, T. F. Günzler, O. Kurapova, F. Zontone, A. Snigirev, and I. Snigireva, "Refractive x-ray lenses," *Journal of Physics D: Applied Physics*, vol. 38, pp. A218–A222, may 2005.

[106] V. Aristov, M. Grigoriev, S. Kuznetsov, L. Shabelnikov, V. Yunkin, T. Weitkamp, C. Rau, I. Snigireva, A. Snigirev, M. Hoffmann, and E. Voges, "X-ray refractive planar lens with minimized absorption," *Applied Physics Letters*, vol. 77, no. 24, pp. 4058–4060, 2000.

[107] C. G. Schroer and B. Lengeler, "Focusing hard x rays to nanometer dimensions by adiabatically focusing lenses," *Phys. Rev. Lett.*, vol. 94, p. 054802, Feb 2005.

[108] O. Hignette, P. Cloetens, G. Rostaing, P. Bernard, and C. Morawe, "Efficient sub 100nm focusing of hard x rays," *Review of Scientific Instruments*, vol. 76, no. 6, p. 063709, 2005.

[109] W. Jark, A. Cedola, S. Di Fonzo, M. Fiordelisi, S. Lagomarsino, N. V. Kovalenko, and V. A. Chernov, "High gain beam compression in new-generation thin-film x-ray waveguides," *Applied Physics Letters*, vol. 78, no. 9, pp. 1192–1194, 2001.

[110] T. Salditt and M. Osterhoff, *X-ray Focusing and Optics*, pp. 71–124. Cham: Springer International Publishing, 2020.

[111] J. E. Greivenkamp, *Field guide to geometrical optics*. SPIE field guides ; FG01, Bellingham, Wash.: SPIE, 2004.

[112] J. Engelberg and U. Levy, "The advantages of metalenses over diffractive lenses," *Nature Communications*, vol. 11, no. 1, p. 1991, 2020.

[113] L. R. F.R.S., "Investigations in optics, with special reference to the spectroscope," *The London, Edinburgh, and Dublin Philosophical Magazine and Journal of Science*, vol. 8, no. 49, pp. 261–274, 1879.

[114] B. Yang, "Fresnel and refractive lenses for x-rays," *Nuclear Instruments and Methods in Physics Research Section A: Accelerators, Spectrometers, Detectors and Associated Equipment*, vol. 328, no. 3, pp. 578–587, 1993.

[115] M. Sanchez del Rio and L. Alianelli, "Aspherical lens shapes for focusing synchrotron beams," *Journal of Synchrotron Radiation*, vol. 19, pp. 366–374, May 2012.

[116] K. Evans-Lutterodt, J. M. Ablett, A. Stein, C.-C. Kao, D. M. Tennant, F. Klemens, A. Taylor, C. Jacobsen, P. L. Gammel, H. Huggins, S. Ustin, G. Bogart, and L. Ocola, "Single-element elliptical hard x-ray micro-optics," *Opt. Express*, vol. 11, pp. 919–926, Apr 2003.

[117] C. G. Schroer, M. Kuhlmann, U. T. Hunger, T. F. Günzler, O. Kurapova, S. Feste, F. Frehse, B. Lengeler, M. Drakopoulos, A. Somogyi, A. S. Simionovici, A. Snigirev, I. Snigireva, C. Schug, and W. H. Schröder, "Nanofocusing parabolic refractive x-ray lenses," *Applied Physics Letters*, vol. 82, no. 9, pp. 1485–1487, 2003.

[118] C. G. Schroer, B. Lengeler, B. Benner, T. F. Guenzler, M. Kuhlmann, A. S. Simionovici, S. Bohic, M. Drakopoulos, A. A. Snigirev, I. Snigireva, and W. H. Schroeder, "Microbeam production using compound refractive lenses: beam characterization and applications," in *X-Ray Micro- and Nano-Focusing: Applications and Techniques II* (I. McNulty, ed.), vol. 4499, pp. 52 – 63, International Society for Optics and Photonics, SPIE, 2001.

[119] M. Polikarpov, H. Emerich, N. Klimova, I. Snigireva, V. Savin, and A. Snigirev, "Spectral x-ray glitches in monocrystalline diamond refractive lenses," *physica status solidi (b)*, vol. 255, no. 1, p. 1700229, 2018.

[120] F. Marschall, A. Last, M. Simon, H. Vogt, and J. Mohr, "Simulation of aperture-optimised refractive lenses for hard x-ray full field microscopy," *Opt. Express*, vol. 24, pp. 10880–10889, May 2016.

[121] C. G. Schroer, F.-E. Brack, R. Brendler, S. Hönig, R. Hoppe, J. Patommel, S. Ritter, M. Scholz, A. Schropp, F. Seiboth, D. Nilsson, J. Rahomäki,

F. Uhlén, U. Vogt, J. Reinhardt, and G. Falkenberg, "Hard x-ray nanofocusing with refractive x-ray optics: full beam characterization by ptychographic imaging," in *Advances in X-Ray/EUV Optics and Components VIII* (A. Khounsary, S. Goto, and C. Morawe, eds.), vol. 8848, pp. 38 – 47, International Society for Optics and Photonics, SPIE, 2013.

[122] A. P. Mancuso, A. Aquila, L. Batchelor, R. J. Bean, J. Bielecki, G. Borchers, K. Doerner, K. Giewekemeyer, R. Graceffa, O. D. Kelsey, Y. Kim, H. J. Kirkwood, A. Legrand, R. Letrun, B. Manning, L. Lopez Morillo, M. Messerschmidt, G. Mills, S. Raabe, N. Reimers, A. Round, T. Sato, J. Schulz, C. Signe Takem, M. Sikorski, S. Stern, P. Thute, P. Vagovič, B. Weinhausen, and T. Tschentscher, "The Single Particles, Clusters and Biomolecules and Serial Femtosecond Crystallography instrument of the European XFEL: initial installation," *Journal of Synchrotron Radiation*, vol. 26, pp. 660–676, May 2019.

[123] C. G. Schroer, "Focusing hard x rays to nanometer dimensions using fresnel zone plates," *Phys. Rev. B*, vol. 74, p. 033405, Jul 2006.

[124] K. Keskinbora, C. Grévent, M. Bechtel, M. Weigand, E. Goering, A. Nadzeyka, L. Peto, S. Rehbein, G. Schneider, R. Follath, J. Vila-Comamala, H. Yan, and G. Schütz, "Ion beam lithography for fresnel zone plates in x-ray microscopy," *Opt. Express*, vol. 21, pp. 11747–11756, May 2013.

[125] H. Yan, J. Maser, A. Macrander, Q. Shen, S. Vogt, G. B. Stephenson, and H. C. Kang, "Takagi-taupin description of x-ray dynamical diffraction from diffractive optics with large numerical aperture," *Phys. Rev. B*, vol. 76, p. 115438, Sep 2007.

[126] H. Yan, R. Conley, N. Bouet, and Y. S. Chu, "Hard x-ray nanofocusing by mul-

tilayer laue lenses," *Journal of Physics D: Applied Physics*, vol. 47, p. 263001, jun 2014.

[127] R. Conley, N. Bouet, Y. S. Chu, X. Huang, H. C. Kang, A. T. Macrander, J. Maser, E. Nazaretski, G. B. Stephenson, and H. Yan, "Multilayer laue lens: A brief history and current status," *Synchrotron Radiation News*, vol. 29, no. 4, pp. 16–20, 2016.

[128] H. C. Kang, G. B. Stephenson, C. Liu, R. Conley, A. T. Macrander, J. Maser, S. Bajt, and H. N. Chapman, "High-efficiency diffractive x-ray optics from sectioned multilayers," *Applied Physics Letters*, vol. 86, no. 15, p. 151109, 2005.

[129] K. T. Murray, A. F. Pedersen, I. Mohacsi, C. Detlefs, A. J. Morgan, M. Prasciolu, C. Yildirim, H. Simons, A. C. Jakobsen, H. N. Chapman, H. F. Poulsen, and S. Bajt, "Multilayer laue lenses at high x-ray energies: performance and applications," *Opt. Express*, vol. 27, pp. 7120–7138, Mar 2019.

[130] C. Liu, R. Conley, A. T. Macrander, J. Maser, H. C. Kang, M. A. Zurbuchen, and G. B. Stephenson, "Depth-graded multilayers for application in transmission geometry as linear zone plates," *Journal of Applied Physics*, vol. 98, no. 11, p. 113519, 2005.

[131] X. Huang, H. Yan, E. Nazaretski, R. Conley, N. Bouet, J. Zhou, K. Lauer, L. Li, D. Eom, D. Legnini, R. Harder, I. K. Robinson, and Y. S. Chu, "11 nm hard x-ray focus from a large-aperture multilayer laue lens," *Scientific Reports*, vol. 3, no. 1, p. 3562, 2013.

[132] A. J. Morgan, M. Prasciolu, A. Andrejczuk, J. Krzywinski, A. Meents, D. Pennicard, H. Graafsma, A. Barty, R. J. Bean, M. Barthelmess, D. Oberthuer, O. Yefanov, A. Aquila, H. N. Chapman, and S. Bajt, "High numerical aperture multilayer laue lenses," *Scientific Reports*, vol. 5, no. 1, p. 9892, 2015.

[133] A. Somogyi, C. M. Kewish, F. Polack, and T. Moreno, "The scanning nanoprobe beamline nanoscopium at synchrotron soleil," *AIP Conference Proceedings*, vol. 1365, no. 1, pp. 57–60, 2011.

[134] M. Kahnt, K. Klementiev, V. Haghighat, C. Weninger, T. S. Plivelic, A. E. Terry, and A. Björling, "Measurement of the coherent beam properties at the CoSAXS beamline," *Journal of Synchrotron Radiation*, vol. 28, pp. 1948–1953, Nov 2021.

[135] P. D. Quinn, L. Alianelli, M. Gomez-Gonzalez, D. Mahoney, F. Cacho-Nerin, A. Peach, and J. E. Parker, "The Hard X-ray Nanoprobe beamline at Diamond Light Source," *Journal of Synchrotron Radiation*, vol. 28, pp. 1006–1013, May 2021.

[136] A. Khounsary, C. Morawe, and M. Osterhoff, "Hard x-ray focusing with curved reflective multilayers," *X-Ray Optics and Instrumentation*, vol. 2010, p. 479631, 2010.

[137] H. Mori, T. Okajima, W. W. Zhang, K.-W. Chan, R. Koenecke, J. R. Mazzarella, A. Numata, L. G. Olsen, R. E. Riveros, and M. Yukita, "Reflective coatings for the future x-ray mirror substrates," in *Space Telescopes and Instrumentation 2018: Ultraviolet to Gamma Ray* (J.-W. A. den Herder, S. Nikzad, and K. Nakazawa, eds.), vol. 10699, pp. 1012 – 1019, International Society for Optics and Photonics, SPIE, 2018.

[138] J. Susini, D. Pauschinger, R. Geyl, J.-J. Ferme, and G. Vieux, "Hard x-ray mirror fabrication capabilities in europe," *Optical Engineering*, vol. 34, pp. 388–395, 2 1995.

[139] C. Morawe, O. Hignette, P. Cloetens, W. Ludwig, C. Borel, P. Bernard, and A. Rommeveaux, "Graded multilayers for focusing hard x-rays below 50 nm," in *Proc.SPIE*, vol. 6317, 8 2006.

[140] V. V. Yashchuk, L. V. Samoylova, and I. V. Kozhevnikov, "Specification of x-ray mirrors in terms of system performance: new twist to an old plot," *Optical Engineering*, vol. 54, no. 2, pp. 1 – 13, 2015.

[141] M. Wen, I. V. Kozhevnikov, F. Siewert, A. V. Buzmakov, C. Xie, Q. Huang, Z. Wang, L. Samoylova, and H. Sinn, "Effect of the surface roughness on x-ray absorption by mirrors operating at extremely small grazing angles," *Opt. Express*, vol. 26, pp. 21003–21018, Aug 2018.

[142] K. Yamauchi, H. Mimura, K. Inagaki, and Y. Mori, "Figuring with subnanometer-level accuracy by numerically controlled elastic emission machining," *Review of Scientific Instruments*, vol. 73, no. 11, pp. 4028–4033, 2002.

[143] M. Demmler, M. Zeuner, F. Allenstein, T. Dunger, M. Nestler, and S. Kiontke, "Ion beam figuring (IBF) for high precision optics," in *Advanced Fabrication Technologies for Micro/Nano Optics and Photonics III* (W. V. Schoenfeld, J. J. Wang, M. Loncar, and T. J. Suleski, eds.), vol. 7591, pp. 203 – 211, International Society for Optics and Photonics, SPIE, 2010.

[144] M. Hand, S. G. Alcock, M. Hillman, R. Littlewood, S. Moriconi, H. Wang, and K. Sawhney, "Ion beam figuring and optical metrology system for synchrotron x-ray mirrors," in *Advances in Metrology for X-Ray and EUV Optics VIII* (L. Assoufid, H. Ohashi, and A. Asundi, eds.), vol. 11109, pp. 51 – 57, International Society for Optics and Photonics, SPIE, 2019.

[145] C. Morawe, P. Pecci, J. C. Peffen, and E. Ziegler, "Design and performance of graded multilayers as focusing elements for x-ray optics," *Review of Scientific Instruments*, vol. 70, no. 8, pp. 3227–3232, 1999.

[146] D. L. Windt, F. E. Christensen, W. W. Craig, C. Hailey, F. A. Harrison, M. Jimenez-Garate, R. Kalyanaraman, and P. H. Mao, "Growth, structure,

and performance of depth-graded w/si multilayers for hard x-ray optics," *Journal of Applied Physics*, vol. 88, no. 1, pp. 460–470, 2000.

[147] J. Kim, H. Yokoyama, S. Matsuyama, Y. Sano, and K. Yamauchi, "Improved reflectivity of platinum/carbon multilayers for x-ray mirrors by carbon doping into platinum layer," *Current Applied Physics*, vol. 12, pp. S20–S23, 2012. The 4th International Symposium on Atomically Controlled Fabrication Technology.

[148] A. Rack, L. Assoufid, W.-K. Lee, B. Shi, C. Liu, C. Morawe, R. Kluender, R. Conley, and N. Bouet, "Hard x-ray multilayer mirror round-robin on the wavefront preservation capabilities of w/b4c coatings," *Radiation Physics and Chemistry*, vol. 81, no. 11, pp. 1696–1702, 2012.

[149] C. Burcklen, T. Pardini, J. Alameda, J. Robinson, Y. Platonov, C. Walton, and R. Soufli, "Depth-graded mo/si multilayer coatings for hard x-rays," *Opt. Express*, vol. 27, pp. 7291–7306, Mar 2019.

[150] C. Morawe, R. Barrett, P. Cloetens, B. Lantelme, J.-C. Peffen, and A. Vivo, "Graded multilayers for figured Kirkpatrick-Baez mirrors on the new ESRF end station ID16A," in *Advances in X-Ray/EUV Optics and Components X* (S. Goto, C. Morawe, and A. M. Khounsary, eds.), vol. 9588, pp. 8 – 14, International Society for Optics and Photonics, SPIE, 2015.

[151] S. Matsuyama, T. Inoue, J. Yamada, J. Kim, H. Yumoto, Y. Inubushi, T. Osaka, I. Inoue, T. Koyama, K. Tono, H. Ohashi, M. Yabashi, T. Ishikawa, and K. Yamauchi, "Nanofocusing of x-ray free-electron laser using wavefront-corrected multilayer focusing mirrors," *Scientific Reports*, vol. 8, no. 1, p. 17440, 2018.

[152] W. Chao, P. Fischer, T. Tyliszczak, S. Rekawa, E. Anderson, and P. Naulleau,

"Real space soft x-ray imaging at 10 nm spatial resolution," *Opt. Express*, vol. 20, pp. 9777–9783, Apr 2012.

[153] G. Schneider, "Cryo x-ray microscopy with high spatial resolution in amplitude and phase contrast," *Ultramicroscopy*, vol. 75, no. 2, pp. 85–104, 1998.

[154] Y.-A. Soh, P. G. Evans, Z. Cai, B. Lai, C.-Y. Kim, G. Aeppli, N. D. Mathur, M. G. Blamire, and E. D. Isaacs, "Local mapping of strain at grain boundaries in colossal magnetoresistive films using x-ray microdiffraction," *Journal of Applied Physics*, vol. 91, no. 10, pp. 7742–7744, 2002.

[155] M. L. Rivers, S. R. Sutton, and K. W. Jones, "Synchrotron x-ray fluorescence microscopy," *Synchrotron Radiation News*, vol. 4, no. 2, pp. 23–26, 1991.

[156] H. Ade, X. Zhang, S. Cameron, C. Costello, J. Kirz, and S. Williams, "Chemical contrast in x-ray microscopy and spatially resolved xanes spectroscopy of organic specimens," *Science*, vol. 258, no. 5084, pp. 972–975, 1992.

[157] D. C. O'Shea, T. J. Suleski, A. D. Kathman, and D. W. Prather, *Electromagnetic Analysis of Diffractive Optical Elements*, pp. 37–57. SPIE, 2003. `https://www.spiedigitallibrary.org/ebooks/TT/Diffractive-Optics-Design-Fabrication-and-Test/3/Electromagnetic-Analysis-of-Diffractive-Optical-Elements/10.1117/3.527861.ch3`.

[158] O. Chubar, A. Fluerasu, L. Berman, K. Kaznatcheev, and L. Wiegart, "Wavefront propagation simulations for beamlines and experiments with "synchrotron radiation workshop"," *Journal of Physics: Conference Series*, vol. 425, p. 162001, mar 2013.

[159] J. W. Goodman, *Introduction to Fourier optics*. fourth edition. ed., 2017.

[160] K. F. Riley, M. P. Hobson, and S. J. Bence, *Mathematical methods for physics and engineering [electronic resource]*. 3rd ed. ed., 2006.

[161] H. S. Green and E. Wolf, "A scalar representation of electromagnetic fields," *Proceedings of the Physical Society. Section A*, vol. 66, pp. 1129–1137, dec 1953.

[162] E. W. Marchand and E. Wolf, "Consistent formulation of kirchhoff's diffraction theory∗," *J. Opt. Soc. Am.*, vol. 56, pp. 1712–1721, Dec 1966.

[163] B. B. Baker and E. T. Copson, *The mathematical theory of Huygens' principle*. Providence, Rhode Island: AMS Chelsea Publishing, 3rd ed. ed., 1987.

[164] W. H. Southwell, "Validity of the fresnel approximation in the near field," *J. Opt. Soc. Am.*, vol. 71, pp. 7–14, Jan 1981.

[165] D. Gabor, "A new microscopic principle," *Nature*, vol. 161, no. 4098, pp. 777–778, 1948.

[166] D. Sayre, "Some implications of a theorem due to Shannon," *Acta Crystallographica*, vol. 5, p. 843, Nov 1952.

[167] W.-B. Yun, J. Kirz, and D. Sayre, "Observation of the soft X-ray diffraction pattern of a single diatom," *Acta Crystallographica Section A*, vol. 43, pp. 131–133, Jan 1987.

[168] J. Miao, P. Charalambous, J. Kirz, and D. Sayre, "Extending the methodology of x-ray crystallography to allow imaging of micrometre-sized non-crystalline specimens," *Nature*, vol. 400, no. 6742, pp. 342–344, 1999.

[169] J. R. Fienup, "Reconstruction of an object from the modulus of its fourier transform," *Opt. Lett.*, vol. 3, pp. 27–29, Jul 1978.

[170] J. Miao, T. Ishikawa, B. Johnson, E. H. Anderson, B. Lai, and K. O. Hodgson, "High resolution 3d x-ray diffraction microscopy," *Phys. Rev. Lett.*, vol. 89, p. 088303, Aug 2002.

[171] C. Shannon, "Communication in the presence of noise," *Proceedings of the IRE*, vol. 37, no. 1, pp. 10–21, 1949.

[172] R. W. Gerchberg and W. O. Saxton, "A practical algorithm for the determination of phase from image and diffraction plane pictures," *Optik*, vol. 35, no. 2, pp. 237–246, 1972.

[173] S. Marchesini, H. He, H. N. Chapman, S. P. Hau-Riege, A. Noy, M. R. Howells, U. Weierstall, and J. C. H. Spence, "X-ray image reconstruction from a diffraction pattern alone," *Phys. Rev. B*, vol. 68, p. 140101, Oct 2003.

[174] J. P. Abrahams and A. G. W. Leslie, "Methods used in the structure determination of bovine mitochondrial F_1 ATPase," *Acta Crystallographica Section D*, vol. 52, pp. 30–42, Jan 1996.

[175] D. R. Luke, "Relaxed averaged alternating reflections for diffraction imaging," *Inverse Problems*, vol. 21, pp. 37–50, nov 2004.

[176] V. Elser, "Phase retrieval by iterated projections," *J. Opt. Soc. Am. A*, vol. 20, pp. 40–55, Jan 2003.

[177] S. Marchesini, "Invited article: A unified evaluation of iterative projection algorithms for phase retrieval," *Review of Scientific Instruments*, vol. 78, no. 1, p. 011301, 2007.

[178] R. Hegerl and W. Hoppe, "Dynamic theory of crystalline structure analysis by electron diffraction in inhomogeneous primary wave field," *Berichte Der Bunsen- Gesellschaft Fur Physikalische Chemie*, vol. 74, no. 11, p. 1148, 1970.

[179] H. M. L. Faulkner and J. M. Rodenburg, "Movable aperture lensless transmission microscopy: A novel phase retrieval algorithm," *Phys. Rev. Lett.*, vol. 93, p. 023903, Jul 2004.

[180] J. M. Rodenburg and R. H. T. Bates, "The theory of super-resolution electron microscopy via wigner-distribution deconvolution," *Philosophical Transactions of the Royal Society of London. Series A: Physical and Engineering Sciences*, vol. 339, no. 1655, pp. 521–553, 1992.

[181] G. J. Williams, H. M. Quiney, B. B. Dhal, C. Q. Tran, K. A. Nugent, A. G. Peele, D. Paterson, and M. D. de Jonge, "Fresnel coherent diffractive imaging," *Phys. Rev. Lett.*, vol. 97, p. 025506, Jul 2006.

[182] B. Abbey, K. A. Nugent, G. J. Williams, J. N. Clark, A. G. Peele, M. A. Pfeifer, M. de Jonge, and I. McNulty, "Keyhole coherent diffractive imaging," *Nature Physics*, vol. 4, no. 5, pp. 394–398, 2008.

[183] H. Chang, P. Enfedaque, J. Zhang, J. Reinhardt, B. Enders, Y.-S. Yu, D. Shapiro, C. G. Schroer, T. Zeng, and S. Marchesini, "Advanced denoising for x-ray ptychography," *Opt. Express*, vol. 27, pp. 10395–10418, Apr 2019.

[184] A. Maiden, M. Humphry, M. Sarahan, B. Kraus, and J. Rodenburg, "An annealing algorithm to correct positioning errors in ptychography," *Ultramicroscopy*, vol. 120, pp. 64–72, 2012.

[185] P. Dwivedi, A. Konijnenberg, S. Pereira, and H. Urbach, "Lateral position correction in ptychography using the gradient of intensity patterns," *Ultramicroscopy*, vol. 192, pp. 29–36, 2018.

[186] L. Lötgering, M. Rose, K. Keskinbora, M. Baluktsian, G. Dogan, U. Sanli, I. Bykova, M. Weigand, G. Schütz, and T. Wilhein, "Correction of axial position uncertainty and systematic detector errors in ptychographic diffraction imaging," *Optical Engineering*, vol. 57, no. 8, pp. 1 – 7, 2018.

[187] M. Odstrcil, P. Baksh, S. A. Boden, R. Card, J. E. Chad, J. G. Frey, and W. S. Brocklesby, "Ptychographic coherent diffractive imaging with orthogonal probe relaxation," *Opt. Express*, vol. 24, pp. 8360–8369, Apr 2016.

[188] M. Beckers, T. Senkbeil, T. Gorniak, K. Giewekemeyer, T. Salditt, and A. Rosenhahn, "Drift correction in ptychographic diffractive imaging," *Ultramicroscopy*, vol. 126, pp. 44–47, 2013.

[189] B. Enders and P. Thibault, "A computational framework for ptychographic reconstructions," *Proceedings of the Royal Society A: Mathematical, Physical and Engineering Sciences*, vol. 472, no. 2196, p. 20160640, 2016.

[190] O. Bunk, M. Dierolf, S. Kynde, I. Johnson, O. Marti, and F. Pfeiffer, "Influence of the overlap parameter on the convergence of the ptychographical iterative engine," *Ultramicroscopy*, vol. 108, no. 5, pp. 481–487, 2008.

[191] M. Pham, A. Rana, J. Miao, and S. Osher, "Semi-implicit relaxed douglas-rachford algorithm (sdr) for ptychography," *Opt. Express*, vol. 27, pp. 31246–31260, Oct 2019.

[192] P. Thibault and M. Guizar-Sicairos, "Maximum-likelihood refinement for coherent diffractive imaging," *New Journal of Physics*, vol. 14, p. 063004, jun 2012.

[193] A. Maiden, D. Johnson, and P. Li, "Further improvements to the ptychographical iterative engine," *Optica*, vol. 4, pp. 736–745, Jul 2017.

[194] Y. S. G. Nashed, D. J. Vine, T. Peterka, J. Deng, R. Ross, and C. Jacobsen, "Parallel ptychographic reconstruction," *Opt. Express*, vol. 22, pp. 32082–32097, Dec 2014.

[195] M. Guizar-Sicairos, M. Holler, A. Diaz, J. Vila-Comamala, O. Bunk, and

A. Menzel, "Role of the illumination spatial-frequency spectrum for ptychography," *Phys. Rev. B*, vol. 86, p. 100103, Sep 2012.

[196] M. Odstrčil, M. Lebugle, M. Guizar-Sicairos, C. David, and M. Holler, "Towards optimized illumination for high-resolution ptychography," *Opt. Express*, vol. 27, pp. 14981–14997, May 2019.

[197] P. Li, D. J. Batey, T. B. Edo, A. D. Parsons, C. Rau, and J. M. Rodenburg, "Multiple mode x-ray ptychography using a lens and a fixed diffuser optic," *Journal of Optics*, vol. 18, p. 054008, mar 2016.

[198] G. Geloni, E. Saldin, E. Schneidmiller, and M. Yurkov, "Transverse coherence properties of x-ray beams in third-generation synchrotron radiation sources," *Nuclear Instruments and Methods in Physics Research Section A: Accelerators, Spectrometers, Detectors and Associated Equipment*, vol. 588, no. 3, pp. 463–493, 2008.

[199] J. W. Goodman, *Statistical optics*. Wiley series in pure and applied optics, second edition. ed., 2015.

[200] E. Wolf, "New theory of partial coherence in the space–frequency domain. part i: spectra and cross spectra of steady-state sources," *J. Opt. Soc. Am.*, vol. 72, pp. 343–351, Mar 1982.

[201] K. A. Nugent, "Coherent methods in the x-ray sciences," *Advances in Physics*, vol. 59, no. 1, pp. 1–99, 2010.

[202] I. A. Vartanyants and A. Singer, "Coherence properties of hard x-ray synchrotron sources and x-ray free-electron lasers," *New Journal of Physics*, vol. 12, p. 035004, mar 2010.

[203] P. Li, T. Edo, D. Batey, J. Rodenburg, and A. Maiden, "Breaking ambiguities in mixed state ptychography," *Opt. Express*, vol. 24, pp. 9038–9052, Apr 2016.

[204] A. S. Ostrovsky, *Coherent-Mode Representation of Optical Systems*, pp. 15–30. SPIE, 2006. https://www.spiedigitallibrary.org/ebooks/PM/Coherent-Mode-Representations-in-Optics/2/Coherent-Mode-Representation-of-Optical-Systems/10.1117/3.680516.ch2.

[205] J. Rodenburg and A. Maiden, *Ptychography*, pp. 819–904. Cham: Springer International Publishing, 2019.

[206] T. B. Edo, D. J. Batey, A. M. Maiden, C. Rau, U. Wagner, Z. D. Pešić, T. A. Waigh, and J. M. Rodenburg, "Sampling in x-ray ptychography," *Phys. Rev. A*, vol. 87, p. 053850, May 2013.

[207] J. C. da Silva and A. Menzel, "Elementary signals in ptychography," *Opt. Express*, vol. 23, pp. 33812–33821, Dec 2015.

[208] X. Huang, H. Yan, R. Harder, Y. Hwu, I. K. Robinson, and Y. S. Chu, "Optimization of overlap uniformness for ptychography," *Opt. Express*, vol. 22, pp. 12634–12644, May 2014.

[209] D. J. Batey, *Ptychographic imaging of mixed states*. PhD thesis, University of Sheffield, 2014.

[210] G. Cadenazzi, B. Chen, T. Gureyev, H. M. Quiney, K. A. Nugent, and B. Abbey, "Partial coherence and the influence of overlap and curvature in ptychography," in *Nanophotonics Australasia 2017* (J. W. M. Chon and B. Jia, eds.), vol. 10456, pp. 335 – 343, International Society for Optics and Photonics, SPIE, 2018.

[211] E. P. Goodwin and J. C. Wyant, *Field guide to interferometric optical testing [electronic resource]*. SPIE field guides ; FG10, Bellingham, Wash. (1000 20th St. Bellingham WA 98225-6705 USA): SPIE, 2006.

[212] Y. Takahashi, A. Suzuki, N. Zettsu, Y. Kohmura, Y. Senba, H. Ohashi, K. Yamauchi, and T. Ishikawa, "Towards high-resolution ptychographic x-ray diffraction microscopy," *Phys. Rev. B*, vol. 83, p. 214109, Jun 2011.

[213] M. Van Heel, "Similarity measures between images," *Ultramicroscopy*, vol. 21, no. 1, pp. 95–100, 1987.

[214] W. O. Saxton and W. Baumeister, "The correlation averaging of a regularly arranged bacterial cell envelope protein," *Journal of Microscopy*, vol. 127, no. 2, pp. 127–138, 1982.

[215] J. Vila-Comamala, A. Diaz, M. Guizar-Sicairos, A. Mantion, C. M. Kewish, A. Menzel, O. Bunk, and C. David, "Characterization of high-resolution diffractive x-ray optics by ptychographic coherent diffractive imaging," *Opt. Express*, vol. 19, pp. 21333–21344, Oct 2011.

[216] M. van Heel and M. Schatz, "Fourier shell correlation threshold criteria," *Journal of Structural Biology*, vol. 151, no. 3, pp. 250–262, 2005.

[217] D. J. Batey, T. B. Edo, C. Rau, U. Wagner, Z. D. Pešić, T. A. Waigh, and J. M. Rodenburg, "Reciprocal-space up-sampling from real-space oversampling in x-ray ptychography," *Phys. Rev. A*, vol. 89, p. 043812, Apr 2014.

[218] R. Okuta, T. Unno, D. Nishino, S. Hido, and C. Loomis, "Cupy a numpy-compatible library for nvidia gpu calculations," in *Proceedings of Workshop on Machine Learning Systems (LearningSys) in the Thirty-First Annual Conference on Neural Information Processing Systems (NIPS)*, 2017.

[219] K. Wakonig, H.-C. Stadler, M. Odstrčil, E. H. R. Tsai, A. Diaz, M. Holler, I. Usov, J. Raabe, A. Menzel, and M. Guizar-Sicairos, "*PtychoShelves*, a versatile high-level framework for high-performance analysis of ptychographic data," *Journal of Applied Crystallography*, vol. 53, pp. 574–586, Apr 2020.

[220] M. Odstrčil, A. Menzel, and M. Guizar-Sicairos, "Iterative least-squares solver for generalized maximum-likelihood ptychography," *Opt. Express*, vol. 26, pp. 3108–3123, Feb 2018.

[221] E. H. R. Tsai, I. Usov, A. Diaz, A. Menzel, and M. Guizar-Sicairos, "X-ray ptychography with extended depth of field," *Opt. Express*, vol. 24, pp. 29089–29108, Dec 2016.

[222] K. Tamasaku, Y. Tanaka, M. Yabashi, H. Yamazaki, N. Kawamura, M. Suzuki, and T. Ishikawa, "Spring-8 riken beamline iii for coherent x-ray optics," *Nuclear Instruments and Methods in Physics Research Section A: Accelerators, Spectrometers, Detectors and Associated Equipment*, vol. 467-468, pp. 686–689, 2001. 7th Int.Conf. on Synchrotron Radiation Instrumentation.

[223] C. Rau, U. Wagner, Z. Pešić, and A. De Fanis, "Coherent imaging at the diamond beamline i13," *physica status solidi (a)*, vol. 208, no. 11, pp. 2522–2525, 2011.

[224] R. Celestre, O. Chubar, T. Roth, M. S. del Rio, and R. Barrett, "Recent developments in X-ray lens modelling with SRW," in *Advances in Computational Methods for X-Ray Optics V* (O. Chubar and K. Sawhney, eds.), vol. 11493, pp. 88 – 101, International Society for Optics and Photonics, SPIE, 2020.

[225] F. Mastropietro, D. Carbone, A. Diaz, J. Eymery, A. Sentenac, T. H. Metzger, V. Chamard, and V. Favre-Nicolin, "Coherent x-ray wavefront reconstruction of a partially illuminated fresnel zone plate," *Opt. Express*, vol. 19, pp. 19223–19232, Sep 2011.

[226] C. M. Kewish, M. Guizar-Sicairos, C. Liu, J. Qian, B. Shi, C. Benson, A. M. Khounsary, J. Vila-Comamala, O. Bunk, J. R. Fienup, A. T. Macrander, and L. Assoufid, "Reconstruction of an astigmatic hard x-ray beam and alignment

of k-b mirrors from ptychographic coherent diffraction data," *Opt. Express*, vol. 18, pp. 23420–23427, Oct 2010.

[227] E. L. Church and P. Z. Takacs, "Specification of surface figure and finish in terms of system performance," *Appl. Opt.*, vol. 32, pp. 3344–3353, Jul 1993.

[228] A. Maréchal, "Study of the combined effects of diffraction and geometrical aberrations on the image of a luminous point," *Rev. Opt. Theor. Instrum*, vol. 26, no. 257, 1947.

[229] X. Huang, M. Wojcik, N. Burdet, I. Peterson, G. R. Morrison, D. J. Vine, D. Legnini, R. Harder, Y. S. Chu, and I. K. Robinson, "Quantitative x-ray wavefront measurements of fresnel zone plate and k-b mirrors using phase retrieval," *Opt. Express*, vol. 20, pp. 24038–24048, Oct 2012.

[230] A. Schropp, R. Hoppe, V. Meier, J. Patommel, F. Seiboth, H. J. Lee, B. Nagler, E. C. Galtier, B. Arnold, U. Zastrau, J. B. Hastings, D. Nilsson, F. Uhlén, U. Vogt, H. M. Hertz, and C. G. Schroer, "Full spatial characterization of a nanofocused x-ray free-electron laser beam by ptychographic imaging," *Scientific Reports*, vol. 3, no. 1, p. 1633, 2013.

[231] S. Sala, B. J. Daurer, M. Odstrcil, F. Capotondi, E. Pedersoli, M. F. Hantke, M. Manfredda, N. D. Loh, P. Thibault, and F. R. N. C. Maia, "Pulse-to-pulse wavefront sensing at free-electron lasers using ptychography," *Journal of Applied Crystallography*, vol. 53, pp. 949–956, Aug 2020.

[232] Diamond Light Source, "I13: X-ray imaging and coherence." `https://www.diamond.ac.uk/Instruments/Imaging-and-Microscopy/I13.html`, Jul 2022.

[233] U. H. Wagner, S. Alcock, G. Ludbrook, J. Wiatryzk, and C. Rau, "Ultra-high performance mirror systems for the imaging and coherence beamline i13 at the

diamond light source," *AIP Conference Proceedings*, vol. 1437, no. 1, pp. 9–14, 2012.

[234] M. A. Herráez, D. R. Burton, M. J. Lalor, and M. A. Gdeisat, "Fast two-dimensional phase-unwrapping algorithm based on sorting by reliability following a noncontinuous path," *Appl. Opt.*, vol. 41, pp. 7437–7444, Dec 2002.

[235] S. Ali and C. Jacobsen, "Effect of tilt on circular zone plate performance," *J. Opt. Soc. Am. A*, vol. 37, pp. 374–383, Mar 2020.

[236] J. Antonello and M. Verhaegen, "Modal-based phase retrieval for adaptive optics," *J. Opt. Soc. Am. A*, vol. 32, pp. 1160–1170, Jun 2015.

[237] Z. Cai, B. Lai, W. Yun, E. Gluskin, D. Legnini, P. Ilinski, E. Trakhtenberg, S. Xu, W. Rodrigues, and H.-R. Lee, "Beam size measurement of the stored electron beam at the aps storage ring using zone plate optics and undulator radiation," *AIP Conference Proceedings*, vol. 417, no. 1, pp. 101–105, 1997.

[238] I. Robinson, "Optimisation of coherent x-ray diffraction imaging at ultrabright synchrotron sources," *Zeitschrift fur Kristallographie Supplements*, vol. 2008, 02 2008.

[239] L. W. Whitehead, G. J. Williams, H. M. Quiney, D. J. Vine, R. A. Dilanian, S. Flewett, K. A. Nugent, A. G. Peele, E. Balaur, and I. McNulty, "Diffractive imaging using partially coherent x rays," *Phys. Rev. Lett.*, vol. 103, p. 243902, Dec 2009.

[240] N. Burdet, X. Shi, D. Parks, J. N. Clark, X. Huang, S. D. Kevan, and I. K. Robinson, "Evaluation of partial coherence correction in x-ray ptychography," *Opt. Express*, vol. 23, pp. 5452–5467, Mar 2015.

[241] K. Stachnik, I. Mohacsi, I. Vartiainen, N. Stuebe, J. Meyer, M. Warmer, C. David, and A. Meents, "Influence of finite spatial coherence on ptycho-

graphic reconstruction," *Applied Physics Letters*, vol. 107, no. 1, p. 011105, 2015.

[242] Cheney, *Linear Algebra: Theory and Applications, 2nd Edition.* Jones & Bartlett Learning, 2010.

[243] J. N. Clark, X. Huang, R. J. Harder, and I. K. Robinson, "Dynamic imaging using ptychography," *Phys. Rev. Lett.*, vol. 112, p. 113901, Mar 2014.

[244] H. Xia, S. Montresor, R. Guo, J. Li, F. Yan, H. Cheng, and P. Picart, "Phase calibration unwrapping algorithm for phase data corrupted by strong decorrelation speckle noise," *Opt. Express*, vol. 24, pp. 28713–28730, Dec 2016.

[245] V. Dhamgaye, D. Laundy, S. Baldock, T. Moxham, and K. Sawhney, "Correction of the X-ray wavefront from compound refractive lenses using 3D printed refractive structures," *Journal of Synchrotron Radiation*, vol. 27, pp. 1518–1527, Nov 2020.

[246] J. Probst, C. Braig, E. Langlotz, I. Rahneberg, M. Kühnel, T. Zeschke, F. Siewert, T. Krist, and A. Erko, "Conception of diffractive wavefront correction for xuv and soft x-ray spectroscopy," *Appl. Opt.*, vol. 59, pp. 2580–2590, Mar 2020.

[247] R. Signorato, O. Hignette, and J. Goulon, "Multi-segmented piezoelectric mirrors as active/adaptive optics components," *Journal of Synchrotron Radiation*, vol. 5, pp. 797–800, May 1998.

[248] S. G. Alcock, J. P. Sutter, K. J. Sawhney, D. R. Hall, K. McAuley, and T. Sorensen, "Bimorph mirrors: The good, the bad, and the ugly," *Nuclear Instruments and Methods in Physics Research Section A: Accelerators, Spectrometers, Detectors and Associated Equipment*, vol. 710, pp. 87–92, 2013. The 4th international workshop on Metrology for X-ray Optics, Mirror Design, and Fabrication.

[249] R. Talman, "Possibility of corrector plate tuning of x-ray focusing," *Appl. Opt.*, vol. 48, pp. 2522–2535, May 2009.

[250] D. Laundy, V. Dhamgaye, T. Moxham, and K. Sawhney, "Adaptable refractive correctors for x-ray optics," *Optica*, vol. 6, pp. 1484–1490, Dec 2019.

[251] M. Polikarpov, T. V. Kononenko, V. G. Ralchenko, E. E. Ashkinazi, V. I. Konov, P. Ershov, S. Kuznetsov, V. Yunkin, I. Snigireva, V. M. Polikarpov, and A. Snigirev, "Diamond x-ray refractive lenses produced by femto-second laser ablation," in *Advances in X-Ray/EUV Optics and Components XI* (A. M. Khounsary, S. Goto, and C. Morawe, eds.), vol. 9963, pp. 96 – 104, International Society for Optics and Photonics, SPIE, 2016.

[252] F. Seiboth, A. Schropp, M. Scholz, F. Wittwer, C. Rödel, M. Wünsche, T. Ullsperger, S. Nolte, J. Rahomäki, K. Parfeniukas, S. Giakoumidis, U. Vogt, U. Wagner, C. Rau, U. Boesenberg, J. Garrevoet, G. Falkenberg, E. C. Galtier, H. J. Lee, B. Nagler, and C. G. Schroer, "Aberration correction for hard x-ray focusing at the nanoscale," in *Advances in X-Ray/EUV Optics and Components XII* (C. Morawe, A. M. Khounsary, and S. Goto, eds.), vol. 10386, pp. 41 – 50, International Society for Optics and Photonics, SPIE, 2017.

[253] S. Berujon, H. Wang, S. Alcock, and K. Sawhney, "At-wavelength metrology of hard x-ray mirror using near field speckle," *Opt. Express*, vol. 22, pp. 6438–6446, Mar 2014.

[254] V. P. Dhamgaye, G. S. Lodha, B. Gowri Sankar, and C. Kant, "Beamline BL-07 at Indus-2: a facility for microfabrication research," *Journal of Synchrotron Radiation*, vol. 21, pp. 259–263, Jan 2014.

[255] K. Sawhney, D. Laundy, T. Moxham, O. Fox, and V. Dhamgaye, "Development of pseudo-perfect x-ray optics using refractive compensators," *AIP Conference Proceedings*, vol. 2054, no. 1, p. 060003, 2019.

[256] F. Seiboth, D. Brückner, M. Kahnt, M. Lyubomirskiy, F. Wittwer, D. Dzhigaev, T. Ullsperger, S. Nolte, F. Koch, C. David, J. Garrevoet, G. Falkenberg, and C. G. Schroer, "Hard X-ray wavefront correction via refractive phase plates made by additive and subtractive fabrication techniques," *Journal of Synchrotron Radiation*, vol. 27, pp. 1121–1130, Sep 2020.

[257] T. Baldacchini, *Three-Dimensional Microfabrication Using Two-Photon Polymerization: Fundamentals, Technology, and Applications*. Norwich: Elsevier Science & Technology Books, 2015.

[258] A. W. Lohmann, "A new class of varifocal lenses," *Appl. Opt.*, vol. 9, pp. 1669–1671, Jul 1970.

[259] T. E. J. Moxham, V. Dhamgaye, D. Laundy, O. J. L. Fox, H. Khosroabadi, K. Sawhney, and A. M. Korsunsky, "Two-dimensional wavefront characterization of adaptable corrective optics and kirkpatrick-baez mirror system using ptychography," *Opt. Express*, vol. 30, pp. 19185–19198, May 2022.

[260] O. Salata, "Applications of nanoparticles in biology and medicine," *Journal of Nanobiotechnology*, vol. 2, no. 1, p. 3, 2004.

[261] M. Haruta and M. Daté, "Advances in the catalysis of au nanoparticles," *Applied Catalysis A: General*, vol. 222, no. 1, pp. 427–437, 2001. Celebration Issue.

[262] S. Sun, C. B. Murray, D. Weller, L. Folks, and A. Moser, "Monodisperse fept nanoparticles and ferromagnetic fept nanocrystal superlattices," *Science*, vol. 287, no. 5460, pp. 1989–1992, 2000.

[263] R. Ghosh Chaudhuri and S. Paria, "Core/shell nanoparticles: Classes, properties, synthesis mechanisms, characterization, and applications," *Chemical Reviews*, vol. 112, pp. 2373–2433, 04 2012.

[264] I. Khan, K. Saeed, and I. Khan, "Nanoparticles: Properties, applications and toxicities," *Arabian Journal of Chemistry*, vol. 12, no. 7, pp. 908–931, 2019.

[265] J. Jana, M. Ganguly, and T. Pal, "Enlightening surface plasmon resonance effect of metal nanoparticles for practical spectroscopic application," *RSC Adv.*, vol. 6, pp. 86174–86211, 2016.

[266] M.-C. Daniel and D. Astruc, "Gold nanoparticles: Assembly, supramolecular chemistry, quantum-size-related properties, and applications toward biology, catalysis, and nanotechnology," *Chemical Reviews*, vol. 104, pp. 293–346, 01 2004.

[267] E. C. Dreaden, A. M. Alkilany, X. Huang, C. J. Murphy, and M. A. El-Sayed, "The golden age: gold nanoparticles for biomedicine," *Chem. Soc. Rev.*, vol. 41, pp. 2740–2779, 2012.

[268] M. J. Mitchell, M. M. Billingsley, R. M. Haley, M. E. Wechsler, N. A. Peppas, and R. Langer, "Engineering precision nanoparticles for drug delivery," *Nature Reviews Drug Discovery*, vol. 20, no. 2, pp. 101–124, 2021.

[269] X. Han, K. Xu, O. Taratula, and K. Farsad, "Applications of nanoparticles in biomedical imaging," *Nanoscale*, vol. 11, pp. 799–819, 2019.

[270] E. C. Dreaden, M. A. Mackey, X. Huang, B. Kang, and M. A. El-Sayed, "Beating cancer in multiple ways using nanogold," *Chem. Soc. Rev.*, vol. 40, pp. 3391–3404, 2011.

[271] B. Chu and T. Liu, "Characterization of nanoparticles by scattering techniques," *Journal of Nanoparticle Research*, vol. 2, no. 1, pp. 29–41, 2000.

[272] S. Mourdikoudis, R. M. Pallares, and N. T. K. Thanh, "Characterization techniques for nanoparticles: comparison and complementarity upon studying nanoparticle properties," *Nanoscale*, vol. 10, pp. 12871–12934, 2018.

[273] M. Gallagher-Jones, C. S. B. Dias, A. Pryor, K. Bouchmella, L. Zhao, Y. H. Lo, M. B. Cardoso, D. Shapiro, J. Rodriguez, and J. Miao, "Correlative cellular ptychography with functionalized nanoparticles at the fe l-edge," *Scientific Reports*, vol. 7, no. 1, p. 4757, 2017.

[274] A. Guo, J. Zhang, Y. Wang, J. Fan, B. He, J. Wang, R. Tai, X.-J. Liang, and H. Jiang, "Nanoscale detection of subcellular nanoparticles by x-ray diffraction imaging for precise quantitative analysis of whole cancer cells," *Analytical Chemistry*, vol. 93, pp. 5201–5210, 03 2021.

[275] Y. Takahashi, A. Suzuki, N. Zettsu, Y. Kohmura, K. Yamauchi, and T. Ishikawa, "Multiscale element mapping of buried structures by ptychographic x-ray diffraction microscopy using anomalous scattering," *Applied Physics Letters*, vol. 99, no. 13, p. 131905, 2011.

[276] R. Hoppe, J. Reinhardt, G. Hofmann, J. Patommel, J.-D. Grunwaldt, C. D. Damsgaard, G. Wellenreuther, G. Falkenberg, and C. G. Schroer, "High-resolution chemical imaging of gold nanoparticles using hard x-ray ptychography," *Applied Physics Letters*, vol. 102, no. 20, p. 203104, 2013.

[277] J. B. Vines, J.-H. Yoon, N.-E. Ryu, D.-J. Lim, and H. Park, "Gold nanoparticles for photothermal cancer therapy," *Frontiers in Chemistry*, vol. 7, 2019.

[278] A. Salek Maghsoudi, S. Hassani, M. Rezaei Akmal, M. R. Ganjali, K. Mirnia, P. Norouzi, and M. Abdollahi, "An electrochemical aptasensor platform based on flower-like gold microstructure-modified screen-printed carbon electrode for detection of serpin a12 as a type 2 diabetes biomarker.," *Int J Nanomedicine*, vol. 15, pp. 2219–2230, 2020.

[279] P. Singh, Y. J. Kim, C. Wang, R. Mathiyalagan, and D. C. Yang, "Microbial synthesis of flower-shaped gold nanoparticles.," *Artif Cells Nanomed Biotechnol*, vol. 44, pp. 1469–1474, Sep 2016.

[280] S. Sasidharan, R. Poojari, D. Bahadur, and R. Srivastava, "Embelin-mediated green synthesis of quasi-spherical and star-shaped plasmonic nanostructures for antibacterial activity, photothermal therapy, and computed tomographic imaging," *ACS Sustainable Chemistry & Engineering*, vol. 6, pp. 10562–10577, 08 2018.

[281] M. Dierolf, P. Thibault, A. Menzel, C. M. Kewish, K. Jefimovs, I. Schlichting, K. von König, O. Bunk, and F. Pfeiffer, "Ptychographic coherent diffractive imaging of weakly scattering specimens," *New Journal of Physics*, vol. 12, p. 035017, mar 2010.

[282] J. Hubbell and S. Seltzer, "Tables of x-ray mass attenuation coefficients and mass energy-absorption coefficients." [Online] Available: http://physics.nist.gov/xaamdi, 2004.

[283] J. N. Clark, X. Huang, R. J. Harder, and I. K. Robinson, "Continuous scanning mode for ptychography," *Opt. Lett.*, vol. 39, pp. 6066–6069, Oct 2014.

[284] X. Huang, H. Miao, J. Steinbrener, J. Nelson, D. Shapiro, A. Stewart, J. Turner, and C. Jacobsen, "Signal-to-noise and radiation exposure considerations in conventional and diffraction x-ray microscopy," *Opt. Express*, vol. 17, pp. 13541–13553, Aug 2009.

[285] A. Kale and B. Karthick, "The diatoms," *Resonance*, vol. 20, no. 10, pp. 919–930, 2015.

[286] C. Field, M. Behrenfeld, J. Randerson, and P. Falkowski, "Primary production of the biosphere: integrating terrestrial and oceanic components.," *Science*, vol. 281, pp. 237–240, Jul 1998.

[287] A. M. Korsunsky, Y. D. Bedoshvili, J. Cvjetinovic, P. Aggrey, K. I. Dragnevski, D. A. Gorin, A. I. Salimon, and Y. V. Likhoshway, "Siliceous diatom

frustules – a smart nanotechnology platform," *Materials Today: Proceedings*, vol. 33, pp. 2032–2040, 2020. 10th International Conference on Key Engineering Materials 2020.

[288] Y. Bedoshvili, K. Gneusheva, M. Popova, A. Morozov, and Y. Likhoshway, "Anomalies in the valve morphogenesis of the centric diatom alga Aulacoseira islandica caused by microtubule inhibitors," *Biology Open*, vol. 7, 08 2018. bio035519.

[289] A. I. Salimon, P. V. Sapozhnikov, J. Everaerts, O. Yu. Kalinina, C. Besnard, C. Papadaki, J. Cvjetinovic, E. S. Statnik, Y. Kan, P. Aggrey, V. Kalyaev, M. Lukashova, P. Somov, and A. M. Korsunsky, "A mini-atlas of diatom frustule electron microscopy images at different magnifications," *Materials Today: Proceedings*, vol. 33, pp. 1924–1933, 2020. 10th International Conference on Key Engineering Materials 2020.

[290] J. E. N. Dolatabadi and M. de la Guardia, "Applications of diatoms and silica nanotechnology in biosensing, drug and gene delivery, and formation of complex metal nanostructures," *TrAC Trends in Analytical Chemistry*, vol. 30, no. 9, pp. 1538–1548, 2011. On-site and In-Vivo Special Issue.

[291] M. Mishra, A. P. Arukha, T. Bashir, D. Yadav, and G. B. K. S. Prasad, "All new faces of diatoms: Potential source of nanomaterials and beyond," *Frontiers in Microbiology*, vol. 8, 2017.

[292] C. E. Hamm, R. Merkel, O. Springer, P. Jurkojc, C. Maier, K. Prechtel, and V. Smetacek, "Architecture and material properties of diatom shells provide effective mechanical protection," *Nature*, vol. 421, no. 6925, pp. 841–843, 2003.

[293] A. M. Korsunsky, P. V. Sapozhnikov, J. Everaerts, and A. I. Salimon, "Nature's neat nanostructuration: The fascinating frustules of diatom algae," *Materials Today*, vol. 22, pp. 159–160, 2019.

[294] A. M. Korsunsky, O. Y. Kalinina, P. V. Sapozhnikov, J. Everaerts, and A. I. Salimon, "Pyrite 'poste restante': Intra-diatom framboids," *Materials Today*, vol. 32, pp. 293–294, 2020.

[295] A. Gibaud, J. Villanova, O. Cherkas, A. Bulou, L. K. Ouanssi, A. Mcheik, S. Cassaignon, P. Lopez, and S. Berthier, "Analysis of diatoms by holotomography," *Surfaces and Interfaces*, vol. 17, p. 100358, 2019.

[296] K. Giewekemeyer, M. Beckers, T. Gorniak, M. Grunze, T. Salditt, and A. Rosenhahn, "Ptychographic coherent x-ray diffractive imaging in the water window," *Opt. Express*, vol. 19, pp. 1037–1050, Jan 2011.

[297] C. Rau, S. Marathe, A. J. Bodey, M. Storm, D. Batey, S. Cipiccia, P. Li, and R. Ziesche, "Operando and high-throughput multiscale-tomography," in *Developments in X-Ray Tomography XIII* (B. Müller and G. Wang, eds.), vol. 11840, pp. 192 – 200, International Society for Optics and Photonics, SPIE, 2021.

[298] R. M. Crawford, "The diatom genus aulacoseira thwaites: its structure and taxonomy," *Phycologia*, vol. 20, no. 2, pp. 174–192, 1981.

[299] M. Guizar-Sicairos, A. Diaz, M. Holler, M. S. Lucas, A. Menzel, R. A. Wepf, and O. Bunk, "Phase tomography from x-ray coherent diffractive imaging projections," *Opt. Express*, vol. 19, pp. 21345–21357, Oct 2011.

[300] M. Kahnt, J. Becher, D. Brückner, Y. Fam, T. Sheppard, T. Weissenberger, F. Wittwer, J.-D. Grunwaldt, W. Schwieger, and C. G. Schroer, "Coupled ptychography and tomography algorithm improves reconstruction of experimental data," *Optica*, vol. 6, pp. 1282–1289, Oct 2019.

[301] P. Li and A. Maiden, "Multi-slice ptychographic tomography," *Scientific Reports*, vol. 8, no. 1, p. 2049, 2018.

[302] J. C. da Silva, K. Mader, M. Holler, D. Haberthür, A. Diaz, M. Guizar-Sicairos, W.-C. Cheng, Y. Shu, J. Raabe, A. Menzel, and J. A. van Bokhoven, "Assessment of the 3 d pore structure and individual components of preshaped catalyst bodies by x-ray imaging.," *ChemCatChem*, vol. 7, pp. 413–416, Feb 2015.

[303] W. De Boever, A. Diaz, H. Derluyn, T. De Kock, J. Van Stappen, J. Dewanckele, T. Bultreys, M. Boone, T. De Schryver, E. T. Skjønsfjell, M. Holler, D. W. Breiby, and V. Cnudde, "Characterization of composition and structure of clay minerals in sandstone with ptychographic x-ray nanotomography," *Applied Clay Science*, vol. 118, pp. 258–264, 2015.

[304] D. C. Ghiglia and M. D. Pritt, *Two-dimensional phase unwrapping : theory, algorithms, and software*. Wiley-Interscience publication, New York ; Chichester: Wiley, 1998.

[305] I. Zanette, R. Clare, D. Eastwood, C. Venkata, F. Pfeiffer, P. Cloetens, and P. Thibault, "Phase-vortex removal for quantitative x-ray nanotomography with near-field ptychography," *Phys. Rev. Applied*, vol. 14, p. 064078, Dec 2020.

[306] M. Odstrčil, M. Holler, J. Raabe, and M. Guizar-Sicairos, "Alignment methods for nanotomography with deep subpixel accuracy," *Opt. Express*, vol. 27, pp. 36637–36652, Dec 2019.

[307] D. Ress, M. L. Harlow, M. Schwarz, R. M. Marshall, and U. J. McMahan, "Automatic acquisition of fiducial markers and alignment of images in tilt series for electron tomography," *Journal of Electron Microscopy*, vol. 48, pp. 277–287, 01 1999.

[308] J. Frank and B. F. McEwen, *Alignment by Cross-Correlation*, pp. 205–213. Boston, MA: Springer US, 1992.

[309] D. Gürsoy, Y. P. Hong, K. He, K. Hujsak, S. Yoo, S. Chen, Y. Li, M. Ge, L. M. Miller, Y. S. Chu, V. De Andrade, K. He, O. Cossairt, A. K. Katsaggelos, and C. Jacobsen, "Rapid alignment of nanotomography data using joint iterative reconstruction and reprojection," *Scientific Reports*, vol. 7, no. 1, p. 11818, 2017.

[310] J. Dengler, "A multi-resolution approach to the 3d reconstruction from an electron microscope tilt series solving the alignment problem without gold particles," *Ultramicroscopy*, vol. 30, no. 3, pp. 337–348, 1989.

[311] M. Guizar-Sicairos, J. J. Boon, K. Mader, A. Diaz, A. Menzel, and O. Bunk, "Quantitative interior x-ray nanotomography by a hybrid imaging technique," *Optica*, vol. 2, pp. 259–266, Mar 2015.

[312] F. Pfeiffer, C. Kottler, O. Bunk, and C. David, "Hard x-ray phase tomography with low-brilliance sources," *Phys. Rev. Lett.*, vol. 98, p. 108105, Mar 2007.

[313] A. C. Kak and M. Slaney, *Principles of computerized tomographic imaging*, vol. 33 of *Classics in Applied Mathematics*. Philadelphia: Society for Industrial and Applied Mathematics, 2001.

[314] A. Andersen and A. Kak, "Simultaneous algebraic reconstruction technique (sart): A superior implementation of the art algorithm," *Ultrasonic Imaging*, vol. 6, no. 1, pp. 81–94, 1984.

[315] M. Dierolf, *Ptychographic X-ray Microscopy and Tomography*. PhD thesis, Technische Universitat Munchen, 2015.

[316] S. A. Spaulding, M. G. Potapova, I. W. Bishop, S. S. Lee, T. S. Gasperak, E. Jovanoska, P. C. Furey, and M. B. Edlund, "Diatoms.org: supporting taxonomists, connecting communities," *Diatom Research*, vol. 36, no. 4, pp. 291–304, 2021.